ISBN 978-82-326-2194-1 (printed version)
ISBN 978-82-326-2195-8 (electronic version)
ISSN 1503-8181

Doctoral theses at NTNU, 2017:61

Jakob Mahler Hansen

Nonlinear Observers for Inertial Navigation Systems aided by Real-Time Kinematic Global Satellite Navigation System

NTNU
Norwegian University of
Science and Technology
Faculty of Information Technology
and Electrical Engineering
Department of Engineering Cybernetics

NTNU
Norwegian University of
Science and Technology

Doctoral Thesis

Jakob Mahler Hansen

Doctoral theses at NTNU, 2017:61

NTNU

NTNU
Norwegian University of
Science and Technology

Jakob Mahler Hansen

Nonlinear Observers for Inertial Navigation Systems aided by Real-Time Kinematic Global Satellite Navigation System

Thesis for the degree of Philosophiae Doctor

Trondheim, January 2017

Norwegian University of Science and Technology
Faculty of Information Technology and Electrical Engineering
Department of Engineering Cybernetics

NTNU
Norwegian University of
Science and Technology

NTNU
Norwegian University of Science and Technology

Thesis for the degree of Philosophiae Doctor

Faculty of Information Technology and Electrical Engineering
Department of Engineering Cybernetics

ISBN 978-82-326-2194-1 (printed version)
ISBN 978-82-326-2195-8 (electronic version)
ISSN 1503-8181

Doctoral theses at NTNU, 2017:61

Printed by Skipnes Kommunikasjon as

Dedicated to my father

Summary

This thesis is motivated by recent interest in nonlinear observers for navigation. The field of navigation is dominated by the Kalman filter and its variants. However, nonlinear observers offer some advantages, compared to the Kalman filters, which will be highlighted in the thesis.

Nonlinear observers for navigation estimating the position, linear velocity and attitude of a vehicle is of interest. The navigation solutions presented in the following are vehicle independent and can be used for ground, surface and air vehicles, or any moving body in general. However, for the experimental verifications small aircraft will be used as they have fast dynamics and can be seen as worst-case scenarios. The proposed observers will be benchmarked against state-of-the-art Kalman filters to ascertain performance and robustness.

The proposed navigation solutions use inertial measurements to propagate the navigation states, while global navigation satellite system (GNSS) measurements are used for correction of the states. The GNSS measurements will be considered in position as well as range space, allowing for loosely- and tightly-coupled integration. A modular structure is used for the nonlinear observers consisting of an attitude estimator and a translational motion observer (TMO). The attitude estimator represents the attitude as a unit quaternion ensuring resistance to singularities while allowing for semi-global exponential stability results of the observer structure. Global exponential stability results can be obtained by use of hybrid theory and switching. The TMO will be developed to accommodate loose or tight integration without altering the attitude estimator.

The main part of the thesis covers four variants of the nonlinear observer structure. Initially the loosely-coupled observer will be introduced and compared to an extended Kalman filter. Implementation issues, attitude reference vectors and observer gains are considered, while the performance comparison confirms that the nonlinear observer can be used instead of a state-of-the-art state estimator.

The second observer structure to be presented deals with the time delay introduced by the use of GNSS receivers. Due to the computational time and the dissemination time of the electronic signals of the receiver the GNSS measurements are delayed. A measuring approach for the delay is proposed based on timing using satellite time. Two versions of the loosely-coupled observer structure are proposed where the inertial measurements are delayed to correspond with the GNSS measurements, followed by fast simulation for propagating the estimates to current time. Experimental data confirms a significant performance impact compared to uncompensated systems.

The third observer structure introduces a tightly-coupled structure where aiding range and range-rate measurements are utilized. The receiver clock bias is included as a slowly time-varying state. Semi-global exponential stability is achieved by use of nonlinear injection terms. The only linearization takes place when determining the TMO gains by solving a slowly time-varying Riccati equation. Experimental verification confirms the performance to be comparable with the performance of a multiplicative extended Kalman filter. Furthermore, the computational load of the observer is seen to significantly lower the number of operations compared to the state-of-the-art estimator, allowing for implementation on smaller and cheaper platforms.

The fourth observer structure introduces an additional GNSS receiver to be used as a reference base station. The inertial navigation is aided by double-differenced pseudorange, carrier-phase and carrier phase derived Doppler measurements between the two receivers thereby cancelling dominating environmental disturbances. A real-time-kinematic (RTK) solution is thereby formed ensuring high accuracy. Using experimental data the observer using double-differenced GNSS measurements is confirmed to obtain centimetre level accuracy during a 20 minutes flight where high dynamic behaviour is experienced.

The advantages of nonlinear observers compared to Kalman filters cover; proven stability results, reduced need for linearization, and lower computational load, while ensuring high performance. A disadvantage is that the nonlinear observer does not propagate covariance estimates.

Contents

List of figures

List of tables

Preface

This thesis is submitted in partial fulfilment of the requirements for the degree of philosophiae doctor (PhD) at the Norwegian University of Science and Technology (NTNU), Trondheim.

My doctoral studies were conducted at the centre for Autonomous Marine Systems and Operations (NTNU AMOS) at the Department of Engineering Cybernetics (ITK) in the period from August 2013 to January 2017. I would like to thank NTNU AMOS and FRINATEK for sponsoring my doctoral studies. This work was supported by the Norwegian Research Council (projects no. 221666 and 223254) through NTNU AMOS. My supervisor has been Professor Thor I. Fossen (ITK) with co-supervisors Professor Tor Arne Johansen (ITK) and Adjunct Associate Professor Nadezda Sokolova (ITK & SINTEF ICT).

During my PhD studies I had the privilege of visiting Professor Naser El-Sheimy at the University of Calgary. I am very grateful for the hospitality and opportunity offered.

Acknowledgements

During my time at NTNU AMOS I have walked among giants; professors, colleagues, and friends. I have been fortunate to have this opportunity, and owe a great many thanks to the many people who have been directly or indirectly part of my Norwegian adventure. I hope to have grown a couple of inches during my stay at NTNU.

First of all a great thanks to my optimal set of supervisors. With your complementary expertises, inhuman email response time, patience and countless thorough comments, my work has improved tremendously. Thank you for showing me how awe-inspiring working in academia can be. I have a hard time figuring out how I could have had a better supervisor group.

Thanks to all my colleagues at NTNU ITK and NTNU AMOS, who have been a great source of support and reassurance. You have made the good parts more fun and the bad parts tolerable. Thanks especially to Torleiv and Robert for cooperation on papers and projects. Thanks to Kristoffer Gryte for collaboration on papers and the trip to Prague. Thanks to Lars and the team at the UAV lab for making the experiments possible. Thanks to Aiden (SINTEF ICT) for initial input on the navigation payload design. Thanks to the staff at NTNU ITK and NTNU AMOS for helping with all the other stuff we candidates also have to figure out.

Sigurd should be mentioned here with more than a mere thanks. Without him and his wizard-like hardware skills this project would never have been verified so thoroughly with experimental data. I owe more than one beer on this occasion, and countless thanks.

To my collaborators at Czech Technical University in Prague; Prof. Jan Roháč, Ph.D. Ing. M. Šipoš, Mushfiqul Alam and Pavel Brož, a great thanks for the cool experiments and papers we did together.

I would like to thank my family and close friends, who have supported me through the hard parts and shared the good times. Thanks to all the friends, I left behind in Denmark, for accepting my absence. Some special few should be mentioned.

A big thanks goes to Mikkel Viager for keeping me sane with our weekly online meet ups.

To my partners-in-crime; Kim, Signe and Kasper. Our time in the "Danish Asylum" has been truly great. I can honestly say that if we had not shared a house I would never have made it through the first year. Thanks for many hours spend studying together and the endless discussions on relevant (and irrelevant) topics. We have de-cyphered many emails from supervisors and concluded many times that projects can and should not be compared.

To her, Benedikte; my love, my base station, my travel companion. I do not know of anybody who is as patient as you. I am continuously amazed that you tolerate my absence while I fool around in Trondheim. It feels like aeons ago we decided that I should take the opportunity the Ph.D. offered. Every weekend we have had together has been amazing. You took time off your studies to join me for my external stay, which definitely made the stay wonderful. It was amazing to live and explore Canada together. I look forward to new adventures together.

Lastly to my dad for inspiring me to see the world, take on challenges and persist. Although you might think me boring for staying so much inside when I could explore Norway. Your words of wisdom that have stayed with me throughout the studies and which are up for interpretation include; "don't worry about things you cannot change", and "you can only use the time once". Thanks for the endless support.

Trondheim, January 2017 Jakob Mahler Hansen

Nomenclature

Abbreviations

ECEF	Earth-Centered-Earth-Fixed
GNSS	Global Navigation Satellite System
GPS	Global Positioning System
IMU	Inertial Measurement Unit
INS	Inertial Navigation System
NED	North-East-Down
RTK	Real-Time-Kinematic

Symbols

A	Dynamics matrix
b	Angular velocity bias, $[rad/s]$
C	Measurement matrix
e	Injection term
f	Specific force, $[m/s^2]$
K	Observer gain matrix
k	Constant tuning parameter
L	Scaling matrix
l	UWB Geometric distance, $[m]$
N	Integer ambiguity, $[-]$
P	Covariance matrix
p	Position, $[m]$
Q	Measurement covariance matrix
q	Unit quaternion attitude representation
R	State covariance matrix
U	Lyapunov function candidate

v	velocity, $[m/s]$
w	UWB white noise, $[m]$

Greek Symbols

α	UWB rover clock bias
β	GNSS receiver clock bias, $[m]$
χ	Auxiliary state vector
δ	Perturbation term
ϵ	GNSS range atmospheric noise, $[m]$
η	Transformed state vector
λ	Wavelength, $[m]$
μ	UWB range measurement, $[m]$
ν	Vector
ω	Angular velocity, $[rad/s]$
ψ	Geometric distance from satellite to receiver, $[m]$
ρ	Pseudo-range measurement, $[m]$
$\hat{\sigma}$	Attitude observer injection term
φ	Carrier-phase measurement, $[cycles]$
ξ	Auxiliary state

Superscripts

b	Body frame
e	Earth-Centered-Earth-Fixed frame
n	Nort-East-Down frame
r	Rover receiver
s	Base station receiver

Subscripts

i	Satellite number
k	Iteration number

Chapter 1

Introduction

1.1 Motivation

Navigation considers the current position, linear velocity and attitude of an object, and has been an integral part of explorations of all magnitudes, from how to get home from the store, to discovering new continents and visiting other planets. It is important to have reliable and appropriate sensors depending on the application. It might be excessive to have military grade inertial sensors on your step counter, just as it is insufficient for a satellite to only have a map of your home town.

In everyday life navigation is coupled to vehicles, e.g. cars, ships and planes, which commonly use inertial sensors for dead reckoning aided by global navigation satellite systems (GNSS). This is often sufficient for determining position and linear velocity, as long as there is an unobstructed view of the sky. For attitude estimation additional sensors might be required such as; magnetometers, flow sensors, camera systems, specific force, etc.

In recent years interest in Unmanned Aerial Vehicles (UAVs), Autonomous Underwater Vehicles (AUVs), and Unmanned Surface Vehicles (USVs) have been increasing for applications such as mapping and monitoring. The advantages of UAVs are the low cost compared to a manned flight and the reduced risk to personnel. The motivation for accurate navigation is here reflected by the possible applications for UAVs.

The applications for UAVs are diverse and abundant with innovative solutions to previously costly challenges. In the oil and gas industry the interest for using UAVs in monitoring of platforms and areas of interest is motivated by an ambition to reduce the number of surface vessels. A reduction of surface vessels in favour of UAVs will result in lower emissions and a reduction in cost. UAVs can also be used to expand the area of operation. In Fig. 1.1 some applications connected to Arctic drilling for oil are illustrated. Some general applications for UAVs include:

Planning: As shown in the top right corner of Fig. 1.1 UAVs can be used for planning in challenging areas, allowing for snap shot georeferencing over areas of interest. This can be used for mission aiding such as navigation of large vessels in Arctic regions where a UAV might provide an overview of upcoming obstacles and

help plan avoidance of ice fields. This application presents a significant cost saving as a the number of mission hours and manned flights can be reduced. A challenge in Arctic regions is the limited satellite coverage, often resulting in GNSS outage facilitating the need for robust navigation solutions.

Surveillance: The UAV might be preferred for surveillance in dangerous or inaccessible environments to eliminate the risk of human injury or loss of life. Such surveillance can be used to aid in search and rescue operations from house fires to catastrophes such as reactor decay or volcanic eruption.

Transport: Precision drop of packages, such as sensor payloads on icebergs (see Fig. 1.1 top left) facilitates large scale deployment. In such applications as iceberg drift monitoring the UAV can also be used to transfer information by broadcasting or receiving data when flying over areas with deployed sensory payloads. This can also be used between vehicles or vessels in areas of sparse satellite coverage or when using short range transmitters.

Monitoring: Monitoring of off-site structures, such as wind turbines, is of interest both in offshore and land applications where manned inspection of the propeller is costly and time consuming. This application require high accuracy and precision to guarantee operational safety for the equipment.

Figure 1.1: Arctic exploration and drilling assisted by UAVs, Copyright: Bjarne Stenberg, NTNU.

For all of these applications automated landing of the UAV is of interest to ensure repeatability and safe operations. Automated landing of UAVs can be achieved using vertically placed nets at landing sites or on the side of ships, and requires high accuracy.

In high latitude regions the satellite coverage is sparse due to the trajectories of the satellites not crossing the pole, thereby leaving a large area around the poles uncovered. In Fig. 1.2 sky plots over the North pole and Trondheim depicts the GPS satellite trajectories, where the receiver is at the center and the concentric circles show the elevation of the satellites. It is clear that operation at high latitude is limited by poor satellite coverage. The navigation systems must therefore be equipped to handle satellite outages and low numbers of available satellites, in order to safely operate in high latitude areas.

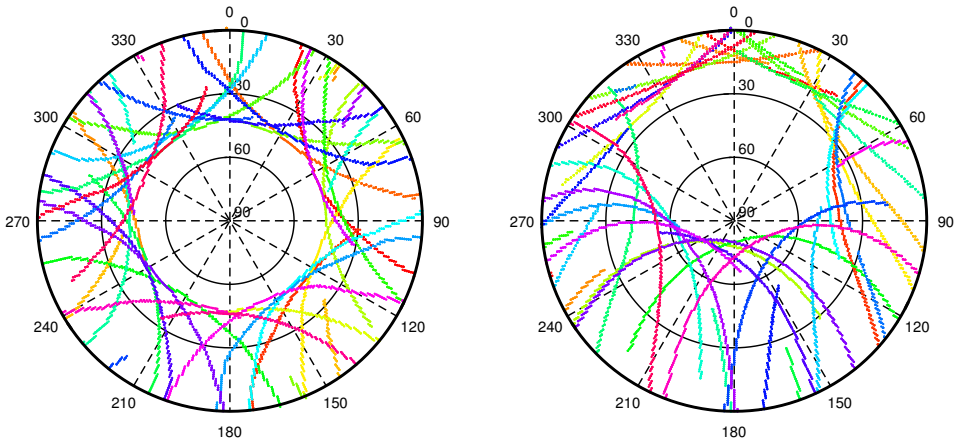

(a) Satellite coverage at the North Pole.

(b) Satellite coverage at Trondheim.

Figure 1.2: Satellite paths (azimuth and elevation) over two locations for 10 hours. (Thanks to Hans-Martin Heyn, NTNU AMOS, for the North Pole data.)

The objective of this thesis is to develop state estimators for use in the air, sea surface or on ground for mapping and monitoring. The focus will be on navigation using nonlinear observers as an alternative to Kalman filters. The nonlinear observers proposed will be compared to Kalman filters ensuring that the performance is at least comparable, while also the computational load will be investigated. A reduction in computational load will allow for implementation on smaller and cheaper platforms. Both loosely- and tightly-coupled systems will be considered where a inertial navigation system (INS) is aided by satellite measurements. In the loosely-couple scenario the focus will be the time-delay introduced by the GNSS receiver and how to improve performance by taking the delay into account in the observer. A tightly-coupled observer will be proposed and further augmented to include an additional base station receiver to counteract atmospheric disturbances.

The nonlinear observers and methods proposed here are vehicle independent and can be used for all types of vehicles and moving bodies in general. In the following the performance of the proposed methods will be tested on small aircraft

as they have fast dynamics and can be considered worst-case scenarios.

1.2 Background

Navigation of vehicles often rely on sensory information from multiple sources, and can include measurements of a vehicle's acceleration, angular rate and velocity. The measurements are diverse and covers different aspects of the vehicle behaviour. By including multiple sensors it is possible to estimate the position, linear velocity and attitude of the vehicle. The position and velocity can be determined directly by a satellite receiver, however, these are vulnerable to outages, e.g. a car going through a tunnel. The navigation of vehicles is therefore based on inertial navigation where high rate sensors are used to determine the difference in position, while satellite receivers can be employed to help the navigation system by correcting when the estimation diverges off course. In the following the most common ways of integrating the various sensors will be introduced.

1.2.1 State-of-the-art of state estimators

Many physical systems are considered partly closed systems with no means of measuring internal signals, where only the inputs and outputs are available. However, it is often of interest to know the current value of the internal states, e.g. such that appropriate action can be taken using a control element. There might be multiple internal states and only a few measured outputs due to lack of appropriate sensors, cost, or insufficient data rate. The state estimation problem describes the need to estimate variables of interest in a model that are not otherwise directly observable, Farrell [52].

The model states describe the dominating dynamics of the system, while less important dynamics might be removed for simplicity. The states for navigation systems often include position, linear velocity and attitude of the vehicle, while inclusion of auxiliary states is possible. These auxiliary states might describe specific force of the vehicle or inertial sensor errors, Groves [76].

State estimators consists of two categories; "filters" and "observers". Filters take the stochastic approach to finding the current state values and consider the measurement and state noise as well as the covariance estimate of the states. Observers use a deterministic approach based on control theory focusing on the stability of the proposed dynamics equations. In both cases a model of the physical system is duplicated to propagate the states while comparing with the system outputs. In the literature the terms "filter" and "observer" are used somewhat interchangeably.

The following sections will include a review of previous work on Kalman filters and nonlinear observers for navigation.

Kalman filter review

Modern filtering theory began around 1959-60 with publications by Swerling [163], and Kalman [105], presenting error propagation methods using a minimum variance estimation algorithm for linear systems. The discrete method presented by R. E.

Kalman have received large attention and is now a coined term in multiple fields, Hendricks et al. [90].

The Kalman filter (KF) introduced a recursive algorithm for state estimation of linear systems, which is optimal in the sense of minimum variance or least square error. Changing from analytical solutions to a recursive algorithm had the advantage of being easily implementable in digital computers. Another advantage was that the previous non-recursive estimation methods used the entire measurement set, whereas the recursive estimation of the KF use current measurements as well as prior state estimates to propagate the states from an initial value. The KF is therefore more computational efficient as it can discard previous measurements and update the state estimates with only the present measurements, Groves [76]. The KF theory was expanded upon in 1961 by Kalman and Bucy [106], introducing a continuous-time variant.

The Kalman filter's stochastic approach to the state estimation problem assumes noise on the measurements as well as the state equations of the filter. This is a well-established state estimation approach, Dissanayake et al. [47], which excels in working with normal-distributed inputs characterized by their mean and covariance values and a linear time-varying state space model in its basic form. A requirement is that the measurements have to be functions of the states, as the residual measurement (the difference between measured and estimated measurements) is used to update the states and keep them from diverging. The process and measurement noise is assumed to be Gaussian white noise. In some cases where the noise of the physical system can not be confirmed to be white, the KF might be augmented, by so called "shaping filters", with additional linear state equations to let the coloured noise be driven by Gaussian white noise, Farrell [52]. In addition to the recursive estimation of the model states the Kalman filter also propagates a covariance matrix describing the uncertainties of the state estimates as well as the correlation between the various states, Groves [76].

Even though the Kalman filter was designed for linear systems, it can be applied to nonlinear systems without changing the structure or the operational principles. However, the optimality of minimal variance of the errors is lost, and the filter is no longer an optimal estimator. The kinematic equations for navigation are inherently nonlinear and must be addressed by nonlinear techniques or approximations to maintain the performance and stability of the modeled system. Nonlinear problems are commonly handled by the Linearised KF (LKF), Extended KF (EKF) or sample-based methods such as unscented KF (UKF) Chen, Gustafsson et al. [37, 80]. The UKF is an extension to nonlinear systems that does not involve an explicit Jacobian matrix, see e.g. Julier and Uhlmann [104]. Probably the most popular of the mentioned methods is the EKF, which has been applied in an enormous number of applications where it achieved excellent performance, p. 210 in Grewal et al. [69]. In the time propagation of the state estimates the EKF uses the nonlinear model. However, for the time propagation of the covariance estimates and in the gain computation the EKF linearises the model around an estimate of the current state using multivariate Taylor expansions to adapt to the nonlinear model; this makes the EKF more susceptible to errors in the initial estimates and modelling errors compared to the KF.

The KF and EKF are seen as the standard theory and are therefore used as

benchmark for comparison when developing new methods. The KF and its variants are widely used in the navigation related literature where a few examples are mentioned here: An introduction to choice of states and sensor alignment consideration can be found in Stimac and Kennedy [162], while Markley [122] considers alternative attitude error representations. For extensive details on Kalman filtering see Brown and Hwang, Farrell, Fossen, Gelb et al., Grewal et al., Groves [28, 52, 55, 62, 69, 76]. Among the extensions to nonlinear systems other examples can be found, e.g. Draganov et al. [50], where a method for evaluating the linearisation quality is presented alongside a Kalman filter extension for nonlinear systems. Studies on time-correlated noise, as opposed to the white noise assumption, without state augmentation have been carried out in e.g. Schmidt [153], Petovello et al. [141]. The adaptive Kalman filter might be used in applications where tuning of the Kalman filter is uncertain at initialization, see Magill, Mehra, Mohammed and Schwarz [118, 125, 129]. If the application is not real-time critical, such as surveying, the estimate can be enhanced by use of a smoother. In Fraser and Potter [56] a forward-smoother was proposed while in Rauch et al. [146] a backwards-smoother was introduced. When nonlinear systems are considered another alternative to the EKF is the particle filter. Particle filters are based on sequential Monte Carlo estimation algorithms, which compared to the Kalman filter are more computationally demanding, however, they are noise distribution independent, see e.g. Doucet and Johansen, Doucet et al., Gordon et al., Gustafsson et al., Ristic et al. [48, 49, 65, 80, 148]. The advantage of the particle filter is its use in nonlinear non-Gaussian systems. However, since this approach is computationally heavy in current navigation systems it is not often used. Therefore, the particle filter is considered outside the scope of this chapter.

Nonlinear observer review

In comparison to the Kalman filter the nonlinear observers have a shorter history, motivated by drawbacks of the KF when applied to nonlinear systems. These drawbacks include: unclear convergence properties, difficulty of tuning, and large computational load.

Nonlinear observers are contrary to the Kalman filters based on a deterministic approach. The noise is not assumed to have specific properties, except that the difference between the measured and estimated signal is smallest when the estimate reflects the true signal. Like the Kalman filter, nonlinear observers commonly utilize an injection term consisting of the difference between measured and estimated system output to drive the observer states toward the true values.

The field of nonlinear observers have expanded within groups dealing with specific problems. Nonlinear attitude estimation has been the focus of extensive research, Batista et al., Batista et al., Grip et al., Mahony et al., Thienel and Sanner [12, 13, 71, 120, 172], see in particular Crassidis et al. [39] for an extensive survey including EKF methods. One method used have centred on the comparison of two attitude measurement vectors in the Body-frame with two corresponding vectors in an Earth-fixed or inertial frame. One such attitude observer was proposed by Salcudean [150], and was later expanded upon by Vik and Fossen [176] to include a gyro bias estimate. A vector-based attitude observer was proposed by Hamel. and

Mahony [81] which depended on inertial measurements, magnetometer readings and GNSS velocity measurements. Expanding on this framework Hua [94] introduced an attitude observer that utilized the derivative of the GNSS velocity as the vehicle acceleration allowing for comparison with accelerometer measurements.

Where the Kalman filter computes new gains for each iteration some nonlinear observers have proven convergence with fixed or slowly time-varying gains, e.g. Grip et al. [72]. This is a computational improvement as the dominating computational burden of the KF is the covariance update which in turn is used for the gain determination, see Section 5.6.1 in Farrell [52].

One of the design challenges of nonlinear observers is the requirement for proven stability. The Kalman filter is globally exponentially stable and optimal in the sense of minimum variance under some conditions for linear systems, while nonlinear approximations, e.g. the extended Kalman filter, in general loose optimality due to linearization of the system around the estimated state trajectory. Nonlinear observers, while presenting strong stability results, are often designed without optimality objectives regarding disturbances. Recently the eXogeneous Kalman Filter (XKF) has been proposed to account for these drawbacks, by use of a two-stage estimator framework, see Johansen and Fossen [99]. In the XKF a cascade is formed by a globally stable nonlinear observer and a linearized Kalman filter, where the KF is linearized about the state estimate of the nonlinear observer. The XKF retains global stability properties while also estimating the covariance of the states, thereby combing the advantages of the nonlinear observer and the KF. While the stability properties are proven for nonlinear observers, stochastic properties can only be experimentally verified, as no stochastic model is assumed.

The field of nonlinear observers is recent and rapidly expanding. A few publications within navigation are mentioned here: Considerations of a nonlinear attitude estimator for use on a small aircraft was presented in Hua et al. [95], while a globally exponentially stable observer for long baseline navigation was presented in Batista [10] with clock bias estimation in a tightly-coupled system.

1.2.2 Loosely- and tightly-coupled systems

The most common integration scheme is the loosely-coupled approach where inertial measurements are integrated with GNSS position and velocity estimates. The position and velocity estimates used in a loosely-coupled system are supplied by a GNSS receiver, where the navigation solution is determined by an integration algorithm, most typically a Kalman filter. Due to the unknown tuning of the filter in the GNSS receiver it can be preferred to use the measurements from the satellites directly in navigation systems to optimize its performance. A tightly-coupled integration scheme can be utilized where inertial measurements are integrated with pseudorange, carrier-phase and Doppler measurements, thereby correcting the state estimates using measurements in range domain rather than the position domain. The measurement vector is expanded as measurements from all available satellites are considered, whereas for the loosely-coupled system the receiver would take care of the satellite signals. In general tightly-coupled systems have higher performance than loosely-coupled systems as a higher level of control of the nuisance and noise terms can be accounted for. A further advantage of the tightly-coupled system

is that aiding from even a few satellites can be used, whereas for loosely-coupled systems at least four satellites must be available for position determination in the receiver and thereby aiding. This increases the robustness of tightly-coupled solutions to satellite obstruction. When using carrier-phase measurements in a tightly-coupled system an offset represented by a fixed number of wavelengths, denoted the integer ambiguity, is introduced in the range measurement.

Tightly-coupled multi-sensor systems using filters, as the Extended Kalman Filter (EKF), have been subject of extensive research, see Groves [76] and Farrell [52]. In George and Sukkarieh [63] enhancements for a tightly-coupled integration on small unmanned vehicles (UAVs) are presented. A low-cost integrated GPS/IMU system using a Micro-Electro-Mechanical System (MEMS) IMU while adopting a nonlinear KF is developed in Li et al. [117], while Grejner-Brzezinska et al. [67] considers a tightly-coupled integration using a Kalman filter for accurate mapping using an aerial platform. A comparative study of loosely, tightly and ultra-tightly coupled systems was investigated by Gautier and Parkinson [61] using a wide range of inertial sensor grades, and the GIGET tool.

Higher accuracy can be achieved by taking atmospheric disturbances into account, such as ionospheric and tropospheric delay of the satellite signals. These disturbances can, to some extend, be modelled in nominal conditions, or mitigated by using dual or multi frequency GNSS receivers. Multi-frequency receivers facilitate estimation and compensation of the ionospheric delay, see Section 8.6 in Farrell [52] or Grejner-Brzezinska and Toth [66]. However, for low-cost applications the high cost of the necessary receiver front-ends presently prevents wide applicability of multi-frequency systems.

Inclusion of the carrier-phase measurement allows for achieving higher accuracy if the introduced integer ambiguities can be resolved. In Hirokawa and Ebinuma [91] a low-cost multiple GNSS antenna configuration is utilized to aid in the ambiguity resolution performed on the basis of the estimated attitude. Multiple approaches for estimation of the integer ambiguities have been studied, e.g. Teunissen [169], Teunissen. et al. [170], Teunissen et al. [171] proposing the widely used LAMBDA method, or Chen et al. [36] where a computationally efficient method was proposed using a common-position-shift approach. In Chen et al. [33] an approach using an aiding INS to resolve the ambiguities was investigated, while Chen et al. [34] proposes a near-real-time method based on measurements from multiple epochs. Another method is the real-time-kinematic (RTK) solution where a dual-receiver configuration with a stationary base station and a static or moving rover (i.e. a vehicle) is used. The base station broadcasts its satellite measurements to the rover, which in turn performs differencing of the measurements for use in the navigation system. With a known base station position precise positioning of the rover is possible. It is also possible to utilize a moving base station: if the base station position is always known the precision can be retained, otherwise inertial sensors might be added to the base station to offer similar state estimation as for the rover. The RTK solution operates under the assumption that the separation between the rover and base station (called the baseline) is short such that the atmospheric signal delays observed by the two receivers are similar. In Takasu and Yasuda [164] and Takasu and Yasuda [165] a low-cost open source RTK solution is developed. Some environments can decrease the accuracy of the acquired solution due to satellite blockage,

which is the topic of Bahrami and Zeibart [6] where Doppler measurements are used to aid in the RTK computations. Multipath caused by reflected satellite signals can also cause errors in the pseudorange and carrier-phase measurements, but can to some extent be remedied, e.g. by the proposed method of Miura et al. [127]. In Wendel et al. [179] the time differenced carrier-phase measurements are used instead of delta-range measurements in a tightly-coupled single receiver system, showing improvements to velocity and attitude estimation, while introduction of a base station was encouraged to obtain centimetre accuracy. Other approaches include the precise point positioning (PPP), see e.g. Watson et al. [177], or differential GNSS, see e.g. Farrell et al. [53], which can give results with precision similar to RTK systems.

When low-cost sensors are used, care should be taken to avoid long time periods of satellite obstruction, as the inertial sensors will introduce fast diverging state estimates. The measurement noise levels will be higher for low-cost sensors, which will introduce large output noise and might prevent correct resolution of the phase ambiguities.

Applications for tightly-coupled RTK GNSS/INS integration focused on UAVs could include monitoring of wind turbines or oil and gas platforms requiring high accuracy, where a base station could be placed on the platform ensuring short baselines. Applications such as automated landing in vertically placed nets at landing sites or on ships could also be of interest. Another example might be mapping and surveying of an area in front of a ship in Arctic regions, thereby allowing for path planning around ice fields. These applications facilitates the UAV being close to the base station making the assumption of similar experienced atmosphere valid.

Previously only loosely-coupled GNSS/INS nonlinear observers have been proposed, leaving the EKF based observers to dominate the field of tight integration. However, recently nonlinear observers have gained interest for tightly-coupled GNSS/INS integration e.g. Batista [10], Batista [11], Batista et al. [14], Batista et al. [17], where long baseline configurations have been considered.

1.3 Publications

The results presented in this thesis are based on the following book chapter, journal papers and conference papers:

1.3.1 Book chapter

- [85] J. M. Hansen, J. Roháč, M. Šipoš, T. A. Johansen and T. I. Fossen, "Validation and Experimental Testing of Observers for Robust GNSS-Aided Inertial Navigation", chapter 6 in "Recent Advances in Robotic Systems" edited by Guanghui Wang, ISBN 978-953-51-2571-6, Print ISBN 978-953-51-2570-9, InTech, September 9, 2016.

1.3.2 Journal papers

- [87] J. M. Hansen, T. A. Johansen, N. Sokolova and T. I. Fossen, "Nonlinear Observer for Tightly-Coupled Integrated Inertial Navigation Aided by RTK-

GNSS Measurements", IEEE Transactions on Control Systems Technology, (submitted).

- [86] J. M. Hansen, T. I. Fossen and T. A. Johansen, "Nonlinear Observer Design for GNSS-Aided Inertial Navigation Systems with Time-Delayed GNSS Measurements", Control Engineering Practice, 2017, (to appear).
- [31] T. H. Bryne, J. M. Hansen, R. H. Rogne, N. Sokolova, T. I. Fossen and T. A. Johansen, "Nonlinear Observers for Integrated INS/GNSS Navigation - Implementation Aspects", IEEE CSM, 2017, (to appear).
- [101] T. A. Johansen, J. M. Hansen and T. I. Fossen, "Nonlinear Observer for Tightly Integrated Inertial Navigation Aided by Pseudo-Range Measurements", ASME Journal of Dynamic Systems, Measurement and Control, Vol. 139, 2017.

1.3.3 Conference papers

- [83] J. M. Hansen, T. I. Fossen and T. A. Johansen, "Nonlinear Observer for INS Aided by Time-Delayed GNSS Measurements: Implementation and UAV Experiments", Proc. of International Conference on Unmanned Aircraft Systems, Denver, 2015, pp. 157-166.
- [84] J. M. Hansen, T. A. Johansen, T. I. Fossen, "Tightly Coupled Integrated Inertial and Real-Time-Kinematic Positioning Approach Using Nonlinear Observer", American Control Conference, Boston, 2016, pp. 5511-5518.
- [77] K. Gryte, J. M. Hansen, T. A. Johansen, T. I. Fossen, "Robust Navigation of UAV using Inertial Sensors Aided by UWB and RTK GPS", Proc. of the AIAA Guidance, Navigation, and Control Conference, 2017, (to appear).
- [100] T. A. Johansen, A. Cristofaro, K. L. Sørensen, J. M. Hansen and T. I. Fossen, "On Estimation of Wind Velocity, Angle-of-Attack and Sideslip Angle of Small UAVs using Standard Sensors", Proc. of International Conference on Unmanned Aircraft Systems, Denver, 2015, pp. 510-519.

1.4 Contributions of the Thesis

The thesis is organised into seven chapters and four appendices. The topic and contribution of the chapters are presented in the following.

Chapter 2

Topic: This chapter serves as a background for the following chapters and includes introduction of; the utilized coordinate frames, the strapdown navigation equations, and the signal structure and error sources of GNSS measurements in position and range domain.
The content of this chapter is based on literature by other authors; [55], [76], [52], [126], [175], and is included here as background material.

Chapter 3

Topic: Inertial navigation aided by position and velocity measurements provided by a Global Navigation Satellite System (GNSS) receiver is widely used for navigation of various vehicle types. The integration of the inertial and global position measurements has previously been achieved by use of Kalman filters. However, a recent trend from control theory is to propose nonlinear observers for estimating the position, velocity and attitude of a vehicle.

Contributions: This chapter presents a comparative study of the Extended Kalman filter and a previously published nonlinear observer. The two state estimators will be compared on performance using experimental data from flights with Unmanned Aerial Vehicles (UAVs). Furthermore, implementation issues will be discussed for the nonlinear observer. The content is based on [31] and [85].

Chapter 4

Topic: Global navigation satellite system receivers suffer from an internal time-delay of up to several hundred milliseconds leading to a degeneration of position accuracy in high-dynamic systems. The delay is due to the translation and computation of the satellite measurements to position information. The effect of the delay depends on the velocity of the receiver, i.e. with high velocity the distance between the actual and measured position is large. For pedestrian use the error introduced by the delay is insignificant whereas for high speed applications, such as cars or planes, the error can be several meters.

Contributions: This chapter presents a nonlinear observer structure for estimating position, linear velocity, and attitude (PVA) as well as gyro bias, using inertial measurements and time-delayed GNSS measurements. The observer structure consists of four parts; a) attitude and gyro bias estimation, b) time-delayed translational motion observer estimating position and linear velocity, c) input delays for inertial and magnetometer measurements, and d) a faster than real-time simulator. The delayed PVA and gyro bias estimates are computed using a semi-globally exponentially stable (SGES) nonlinear observer. The high-rate inertial measurements are delayed and synchronized with the GNSS measurements in the state observer. The fast simulator integrates the inertial measurements from the delayed state estimate to provide a state estimate at current time. The sensor measurements are carefully synchronized and the estimation procedure for the GNSS receiver delay is discussed. Experimental data from a small aircraft are used to validate the results. The chapter is based on the publications [83] and [86].

Chapter 5

Topic: In a tightly-coupled system the inertial navigation is aided by the range and range-rate measurements from the GNSS receiver rather than the position and velocity estimates. The aiding measurements are thereby changed

from position to range domain, with the advantage of circumventing the unknown filters in the GNSS receiver. The tightly-coupled system requires information about the placement of the satellites in the constellation and corrections for the measurements are needed to obtain accurate position estimates.

Contributions: A nonlinear observer for inertial navigation aided by GNSS range and range-rate measurements is proposed. The attitude estimator presented with the loosely-coupled nonlinear observer is utilized with a translational motion observer based on range and range-rate measurements from a satellite constellation, making the observer tightly coupled. An initialization method is proposed for the observer, and experimental data from a UAV flight are used for verification and comparison with a Multiplicative Extended Kalman Filter (MEKF). Furthermore, the computational load of the proposed nonlinear observer is compared to the MEKF. The results of this chapter has been published in [101].

Chapter 6

Topic: In GNSS/INS systems the atmospheric disturbances contribute with significant error sources to the range measurements. By introducing a base station, consisting of a GNSS receiver, close to the area of interest the atmospheric effects can be cancelled by differencing the measurements between the vehicle and base station receivers.

Contributions: In this chapter a nonlinear observer for inertial navigation aided by dual receiver pseudorange, carrier-phase and carrier phase derived Doppler measurements is proposed. A double-differenced scenario is considered where satellite measurements are differenced between the vehicle and base station, and additionally differenced with a reference satellite to cancel the clock range bias. The proposed observer is experimentally verified using flight data from a UAV. The results of this chapter is based on [84], [77] and [87].

Chapter 7

This chapter presents concluding remarks and offers some suggestions for further work.

Appendix A

The equations relevant for determination of satellite position and velocity is included for completeness.

Appendix B

A description of the navigation payload used for acquiring experimental data is explained. Component overview, hardware design and accurate timestamping is introduced.

Appendix C

Implementation schemes for the loosely- and tightly-coupled translational motion observers, as well as the attitude observer are presented.

Appendix D

This appendix offers larger copies of previously included figures for ease of reading and detailed viewing.

Chapter 2

Navigation Kinematics and GNSS/INS Preliminaries

Estimating the position, linear velocity and attitude (PVA) of a vehicle is the foundation of navigation. This chapter will introduce the required background for the thesis and understanding of the observers proposed in the following chapters. The observers proposed are vehicle independent and can be used for any type of vehicle satisfying the fundamental requirements: a) its movement and rotation are governed by the general kinematic equations, b) inertial measurements from a strapdown unit are available, and c) global positioning measurements are acquired.

The position of the vehicle is either determined as a local or global coordinate in 3D space while the attitude relates the orientation of the vehicle relative to some origin. The various coordinate frames used for describing the vehicle position and the obtained measurements will be introduced, as well as the kinematic equations for PVA estimation of the vehicle based on inertial measurements.

The GNSS signal structure and satellite measurements will be presented for use as aiding measurements when integrating inertial navigation with global measurements.

Organization of this Chapter: This chapter is organized as follows. In Section 2.1 the coordinate frames are defined, followed by the general notation used in Section 2.2. Section 2.3 intoduces MEMS-based inertial sensors while Section 2.4 presents the kinematic equations describing vehicle movement and attitude. The GNSS signal structure and positioning is described in Section 2.5, where also the common error sources are described. In Section 2.6 the integration between measurements from inertial sensors and GNSS receivers are explained.

The material in this chapter is largely gathered from [55], [76], [52], [126], [175], and is included here as background to the following chapters.

2.1 Coordinate Frames

The position and attitude of a vehicle can be expressed in various coordinate frames depending on the measurements and the recipient. Some sensors such as GNSS

receivers measure a global position whereas inertial measurements can be used to determine a relative local position increment. Four coordinate frames will be considered (see e.g. [55], [52]):

- **ECI**: The Earth-Centered-Inertial frame, denoted by $\{i\} = [x^i; y^i; z^i]$, is a non-accelerating frame with origin at the Earth's centre of mass. The z^i axis points up through the terrestrial North Pole, with x^i pointing towards the vernal equinox and y^i completing a right-handed coordinate system. The x^i and y^i axis lie in the equatorial plane. The ECI frame does not rotate with the Earth.
- **ECEF**: The Earth-Centered-Earth-Fixed frame, $\{e\} = [x^e; y^e; z^e]$, has origin at the Earth's centre of mass and rotates with the Earth such that the x^e-axis always extends at the intersection of the prime median and equator. The rate of rotation, relative to the inertially fixed ECI frame, has angular velocity $\omega_{ie} = 7.2921 \cdot 10^{-5}$ rad/s around the z^e-axis which is always coinciding with the z^i-axis.
- **NED**: The North-East-Down frame is a local reference frame, where the Earth is approximated to a flat surface in a small area, despite the curvature of the Earth. The $\{n\} = [x^n; y^n; z^n]$ has origin at some chosen point which serves as the basis for the tangent plane approximation. The x^n-axis points towards the North pole, z^n points towards the centre of the Earth, and y^n completes a right-handed coordinate system. Alternatively the East-North-Up (ENU) frame can be used. The relation between the e and n origins is given by the two angles latitude and longitude.
- **Body**: The body-frame, $\{b\} = [x^b; y^b; z^b]$, is fixed to the vehicle of interest at the centre of mass, and moves with the vehicle. The position and attitude is therefore expressed relative to another coordinate frame, while linear and angular velocities can be expressed in the body-frame. The three principle axes of a vehicle are depicted in Fig. 2.1, to illustrate the free rotations: roll, pitch and yaw.

A vector in one coordinate frame can be transformed into another frame by multiplication with a 3×3 rotation matrix. The rotation matrix can either be represented by a set of Euler angles or by a four parameter quaternion representation.

2.2 Notation

A column vector with three elements, $x \in \mathbb{R}^3$, has a transpose $x^\intercal$ and vector norm $\|x\|_2$, and is denoted $x := [x_1; x_2; x_3]$. The skew-symmetric matrix, $S(\cdot)$, of the vector x is given as:

$$S(x) := \begin{bmatrix} 0 & -x_3 & x_2 \\ x_3 & 0 & -x_1 \\ -x_2 & x_1 & 0 \end{bmatrix}, \tag{2.1}$$

such that the cross product of two vectors, x_a and x_b, is $x_a \times x_b = S(x_a)x_b$. A unit quaternion, $q = [r_q; s_q]$, consisting of a real part $r_q \in \mathbb{R}$ and a vector part $s_q \in \mathbb{R}^3$, will have the quaternion norm $\|q\|_2 = 1$. A vector $x \in \mathbb{R}^3$ can be expressed as a

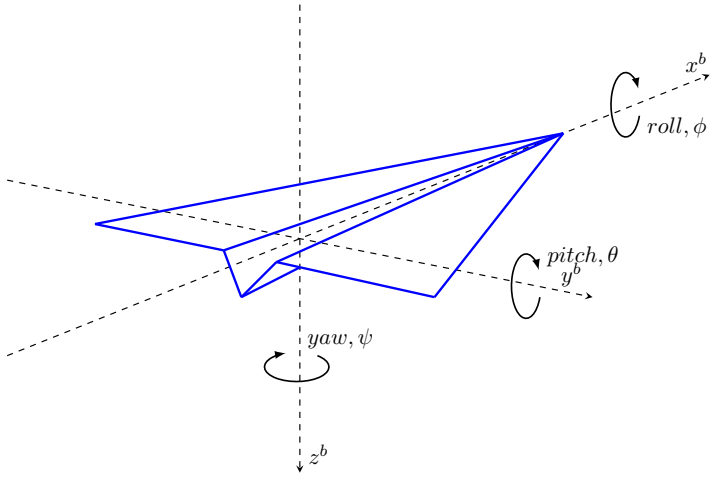

Figure 2.1: The body-frame coordinate system, $\{b\} = [x^b; y^b; z^b]$, with the three principle axes of inertia.

quaternion with zero real part; $\bar{x} = [0; x]$. The product of two quaternions, q_1 and q_2, is given by the Hamiltonian product denoted $q_1 \otimes q_2$:

$$q_1 \otimes q_2 := \begin{bmatrix} s_{q_1} s_{q_2} - r_{q_1}^\intercal r_{q_2} \\ s_{q_1} r_{q_2} + s_{q_2} r_{q_1} + r_{q_1} \times r_{q_2} \end{bmatrix}. \tag{2.2}$$

In the following 0 denotes a zero-matrix of appropriate dimensions, and I_a is an identity matrix with a diagonal elements.

Vectors in one frame can be transformed to another frame by use of a rotation matrix, $R \in \mathbb{R}^3$. For example, a vector in body-frame, v^b, can be related to the corresponding vector in NED-frame, v^n, by;

$$v^n = R_b^n v^b, \qquad v^b = R_n^b v^n, \tag{2.3}$$

where the rotation matrix belongs to the special orthogonal group, $R \in SO(3)$, with $\det(R) = 1$ and $R^{-1} = R^\intercal$. The subscript denotes the frame from which the rotation is initiated, while the superscript denotes the resulting frame.

Rotation between coordinate frames may be represented by either Euler angles, Θ_a^c, or quaternions, q_a^c, describing the rotation from coordinate frame a to c. The Euler angles are given as roll, pitch and yaw; $\Theta = [\phi, \theta, \psi]^\intercal$, as seen in Fig. 2.1. The rotation matrix R_a^c can be determined as $R_a^c = R(\Theta_a^c) = R(q_a^c)$, where:

$$R(\Theta_a^c) := \begin{bmatrix} c\psi c\theta & -s\psi c\phi + c\psi s\theta s\phi & s\psi s\phi + c\psi c\phi s\theta \\ s\psi c\theta & c\psi c\phi + s\phi s\theta s\psi & -c\psi s\phi + s\theta s\psi c\phi \\ -s\theta & c\theta s\phi & c\theta c\phi \end{bmatrix}, \tag{2.4}$$

Here the trigonometric functions have been abbreviated, e.g. $\sin(\phi) = s\phi$ and $\cos(\phi) = c\phi$. The rotation matrix determined from quaternions are given as; $R(q_a^c) := I_3 + 2s_{q_a^c} S(r_{q_a^c}) + 2S(r_{q_a^c})^2$.

It can be difficult for an operator to get an intuitive understanding of position and attitude related to the ECEF-frame, which often facilitate a transformation from ECEF- to NED-frame, when displaying results. The rotation matrix, $R(\Theta_n^e)$, required to rotate a vector from NED- to ECEF-frame depends on the latitude, μ, and longitude, l, of the position, [55]:

$$R(\Theta_n^e) = \begin{bmatrix} -cls\mu & -sl & -clc\mu \\ -sls\mu & cl & -slc\mu \\ c\mu & 0 & -s\mu \end{bmatrix}, \tag{2.5}$$

where abbreviations for the trigonometric functions have been used. The position used in the rotation matrix determination serves as the origin of the NED approximation to the ECEF-frame.

Quaternions can be converted from ECEF- to NED-frame by using the estimated latitude, $\hat{\mu}$, and longitude, $\hat{l}$, of the NED origin, see [72]:

$$\hat{q}_l = \begin{bmatrix} \cos(\hat{l}/2) \\ 0 \\ 0 \\ -\sin(\hat{l}/2) \end{bmatrix}, \quad \hat{q}_\mu = \begin{bmatrix} \cos(\hat{\mu}/2 + \pi/4) \\ 0 \\ \sin(\hat{\mu}/2 + \pi/4) \\ 0 \end{bmatrix}, \quad \hat{q}_b^n = \hat{q}_\mu \otimes \hat{q}_l \otimes \hat{q}_b^e. \tag{2.6}$$

The Euler angle representation of attitude is often preferred by operators as they are intuitively understandable, however, the time derivatives are limited to pitch not being $\pm 90°$ which introduces singularities. Due to the singularities the Euler angles can only give local stability results when proposing nonlinear observers. The four parameter representation of the quaternion does not have singularities. However, due to $r_q = 1$ and $r_q = -1$ representing two equilibrium points it is possible to obtain almost- and semi-global stability results, see [21, 122].

Two terms are often used interchangeably when evaluating the performance of state estimators; precision and accuracy. In the following these concepts will be distinguished by their definitions; a) *precision*: the consistency of the results (low spread equate high precision), b) *accuracy*: the proximity to the correct answer (short distance equate high accuracy). In a statistical sense high precision is achieved with low standard deviation, whereas high accuracy is attained with small mean error. When testing observers it is important to have both precision and accuracy.

2.3 Inertial Sensors

In the following inertial sensors suitable for cost-efficient navigation systems will be introduced as well as topics concerning deterministic and stochastic sensor parameters.

Navigation systems providing the tracking of an object's attitude, position, and velocity are vital in a wide range of applications, e.g. in aeronautics, astronautics, robotics, automotive industry, underwater vehicles, or human motion observation. Commonly, navigation systems are based on dead reckoning using inertial sensors aided by some sensor supplying position, range or velocity measurements.

One technique for dead reckoning is to use an initial position, linear velocity, and attitude to consecutively update the estimates based on specific force and angular rate measurements. These measurements are generally provided by three axial accelerometers and angular rate sensors forming an Inertial Measurement Unit (IMU). The aiding systems in navigation applications commonly provide corrections for position, velocity, or attitude. Those systems might be based on; satellite systems, electrolytic tilt sensors, pressure based altimeter, odometer, laser scan or vision based odometry.

The quality of inertial sensors span a wide range from cheap sensors used in mobile phones to highly accurate ring laser gyros used for missiles, where price increases with quality. The inertial sensors should be chosen according to the required accuracy of the application, as they are a major source of errors in the navigation system. The accuracy of the performed navigation is related to the characteristics of inertial sensors such as; bias instability, scale factor nonlinearity, measurement noise, etc. Undesired deterministic behaviour can be reduced by calibration whereas stochastic parameters such as initial offset and bias instability can be described by statistical values. Stochastic sensor parameters can generally be estimated via Power Spectral Density (PSD) analyses or with Allan Variance Analysis (AVAR).

The price of accelerometers and angular rate sensors depends on the technology used in the sensors, e.g. solid-state or moving parts. In Fig. 2.2 and Fig. 2.3 the current state of gyroscope and accelerometer technology are depicted. Recently the Micro-Electro-Mechanical-Systems (MEMSs) have progressed with increased sensitivity of the angular rate sensors, which allow for performance comparable with traditional gyros such as Fibre Optic Gyros (FOGs). The advantage of the MEMS technology is a decrease in cost and size compared to the FOG and Ring Laser Gyros (RLGs). MEMS gyros can be purchased with bias stability around $5°/h$, e.g. ADIS 16488 or STIM300. For military applications a bias stability of less than one nautical mile per hour is often required.

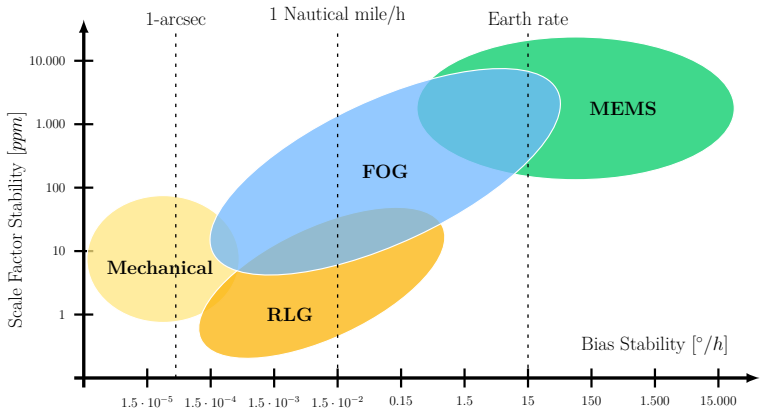

Figure 2.2: Gyro technology and performance, inspired by [152, Fig. 4].

For applications without aiding measurements the accelerometer is required

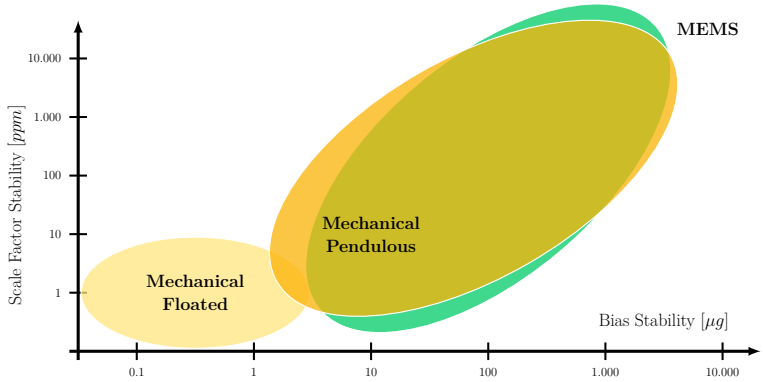

Figure 2.3: Accelerometer technology and performance, inspired by [152, Fig. 6].

to have low stability, to prevent fast drift and diverging navigation estimates. For military applications such as self-aligning missiles a bias stability of less than $1\mu g$ is required, whereas autonomous submarine navigation use accelerometers with bias stability around $10\mu g$. The consumer products is in the cheap end of the spectrum with bias stability around $1.000 - 10.000\mu g$.

For accelerometers the quartz-resonators can be used in low-cost applications requiring high accuracy, whereas the MEMS-based accelerometers have slightly poorer bias stability. For applications requiring higher accuracy mechanical accelerometers are advised. Typically the mechanical inertial sensors presents an increase in size, power-consumption and price, compared to the MEMS sensors, which is the trade-off for higher accuracy. For low-cost applications, such as navigation of small aircraft and unmanned vehicles both terrestrial and aerial, where size and power-consumption are of limited availability the MEMS sensors are preferred. In contrast, MEMS based systems might suffer from low resolution, noisy output, bias instability, temperature dependence etc. Nevertheless, their applicability in navigation is wide due to fast technology improvements, applied data processing algorithms, and aiding systems.

The current MEMS technology cannot compete with high-performance types and cannot be implemented to stand-alone inertial navigation systems due to their drawbacks. Generally, this type of IMU is used in navigation systems where a GNSS receiver is also implemented to compensate position errors, or in attitude and heading reference systems in which the position is not required and thus the IMU is used just for attitude estimation.

2.4 Strapdown Navigation Equations

Inertial navigation utilize measurements of specific force and angular velocity in the body-frame to estimate the change in position and attitude of a vehicle. The specific force is measured by an accelerometer, while a gyroscope supplies the angular rate measurements. It is common to have magnetometers included in the IMUs, to measure the magnetic field, which can be employed for aiding in attitude

estimation. In the following the term inertial measurements will cover all measurements from an IMU, including the magnetic field measurements, even though magnetometers are not inertial sensors.

The navigation of vehicles, will in the following, be expressed in the ECEF-frame, to attain higher model accuracy, with the attitude represented as a unit quaternion describing the rotation from body-frame to ECEF-frame. The kinematic vehicle model describing the position, p^e, linear velocity, v^e, and attitude, q_b^e, is given as:

$$\dot{p}^e = v^e, \tag{2.7}$$

$$\dot{v}^e = -2S(\omega_{ie}^e)v^e + f^e + g^e(p^e), \tag{2.8}$$

$$\dot{q}_b^e = \frac{1}{2}q_b^e \otimes \bar{\omega}_{ib}^b - \frac{1}{2}\bar{\omega}_{ie}^e \otimes q_b^e, \tag{2.9}$$

where f^e is the specific force, $g^e(\cdot)$ is the position-dependent gravitational vector found by e.g. [123], and ω_{ib}^b is the angular velocity experienced between the body- and ECI-frame decomposed in the body-frame.

An Inertial Navigation System (INS) typically consists of accelerometers, gyroscopes and embedded software estimating PVA based on the dead reckoning equations: (2.7)–(2.9). INS solutions span a wide price range based on the quality of the sensors.

The navigation equations considered here are related to strapdown navigation, where the inertial sensors are mounted directly to the vehicle, preferably at the body frame origin. The lever arm between the origin of the body-frame and the sensor frame can be considered negligible for smaller vehicles. An alternative to the strapdown approach is the gimbal system, where the inertial sensors are mounted on a stabilized platform, which retains it orientation relative to the inertial frame regardless of the motion of the vehicle. In a gimbal system only the vertical component of the accelerometer considers the gravitational field, whereas for strapdown systems the gravity affects all components of the measured specific force. Strapdown systems are easier to maintain and cheaper to install.

2.4.1 Navigation errors caused by biases

Inertial sensors suffer from multiple systematic error sources; bias (constant offset), scale factor (slope on sensor output), nonlinearities (higher order effects), etc. These systematic errors can often be eliminated by thorough calibration of the IMU, except for the turn-on bias which will have a random magnitude each time. It is vital to take these errors into account, as the performance of the sensor and thereby the navigation system depends on it. As an example: for an uncompensated constant accelerometer bias the integration to velocity introduces a linear error over time, while the error for position, when further integration is applied, results in a time dependent quadratic error. Moreover, an uncompensated accelerometer bias, b_f, contributes to position errors with $\Delta p = 1/2 b_f t^2$, where t is time. Even small deviations in sensed acceleration will cause unbounded error in position with time. For instance, if $b_f = 0.1\ mg$ is considered, the position error will be 0.05 m after 10 s, and increase to 177 m after 600 s.

The gyroscope bias will introduce a small misalignment of the accelerometer resulting in a projection of the acceleration vector. For small angles the error introduced in acceleration will approximately be proportional to time, leaving the error in velocity quadratic and the error in position cubic. The accuracy of the estimated navigation solution rapidly degenerates in the presence of accelerometer and gyroscope biases. The accuracy of an INS depends on time and the rate of increase depends on the bias magnitude. Increasing the quality of the sensor will ensure a slower error growth. In Table 2.1 the performance grades of IMUs have been summaried based on the gyroscope stability, [114]. The transition between the grades is constantly changing as new technologies are developed and cheaper sensors become available to the consumer.

Table 2.1: Inertial sensor performance grades based on gyro bias stability, [114].

Grade	Bias Stability
Consumer	$30 - 1000°/hr$
Industrial	$1 - 30°/hr$
Tactical	$0.1 - 1°/hr$
Navigation	$0.01 - 0.1°/hr$
Strategic	$0.0001 - 0.01°/hr$

The bias stability indicates how much the measurement drift over one hour. For consumer products such as mobile phones the measurements are not required to be highly accurate, however, for precision critical systems such as driverless cars or weapons systems, the sensors need to be of high quality to ensure safety and performance. The price of the IMU follow the performance grade, where cheap MEMS-based sensors are available for use in tactical grade, whereas expensive FOGs are required for strategic applications. Using low-cost sensors in navigation applications necessitate the estimation of gyroscope biases.

2.5 GNSS Signals and Positioning

This section will introduce the general signal structure used in a Global Navigation Satellite System (GNSS) and how pseudorange, carrier-phase and Doppler measurements can be utilized to estimate receiver position and velocity. Multiple GNSS constellations are available, the most commonly used being the American *Global Positioning System* (GPS), but also the Russian GLONASS, the European Galileo, and the Chinese BeiDou are prominent. The presentation will strive to be general to cover all GNSSs when possible, however, details will be supplied on GPS as this system was used in the experimental verification of the included papers.

A GNSS system consist of three segments; *user*, *control*, and *space*. The *user* segment is comprised of antennas and receivers, tracking and processing the satellite signals. The user segment can typically output either raw pseudorange, carrier-phase or Doppler measurements, as presented in Section 2.5.3, or as processed measurements in the form of global position and velocity estimates. The processed measurements are more commonly utilized by the *user* segment as they can be used directly in a standalone solution, whereas the raw measurements require implementation of a navigation filter. The receiver position and velocity are often estimated by some variant of the Kalman filter, which will be unavailable for tuning by the user. The accuracy of the position estimates provided by standalone GNSS receivers are commonly within 10 m, where [126, Section 6.1.5] shows a 24

hour dataset with median error of 4 m. A limitation of the *user* segment is that the signal path from satellite to receiver must be unobstructed. A GNSS receiver needs line-of-sight of the satellites and will therefore not work underwater or in some indoor environments. For some houses consisting primarily of wood or non coated glass windows the High Sensitivity GNSS (HSGNSS) receivers might be used.

The *control* segment consists of several stations well spread around the globe supplying orbital, timing and correction information to the satellites while monitoring the health and status of the satellites. The *space* segment covers the orbiting satellites which continuously broadcast signals to the *user* and *control* segments. Each GNSS has different constellation structure, orbital patterns, and control segment locations. For the GPS the satellites have an orbital period of 11 hours and 58 mins corresponding to two rotations per sidereal day (the time it takes Earth to rotate 360 degrees). The satellites are spaced to 6 nearly circular orbital planes with (normally) four satellites unevenly placed in the planes. The satellites travel at an altitude of approximately 20200 km, in the planes with a 55° inclination angle to equator. The inclination angle results in an uncovered area at both poles, see Fig. 1.2. The Medium Earth Orbit (MEO) satellites in the BeiDou and Galileo systems have similar inclination angles, whereas the GLONASS system covers the higher latitude areas better with an inclination angle of 64.8°. The BeiDou Phase III (completion due 2020) constellation will consist of three types of satellites, [76]; the MEO (similar to GPS and Galileo), Geosynchronous Orbit (GEO) satellites which in this case will serve as geostationary transmitters, and Inclined Geosynchronous Orbit (IGSO) satellites which will trace an analemma (elongated figure-of-eight) in the sky. This composition of satellites is intended to ensure better coverage over the Asia-Pacific region.

A main difference between GPS and GLONASS is the multiple access method. GPS, as well as Galileo and BeiDou, use Code Division Multiple Access (CDMA) which allows the satellite to transmit on the same frequency by encoding an identification signal into the transmitted data, thereby allowing for identification of the satellite. GLONASS use the Frequency Division Multiple Access (FDMA) where each satellite transmits on an individual frequency for identification purposes. Recently GLONASS has begun to undergo development to change to CDMA allowing for increased interoperability with other GNSS.

2.5.1 GNSS signals

In this thesis only the single-frequency GPS L_1 constellation will be considered, with few expansions to dual-frequency applications, see Section 5.4, and when determining high accuracy reference for the experimental trajectories, as in Section 4.7. However, other constellations and frequencies can be used instead or in addition. The GPS satellites broadcast on the L_1 and L_2 frequencies, which will be considered in the following. A conceptual illustration of the components in the signal structure of the GPS L_1 and L_2 signals is shown in Fig. 2.4, where $\bigoplus$ signifies the modulo-2 addition (if both signals are 0s or both are 1s the result is 0, otherwise 1) and $\bigotimes$ is the binary phase shift keying (BPSK) modulation (if the entering bit is 0 the carrier signal is unchanged, if the bit is 1 the carrier signal is multiplied with -1).

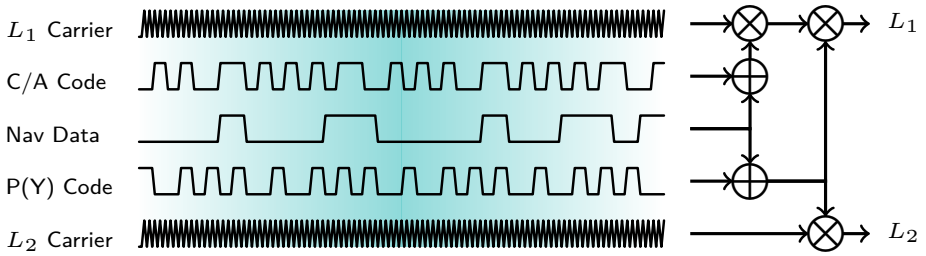

Figure 2.4: Structure and components of the GPS L_1 and L_2 signals.

The frequencies of the signals in Fig. 2.4 are not to scale, but illustrate the carrier signals having a higher frequency than the code signals, which in turn have a higher frequency than the navigation data.

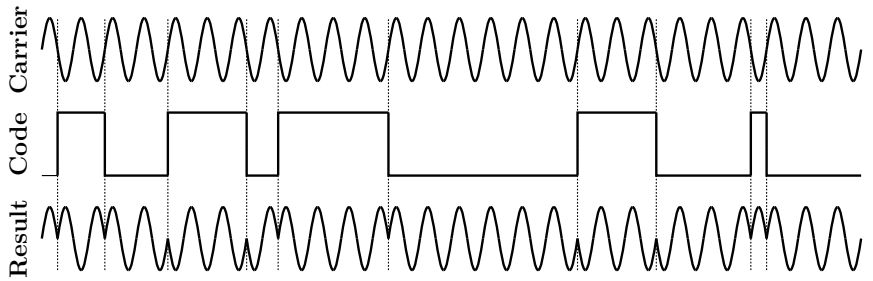

Figure 2.5: BPSK modulation of carrier, [76].

An example of a BPSK modulated signal is shown in Fig. 2.5, where the general model of a GNSS signal can be expressed as, [76]:

$$y(t) = \sqrt{2P}C(t)D(t)\cos(2\pi f_{ca}t + \phi_0), \tag{2.10}$$

where the signal $y(t)$ has carrier power, P. The ranging code and navigation data are denoted C and D, and can switch between the values ± 1. The phase offset is ϕ_0 and f_{ca} is the centre frequency of the carrier. For the legacy L_1 signal the frequency is $f_{L_1} = 1575.42\ MHz$ and wavelength $\lambda_1 = f_{L_1}/c \approx 0.1903\ m$, where c is the propagation speed of light.
The GPS signal consists of components divided into three categories:

- *Carrier*: The carrier are sinusoidal with high frequency. The other components are modulated onto the carrier.
- *Code*: The code consists of a pseudo random noise (PRN) signal, which is individual for each satellite and known by the receiver.
  - *C/A Code*: The Coarse/Acquisition PRN signal has period of 1 ms. The PRN codes are highly orthogonal to each other, making it possible to distinguish between satellites. One receiver can therefore obtain signals from multiple transmitters on the same frequency.

  - *P(Y) Code*: The P code is more precise than the C/A code, and is the only code signal modulated onto the L_2 signal. This code can be encrypted for military use, in which case it is denoted the Y-code. The P(Y) PRN code is 267 days long with each satellite having one week of the PRN code each.

- *Navigation Data*: The navigation data includes almanac (satellite health and status), ionospheric correction terms, satellite clock information, ephemeris data, etc. The ephemeris data can be used to determine the position and velocity of the satellites.

When the GNSS receiver is turned on it searches for satellites, and correlates the received signals with the locally generated signal replicas to determine which satellites are present in the constellation. The correlation is performed in phase, frequency and code. Once the acquisition of the satellite signal is complete the receiver changes to tracking mode, which in general can operate in worse signal-to-noise conditions, [76]. Determining the position of the available satellites can be done using the navigation data, by decoding the transmitted ephemeris data and using the algorithms summarised in Appendix A. With known satellite positions the receiver clock error and position of the receiver can be determined. If the receiver has been turned off recently, e.g. within a couple of hours, it might (depending on receiver settings, and age of ephemeris) be able to estimate the satellite position from stored ephemeris data.

2.5.2 Present GPS generation

GPS offers two navigation services; the civilian Standard Positioning Service (SPS) and the restricted Precise Positioning Service (PPS) for licensed users, e.g. military forces. The horizontal and vertical accuracy of the SPS is around 3.8 m (1σ) and 6.2 m (1σ), respectively, while the PPS has accuracies of 1.2 m (1σ) and 1.9 m (1σ), [76, Section 8.2.1].

Table 2.2: GPS satellite generations, [76, Section 8.2.1]

Satellite Block	Dates	SVs
Block IIA	1990-1997	19
Block IIR	1997-2004	12
Block IIR-M	2005-2009	7
Block IIF	2010-2015	12
Block III	2015-2024	24†

In Table 2.2 the present and planned generations of the GPS satellite network is shown, with launch dates and number of satellite vehicles (SVs). Here † indicates the planned number of satellites in the coming Block III expansion, which will broadcast new signals and increase the power of other signals, [76, Section 8.2.1].

The C/A- and P(Y)-code described above are called the legacy GPS signals, as they are present in all of the GPS generations. Presently ten GPS navigation signals are broadcasted on the L_1, L_2, and L_5 bands, where the L_5 bands were introduced in the IIF block. The motivation for introducing more frequencies is; frequency diversity allows for ionospheric delay estimation, increases performance of carrier-phase positioning, and reduces the interference on the individual frequencies.

In the IIR-M block the M-code and L2C signals were introduced, where the M-code is a military signal using a Binary Offset Carrier (BOC) modulation in contrast to the BPSK modulation. The advantage of the M-code is spectral separation from the SPS signal thereby offering increased robustness to jamming compared to the Y-code, [8].

The L2C signal consists of two components; the civil-moderate (CM) code and the civil-long (CL) code. The CM code has faster acquisition than the CL code, which in turn has better performance in poor signal-to-noise conditions and more accurate carrier tracking, [76, Section 8.3.2]. Compared to the C/A code the CM has better correlation properties with the trade-off of being more difficult to acquire.

The $L5$ signal was introduced with the IIF block to supply a third civilian signal to increase safety-of-flight applications. The advantages of using the $L5$ are; wider bandwidth and better interference management compared to the L_2 signal, [135].

2.5.3 GNSS measurements

In the following the pseudorange, carrier phase and Doppler measurements from the L_1 signal will be introduced in detail. The measurements will utilize different components of the transmitted L_1 signal; pseudorange measurement considers the C/A Code, whereas the carrier-phase measurements employ the carrier.

Pseudorange

The pseudorange measurement, ρ, is determined as the time between signal transmission from the satellite to the signal acquisition at the receiver, multiplied with the speed of light; $\rho = c\Delta t$. The speed of light, c, is constant in an inertial frame, e.g. ECI, [76, Section 8.5.3]. In the following it will be assumed that c can be considered constant in the rotating ECEF-frame. The time difference is estimated by time shifting the known PRN codes until it matches the received C/A Code signal. The pseudorange measurements are also called code measurements to emphasize the signal used and distinguish it from the carrier-phase measurements. Since only the satellite has a high accuracy atomic clock, the estimated time difference will include an offset due to the imprecise receiver clock. The measurement is called "pseudo" to indicate that the time difference is not exactly known. The pseudorange measurement from the ith satellite, ρ_i, can be written as:

$$\rho_{L_1,i} = \psi_i + \beta_i + \frac{f_{L_2}}{f_{L_1}} I + T + M_{L_1,\rho} + E + n_{L_1,\rho}, \tag{2.11}$$

where $\psi_i = \|p^e - p_i^e\|_2$ is the true geometric range between the receiver at position p^e and the ith satellite at p_i^e. The clock range bias, β, covers the residual inaccuracy between the receiver and satellite clock when the satellite clock corrections have been applied; $\beta = c\Delta_c$, where Δ_c is the clock bias. The satellite clock can be corrected with ephemeris parameters, see A.2. The pseudorange measurement is subject to delays imposed by the atmosphere and stochastic errors such as signal multipath, M_ρ, and measurement noise n_ρ. The atmosphere is considered to consist of two parts; the frequency dispersive ionosphere, I, and the non-dispersive

troposphere, T. The ephemeris data, E, accounts for errors in the determination of the satellite position.

Carrier-phase

The carrier-phase measurement is determined by counting the number of cycles received of the (sinusoid) carrier-signal. The unit of the carrier-phase is therefore given in *cycles* instead of *meters*, but can be converted by multiplication of the wavelength. The measurement from the ith satellite is given as:

$$\lambda_{L_1}\varphi_{L_1,i} = \psi_i + \beta_i + N_{L_1}\lambda_{L_1} - \frac{f_{L_2}}{f_{L_1}}I + T + M_{L_1,\varphi} + E + n_{L_1,\varphi}, \tag{2.12}$$

where the ionospheric effect is opposite in sign compared to the pseudorange. The multipath and noise term are complementary to the terms for the pseudorange measurement. However, the multipath effect is maximum 25% of a wavelength, and thereby much smaller than on the pseudorange measurement. The unknown integer ambiguity, N, denotes an offset of a whole number of wave lengths and is individual for the satellite. Furthermore, the ambiguity is constant as long as the satellite is tracked by the receiver, i.e. if the tracking of the satellite is interrupted the integer ambiguity will have assumed a different value.

The carrier-phase measurement is more precise than the pseudorange, which might seem counter-intuitive when the integer ambiguity is unknown. However, it is analogous to measuring the length of a room with a 19.03 cm ruler; you might forget how many times you had to slide the ruler along the floor, but you know the final fraction of the ruler very precisely.

Doppler

The range-rate measurement is the difference between received frequency and transmitted frequency, and can be considered as:

$$\lambda_{L_1}\nu_{L_1,i} = \left(\frac{p^e - p_i^e}{\|p^e - p_i^e\|_2}\right)^{\mathsf{T}}(v^e - v_i^e) + \dot{\beta}_i + \frac{f_{L_2}}{f_{L_1}}\dot{I} + \dot{T} + \dot{M}_{L_1,\nu} + n_{L_1,\nu}, \tag{2.13}$$

where ν_i is the Doppler measurement in Hz with noise term n_ν. The ionospheric and tropospheric delay rates, $\dot{I}$ and $\dot{T}$, will generally be small as the atmosphere will be slowly time-varying for most user applications. The multipath rate, $\dot{M}$, is a function of the receiver velocity denoted v^e, while v_i^e is the velocity of the ith satellite.

For high-velocity applications additional correction terms due to the relativistic frequency shift must be applied, see [76, Appendix G.5]. These terms cover time dilation due to special and general relativity, and is considered outside the scope of this thesis.

L_N measurements

Introducing the L_N as a common notation for the L_2 and L_5 signal the range and range-rate can be expressed similarly to the L_1 measurements. Some of the terms,

such as geometric distance and clock range bias, are the same for the two frequency measurements while others, including the multipath and noise terms, vary from the two measurements. The L_N measurements are given as:

$$\rho_{L_N,i} = \psi_i + \beta_i + \frac{f_{L_1}}{f_{L_N}} I + T + M_{L_N,\rho} + E + n_{L_N,\rho}, \tag{2.14}$$

$$\lambda_{L_N}\varphi_{L_N,i} = \psi_i + \beta_i + N_{L_N}\lambda_{L_N} - \frac{f_{L_1}}{f_{L_N}} I + T + M_{L_N,\varphi} + E + n_{L_N,\varphi}, \tag{2.15}$$

$$\begin{aligned}\lambda_{L_N}\nu_{L_N,i} = &\left(\frac{p^e - p_i^e}{\|p^e - p_i^e\|_2}\right)^\mathsf{T}(v^e - v_i^e) + \dot{\beta}_i + \frac{f_{L_1}}{f_{L_N}}\dot{I} + \dot{T} \\ &+ \dot{M}_{L_N,\nu} + n_{L_N,\nu}.\end{aligned} \tag{2.16}$$

The ionospheric effect on L_2 can be scaled to L_1 such that the ionospheric effect has the inverse factor compared to the L_1 signal, i.e. f_{L_1}/f_{L_2} instead of f_{L_2}/f_{L_1}. This feature allows for creation of the ionospheric-free linear combination of the L_1 and L_2 range measurements. The most common linear combinations will be introduced in Section 5.4. In the following the L_1 and L_N notation will only be used when dual-frequency measurements are considered, and leave the dropped notation for describing L_1 measurements, as these are most commonly considered.

2.5.4 Error sources and implementation considerations

The various error sources impacting the accuracy of the pseudorange, carrier-phase and Doppler measurements will be introduced in the following with typical standard deviations for pseudoranges, [52, Table 8.5]. Notice that even small errors in timing can have a huge impact as the satellite signals propagate at the speed of light. The error sources of the GNSS range and range-rate measurements are:

- **Satellite clock bias ($2\ m$):** The satellite clocks will drift despite being atomic clocks. The ephemeris data includes parameters for correcting the satellite clock, see Appendix A.2. The pseudorange and carrier-phase measurements can be corrected by adding $c\delta t_{sat}$, where δt_{sat} is the satellite clock bias correction.
- **Receiver clock bias:** The receiver clock is imprecise compared to the satellite clock, and estimation of the receiver clock bias is therefore required, and is usually included in the navigation filter as a state. There are predominantly two ways of handling the bias in the receiver: a) accumulated clock bias where the receiver clock bias is unbounded, and b) steered clock bias where the clock bias is steered towards zero when exceeding a threshold.
- **Ionospheric delay ($7 - 10\ m$):** The satellite signal is delayed in the ionosphere; top part of atmosphere ($50 - 1.000\ km$). The signal path can be obstructed by particles (free electrons and positively charged molecules) which will act as a frequency dispersive medium and delay the signal. In the dispersive medium the propagation velocity will depend on the frequency, delaying code and navigation data but advancing the carrier phase, [76, Section 9.3.2]. A linear combination of the L_1 and L_2 signals can be created to remove the effect of the ionosphere. Additionally, several models (e.g. the Klobuchar

and NeQuick models) exist and can describe the nominal ionospheric effect based on time of day, user location, satellite elevation and azimuth, as well as broadcast correction terms. Using only the broadcast correction terms it is possible to remove approximately half of the ionospheric delay at midlatitude. Larger errors ($> 10\ m$) can occur for low elevation satellites or during additional environmental disturbance (e.g. solar storm).

- **Tropospheric delay ($1\ m$):** The lower part of the atmosphere ($< 50\ km$) is the non-dispersive troposphere, which will affect the satellite signal time of flight due to changes in temperature, pressure and humidity. Moreover, the satellite elevation angle and the user position will affect the propagation path length, and thereby the delay imposed by the troposphere. The tropospheric delay can be modelled (e.g. the Saastamoinen troposphere delay model) based on average parameters at the receiver position and weather forecasts. Larger errors ($> 3\ m$) can occur for low elevation satellites.
- **Ephemeris errors ($2\ m$):** The satellite position and velocity is determined based on the ephemeris data, which are valid for no more than two to four hours, depending on the desired level of accuracy. However, the ephemeris model, see Appendix A, is a curve fit, and variations might occur. An error will result in a difference between estimated and true position of the satellite, thereby introducing a small angle between true and estimated signal path resulting in a range error due to the long distance from transmitter to receiver.
- **Multipath ($0.1 - 3\ m$):** The satellite signal might be reflected or refracted by obstructions in the signal path thereby extending the range from satellite to receiver. It is especially common in urban canyons where buildings will reflect the signals to the receiver.
- **Receiver noise ($0.1 - 0.7\ m$):** Measurement noise caused by the receiver is often considered random white noise, see [52, Section 8.4.8].

The error sources can be divided into two categories; systematic (satellite clock bias, ephemeris errors, ionospheric and tropospheric disturbances) and stochastic (multipath and receiver noise). The stochastic errors will be receiver and environment specific, whereas the systematic errors depend on the position of the receiver compared to the satellite, and will be the same for multiple receivers placed closely together.

When implementing GNSS-based navigation systems, care should be taken when comparing the timing of various GNSS data, especially when comparing with other sensors. Two time scales are used to timestamp the GNSS signals; the UTC (Coordinated Universal Time) and the iTOW (integer millisecond Time Of Week) time scales. The iTOW (e.g. 569134120 for approximately two hours after noon) corresponds to the UTC (e.g. 14:05:34.12 same time on a Sunday), by counting the number of milliseconds since Sunday midnight. However, there is a growing offset between the two time scales in the form of leap seconds. Currently the leap second offset is 17 seconds which should be applied to the UTC in order to correspond with the atomic time. The Russian version of the UTC, synchronized with Moscow local time, applies leap seconds when timestamping in the GLONASS system.

Due to the large distance between transmitter and receiver it is vital to compensate the range measurements for the rotation of the Earth during signal transit

time. The range can either be over- or underestimated depending on the placement of the satellite relative to the receiver as the receiver will either rotate closer or further away from the position at initiated transmission. The Sagnac correction can be employed to counteract this effect, which at the equator can result in a range error of 41 m, [76, Section 8.5.3]. The range correction, r_c, is determined as $r_c = \omega_{ie}/c(y_i x_r - x_i y_r)$, where the satellite and receiver position are given as $[x_i; y_i; z_i]$ and $[x_r; y_r; z_r]$, see [76, Section 8.5.3] for more details.

2.5.5 DGNSS and Real-Time-Kinematic solutions

Motivated by the systematic errors described in Section 2.5.4 it is often of interest to include additional receivers in an area of operation, in order to estimate and take the errors into account. The satellite clock bias is the same for all receivers and the ephemeris error has very small spatial variation, [76, Section 10.1.2]. These errors will therefore affect receivers similarly if the satellites are visible for both receivers. Since the line-of-sight to the satellites is slowly changing relative to the receivers and the atmosphere is somewhat uniform the effect of the ionospheric and tropospheric errors on the measurements will be similar for receivers in close proximity to each other.

In Differential GNSS (DGNSS) applications an additional stationary receiver, often denoted *reference* or *base station*, is placed at a known location. The base station estimates and broadcasts the corrections for the systematic errors, thereby leaving only multipath and receiver noise errors to influence the measurements of the moving receivers, often called *rovers*. A single base station can service multiple rovers, with the separation between a rover and base station denoted the baseline. It is possible for the position of the base station to be slowly time-varying, although it is most common to be stationary. The base station is commonly placed in a presurveyed position with minimal multipath effect to ensure accurate estimation of the systematic errors.

Depending on the application, additional base stations can be placed to ensure increased coverage and accuracy of the estimated errors. In local area applications only a single base station is exploited, where the quality of the corrections depends on the baseline length. Shorter baselines supply higher accuracy, where rovers within 150 km can get accuracy of 1 m, [76, Section 109.1.2]. In wide area DGNSS applications multiple base stations are spread over a large area, e.g. a whole country, to provide increased accuracy for rovers within the area. The method of broadcasting the base station corrections is typically some type of radio signal. The significant short-term correlation of the systematic errors facilitate the broadcast of corrections rather than the full measurements at the base station receiver, to increase efficiency, [52, Section 8.8.2].

Local area DGNSS can be utilized in mission critical areas such as airports or along coastlines. A maritime DGNSS system has been operational since 1999 and maintained by the U. S. Coast Guard. The differential corrections are broadcast on maritime radio frequencies, and can give accuracy of 1-3 m with baselines of 100 km, [126, Section 2.5]. While such a system will not be cost efficient for global coverage due to the large number of base stations required it can have a vital impact in dangerous areas with large reefs or troublesome currents. A similar network has

been proposed for covering airports for assisted landing of planes, [126, Section 2.5].

A special case of DGNSS is the real-time-kinematic (RTK) solution, where the raw measurements are shared by the base station. The rover can then compute the single-differenced measurements, as the difference between measurements acquired by the base station and rover. Furthermore, the double-differenced measurements can be determined by selecting a satellite as a reference satellite to further reduce the effect of the receiver clock bias. The single- and double-differenced measurements will be introduced in more detail in Chapter 6. In [103] a wide area RTK solution based on reference stations throughout Europe used ionospheric corrections as an additional constraint for faster carrier ambiguity resolution, resulting in root-mean-square errors of 10 cm.

The quality of the RTK solution depends on the successful resolution of the integer ambiguities of the carrier measurements, which will still be integer in the single- and double-differenced measurements. Three categories for the RTK quality are introduced; *single*, *float*, and *fixed*. When the quality is *single* the performance of the RTK solution is similar to a standalone receiver application, whereas *float* indicates that the ambiguities are estimated as real valued numbers. When the quality is *fixed* the ambiguities of the double-differenced measurements have been successfully resolved. It is customary to use the double-differenced measurements in the injection terms of the navigation solution, thereby negating the need for estimating the undifferenced ambiguities. With resolved ambiguities (*fixed* quality) the RTK solution provides centimetre-accuracy, while *float* can give accuracy on decimetre level.

Other DGNSS cases are available, such as relative DGNSS using pseudoranges (see [52, Sectio 8.8.1.1]), however this has an accuracy approximately 100 times worse than the RTK solution. In the following chapters RTK solutions will be used as reference when evaluating the performance of the proposed nonlinear observers. To achieve highly accurate position estimates the resolution of the carrier ambiguity is of high importance.

High end and low cost receivers

Similar to IMUs GNSS receivers are available in a large price-range, from cheap receivers used for mobile phones to expensive receivers used for mapping applications. The receivers can be purchased as chipsets for circuit board integration, original equipment manufacturer modules, or as a complete solution with interface and possibly integrated antenna, where the price increases with complexity.

The price will further depend on the desired application as some features might be required. One such feature might be access to pseudorange, carrier-phase and Doppler measurements which are typically not available on cheaper receivers only suppling position estimates. Other features might include; multiple constellation access, multiple frequency access or low cold start time. The receivers can be divided into the categories; consumer-, professional- and military-grade, with increasing complexity. For consumer-grade products low accuracy and limited number of features can be tolerated for low price ($1-$100), whereas military-grade receivers must robustly supply accurate estimates and have access to restricted signals for

higher costs (>$10.000), [76]. High accuracy applications in the professional-grade category presents a price-range around $100-$1.000, e.g. the u-Blox LEA series, where multi constellations are supported and range and range-rate measurements are available allowing use in tightly-coupled navigation systems. For UAV applications further design parameters might be considered, such as: dimension, weight, and power consumption to insure long flight times.

2.5.6 Integer ambiguity

The ambiguity introduced in (2.12) needs to be resolved to get high precision range measurements and thereby accurate position estimates. The ambiguity is an integer number of cycles, $N \in \mathbb{Z}$, and represents a large range offset. The offset is constant in time as long as the carrier-phase tracking of the receiver is maintained. If line-of-sight to the satellite is obstructed a new ambiguity will be present when the satellite is reintroduced to the constellation. If the ambiguity is unresolved the carrier-phase measurement is inaccurate and does not offer better range information than the pseudorange. Moreover, the unresolved ambiguity will present a large offset between the pseudorange and carrier-phase measurements. However, if the ambiguity is resolved to the correct integer centimetre accuracy can be achieved for position estimation. Applications are often divided into two categories; static (e.g. surveing) or kinematic (moving receiver), where applications such as real-time long-baseline kinematic solutions integrates the two categories, [112]. However, most resolution methods can be used for both categories.

Extensive research has been carried our for single-frequency single-constellation applications. One method consists of a bank of Kalman filters where multiple filters each hypothesizing a different ambiguity set, e.g. [89]. Another approach is the Ambiguity Function Method (AFM) proposed in [38] (extended to dual-frequency in [82]) which is insensitive to cycle-slip. Drawbacks of the AFM include long computation time and possibly multiple maxima that must be descriminated between to find the optimal position, [82].

The ambiguities can either be resolved using measurements from a single epoch, or by averaging over multiple epochs. A single-epoch resolution method is the Least-Squares Ambiguity Search Technique (LSAST), proposed in [88], utilizing dual frequency measurements in a DGNSS setup. In [57] the Fast Ambiguity Resolution Approach (FARA) method uses the double-differenced code observations to initialize the estimation based on carrier measurements. The float solutions are then used to find a set of ambiguities that are then tested and possibly fixed if accepted. A recursive filter approach was presented in [35] for the Fast Ambiguity Search Filter (FASF), where the search range is determined recursively for each ambiguity. The FASF method is based on Kalman filter theory and offers a significant reduction in computational load compared to least-squares methods. The modified Cholesky Decomposition Method offers an alternative to the quadratic form of the residuals, and is based on decomposition of matrices, and will have high computational time for fast data collection. It is therefore not advised for real time applications. In order to save computational load the ambiguity search space can be reduced. Extensive work has been done by P. J. G. Teunissen et al within ambiguity resolution; e.g. in [167, 169] where a fast ambiguity estimation approach

for GPS was proposed. In [168] the Least-Squares Ambiguity Decorrelation Adjustment (LAMBDA) was proposed which uses downscaling of the integer search space. Another method focused on faster solutions is the Optimal Method for Estimating GPS Ambiguites (OMEGA) employing a scaling and screening process to reduce the ambiguity search space, [111]. A comparitive study on the characteristics of the methods is presented in [112].

For multi-frequency applications linear combinations of the carrier measurements can aid the resolution. [54] considers the use of carrier-phase measurements on three different frequencies to reduce the effect of the ionosphere and increase the success rate of ambiguity resolution. The geometry-free linear combination of the L_1 and L_2 signals was investigated in [42] and [43] presents an extensive survey covering short and long baselines, as well as undifferenced, single- and double-differenced configurations. A ratio test for future GNSS ambiguity resolution was proposed in [174]. New methods for solving the ambiguities using multiple epochs were presented in [34] and [36] with focus on the reduction in computational load. Surveys on various methods for partial or full resolution were carried out in [25] and [26]. On-the-fly resolution of the ambiguity was investigated in [67], where also GPS error modelling is considered in an GNSS/INS setting. Further considerations on the ambiguities can be found in [126], [52] and [76].

In the following a few methods will be introduced for resolving the ambiguity. Several of the presented methods are based on double differenced measurements, where a reference base station receiver and reference satellite is used to cancel most of the nuisance terms in the range equations, (2.11) and (2.12). The single- and double-difference schemes will be introduced in detail in Chapter 6. Double-differenced measurements will be denoted $\nabla\Delta\cdot$, e.g. $\nabla\Delta N$ being the double-differenced ambiguity. Here the notation $\lfloor\hat{N}\rceil = \breve{N}$, from [52], will be adopted for the rounding of floating valued estimate $\hat{N}$ to the integer $\breve{N}$.

Average range measurements

The ambiguity can be solved individually for each satellite by differencing the double-differenced pseudorange and carrier-phase measurements, and averaging over time:

$$\nabla\Delta\hat{N} = \frac{1}{n\lambda}\sum_{k=1}^{n}(\lambda\nabla\Delta\varphi - \nabla\Delta\rho) \tag{2.17}$$

where k is the current epoch and n is the number of epochs used. In the averaging it is exploited that the ambiguities are constant. This method takes a long time to converge and the obtained ambiguity estimate is not precise, furthermore it has to be carried out for all satellites in the constellation individually. Care should be taken not to average over tracking loss where the ambiguity will reinitilise. The standard deviation of the estimate is approximately 5 cycles ($\approx 1\ m$), i.e. similar to that of pseudorange measurements, see [126, Section 7.4.1]. According to [143] the residual measurement error should be less than 25% of a wavelength for the integer ambiguity resolution to have high probability of resolving to the correct integer.

Dual-frequency method

Utilizing a linear combination of the L_1 and L_2 signals it is possible to enhance the ambiguity estimation. This method can be used in the non-differenced case as well as single- and double-differenced configurations. Using the wide-lane linear combination a new carrier-phase measurement is constructed by differencing the L_1 and L_2 measurements:

$$\varphi_w = \frac{f_{L_1}}{f_{L_1} - f_{L_2}}\varphi_{L_1} - \frac{f_{L_2}}{f_{L_1} - f_{L_2}}\varphi_{L_2}, \tag{2.18}$$

where the ambiguity of the wide-lane combination; $N_w = N_{L_1} - N_{L_2}$ is still integer. The wide-lane measurement have a longer wavelength making the ratio between the ambiguity and uncertainty larger, and easier to resolve. The drawback of this method is the increase in noise and that the wide-lane ambiguity is resolved instead of the individual ambiguities.

Another option for use of dual-frequency measurements is to solve the two carrier-phase measurements (for the two frequencies) with respect to the ambiguities:

$$N_{L_1} - \frac{\lambda_{L_2}}{\lambda_{L_1}}N_{L_2} = \varphi_{L_1} - \frac{\lambda_{L_2}}{\lambda_{L_1}}\varphi_{L_2} + \epsilon, \tag{2.19}$$

where ϵ is a collection term for all the nuisance terms (e.g. multipath and ionospheric delay). By further utilizing the wide-lane ambiguity the L_1 and L_2 ambiguities can be determined as:

$$\hat{N}_{L_1} = \frac{\lambda_{L_1}\varphi_{L_1} - \lambda_{L_2}\varphi_{L_2} - \lambda_{L_2}N_w}{\lambda_{L_1} - \lambda_{L_2}}, \qquad \hat{N}_{L_2} = \frac{\lambda_{L_2}\varphi_2 - \lambda_{L_1}\varphi_{L_1} - \lambda_{L_1}N_w}{\lambda_{L_1} - \lambda_{L_2}}$$

Averaging can be applied to enhance the accuracy of the ambiguity estimates.

Geometry based

The ambiguities of multiple simultaneous carrier-phase measurements can be resolved by considering a vector of double-differenced ambiguity estimates, x_N. By resolving all ambiguities together the geometry of the satellite constellation can be utilized when the navigation solution is overdetermined, [76, Section 10.2.3]. When more than four satellites are available only certain solutions to the range ambiguity will provide consistent solutions for all the measurements.

Here the float-and-fix method will be considered due to its high efficiency, [76, 126]. The process follows the general steps, [52, Section 8.9]:

- *Initialization:* The ambiguities are initially considered as floating values, later to be fixed to integer for increase in precision. The initial estimates are based on the difference between the carrier-phase and pseudorange, as with the averaging method:

$$\hat{x}_N = \nabla\Delta\varphi - \lambda^{-1}\nabla\Delta\rho. \tag{2.20}$$

- *Candidate generation:* Candidate vectors for the fixed integer ambiguities are generated in the vicinity of the estimates, based on the estimate covariance. The candidate vectors, $\breve{x}_N$, cover all combinations of integer values around the ambiguities estimates. The search space is therefore often large, and methods for decreasing the search space are common use.

  The candidates might be proposed based on the space:

$$S := \{\breve{x}_N \in \mathbb{Z}^{m-1} | \hat{x}_N - c_r\sigma_N \leq \breve{x}_N \leq \hat{x}_N + c_r\sigma_N\}, \tag{2.21}$$

  where σ_N is the variance of the ambiguity estimates determined by the diagonal elements of the ambiguity covariance matrix P_N; $\sigma_N = \sqrt{\text{diag}(P_N)}$. The constant c_r denotes the confidence interval, which for the 99.9% confidence interval will be considered as; $c_r = 3.29$, assuming normal distribution.

- *Candidate evaluation:* The candidate vectors are evaluated by the test statistic:

$$s^2 = (\breve{x}_N - \hat{x}_N)^\intercal P_N^{-1} (\breve{x}_N - \hat{x}_N), \tag{2.22}$$

  where the candidate vector that is closest to the estimates minimizes the test, and is presumed to be the likeliest solution.

- *Candidate validation:* The candidate vector chosen based on the minimization of (2.22) during the evaluation can be validated by ideally being significantly smaller than the next best candidate vector. Due to measurement noise and additional error sources the most consistent solution might not be the true candidate set. The ratio between the s^2 values of the most likely and second likeliest candidate vectors can be used as a threshold test for verification. Failure of the validation step will prompt the generation, evaluation and verification of new candidate vectors for a new epoch.

Once the candidate vector have been validated the ambiguities can be assigned to integer value; $\hat{x}_N = \breve{x}_N$, and can be kept constant. If satellites are lost and reintroduced into the constellation a new iteration of the process has to be carried out.

LAMBDA

The Least-squares AMbiguity Decorrelation Adjustment (LAMBDA) method is a Mixed-Integer-Least-Squares (MILS) approach to limiting the search space by transformation of the ambiguities. The intention is to utilize a change of variables to transform the confidence interval of the ambiguities to cover a smaller area, thereby reducing the search space. Collecting the double-differenced ambiguities in the vector, $\hat{x}_N$, the ambiguities and the covariance matrix, P_N, is transformed by use of the decorrelation matrix, Z, see [76, Appendix G]:

$$\hat{x}_Z = Z\hat{x}_N, \qquad P_Z = ZP_NZ^\intercal. \tag{2.23}$$

The decorrelation matrix is determined from the Cholesky factorization of the covariance matrix; $P_N = LD_LL^\intercal$, where D is a diagonal matrix and L is a lower

triangular matrix with unit elements in the diagonal. The decorrelation matrix is then found as; $Z = \lfloor L^{-1} \rceil$.

After the ambiguity transformation the search space has decreased in size, leaving fewer candidate sets to be tested, making for a faster evaluation. The LAMBDA method is often used in connection with other resolution methods such as the geometry-based approach. Once the ambiguities have been fixed the transformation can be reversed. A key feature of this approach is that due to the rounding operation when determing Z an integer valued $\hat{x}_N$ corresponds to an integer valued $\hat{x}_Z$, and vice versa. Implementation aspects of the LAMBDA method are considered in [44] and [102].

2.5.7 Least-squares: receiver position from pseudoranges

The position of a receiver can be determined from range measurements using a least-squares method. In Fig. 2.6 a two dimensional example is introduced, including a receiver, R, and three satellites; A, B, and C. The range measurements from the satellites are depicted as solid circles extending from the center of the satellites, whereas the true geometric range is shown as a dashed circle. This illustrates the effect of the inaccurate range measurements offered by the pseudoranges. If the true ranges were available the receiver position would be found at the intersection of the three dashed circles. However, when using the pseudoranges the position estimation is uncertain, as the position is limited to an intersection area, here shown in gray. The least-squares method can be used to find the most likely position of the receiver in the restricted area.

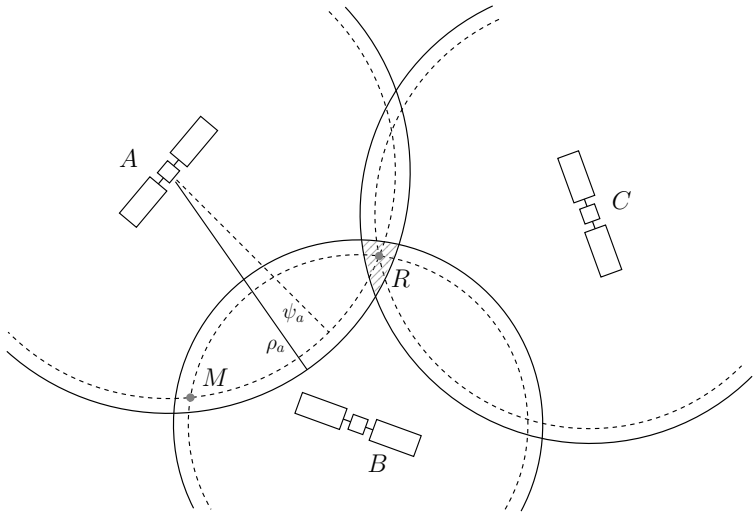

Figure 2.6: 2D example of pseudorange positioning of receiver R using measurements from satellites; A, B, and C.

In the two dimensional example three satellites are required to find the receiver position. If only two satellites are used there are two possible positions for the

receiver location; at the intersections of the two circles. If the true ranges from satellite A and B are used the receiver can be either at R or M. It is often possible to guess at the right option if fewer satellites are used, and multiple solutions to the position estimation problem are presented, as one option often lies out in space or inside the Earth. Prior knowledge of the receiver position at an earlier epoch can also limit the options. In the three dimensional case, four satellites are needed to estimate the receiver position, as four parameters must be estimated; the three spacial coordinates of the receiver, and the clock range bias. The receiver position is then found at the intersection of four spheres.

The accuracy of the position estimate is influenced by the constellation geometry; if all the satellites used are clustered closely together in the sky the position estimate will have a large error, as the intersection area will be large and follow the curvature of the signal paths. However, if the satellites are spaced out over the sky, with some satellites at high elevation and some at lower elevation the intersection area will be smaller and the position can be determined with higher accuracy.

Considering the three dimensional case, the receiver position, $\hat{p}^e = [\hat{x}^e; \hat{y}^e; \hat{z}^e]$, and clock bias, β, can be combined to the state vector; $\hat{x} = [\hat{p}; \beta]$. The cost function to minimize is; $J(\hat{x}) = \|\hat{\rho} - \rho(\hat{x})\|$, see [52]. Intuitively the cost function makes sense, as it is desired to minimize the difference between the measured and estimated pseudoranges. The iterative algorithm is:

$$\hat{x}_{k+1} = \hat{x}_k + (H_k^\intercal H_k)^{-1} H_k^\intercal (\rho - \hat{\rho}(\hat{x}_k)), \tag{2.24}$$

where $k = 1, 2, 3, \ldots$ is the iteration index. A weight matrix can be introduced to alter the algorithm to the weighted least square (WLS) problem. The estimated pseudorange is determined as; $\hat{\rho}(\hat{x}_k) = \|\hat{p}_k^e - p_i^e\|_2 + \hat{\beta}_k$, where the known position of the ith satellite is denoted, p_i^e. Assuming four linearly independent satellites are available the H matrix is given by; $H_k = [h_{1,k}^e,\ 1; h_{2,k}^e,\ 1; \ldots; h_{4,k}^e,\ 1]$, where $h_{i,k}^e = (\hat{p}_k^e - p_i^e)\|\hat{p}_k^e - p_i^e\|_2^{-1}$ is the line-of-sight vector of the ith satellite.

The requirement of at least four linearly independent satellite measurements ensures that the matrix inverse in (2.24) exist. The algorithm, (2.24), is iterated until convergence. As shown in [52] this method can take several iterations to converge to a position estimate, when initiated at Earth's center. However, normally a better initial guess can be provided and the algorithm will converge in fewer iterations. The position precision using this method is low; an example in [52, Section 8.2.2] shows errors after convergence of 90 meters. The least-squares method suffers from several drawbacks; low precision and requires multiple iterations for convergence. Additional accuracy can be achieved by implementing a Kalman filter, however, the complexity of implementation and tuning will increase. The error sources and degradation of the GNSS measurements motivate the integration of satellite measurements with inertial sensors, such that higher sample rate of the estimates can be achieved while the navigation solution becomes more robust to outages in the GNSS signals.

2.6 GNSS/INS Integration

Navigation using only inertial sensors lack long term stability, whereas navigation using only GNSS measurements have low sample rate. The integration of GNSS and INS navigation is motivated by the complementary features of the individual systems. Complementary filtering can be used to obtain the advantages of both approaches, by integrating two different measurements of the same signal with different errors. The GNSS position and velocity measurements can be used to aid the inertial estimates based on integration from acceleration measurements. The advantages and drawbacks of navigation based on GNSS and INS is summarised in Table 2.3, where the desired qualities are marked in green.

Table 2.3: Complementary features of GNSS/INS integration

GNSS	**INS**
Bounded errors	Unbounded errors
Good long-term accuracy	Poor long-term accuracy
Poor short-term accuracy	Good short-term accuracy
Requires external information	Self contained
Attitude not estimated	Attitude estimated
Low rate	High rate

It should be noted that it is possible to estimate the attitude in a GNSS navigation system when using multiple receivers on the vehicle. However, this is not common practice and the attitude estimation is often done by compass or INS. By aiding an INS with GNSS measurements the time dependent accuracy of the INS can be limited by the uniform accuracy of the GNSS measurements.

When mounting the inertial sensors and GNSS receiver the lever arm in between should be considered. For small vehicles such as Unmanned Aerial Vehicles this has little effect. However, for large vessels where the IMU might be placed at the center of gravity and the GNSS receiver on top of the bridge the lever arm can introduce large errors if uncompensated. The GNSS measurement should be compensated for the distance to the IMU, such that the GNSS measurements appear to be received at the IMU location.

Multiple strategies for GNSS/INS integration have been proposed, where the main categories are; uncoupled, loosely-coupled, tightly-coupled, and deep integration. The uncoupled system has the GNSS and INS navigation systems implemented independently of each other. This integration scheme is not commonly used due to the drawbacks of the individual systems as seen in Table 2.3. The loosely-coupled integration scheme use position and velocity measurements from a GNSS receiver to aid the inertial navigation. In the tightly-coupled integration the GNSS receiver supplies the range and range-rate measurements, circumventing the unknown navigation system of the GNSS receiver, and aids the INS with measurements in the range domain rather than the position domain. The deep integration utilize the GNSS range measurements to estimate INS errors while using IMU measurements to aid the tracking loops of the GNSS receiver. This method

requires access to the firmware of the GNSS receiver and IMU, and is therefore not common due to the complexity of implementation and loss of interchangeability of sensors.

In the following chapters nonlinear observers for estimation of position, linear velocity and attitude will be proposed for loosely- and tightly-coupled inertial navigation systems aided by GNSS measurements.

Chapter 3

Loosely-Coupled GNSS/INS Integration

The topic of this chapter is the study of state estimators for robust navigation. Navigation of vehicles is a vast field with multiple decades of research. A main aim is to estimate position, linear velocity, and attitude (PVA) under all dynamics, motions and conditions via data fusion. A comparative study of strapdown inertial navigation methods for estimating PVA of aerial vehicles fusing inertial sensors with global navigation satellite system (GNSS) based positioning will be presented. The state estimation problem will be considered from two different perspectives using a strapdown kinematic vehicle model. First the Extended Kalman filter (EKF) will be reviewed, as an example of a stochastic approach, secondly a recent nonlinear observer will be considered as a deterministic case. The focus will be on the loosely-coupled integration methods and performance analysis to compare the state estimators in terms of their stability, robustness to vibrations, and disturbances in measurements.

Contributions of this Chapter: The contribution of this chapter is dedicated to comparison of two approaches suitable for navigation solutions and provides an understanding of the differences in the studied approaches. These approaches are tuned to satisfy a certain level of accuracy and applied on real flight data. The results are compared to an accurate referential attitude obtained from a multi-antenna GPS receiver. The comparison with an independent referential system provides a thorough evaluation of performances of the studied approaches and shows their capabilities to handle sensor imperfections and vibration impacts of harsh environment on the accuracy of attitude estimation in aerial applications.

Organization of this Chapter: This chapter is organized as follows: the preliminary assumptions are introduced in Section 3.2, Section 3.3 presents the EKF used for comparison of the nonlinear observer introduced in detail in Section 3.4. In Section 3.5 the two state estimators are compared using UAV flight data, while Section 3.6 summaries the chapter.

Publications: The material in this chapter is based on the journal Bryne et al. 2017 [31] and the book chapter Hansen et al. 2016 [85].

3.1 Introduction

Inertial Navigation Systems (INSs) are widely employed with price being a crucial factor predetermining the application. In case of unmanned vehicles "low-cost" or "cost-effective" systems are preferred in general applications. As long as low-cost Inertial Measurement Units (IMUs) use MEMS-based inertial sensors they are small in dimensions, light weight, have low-power consumption and thus their presence can be found for instance in mobile phones, terrestrial vehicles, robots, stabilized platforms as well as in Unmanned Aerial Vehicles (UAVs), small aircraft, and satellites. Even if the applications are cost-effective, the performance commonly requires data fusion from various sources due to the imperfections of the inertial sensors, such as insufficient resolution for navigation purposes, bias instabilities, noise etc. Therefore, special data treatment is required. In sense of aerial applications the usage of UAVs has increased rapidly in recent years. UAVs can be employed in many applications fulfilling a broad spectrum of assignments in fields of reconnaissance, surveillance, search and rescue, remote sensing for atmospheric measurements, traffic monitoring, natural disaster response, damage assessment, inspection of power lines, or for aerial photography [166], [113]. These applications generally require navigation to be carried out which includes the position, velocity, and attitude estimation and thus cost-effective solutions have been commonly studied and implemented with advantage.

Current research and development in the area of low-cost navigation systems are focused on small scale and integrated solutions [115]. As mentioned, as long as MEMS-based IMUs are used the evaluation process requires data fusion from other aiding sources available. These sources stabilize errors in navigation solutions and thus increase navigation accuracy. For applications without absolute position measurements provided by GNSS or radio frequency beacons, e.g. for indoor or low altitude navigation, the use of cameras, laser scanners, or odometers are popular [29], [178]. However, the solutions fusing inertial and GNSS measurements are still preferable for aerial vehicles operating outside in large areas due to the properties of the GNSS signals. The implementation of other aiding sensors, such as magnetometer or pressure sensors, can further enhance the overall accuracy, reliability, and robustness of a navigation system, e.g. [181]. Attention is also paid to data processing algorithms used for PVA estimation, where the extensive literature of filtering techniques cover the use of complementary filters [51], particle filters [161], or Kalman filters (KFs) [5], [39]. For Kalman filters the most widely used variant is the Extended KF (EKF) since it provides accuracy and a reasonable computational load for nonlinear systems. Therefore, KF represents one of the most used algorithms for UAV attitude estimation (see comprehensive survey of estimation techniques in [132]) and is often complemented by other algorithms and decision-based aiding [45].

3.2 Models and Preliminaries

Estimating the position, linear velocity and attitude of a vehicle is commonly achieved through GNSS/INS integration, where the INS consists of an IMU provid-

ing inertial navigation between updates from a GNSS receiver. The GNSS receiver usually has a lower sample rate than the IMU, and is used to update the PVA estimates by correcting for the drift of the inertial sensors.

The inertial navigation is governed by the strapdown equations of (2.7)–(2.9) where the inertial measurements are used to propagate the navigation states. Some measurement assumptions are required.

3.2.1 Measurement assumptions

It is assumed that the vehicle is equipped with an IMU and a GNSS receiver, as well as a magnetometer. The following assumptions on the measurements are made:

Assumption 1. Position measurements from a GNSS receiver, $p^e_{\text{GNSS}} = p^e$, are available.

Assumption 2. Velocity measurements from a GNSS receiver, $v^e_{\text{GNSS}} = C_v v^e$, are available.

Remark 3.1. The velocity measurement can be a full or partial measurement where C_v can be zero.

Assumption 3. Specific force measurements are available, $f^b_{\text{IMU}} = f^b + b^b_f$, with bias b^b_f. Furthermore, knowledge of bounds on the magnitude of specific force, denoted M_f, is assumed.

Assumption 4. Angular rate measurements are available, $\omega^b_{ib,\text{IMU}} = \omega^b_{ib} + b^b$, with bias b^b. It is further assumed that the upper bound of the gyro bias, M_b, is known.

Assumption 5. Magnetic field measurements are available, $m^b_{\text{MAG}} = m^b$, of the Earth's magnetic field at vehicle position. The natural magnetic field at any position is assumed known in NED- and ECEF-frame, as m^n and m^e, respectively.

In the following the state estimators will be introduced. First the EKF will be presented where stochastic noise considerations are used to tune the covariance matrices. Secondly the nonlinear observer will be introduced consisting of two parts: a nonlinear attitude estimator and a translational motion observer.

3.3 Extended Kalman Filter

Kalman filters have been extensively used in applications requiring sensor fusion. Whereas the Kalman filter (KF) operates optimally on a linear system model the Extended Kalman Filter (EKF) was introduced as an approximation for nonlinear systems. The general system can be described by the differential equations:

$$\dot{x}(t) = f(x(t), u(t), t) + G_s(t)w_s(t), \qquad y = h(x(t), t) + w_m(t), \tag{3.1}$$

where the system and output dynamics are described by the functions $f(\cdot)$ and $h(\cdot)$ which can be linear or nonlinear. In the linear case the system function decomposes into state, $x(t)$, and input, $u(t)$, multiplication with the transition and input matrix;

$f_{linear}(x(t), u(t), t) = A(t)x(t) + B(t)u(t)$, which can be utilized in the linear KF with:

$$A = \left.\frac{\partial f(x(t), u(t), t)}{\partial x(t)}\right|_{x=\hat{x}}, \qquad B = \left.\frac{\partial f(x(t), u(t), t)}{\partial u(t)}\right|_{x=\hat{x}}. \tag{3.2}$$

The transition and input matrices are determined through linearization using a current state estimate $\hat{x}$. The input vector commonly consists of measurements of specific force and angular rates. For nonlinear systems linearization should be avoided to maintain a high level of detail. The $G_s(t)$ matrix describe the influence of the state noise $w_s(t)$ on the estimation states, while $w_m(t)$ denotes the measurement noise. The system noise vectors consist of multiple error sources all considered to be Gaussian white distributions, see [76, Section 3.2.2].

Formulating the state estimate $\hat{x}$ as the estimate of the true state, the discrete representation of the estimate is separated into an *a priori* and *a posteriori* state, $\hat{x}^-$ and $\hat{x}^+$, respectively. The *a priori* state denotes the predicted estimate determined from state transition while the *a posteriori* state is the updated (also called the corrected) state. The discrete iteration counter k is used to distinguish between current and previous states.

Remark 3.2. For linear systems $\hat{x}$ expresses the expected value of the true state. However, due to the nonlinearity of the system such an interpretation cannot be made for the EKF.

Assumption 6. It is assumed that $f(\cdot)$ is constant over the IMU sampling interval $[t_{k-1}, t_k)$.

The predicted state is calculated using state propagation which can be formulated from the system dynamics under Assumption 6:

$$\hat{x}_k^- = \hat{x}_{k-1}^+ + f(\hat{x}_{k-1}^+, t_k)T \tag{3.3}$$

where $T = t_k - t_{k-1}$ is the time interval between IMU measurements.

Remark 3.3. Assumption 6 can in general be satisfied by employing the prediction of (3.3) at a high enough sample rate. If the assumption is not valid the last term of (3.3), i.e. $f(\hat{x}_{k-1}^+, t_k)T$, should be substituted for an integral over the time interval, see [76, Section 3.4.1].

The state is predicted with (3.3) at IMU frequency, e.g. at 200 Hz. Whenever aiding measurements are available the state can be corrected. However, aiding measurements are often provided at lower rates, e.g. GNSS receiver positions at 1 Hz. The prediction will therefore, in this example, run 200 times between two consecutive aiding measurements, at which time the correction is carried out.

The corrected *a posteriori* state is determined using the measurement vector as:

$$\hat{x}_k^+ = \hat{x}_k^- + K_k\left(y_k - h(\hat{x}_k^-, t_k)\right), \tag{3.4}$$

where the current measurement y_k and *a priori* state estimate is used. The measurement is denoted y_k to signify that it corresponds to the new measurement

at time t_k, although the counter k denotes the increment in IMU samples. The correction in (3.4) is only used when new aiding measurements are available. The Kalman gain, K_k, is multiplied by the injection term consisting of the difference between measured and estimated output. If the estimation is perfect the difference will consist exclusively of noise components, which would average to zero over time as;

$$y_k - h(\hat{x}_k^-, t_k) = h(x_k, t_k) - h(\hat{x}_k^-, t_k) + w_{mk}. \tag{3.5}$$

The Kalman filter propagates the state estimate along with the error covariance matrix P, which indicates the expectation of the squared difference between true and estimated states; $P_k = E\{(x_k - \hat{x}_k)(x_k - \hat{x}_k)^\intercal\}$, [76, Section 3.2.1]. The error covariance matrix is symmetric and positive definite where the diagonal elements are the variance of the estimated states, thereby indicating how trustworthy the estimates are. The error covariance matrix can be used to determine the gain matrix K_k to ensure reasonably good gain selection by solving the Riccati equation, [90]:

$$P_k = F_k P_k F_k^\intercal + G_{s,k} R_k G_{s,k}^\intercal - K^\intercal H_k P_k F_k^\intercal, \tag{3.6}$$

where the discrete-time state transition matrix, F_k, and the discrete-time output matrix, H_k, are:

$$F_k = e^{AT}, \qquad H_k = \left.\frac{\partial h(x, t_k)}{\partial x}\right|_{x=\hat{x}_k^-} \tag{3.7}$$

while $G_{s,k} = G_s(t_k)$. The initial conditions are: $\hat{x}_0 = E\langle x_0 \rangle$ and $P_0 = E\langle x_0, x_0^\intercal \rangle$.

Assumption 7. The process noise and measurement noise are assumed to be uncorrelated Gaussian white noise, $w_s \sim N(0, Q_k)$ and $w_m \sim N(0, R_k)$. Furthermore, the process and measurement noise are uncorrelated with the state, x_k, for all $k \geq 0$.

The matrices Q_k and R_k describe the covariance of the state and measurement noise respectively. The Q_k and R_k matrices are determined from the power spectral densities of the driving noise $w_s(t)$ and $w_m(t)$, respectively.

Remark 3.4. If the process and measurement noise cannot be assumed Gaussian white the state model can be augmented to include noise models with white driving noise. Following this approach colored process and measurement noise can be achieved, while satisfying Assumption 7.

Assumption 8. The system dynamics function, $f(\cdot)$, and the measurement function, $h(\cdot)$, are constant for small state increments.

Assumption 9. When the state estimates have converged to the true states the injection term will be small.

Satisfying Assumption 8 and Assumption 9 the state residual, $\delta x_k = x_k - \hat{x}_k$, can be described by the linear model:

$$\delta x_k \approx F_k \delta x_k + G_k u_k + G_{s,k} w_{sk}, \qquad \delta y_k \approx H_k \delta x_k + w_{mk}, \tag{3.8}$$

thereby allowing for implementation as an in-direct filter. In an in-direct filter the residual state is estimated rather than the states as done in a direct filter. The error covariance is propagated with the linearized model of (3.8), while the nonlinear model is used for propagation of the state estimate, see (3.3).

The discrete input matrix G_k is determined through discretization of B_k as:

$$G_k = \int_{kT}^{(k+1)T} e^{A\left((k+1)T-\tau\right)} B(\tau)u(\tau)\mathrm{d}\tau. \tag{3.9}$$

Remark 3.5. Due to the linearization, and following discretization, of $f(\cdot)$ and $h(\cdot)$, resulting in the matrices F_k and H_k, the error covariance and the gain matrices will be functions of the state estimates. This can lead to stability issues and leave the EKF more vulnerable to poor tuning of the P matrix compared to the KF, [76, Section 3.4.1].

Remark 3.6. The validity of the linearization point, i.e. that the estimate is sufficiently close to the true states, can be verified by the condition, [76, Section 3.4.1]:

$$\left.\frac{\partial \Upsilon(x,t_k)}{\partial x}\right|_{x=\hat{x}_k^+ + \Delta x_k^{+i}} \approx \left.\frac{\partial \Upsilon(x,t_k)}{\partial x}\right|_{x=\hat{x}_k^+ - \Delta x_k^{+i}}, \qquad \Delta x_k^{+i} = \sqrt{P_{k,ii}^+} \tag{3.10}$$

which is tested for each state, i, and where Υ is a place-holder for either the system dynamics function, $f(\cdot)$, or the measurement function, $h(\cdot)$. The condition investigates whether the gradient of the function Υ varies significantly over the uncertainty bounds of the state estimate, [76]. Failure of this condition commonly occurs at initialization, where the initial conditions might have been too optimistic. If the condition is compromised during iteration a higher order approach can be employed, such as the unscented Kalman filter or a second-order KF, [76].

Remark 3.7. The validity of Assumption 8 is secured by re-linearization around the estimated state for each iteration of the filter. However, this extension leads to the loss of optimality offered by KF for linear systems. The stability results for the general EKF is difficult to state theoretically. However, local exponential stability can be acquired under some conditions, see [151].

Implementation

During implementation of the EKF in a discrete system the error covariance matrix is also divided into *a priori* and *a posteriori* estimates. The *a priori* and *a posteriori* state estimates and covariance matrices can be implemented as, [68]:

$$\hat{x}_k^- = f(\hat{x}_{k-1}^+, u_{k-1}) \tag{3.11}$$

$$P_k^- = F_{k-1}P_{k-1}^+F_{k-1}^\intercal + Q_{k-1} \tag{3.12}$$

$$K_k = P_k^- H_k^\intercal \left(H_k P_k^- H_k^\intercal + R_k\right)^{-1} \tag{3.13}$$

$$\hat{x}_k^+ = \hat{x}_k^- + K_k\left(y_k - h(\hat{x}_k^-)\right) \tag{3.14}$$

$$P_k^+ = \left(I - K_k H_k\right) P_k^- \left(I - K_k H_k\right)^\intercal + K_k R_k K_k^\intercal. \tag{3.15}$$

The estimation and correction stages of the EKF can be implemented at different rates, where it is common to combine the correction stage, (3.13)–(3.15) with the

measurement update. For navigation systems the measurement update might be GNSS position measurements at $1 - 10\ Hz$. The estimation stage, (3.11)–(3.12), must be implemented at high rates corresponding to the inertial sensor used, to satisfy Assumption 6. Inertial sensors can supply measurements of specific force and angular rate at $10 - 2.000\ Hz$ (or even higher for high-end applications).

The implementation procedure is visualized in Fig. 3.1 where Fig. 3.1a–3.1c show the propagation through epoch one, while Fig. 3.1d–3.1f show the further propagation through a second epoch. The example in Fig. 3.1 considers an estimate of two states x_1 and x_2, where the covariance is visualized as a dashed region around the estimate. The procedure follows; an initial estimate with large uncertainty in epoch one is corrected with a linear measurement in Fig. 3.1b, where the measurement is in the dashed uncertainty region. The estimate after the measurement update, corresponding to (3.13)–(3.15), is shown to have smaller uncertainty in Fig. 3.1c. The estimate is propagated from epoch one to epoch two by use of (3.11)–(3.12), thereby extending the uncertainty, to account for possible movement of the vehicle, as visualized in Fig. 3.1d. A new measurement supplying additional information allows for the correction stage to arrive at a smaller uncertainty in Fig. 3.1f. This procedure will continue iteratively.

Case study: 12-state EKF

The EKF can be extended to include more dynamics by expanding the state vector, the number of states can therefore often indicate the level of detail used in the modelling of the system. Here a 12 state navigation EKF will be introduced for comparison to the nonlinear observer structure presented later in this chapter.

The strapdown kinematic equations of a vehicle in NED-frame are used, which differ from the ECEF-frame kinematic equations (2.7)–(2.9) by excluding the Earth rotation:

$$\dot{p}^n = v^n, \tag{3.16}$$
$$\dot{v}^n = f^n + g^n(p^n), \tag{3.17}$$
$$\dot{\Theta}_b^n = T(\Theta_b^n)\omega_{nb}^b, \tag{3.18}$$
$$\dot{b}^b = 0, \tag{3.19}$$

where the NED-frame has been assumed to be an inertial frame, such that ω_{nb}^b is considered rather than ω_{ib}^b. Here the attitude will be represented as Euler angles, $\Theta_n^b = [\phi; \theta; \psi]$, where the transformation matrix is given by, [55]:

$$T(\Theta_n^b) = \begin{bmatrix} 1 & \sin(\phi)\tan(\theta) & \cos(\phi)\tan(\theta) \\ 0 & \cos(\phi) & -\sin(\phi) \\ 0 & \sin(\phi)/\cos(\theta) & \cos(\phi)/\cos(\theta) \end{bmatrix}. \tag{3.20}$$

The state vector is given as; $x = \left[p^n; v^b; \Theta_b^n; b^b\right]$, with the loosely-coupled GNSS/INS integration scheme visualized in Fig. 3.2. The inertial measurements are low-pass filtered and used to construct an input vector u consisting of measured specific force and angular rates. The GNSS measurements are validated and used for aiding of the inertial navigation in the EKF.

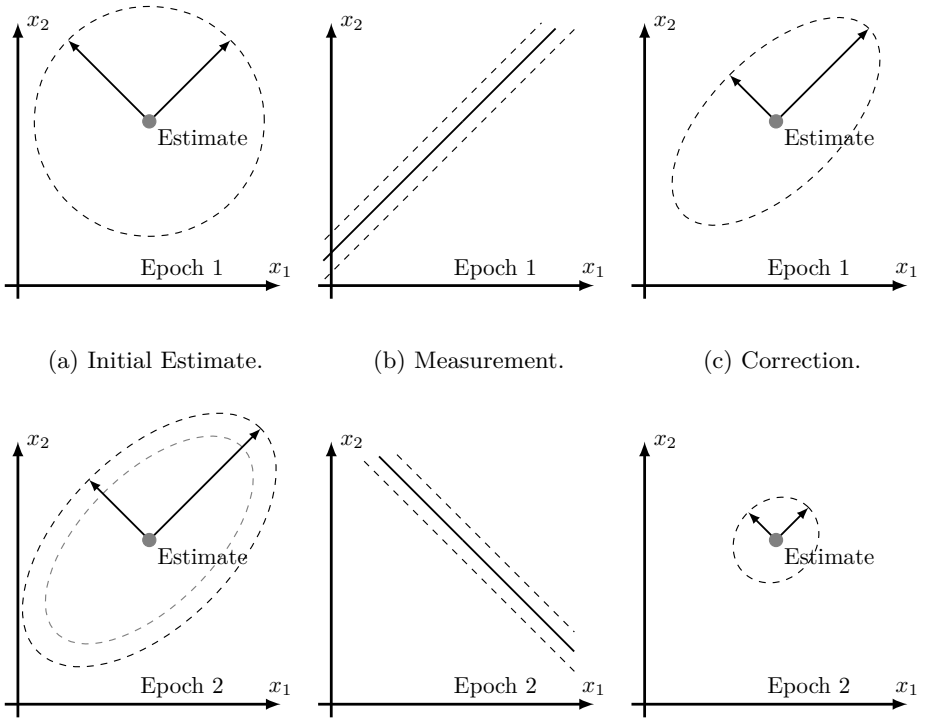

(a) Initial Estimate. (b) Measurement. (c) Correction.

(d) After propagation. (e) Measurement. (f) Correction.

Figure 3.1: Kalman filter procedure during two epochs, inspired by [76, Section 3.1.2].

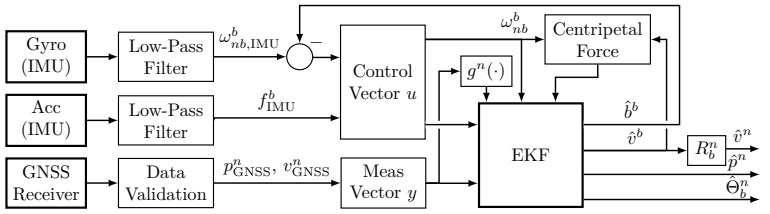

Figure 3.2: Block diagram of Extended Kalman Filter

The state estimates are propagated according to the observer model of the

kinematic equations:

$$f(\hat{x},t) = \begin{cases} \dot{\hat{p}}^n = R(\hat{\Theta}_b^n)\hat{v}^b \\ \dot{\hat{v}}^b = f^b + \hat{v}^b \times \left(\omega_{ib,\text{IMU}}^b - \hat{b}^b\right) - R(\hat{\Theta}_b^n)^\intercal g^n \\ \dot{\hat{\Theta}}_n^b = T(\hat{\Theta}_n^b)\left(\omega_{ib,\text{IMU}}^b - \hat{b}^b\right) \\ \dot{\hat{b}}^b = 0, \end{cases} \tag{3.21}$$

$$y = \begin{bmatrix} I_3 & 0 & 0 & 0 \\ 0 & I_3 & 0 & 0 \end{bmatrix} x + w_m \tag{3.22}$$

where $g^n = [0\ 0\ g]^\intercal$ is the known gravity vector. The injection terms for the observer are based on the difference between measured and estimated position and velocity. The process and measurement noise covariance matrices Q and R are defined as follows, see (3.6):

$$Q = \text{blockdiag}\left(\sigma_p^2, \sigma_v^2, \sigma_\Theta^2, \sigma_b^2\right), \qquad R = \text{blockdiag}\left(\sigma_{p_{\text{GNSS}}}^2, \sigma_{v_{\text{GNSS}}}^2,\right) \tag{3.23}$$

where blockdiag$(\cdot)$ denotes a block diagonal matrix and $\sigma_\star^2 \in \mathbb{R}^{3\times3}$ are matrices with diagonal elements of covariance for position, velocity, attitude, gyroscope biases and GNSS based position and velocity.

Tuning of the EKF is done by determining appropriate values for the Q and R matrices based on the power spectral densities of the driving noise. The driving noise terms of the Q matrix can be interpreted as originating from the IMU noise. The inertial noise propagates through the kinematic equations such that the noise on position and velocity is the propagated noise from the acceleration and gyro measurements. Due to this propagation σ_p and σ_v cannot be directly coupled to IMU performance parameters, and are often chosen small. Even when properly tuned, the state estimates rely strongly on the availability of the GNSS signal. If the GNSS signal is obstructed the estimates begin to diverge quickly and estimates may become unstable if the filter parameters are not adjusted. It is recommended to augment the system model with accelerometer bias estimates if the application is expected to experience GNSS outage.

3.3.1 Multiplicative EKF

The EKF introduced above estimates the attitude using the Euler angle representation, which introduces singularities at pitch angles of $\pm90°$, corresponding to vertical. In [122] a multiplicative EKF (MEKF) was introduced by inclusion of a three-component attitude error vector, $a(t) \in \mathbb{R}^{3\times1}$, while the global attitude is parameterized as a quaternion. The quaternion parameterization cannot be used directly in the state vector due to the nonlinear representation. However, by introducing the attitude error in the state vector it is possible to recreate the quaternion representation. Only the attitude error vector, $a(t)$, is included in the state vector, thereby retaining the linear characteristics of the residual model. The concept relies on the 4×4 quaternion representation having rank three, and therefore can be projected onto a 3×3 rotation matrix without loss of information.

A redundant formulation of the true nonlinear attitude state with some reference quaternion, $q_{ref}(t)$, is presented as:

$$q(t) = \delta q(a(t)) \otimes q_{ref}(t), \tag{3.24}$$

where $\delta q(a(t))$ denotes the unit quaternion representing the rotation from the reference to the true attitude $q(t)$. With the estimate of the error vector, $\hat{a}(t)$, the estimated unit quaternion is:

$$\hat{q}(t) = \delta q(\hat{a}(t)) \otimes q_{ref}(t), \tag{3.25}$$

The redundancy can be removed by choosing $q_{ref} = \hat{q}$ such that the expectation of $\hat{a}(t)$ is zero when all information is included.

Several representations for the unconstrained attitude error are introduced in [122], where the Gibbs vector might be preferred due to its infinite limiting value. The Gibbs vector is given as:

$$\delta q(a) = \frac{1}{\sqrt{4 + \|a\|_2^2}} \begin{bmatrix} a \\ 2 \end{bmatrix}. \tag{3.26}$$

Only the attitude error is included in the EKF, while the globally nonsingular attitude representation of q is updated for each filter iteration. In addition to the time propagation and measurement update of the EKF a reset of the attitude error is introduced in the MEKF. The reset is included to avoid propagation of two attitude representations by shifting the information of the attitude error to the quaternion representation, following an assignment of $a = 0$, [122].

3.4 Nonlinear Observer

Numerous nonlinear observers have been proposed for integration of IMU and GNSS data, however, in the following the observer proposed in [72] will be considered, estimating position and velocity in the ECEF-frame and describing the attitude as a unit quaternion.

The nonlinear observer presented here has a modular structure consisting of an attitude estimator and a translational motion observer. The two subsystems are feedback interconnected, where the specific force estimate is fed back from the motion observer to the attitude estimator. An advantage of the modular design is that the stability properties of the subsystems can be investigated individually leading to the stability result of the entire observer system using nonlinear stability theory, see [72] for further details. The observer structure is depicted in Fig. 3.3.

An implementation overview of the attitude estimator can be found in Algorithm 1, while the translational motion observer implementation is included in Algorithm 2, in Appendix C. The attitude estimator and translational motion observer (TMO) subsystems will be introduced in detail in the following sections.

3.4.1 Attitude estimation

The attitude of the vehicle is represented as a unit quaternion, $\hat{q}_b^e$, describing the rotation between body- and ECEF-frame. The attitude observer is a complementary

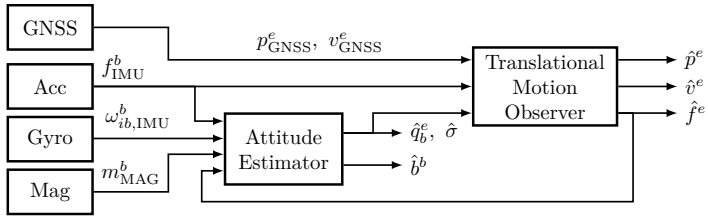

Figure 3.3: Block diagram of nonlinear observer

filter fusing data from an accelerometer and gyroscope to estimate the vehicle attitude. It can be further aided by other measurement and reference vectors. The nonlinear observer estimating the attitude and gyro bias, $\hat{b}^b$, is given as, [71, 72, 120]:

$$\dot{\hat{q}}^e_b = \frac{1}{2}\hat{q}^e_b \otimes \left(\bar{\omega}^b_{ib,IMU} - \bar{\hat{b}}^b + \bar{\hat{\sigma}}\right) - \frac{1}{2}\bar{\omega}^e_{ie} \otimes \hat{q}^e_b, \tag{3.27}$$

$$\dot{\hat{b}}^b = \text{Proj}(\hat{b}^b, -k_I\hat{\sigma}), \tag{3.28}$$

$$\hat{\sigma} = k_1 \underline{v}^b_1 \times R(\hat{q}^e_b)^\intercal \underline{v}^e_1 + k_2 \underline{v}^b_2 \times R(\hat{q}^e_b)^\intercal \underline{v}^e_2, \tag{3.29}$$

where $k_1 > k_P$, $k_2 > k_P$, and $k_I > 0$ are positive and sufficiently large tuning constants, $k_P > 0$. The projection operator, $\text{Proj}(\cdot,\cdot)$, limits the gyro bias estimate to a sphere with radius $M_{\hat{b}}$ where $M_{\hat{b}} > M_b$ is a design parameter. In [72] it was shown that the combined error variable $\tilde{\varsigma} := \left[\tilde{r}; \tilde{b}\right]$ converges exponentially to zero, where $\tilde{b} := b^b - \hat{b}^b$ and $\tilde{r}$ is the real part of $\tilde{q} := q^e_b \otimes (\hat{q}^e_b)^*$ with $(\hat{q}^e_b)^*$ being the conjugate of $\hat{q}^e_b$. The convergence of the combined variable can be ensured from an arbitrarily large set of initial conditions.

The projection function is defined as $\text{Proj}(x, y) = p(x, y)y$ where, [74]:

$$p(x,y) = \begin{cases} I - c(x)\Lambda\frac{xx^\intercal}{x^\intercal\Lambda x}, & x^\intercal x > M^2 \text{ and } x^\intercal y > 0 \\ I, & \text{otherwise,} \end{cases} \tag{3.30}$$

$$c(x) = \min\left(1, \frac{x^\intercal x - M^2}{\hat{M}^2 - M^2}\right), \tag{3.31}$$

where M and $\hat{M}$ are bounds and Λ is a gain matrix.

The injection term, $\hat{\sigma}$, consists of two vectors in body-frame and their corresponding vectors in ECEF-frame, but can easily be extended to include additional terms.

Assumption 10. The two attitude reference vectors are not collinear, i.e. their cross product is non-zero. This is satisfied if there exists a constant $c_{obs} > 0$ such that $||\underline{v}^e_1 \times \underline{v}^e_2||_2 \geq c_{obs}$.

Remark 3.8. Temporary violation of Assumption 10 can be tolerated since the attitude estimate can be updated using only the angular rate measurements for shorter periods of time.

In the following different configurations of the measurement, $\underline{v}^b$, and reference, $\underline{v}^e$, vectors will be investigated based on the available sensors.

Magnetometer

With a magnetometer a three dimensional magnetic field measurement can be obtained and compared to the magnetic field of the Earth, thereby determining rotation of the magnetometer in a global frame. The magnetic field can be affected by hard- and soft-iron which can cause significant errors, if not compensated, when used on large vehicles such as cars or vessels. For lightweight aircraft the amount of metal and wiring is small and the magnetometer will be able to determine the magnetic field around the aircraft. It can be advantageous to place the magnetometer far from error sources or shield parts of engines and electronics such that the effect on the magnetometer is minimized.

Using a magnetometer the normalized measurement and reference vectors can be expressed as:

$$\underline{v}^b = \frac{m^b_{\text{MAG}}}{\|m^b_{\text{MAG}}\|_2}, \qquad \underline{v}^e = \frac{m^e(\hat{p}^e)}{\|m^e(\hat{p}^e)\|_2}, \tag{3.32}$$

where m^b_{MAG} is the magnetic field experienced by the magnetometer, and the reference magnetic field, $m^e(\hat{p}^e)$ can be determined from look-up tables based on the current position estimate, see e.g. [124]. As the magnetic field of the Earth is slowly time-varying a small error in the position estimate will have negligible effect on the magnetic field reference.

Specific force

The specific force exerted on the vehicle is measured by the IMU, f^b_{IMU}, while the specific force in global frame is estimated in the translational motion observer. The scaled vectors are then:

$$\underline{v}^b = \frac{f^b_{\text{IMU}}}{\|f^b_{\text{IMU}}\|_2}, \qquad \underline{v}^e = \frac{\hat{f}^e}{\|\hat{f}^e\|_2}. \tag{3.33}$$

As an example: In a stationary scenario, such as prior to flight, the measurement vector will approximately be; $\underline{v}^b \approx [0; 0; -1]$, as the complete measured specific force will be in the Down direction. However, the use of (3.33) does not make any assumption on stationarity.

Optical flow

In surveillance and georeferencing applications it is common to use aircraft with cameras to take images of an overflown area. Using machine vision the optical flow can be determined by object recognition in consecutive images and be used to estimate the vehicle velocity, see e.g. [60]. The linear velocity of the vehicle determined from optical flow is denoted v^b_F and can be used to construct measurement vectors for attitude estimation. In [60] the attitude was determined as a rotation matrix and the measurement and reference vectors where therefore matrices; $\underline{V}^* \in \mathbb{R}^{3\times 3}$ determined as:

$$\underline{V}^b = \begin{bmatrix} v^b_F & v^b_F \times f^b_{\text{IMU}} & v^b_F \times (v^b_F \times f^b_{\text{IMU}}) \end{bmatrix} \tag{3.34}$$

$$\underline{V}^n = \begin{bmatrix} \hat{v}^n & \hat{v}^n \times \hat{f}^n & \hat{v}^n \times (\hat{v}^n \times \hat{f}^n) \end{bmatrix}. \tag{3.35}$$

The reference matrix is here given in NED frame, with linear velocity and specific force estimates, $\hat{v}^n$ and $\hat{f}^n$, from the corresponding translational motion observer. Similar vectors can be designed when the attitude is expressed as quaternions.

Velocity

The vehicle velocity can be used as a reference vector for the attitude estimation by considering the forward velocity of the vehicle as a measurement. In the presence of wind the velocity of the vehicle can be described by the wind triangle, see [19, Section 2.4]. In Fig. 3.4 and Fig. 3.5 the vertical and horizontal components are visualized, where the velocity with respect to the inertial frame, v_g, is the sum of the wind velocity, v_w, and the velocity of the vehicle with respect to the surrounding air, v_a. The point P specifies the vehicle position with initial direction along the dashed line.

Considering the vertical component, the dotted line denotes a level trajectory corresponding to the horizontal plane, while γ and γ_a are the flight path angles and the air-mass-referenced flight path angle, respectively. The angle-of-attack, α, describes the positive angle between the vehicle frame and airspeed vector. For aircraft this angle is required to generate lift.

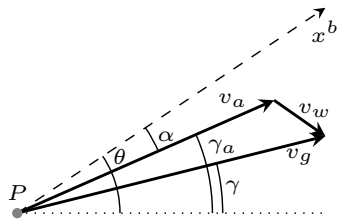

Figure 3.4: Vertical component of the wind triangle, [19].

The horizontal component, shown in Fig. 3.5, has a side-slip angle, β, between the initial direction and the airspeed vector, such that the body frame can be rotated by β around the z^b-axis to obtain the wind frame. The dotted line denotes the north direction thereby determined the yaw angle as the relative rotation of the x^b-axis. The course angle and crab angle are denoted χ and χ_c, respectively, and describe the rotation of the vehicle velocity in inertial and air frame.

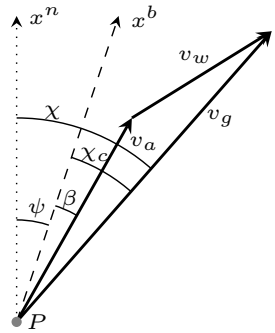

Figure 3.5: Horizontal component of the wind triangle, [19].

The vehicle velocity with respect to the surrounding air decomposed in the body frame can be expressed as, [19]:

$$v_a^b = v_g^b - v_w^b = R_w^b v_a^w = \|v_a\|_2 \begin{bmatrix} \cos(\alpha)\cos(\beta) \\ \sin(\beta) \\ \sin(\alpha)\cos(\beta) \end{bmatrix}, \tag{3.36}$$

where $v_a^w = [\|v_a\|_2; 0; 0]$ is the velocity of the vehicle relative to the wind in the wind frame, and R_w^b is the rotation matrix from wind to body frame.

In connection to the wind triangle the following relations can be expressed:

$$\gamma_a = \theta - \alpha, \qquad \chi_c = \chi - \psi, \tag{3.37}$$

The side-slip angle cannot be readily expressed from the wind triangle relations. However, from (3.36) the angle-of-attack and side-slip angle can be expressed as:

$$\alpha = \tan^{-1}\left(\frac{w_r}{u_r}\right), \qquad \beta = \sin^{-1}\left(\frac{v_r}{\|v_a\|_2}\right), \tag{3.38}$$

where the velocity vector has been decomposed into its three dimensional components, $v_a^b = [u_r; v_r; w_r]$.

Assumption 11. The wind vector can be ignored, i.e. $v_w = 0$, $\beta = \chi_c$, $\gamma_a = \gamma$.

If the angle-of-attack and side-slip angles cannot be assumed to be small an estimation scheme using a pitot-static tube and altimeter, in addition to the IMU and GNSS-receiver, can be employed. Such a sensor-based approach was proposed in [100] where a Kalman filter using only kinematic relationships, negating the need for aircraft parameters, was used to estimate wind velocity, angle-of-attack and side-slip angles for small UAVs. Another approach is the model-base approach proposed in [24] where a detailed model of a UAV is utilized to estimate angle-of-attack, wind speed and side-slip angle. The proposed observer was shown to be exponentially stable without requiring persistent excitation during flight.

Furthermore it is possible to utilize GNSS measurements to estimate γ and β. Under Assumption 11 the angle-of-attack and side-slip angles can be expressed as:

$$\alpha = \theta - \gamma, \qquad \beta = \chi - \psi. \tag{3.39}$$

The course over ground can be determined from a GNSS velocity measurement as:

$$\chi = \tan^{-1}\left(\frac{v_{north}^n}{v_{east}^n}\right), \tag{3.40}$$

with v_{north}^n and v_{east}^n being the velocity in North and East direction, respectively. If the GNSS receiver only allows for position measurements the course can be determined from two consecutive position measurements, $p_1^n = [x_1^n; y_1^n; z_1^n]$ and $p_2^n = [x_2^n; y_2^n; z_2^n]$, as; $\chi = \tan^{-1}((y_2^n - y_1^n)/(x_2^n - x_1^n))$.

The flight-path angle can be determined from the relation, [19]:

$$\frac{\partial h}{\partial t} = \|v_g\|_2 \sin(\gamma) \quad \Leftrightarrow \quad \gamma = \sin^{-1}\left(\|v_g\|_2^{-1}\frac{\partial h}{\partial t}\right), \tag{3.41}$$

where h is the altitude measurement from the GNSS receiver.

The body velocity vector can then be expressed as:

$$v_a^b = \|v_a\|_2 \begin{bmatrix} \cos(\theta - \sin^{-1}(\|v_g\|_2^{-1}\frac{\partial h}{\partial t}))\cos(\tan^{-1}(\frac{y_2-y_1}{x_2-x_1}) - \psi) \\ \sin(\tan^{-1}(\frac{y_2-y_1}{x_2-x_1}) - \psi) \\ \sin(\theta - \sin^{-1}(\|v_g\|_2^{-1}\frac{\partial h}{\partial t}))\cos(\tan^{-1}(\frac{y_2-y_1}{x_2-x_1}) - \psi) \end{bmatrix}. \tag{3.42}$$

The body velocity vector can be normalized and used in the attitude injection term with the reference vector being based on the estimated velocity, $\underline{v}^e = \hat{v}^e / \|\hat{v}^e\|_2$.

The use of pitch and yaw angles in the velocity estimation creates a feedback which might introduce stability issues. It can therefore be advantages to approximate the velocity vector to a simpler expression.

Remark 3.9. *(Small Angle Approximation)* For small angles the relations in (3.38) can be approximated to; $\alpha \approx w_r/u_r$ and $\beta \approx v_r/\|v_a\|_2$. The velocity vector can then be rewritten as; $v^b = 1/u_r\,[u_r; v_r; w_r] \approx [1; \beta; \alpha]$, where β has been approximated as $\beta \approx v_r/u_r$.

Remark 3.10. *(Roll and pitch)* Using a pitot tube the magnitude of the airspeed can be determined. In [96, 121] a small aircraft during a level turn is considered, and it was shown that using a pitot tube estimation of roll and pitch was possible with the recovered measurement: $v_a = \|v_a\|_2\,[\cos(\alpha); 0; \sin(\alpha)]$. The yaw angle can be estimated by inclusion of an additional sensor, e.g. a magnetometer. Only the angle-of-attack is included as β is assumed negligible. Furthermore, [121] proposes a method for estimation of angle-of-attack based on a linearized version of flight dynamics; $\dot{\alpha} = -c_0\alpha/\|v_a\|_2 + \dot{\theta} + \alpha_0$, where c_0 and α_0 are constants that can be found with system identification and training data. A sensor-based approach such as [100] or [24] can also be used to determine the angle-of-attack from pitot tube measurements.

Remark 3.11. *(Negligible Angles)* A rough approximation, under Assumption 11, considering negligible angle-of-attack and side-slip angles is $\beta = \chi - \psi = 0$ and $\alpha = \theta - \gamma = 0$ results in the normalized vehicle velocity in body frame; $v^b = [1; 0; 0]$. The measurement vector for the attitude injection term is $\underline{v}^b = v^b$.

Compass

Similarly to a magnetometer a compass can be used to determine heading by measuring the local magnetic field relative to the magnetic north. In a classical navigation sense a magnetometer offers the strength of a magnetic field, often in three dimensions, whereas a compass offers a direction of the magnetic field. However, with recent advances within sensor technology the lines between products are getting blurred. Here a compass is intended to consider a sensor given a heading relative to the magnetic north. The declination, δ, is the angle difference between geometric and magnetic north, and it is position dependent, $\psi = \psi_{\text{MAG}} + \delta$, where ψ is the heading. In analog compasses the heading is directly measured, whereas modern digital compasses use a three dimensional magnetic field measurement. In level flights only the two horizontal axes are necessary, whereas a vertical component is required to compensate for the inclination angle of the magnetic field relative to the horizontal plane, [19]. The magnetic heading can be determined as $\psi_{\text{MAG}} = tan^{-1}(m_y^h/m_x^h)$, where m_x^h and m_y^h are the x and y components of the magnetic field measurement projected onto the horizontal plane, [19].

The measurement and reference vectors for the attitude injection term can be

constructed as:

$$\underline{v}^b = \begin{bmatrix} \cos(\psi) \\ -\sin(\psi) \\ 0 \end{bmatrix}, \qquad \underline{v}^e = R_n^e \begin{bmatrix} 1 \\ 0 \\ 0 \end{bmatrix}, \tag{3.43}$$

where the reference vector is transformed from NED- to ECEF-frame by multiplication of the rotation matrix R_n^e.

Remark 3.12. The heading angle can also be determined from GNSS measurements if the wind can be assumed negligible, such that heading coincides with course over ground, i.e. $\psi = \chi$, similarly to the velocity measurement in (3.40).

3.4.2 Accelerometer bias estimation

The accelerometer bias, $b_f^b \in \mathbb{R}^3$, is an additive term to the specific force measurements; $f_{\text{IMU}}^b = f^b + b_f^b$, and can like the gyro bias be considered slowly time-varying, i.e. $\dot{b}_f^b = 0$. By comparing the vector norm of f_{IMU}^b and f^e it is possible to construct an exponentially converging estimator of the bias, see [74]. The main idea is that the two norms will be equal if the bias is zero. Following the outline of [74] a combination of parameters is considered $\Xi = \left[\|b_f^b\|_2^2; b_f^b\right]$. Introducing the time-varying vector $\vartheta = \left[1; -2f_{\text{IMU}}^b\right]$ it is assumed that the accelerometer is experiencing persistently excitation:

$$\int_t^{t+T} \vartheta(\tau)\vartheta^\intercal(\tau)d\tau \geq \varepsilon I, \tag{3.44}$$

where $\varepsilon > 0$ is a constant and the sample interval $T > 0$, such that for each $t \geq 0$ the condition is satisfied and the persistently excitation assumption is valid.

Further assuming that a lower bound M_Ξ on the length of Ξ is known, the estimate $\hat{\Xi}$ has the bound $\|\hat{\Xi}\|_2 \geq M_{\hat{\Xi}}$, where $M_{\hat{\Xi}} > M_\Xi$. An over-parameterized observer was proposed by [71] and [74], to estimate the accelerometer bias similarly to the gyro bias estimation presented in (3.28):

$$\dot{\hat{\Xi}} = \text{Proj}\left(\hat{\Xi}, \Gamma\vartheta\left(\hat{y}_f - \vartheta^\intercal\hat{\Xi}\right)\right), \tag{3.45}$$

where Γ is a positive-definite symmetric gain matrix. If f^e is estimated, e.g. in the translational motion observer, the norm difference of the specific force can be expressed as; $y_f = \max\{\|\hat{f}^e\|_2^2, M_f^2\} - \|f_{\text{IMU}}^b\|_2^2$, where $\|f^i\|_2 = \|R_b^i f^b\|_2 = \|f^b\|_2$. See [71] and [74] for extensive stability proof of the bias estimator.

3.4.3 Translational motion observer

The translational motion observer estimates the position and linear velocity of the vehicle by using injection terms based on the difference between measured and estimated position and velocity. The position and velocity measurements are traditionally provided by a GNSS receiver, p_{GNSS}^e and v_{GNSS}^e. Additionally, the

observer also estimates the specific force of the vehicle by introducing an auxiliary state, ξ. The translational motion observer is described by, [72]:

$$\dot{\hat{p}}^e = \hat{v}^e + \theta K_{pp}\left(p^e_{\text{GNSS}} - \hat{p}^e\right) + K_{pv}\left(v^e_{\text{GNSS}} - C_v\hat{v}^e\right), \tag{3.46}$$

$$\begin{aligned}\dot{\hat{v}}^e = &-2S(\omega^e_{ie})\hat{v}^e + \hat{f}^e + g^e(\hat{p}^e_r) + \theta^2 K_{vp}\left(p^e_{\text{GNSS}} - \hat{p}^e\right)\\ &+ \theta K_{vv}\left(v^e_{\text{GNSS}} - C_v\hat{v}^e\right),\end{aligned} \tag{3.47}$$

$$\dot{\hat{\xi}} = -R(\hat{q}^e_b)S(\hat{\sigma})f^b_{\text{IMU}} + \theta^3 K_{\xi p}\left(p^e_{\text{GNSS}} - \hat{p}^e\right) + \theta^2 K_{\xi v}\left(v^e_{\text{GNSS}} - C_v\hat{v}^e\right), \tag{3.48}$$

$$\hat{f}^e = R(\hat{q}^e_b)f^b_{\text{IMU}} + \xi, \tag{3.49}$$

where K_* are gain matrices. The constant $\theta \geq 1$ serves as a tuning parameter that should be sufficiently large to guarantee global stability of the feedback interconnection of the translational motion observer and attitude observer. It was shown in [70] that the velocity part of the injection term is not required to achieve stability. This allows the velocity measurement matrix C_v to have less than full rank or be zero. Details on the discrete-time implementation of the translational motion observer will be presented in Section 3.4.7.

Gain selection

The gain matrices K_* can be chosen to satisfy $A - KC$ being Hurwitz with:

$$A = \begin{bmatrix} 0 & I_3 & 0 \\ 0 & 0 & I_3 \\ 0 & 0 & 0 \end{bmatrix}, \quad C = \begin{bmatrix} I_3 & 0 & 0 \\ 0 & C_v & 0 \end{bmatrix}, \quad K = \begin{bmatrix} K_{pp} & K_{pv} \\ K_{vp} & K_{vv} \\ K_{\xi p} & K_{\xi v} \end{bmatrix}. \tag{3.50}$$

The translational motion observer is similar to the EKF, and the gain matrix K can therefore be determined similarly to the EKF gain by solving a Riccati equation. This will be considered in more detail in Section 3.4.5. However, an advantage of this nonlinear observer is that the gain matrix is not required to be determined each iteration, but rather on a slower time scale, see [72]. This time scale can be slower than the GNSS update rate, decreasing the computational load substantially. The load can be further reduce by considering the implementation as a fixed gain observer only determining the gains at the initialization phase. It has been shown in [30] that time-varying gains aids in sensor noise suppression and gives faster convergence.

3.4.4 Stability considerations

The estimation errors are defined as the difference between the kinematic model, (2.7)–(2.9), and the observer estimates, introducing the error states as; $\tilde{p} := p^e - \hat{p}^e$, $\tilde{v} := v^e - \hat{v}^e$, and $\tilde{f} := f^e - \hat{f}^e$. Here the specific force has replaced the auxiliary state by combination of (3.48) and (3.49). The combined state vector is then $\tilde{x} = \left[\tilde{p}; \tilde{v}; \tilde{f}\right]$. Following the proof of [72] the estimation errors can be redefined to; $\eta_1 := \tilde{p}$, $\eta_2 := \tilde{v}/\theta$, $\eta_3 := \tilde{f}/\theta^2$ with $\eta = [\eta_1; \eta_2; \eta_3]$, such that the error dynamics in the nominal case, where no sensor errors or noise is present, can be expressed as:

$$\frac{1}{\theta}\dot{\eta} = (A - KC)\eta + \theta_1(t, \eta) + \theta_2(t, \tilde{\varsigma}), \tag{3.51}$$

where the perturbation terms are:

$$\theta_1(t,\eta) = \begin{bmatrix} 0 \\ -\frac{1}{\theta}2S(\omega_{ie}^e)\eta_2 + \frac{1}{\theta^2}(g^e(p^e) - g^e(p^e - \eta_1)) \\ 0 \end{bmatrix}, \tag{3.52}$$

which in [72] was shown to be limited by; $\|\theta_1(t,\eta)\| \leq \frac{1}{\theta}\gamma_1\|\eta\|$ for some constant $\gamma_1 > 0$. Furthermore, $\theta_2(t,\tilde{\varsigma}) = \left[0; 0; 1/\theta^3\tilde{d}\right]$ where:

$$\begin{aligned}\tilde{d} = (I - \tilde{R}^\intercal)R(q_b^e)(S(\omega_{ib,\text{IMU}}^b)f_{\text{IMU}}^b + \dot{f}_{\text{IMU}}^b) - S(\omega_{ie}^e)(I - \tilde{R}^\intercal)R(q_b^e)f_{\text{IMU}}^b \\ - \tilde{R}^\intercal R(q_b^e)S(\tilde{b})f_{\text{IMU}}^b,\end{aligned}$$

with $\tilde{R} = R(\tilde{q})$. An upper limit can be expressed as; $\|\theta_2(t,\tilde{\varsigma})\| \leq \frac{1}{\theta^3}\gamma_2\|\varsigma\|$, for some positive constant $\gamma_2 > 0$.

Proposing the Lyapunov candidate, $U = \frac{1}{\theta}\eta^\intercal P\eta$, with the symmetric $P > 0$ being a solution to the Lyapunov equation $P(A - KC) + (A - KC)^\intercal P = -I$, the derivative along the trajectories of the systems is then:

$$\dot{U} \leq -\left(1 - \frac{2\|P\|\gamma_1}{\theta}\right)\|\eta\|^2 + \frac{2\|P\|\gamma_2}{\theta^3}\|\eta\|\|\tilde{\varsigma}\|. \tag{3.53}$$

Following the steps presented in [72] the stability results can be summarized to: There exist a $\theta^* \geq 1$ such that with $\theta \geq \theta^*$ then for all initial conditions $(\tilde{p}(0) \times \tilde{v}(0) \times \tilde{\xi}(0)) \in \mathcal{K}$, $\tilde{q}(0) \in \tilde{\mathcal{D}}(\bar{\epsilon})$, and $\|\hat{b}^b(0)\| \leq M_{\hat{b}}$, where $\mathcal{K} \in \mathbb{R}^9$ is a compact set containing the origin, $\bar{\epsilon} = [0; 1/2]$ is an arbitrary constant with $\tilde{\mathcal{D}}(\epsilon) = \{|\tilde{q}||\tilde{s}_q| > \epsilon\}$, the convergence is described by:

$$\sqrt{\|\tilde{x}(t)\|^2 + \|\tilde{\varsigma}\|^2} \leq Ke^{-\lambda t}\sqrt{\|\tilde{x}(0)\|^2 + \|\tilde{\varsigma}\|^2}, \tag{3.54}$$

with positive time constant $\lambda > 0$ and some gain $K > 0$. The origin of the nonlinear observer has then been proven semi-global exponential stable (SGES). The practical implication of the SGES stability properties is the robustness to arbitrarily large initialization errors in both position and attitude since no linearization is needed in the nonlinear attitude estimator.

3.4.5 Continuous-time gain selection

The loosely-coupled translational motion observer can be written as a continuous-time linear system:

$$\dot{\hat{x}} = A\hat{x} + Bu + D(t,\hat{x}) + K(y - C\hat{x}), \tag{3.55}$$

with the input vector $u = \left[f_{\text{IMU}}^b; -S(\hat{\sigma})f_{\text{IMU}}^b\right]$, and output $y = [p_{\text{GNSS}}^e; C_v v_{\text{GNSS}}^e]$, and the matrices given in (3.50) and:

$$B = \begin{bmatrix} 0 & 0 \\ R(\hat{q}_b^e) & 0 \\ 0 & R(\hat{q}_b^e) \end{bmatrix}, \qquad D(t,\hat{x}) = \begin{bmatrix} 0 \\ g^e(\hat{p}^e) - 2(\omega_{ie}^e)\hat{v}^e \\ 0 \end{bmatrix},$$

where the system (A, B, C) is controllable and observable.

The gain conditions of [72], reviewed above, are of limited practical use since they are general and sufficient (not always necessary) conditions where a non-conservative bound θ^* may be difficult to find. Moreover, θ^* also depends on the attitude observer gains k_1, k_2, and k_I. In a practical approach to tuning, the gains in the matrix K of the TMO may be tuned using a minimum-variance estimation criterion by taking into account the influences of noise on its measurements. This is done by choosing $\theta = 1$ and designing:

$$Q = \text{blockdiag}(\sigma_p^2, \sigma_v^2, \sigma_f^2), \qquad R = \text{blockdiag}(\sigma_{p_{\text{GNSS}}}^2, \sigma_{v_{\text{GNSS}}}^2),$$

as input and measurement noise covariance matrices, respectively. Regarding R, the matrices $\sigma_{p_{\text{GNSS}}}$ and $\sigma_{v_{\text{GNSS}}}$ represents the covariance matrices of the position and velocity measurement noise components, respectively. In practice the GNSS position and velocity measurements are time-varying and correlated as the user position estimates are used to determine the user-to-satellite line-of-sight (LOS) vector in the velocity computation procedure. An alternative can then be to include cross terms σ_{pv} such that

$$R = \begin{bmatrix} \sigma_p^2 & \sigma_{pv}^2 \\ \sigma_{vp}^2 & \sigma_v^2 \end{bmatrix},$$

where the GNSS subscripts have been dropped. Moreover, the covariance matrices $\sigma_{p_{GNSS}}$ and $\sigma_{v_{GNSS}}$ are often considered as diagonal matrices, where the height component might have a higher covariance than the horizontal components. The covariance matrices the states σ_p^2, σ_v^2, and σ_f^2 are chosen to reflect the expected level of noise on the states, similarly as to in an EKF.

A gain matrix that gives an approximately minimum variance estimate is given by the Riccati equation solution $P = P^\intercal > 0$ motivated by the fact that the TMO's error dynamics are identical to the time-scaled error dynamics of the Kalman-Bucy filter [106]:

$$K = PC^\intercal R^{-1}, \tag{3.56}$$

$$\frac{1}{\theta}\dot{P} = AP + PA^\intercal - PC^\intercal R^{-1} CP + Q. \tag{3.57}$$

One reason for (3.55)–(3.57) only being an approximately minimum variance estimator is that $\hat{q}_b^e$ and $\hat{\sigma}$ are correlated with f_{IMU}^b. The result of [98, Lemma 6] shows that it is possible to choose θ independently from P, using the time-varying Riccati equation (3.57) such that the SGES stability properties posed in [72] still hold when calculating the gains with (3.56)–(3.57). However, choosing $\theta > 1$ is suboptimal with respect to the minimum variance optimization problem the Kalman-Bucy filter solves.

The TMO realization presented above can be referred to as a *direct filter* or *total state* implementation in the navigation literature, [52, Ch. 7.4]. In practice, this means that the filter's Riccati equation (3.57) is implemented at the frequency of the IMU and that the aiding sensors are used to correct the INS when available. As a result, for high integration frequencies, the computational burden might be

considerable. Therefore, more computationally efficient alternatives are desirable, while still maintaining time-varying gains. This is possible to achieve since the time-varying dynamics of (3.57) is slowly-varying. The gain matrix can be either time-varying or constant.

Case study: time-varying and constant gains

The effect of time-varying gain selection as opposed to constant observer gains in the translational motion observer is investigated in a simplified example. The example considers simulated sensors at rest. The measurement noise of the inertial sensors and position measurements are simulated as Gaussian white noise, although the noise in general has colored spectral content. Furthermore, the nonlinear observer will be considered in the NED-frame with only aiding of position measurements. The inertial noise characteristics is chosen as $\varepsilon_\omega \in \mathcal{N}(0, 0.0025^2\ [rad^2/s^2])$ and $\varepsilon_f \in \mathcal{N}(0, 0.05^2\ [m^2/s^4])$, and the GNSS noise in NED-frame is chosen as $\varepsilon_p = (\varepsilon_{p_n}; \varepsilon_{p_e}; \varepsilon_{p_d})$ with $\varepsilon_{p_n} \in \mathcal{N}(0, 1.1^2\ [m^2])$, $\varepsilon_{p_e} \in \mathcal{N}(0, 1.1^2\ [m^2])$, and $\varepsilon_{p_d} \in \mathcal{N}(0, 1.65^2\ [m^2])$ leaving the position measurements less accurate in the vertical component.

By pre- and post-multiplying Q with the input matrix, B, the covariance of the input vector can be considered instead of the covariance of the states. In this case the Q matrix is based on the expected noise of f^b_{IMU} and $-S(\hat{\sigma})f^b_{\text{IMU}}$ which can be somewhat determined from the IMU characteristics. For this case study the nonlinear observer is implemented with $\theta = 1$ and covariance matrices; $Q = \text{blockdiag}(0.05^2 I_3, 0.5 \cdot 0.05^2 I_3)\ [m^2/s^4]$ and $\sigma_p = \text{blockdiag}(1.1^2 I_2, 1.65^2)\ [m^2]$. The unitless attitude gains where chosen as $k_1 = k_2 = 0.5$, and $k_I = 0.01$. The estimation is initialized with an offset from true values, as NED position and attitude errors of $\tilde{p}(0) = [10; -7; 4]$m and $\tilde{\phi}(0) = 10$, $\tilde{\theta}(0) = 7$, $\tilde{\psi}(0) = -10$ degrees, respectively.

Three versions of the nonlinear observer is investigated; a) fixed gain observer, b) time-varying gains, and c) time-varying gains with higher attitude gains. The fixed gains for the observer in the first case where determined by solving the initial algebraic Riccati equation. The third case was simulated with attitude gains of $k_1 = k_2 = 20$ during the first 100 seconds. The transient responses of the position and attitude errors are shown in Figs. 3.6 and Fig. 3.7 for the three observers.

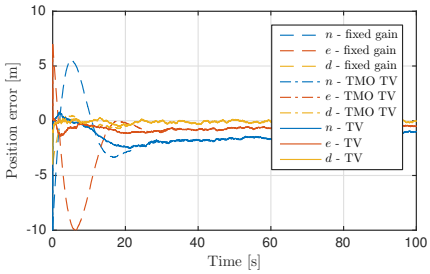

Figure 3.6: Position estimation error presented in NED-frame.

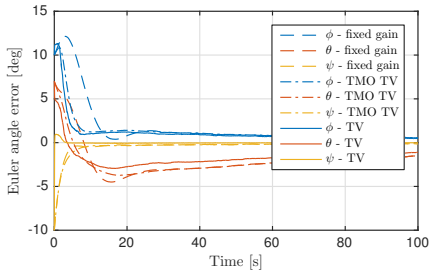

Figure 3.7: Attitude estimation error presented in Euler angles.

Here case a) is shown with dashed lines, case b) is shown with dot-dashed lines, and case c) is shown with solid lines. The transient performance is improved by using the time-varying gain selection. The fastest attitude convergence properties are witnessed in case c) with both time-varying TMO gains and higher initial attitude gains as seen in Fig. 3.7. However, the convergence properties of the position estimates are not improved by higher attitude gains. The errors have not fully converged after 100 seconds, as the gyro bias estimates have not converged to the true gyro biases yet.

3.4.6 Colored position and velocity measurement noise

The position and velocity measurements from a GNSS receiver are subjected to errors from various sources, as presented in Section 2.5.4. The measurement noise is often considered white Gaussian, however due to time-varying error sources such as atmospheric disturbances it should rather be considered colored noise, such that:

$$p^e_{\text{GNSS}} = p^e_{true} + \delta_p, \qquad v^e_{\text{GNSS}} = v^e_{true} + \delta_v, \tag{3.58}$$

where the δ_p and δ_v terms are colored noise terms described by:

$$\dot{z} = Fz + Gn, \qquad \delta = Hz + \varepsilon, \tag{3.59}$$

where $z = [z_p; z_v] \in \mathbb{R}^6$ are the noise state, $\delta = [\delta_p; \delta_v] \in \mathbb{R}^6$ denotes the position and velocity errors, and $\varepsilon^e_{pv} \in \mathbb{R}^6$ and $n \in \mathbb{R}^6$ are vectors with unity white noise where $n \sim (0, 1)$ and $\varepsilon^e_{pv} \sim (0, \sigma^2_{pv})$. Additional Gaussian white noise can be included for realistic measurements due to receiver noise. According to [130, 145] the model describing the position measurements can be chosen as a first-order Gauss-Markov process, hence the dynamic matrices $F = \text{diag}(F_p, F_v)$ can be chosen as $F_\star = -1/T_\star$, where $T_\star$ is the correlation time constant for either the position or velocity noise. The gain $G = [G_p; G_v]$ on the driving noise, n, can be chosen equal to an appropriate standard deviation.

For sufficiently long measurement periods the steady-state covariance of the Gauss-Markov processes z_p and z_v can be obtained by solving solving:

$$F_\star P_{z_\star} + P_{z_\star} F_\star^\intercal + G_\star G_\star^\intercal = 0, \tag{3.60}$$

where $\star$ is a placeholder for p or v. Since the dynamic matrices are symmetric; $F_p = F_p^\intercal$ and $F_v = F_v^\intercal$, (3.60) can be rewritten as;

$$F_\star P_{z_\star} + F_\star P_{z_\star} + G_\star G_\star^\intercal = 0, \tag{3.61}$$

$$2F_\star P_{z_\star} = -G_\star G_\star^\intercal, \tag{3.62}$$

$$P_{z_\star} = -\frac{1}{2} F_\star^{-1} G_\star G_\star^\intercal, \tag{3.63}$$

thereby determining the steady-state covariances:

$$P_{z_p}(\infty) = -\frac{1}{2} F_p^{-1} G_p G_p^\intercal, \qquad P_{z_v}(\infty) = -\frac{1}{2} F_v^{-1} G_v G_v^\intercal. \tag{3.64}$$

The time constants of the Gauss-Markov process can be chosen large, e.g. $T_p = 1100$ s as in [145], [19, Section 7.5], while the time constant for the velocity can be chosen small, e.g. $T_v = 2$ s. The small velocity time constant is based on the assumption that the GNSS velocity measurements are based on the Doppler range-rate measurements.

The translational motion observer can be augmented to include the colored GNSS position domain noise. By defining the state vector as; $x_a = [x; z]$ the dynamics equation can be expressed as:

$$\dot{x}_a = A_a x_a + B_1 u + B_2 n + D_a, \tag{3.65}$$

where the noise dynamics for the position and velocity measurements are:

$$\dot{\hat{z}} = F\hat{z} + K_{pz}(p^e_{\text{GNSS}} - \hat{p}^e - \hat{\delta}_p) + K_{vz}(v^e_{\text{GNSS}} - \hat{v}^e - \hat{\delta}_v). \tag{3.66}$$

The TMO can then be described as:

$$\dot{\hat{x}}_a = A_a\hat{x}_a + B_1 u + D_a(t, \hat{x}) + K_a(y - C_a\hat{x}_a), \tag{3.67}$$

where the matrices of the augmented system are defined by

$$A_a = \begin{bmatrix} A & 0 \\ 0 & F \end{bmatrix}, \qquad C_a = \begin{bmatrix} C & H \end{bmatrix}, \tag{3.68}$$

$$B_1 = \begin{bmatrix} B \\ 0 \end{bmatrix}, \qquad B_2 = \begin{bmatrix} 0 \\ G \end{bmatrix}, \tag{3.69}$$

$$K_a = \begin{bmatrix} K \\ K_z \end{bmatrix}, \qquad D_a(t, \hat{x}) = \begin{bmatrix} D(t, \hat{x}) \\ 0 \end{bmatrix}, \tag{3.70}$$

where $K_z = [K_{pz}, K_{vz}]$. The gain of the augmented system can be determined as $K_a = \theta L_\theta^{-1} K^0 E_\theta$ where $B_a = [B_1, B_2]$, $E_\theta = C L_\theta C^\dagger$ with the Moore-Penrose pseudoinverse $C^\dagger$, and gain:

$$L_\theta = \text{blockdiag}\left(I_3, \frac{1}{\theta} I_3, \frac{1}{\theta^2} I_3, I_{l_p}, \frac{1}{\theta} I_{l_v}\right), \tag{3.71}$$

The K^0 gain can be determined from a augmented equivalent to (3.56)–(3.57) with $Q_a = \text{blockdiag}(Q, I_{l_p}, I_{l_v})$. The dimensions of the position and velocity error models are denoted l_p and l_v.

The matrix pair (A_a, C_a) is always observable for any time constants, $T_p > 0$ and $T_v > 0$, when the model in (3.59) is chosen as Gauss-Markov noise, since the rank of the observability matrix will be full, thereby satisfying the rank condition of observability for linear time-variant systems, [106].

3.4.7 Discretization and Implementaion of TMO

The main principle for the discrete-time implementation is to approximate the continuous time behavior despite the finite data rate. It implies that the estimates are only updated when the output measurements contained in the injection terms

are valid, and otherwise integrate the model using measured inputs at their highest available update rate. Measurement updates can be processed sequentially by a KF, assuming the measurements are uncorrelated such that the R matrix is diagonal, with benefits for processing structure and complexity [52, 76]. Due to the close relationship between (3.56)–(3.57) and the KF, a similar strategy can be applied also for NLOs. The TMO (3.55) is straightforward to discretize due to its linearity and the simple A-matrix, allowing for exact discretization of the unforced dynamics:

$$A_d = \mathrm{e}^{AT} = \begin{bmatrix} I_3 & TI_3 & \frac{T^2}{2}I_3 \\ 0 & I_3 & TI_3 \\ 0 & 0 & I_3 \end{bmatrix}. \tag{3.72}$$

where the subscript d signifies the discrete nature of the matrix, such as to distinguish it from the continuous-time version. The discrete time index is denoted k incrementing for each iteration of the implementation, and will be introduced in subscript to keep track of the iteration. Assuming the specific force input, the rotation matrix and the gravity vector are constant between the IMU sampling intervals, $f^b_{\mathrm{IMU}}(t) = f^b_{\mathrm{IMU},k}$, $R(t) = R(q^e_{b,k})$ and $g^e(p^e(t)) = g^e(\hat{p}^e_k)$, for $t \in [kT, (k+1)T)$, the discrete versions of the matrices in (3.55) are:

$$B_{d,k} := \int_{kT}^{(k+1)T} e^{A\left((k+1)T-\tau\right)} B(\tau)u(\tau)\mathrm{d}\tau = \begin{bmatrix} \frac{T^2}{2}R(\hat{q}^e_{b,k}) & \frac{T^3}{6}R(\hat{q}^e_{b,k}) \\ TR(\hat{q}^e_{b,k}) & \frac{T^2}{2}R(\hat{q}^e_{b,k}) \\ 0 & TR(\hat{q}^e_{b,k}) \end{bmatrix},$$

$$D_{d,k} := \int_{kT}^{(k+1)T} e^{A\left((k+1)T-\tau\right)} D(\tau)\mathrm{d}\tau = \begin{bmatrix} \frac{T^2}{2}\left(g^e(\hat{p}_k) - 2S(\omega^e_{ie})\hat{v}^e_k\right) \\ T\left(g^e(\hat{p}_k) - 2S(\omega^e_{ie})\hat{v}^e_k\right) \\ 0 \end{bmatrix}.$$

This assumption can easily be satisfied by implementing the discrete system at the highest sensor rate possible, typically the IMU rate, such that $T = 1/f_{\mathrm{IMU}}$. The state and covariance matrix can be divided into *priori* and *posteriori* parts and propagated similarly as for the Kalman filter, see Section 3.3. An outline of the implementation of the discrete-time TMO in indirect form is presented in Algorithm 2 in Appendix C.

Discretization of the attitude observer is straightforward as Euler integration can be employed. An overview of the attitude estimator implementation be found in Algorithm 1 in Appendix C.

3.5 Experimental Verification

Experimental measurements from flights with a fixed-wing Bellanca Super Decathlon XXL unmanned aerial vehicle (UAV) are used to verify and compare the performance nonlinear observer with the EKF. The UAV (shown in Fig. 3.8) is equipped with an ADIS 16375 IMU, supplying acceleration and angular rate measurements, a HMR2300 magnetometer and a GARMIN 18X GPS-receiver. The inertial data are sampled at 100 Hz while the position measurements are sampled at 5 Hz. Furthermore, the UAV is equipped with a Polar X2@e (Septentrio) GPS

system consisting of three antennas, placed at the wing tips and tale, providing attitude and position estimates. The attitude accuracy is considered, based on the antenna geometry and manufacturer documentation, of 1σ is 0.2° in roll angle, 0.6° in pitch angle, and 0.3° in yaw angle. The estimates of the Septentrio system is considered highly accurate and is therefore used as a reference for comparison with the estimates of the EKF and nonlinear observer.

Figure 3.8: Bellanca Super Decathlon XXL UAV used for experimetal verification.

The goal of the following experimental verification is to compare the performance of the proposed nonlinear observer and EKF. Two datasets were used in the verification where it was desired to use the same tuning for both datasets to ensure the state estimators were not tuned specifically for a single dataset. The performance has been evaluated by comparison with the reference position, speed and attitude. For each of the datasets figures showing the estimation errors are depicted comparing the state estimators.

3.5.1 Parameters and tuning variables

The state estimators have several parameters and tuning variables to be determined, which will be presented and explained here. In the case of coinciding naming subscripts "EKF" and "NLO" will be used.

Tuning of the EKF consists of choosing reasonable Q_{EKF} and R_{EKF} matrices. While the R_{EKF} matrix relies on the accuracy of the GNSS receiver, the Q_{EKF} matrix describes the expected process noise due to accelerometer and gyro noise and instabilities, and can be tuned for the application. Here only the GNSS receiver position will be considered as velocity measurements were not available. The tuning matrices are initialised as $R_{EKF} = 14.40I_3\ [m^2]$, with $Q_{EKF} = \text{blkdiag}\left(0_3\ [m^2],\ 0.096I_3\ [m^2/s^2], 0.076 \cdot 10^{-4} I_2[rad^2], 0.305 \cdot 10^{-4}[rad^2], 3.046 \cdot 10^{-10} I_3[rad^2/s^2]\right)$, where the units have been given in square brackets. The state vector is driven by measured angular rates and specific force by inertial sensors having particular noise parameters. These parameters should be involved in the Q_{EKF} matrix.

Two versions of the fixed gain nonlinear observer is presented for comparison with the difference being the vectors used for attitude estimation: a magnetometer implementation (denoted NLO-Mag) and a version with velocity vectors (denoted NLO-Vel), where the first set of attitude vectors are $\underline{v}_1^b = f_{\text{IMU}}^b / \|f_{\text{IMU}}^b\|_2$ and

$\underline{v}_1^e = \hat{f}^e / \|\hat{f}^e\|_2$. The NLO-Mag utilize $\underline{v}_2^b = m^b / \|m^b\|_2 \times v_1^b$ and $\underline{v}_2^e = m^e / \|m^e\|_2 \times v_1^e$ while the NLO-Vel version utilize $\underline{v}_2^b = [1; 0; 0]$ and $\underline{v}_2^e = \hat{v}^e / \|\hat{v}^e\|_2$. This approach assumes the heading and course to be coinciding, which is mostly true for straight flight trajectories, ensuring uniformly semi-globally exponential stability through [59]. For flights including numerous turns a magnetometer might be preferred as loitering and cross-winds could affect the heading assumption.

The nonlinear observers include bound parameters which should be chosen sufficiently large $M_b = 0.0087$ $[rad/s]$, while the remaining unitless parameters are; $k_1 = 0.2$, $k_2 = 0.05$, $\theta = 1$, $k_I = 0.00005$. The fixed gains are $K_{pp} = 0.38 I_3$, $K_{vp} = 0.44 I_3$ and $K_{\xi p} = 0.14 I_3$. For the NLO-Vel the attitude injection gain is substituted for $k_2 = 0.01$.

The initial values of the state vectors are chosen from the first available measurements, and are similar for the three estimators (EKF, NLO-Mag, and NLO-Vel). It is important to tune the three state estimator equally thoroughly to keep the comparison fair.

3.5.2 Results

Two datasets are available using the same UAV and sensor suite. The proposed state estimators are tested on both datasets to verify that they are not tuned exclusively for one dataset. The inertial measurements are preprocessed with a low-pass filter whose bandwidth is set according to vibration spectrum.

Results of dataset 1 can be seen in Fig. 3.9, 3.10, 3.11, and 3.12, while the results of dataset 2 are shown in Fig. 3.13, 3.14, 3.15, and 3.16. The EKF solution is shown in red, the NLO-Mag is shown in dashed blue lines, while the NLO-Vel is green, with the reference from the Septentrio system depicted in black. This color scheme is used for all the figures in the verification. The occasional gap in the attitude error is due to temporary loss of reference. The findings are evaluated and summarised in Table 3.1 which compares the two estimators during the two flights.

The trajectory of flight 1 is shown in Fig. 3.9, covering an area of approximately 0.7 km^2 with a maximum altitude of 170m. The estimation errors of speed, attitude and position are shown in Fig. 3.10, 3.11, and 3.12, where the speed estimation error is centred around zero and includes a zoomed view for clarification. The attitude errors shown in Fig. 3.11 have similar behaviour for roll and pitch for the state estimators, whereas the nonlinear yaw estimate has some systematic offset. The position errors of Fig. 3.12 are very similar for the state estimators attesting that the nonlinear observers have comparable results to the EKF.

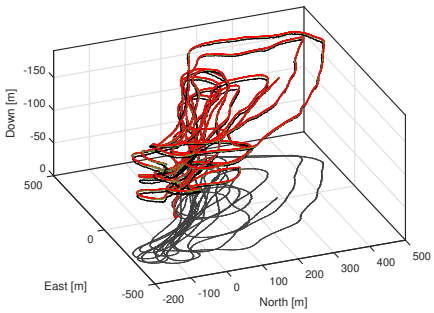

Figure 3.9: Vehicle trajectory (Dataset 1)

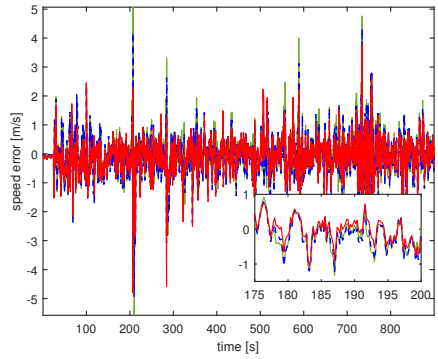

Figure 3.10: Speed estimation error (Dataset 1)

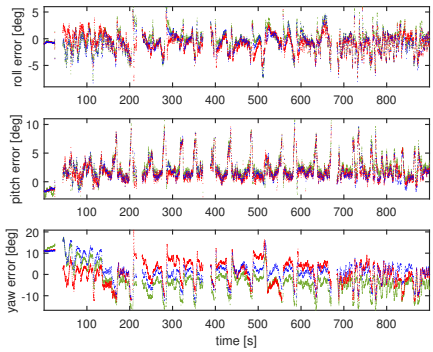

Figure 3.11: Attitude error (Dataset 1)

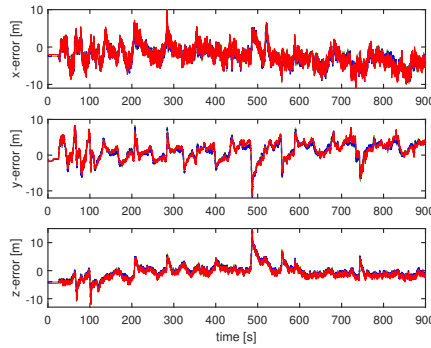

Figure 3.12: Position error (Dataset 1)

The second dataset consisted of approximately a third of the amount of measurements compared to dataset 1. The speed and attitude estimation errors are shown in Fig. 3.13 and Fig. 3.14, with comparable performance between the EKF and nonlinear observers. The position errors depicted in Fig. 3.15 show that an offset is present between the estimates, although the estimates follow the same pattern. Finally, the gyro bias estimates are shown in Fig. 3.16. As there are no reference for the gyro biases these are included to show the similarities across the state estimators.

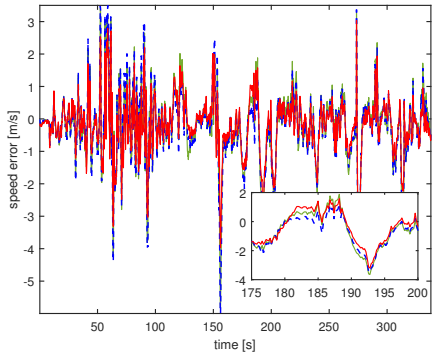

Figure 3.13: Speed estimation error (Dataset 2)

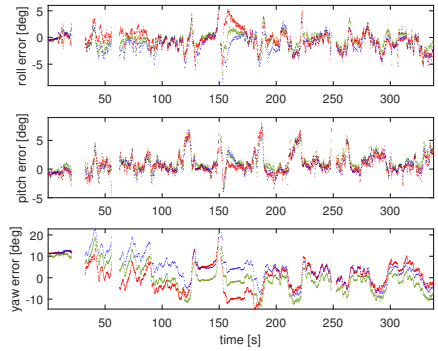

Figure 3.14: Attitude error (Dataset 2)

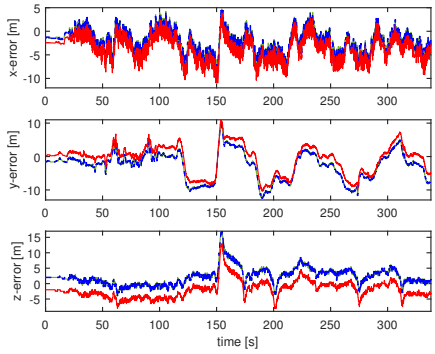

Figure 3.15: Position error (Dataset 2)

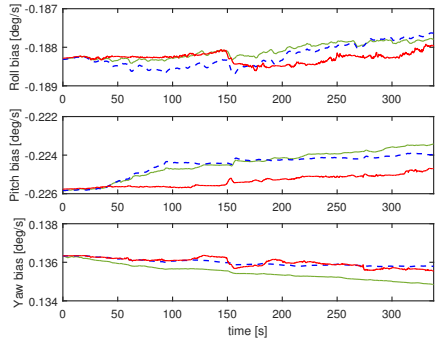

Figure 3.16: Gyro bias estimation (Dataset 2)

According to Table 3.1 and previous figures the EKF and nonlinear observers are seen to have similar performance during both flights. The differences can be assumed negligible and real flight conditions are considered. The attitude estimates shown in Fig. 3.11 and Fig. 3.14 are very alike and correspond well to the reference, although the nonlinear yaw estimation is seen to have a systematic difference.

The position estimation errors depicted in Fig. 3.12 and Fig. 3.15 are within the expected bounds. From Table 3.1 it can be concluded that the three state estimators have good performances with little variation between the estimators. It can further be concluded that the tuning used gave good results for both datasets.

3.6 Chapter Summary

A nonlinear observer consisting of an attitude estimator and a translational motion observer have been introduced. The two parts of the observer are feedback interconnected with the estimate of the specific force in a global coordinate frame. The attitude is represented as a quaternion to avoid singularities. Issues connected to gain selection, stability and implementation have been introduced.

Table 3.1: Observer performance comparison (NED position in m, attitude in deg and speed in m/s)

			EKF			NLO-Mag			NLO-Vel	
Dataset 1	POS RMS:	3.43	2.71	2.62	3.37	2.62	2.50	3.37	2.63	2.50
	POS STD:	2.60	2.44	2.46	2.48	2.41	2.44	2.48	2.42	2.44
	ATT RMS:	1.83	2.59	5.50	2.02	2.69	5.46	1.93	3.01	6.88
	ATT STD:	1.67	1.81	5.42	1.84	1.90	5.28	1.90	1.92	6.15
	SPE RMS:		0.60			0.67			0.69	
	SPE STD:		0.59			0.66			0.69	
Dataset 2	POS RMS:	4.43	4.40	3.43	3.38	5.00	3.63	3.37	5.00	3.63
	POS STD:	2.53	4.35	2.86	2.46	4.20	2.82	2.46	4.20	2.82
	ATT RMS:	1.76	1.87	6.39	2.09	1.87	7.85	1.56	1.94	6.36
	ATT STD:	1.70	1.66	6.34	1.73	1.67	6.28	1.46	1.59	6.36
	SPE RMS:		0.86			1.06			1.05	
	SPE STD:		0.83			1.02			1.02	

An Extended Kalman Filter was introduced for comparison with the nonlinear observer. The advantages and drawbacks of the methods have been presented and experimentally verified using flight data from a fixed-wing UAV. A reference system consisting of a 3-antenna GNSS receiver with the antennas placed at the tail and each wing tip was use for performance comparison of the presented state estimators.

The inertial sensors used in datasets are considered low-cost variants with respect to the reference system utilized. As the performance of the presented methods estimating position, linear velocity, and attitude are reasonably close to the reference it is concluded that the methods are able to overcome the vibrations, disturbances and bias drift connected to low-cost sensors in a reasonable manner and thus provide sufficiently stable and accurate navigation solution.

Furthermore, as the performance of the two state estimators are similar the nonlinear observer is concluded to have high performance of the level of state-of-the-art integration schemes commonly used for adverse applications. The following chapters will therefore proceed to build on the nonlinear observer presented here.

Chapter 4

Time-Delayed GNSS Measurements

Global navigation satellite system (GNSS) receivers suffer from an internal time-delay of up to several hundred milliseconds leading to a degeneration of position accuracy in high-dynamic systems. With the increasing interest in GNSS navigation, handling of time-delays will be vital in high accuracy applications with high velocity and fast dynamics. This paper presents a nonlinear observer structure for estimating position, linear velocity, and attitude (PVA) as well as gyro bias, using inertial measurements and time-delayed GNSS measurements. The observer structure consists of four parts; a) attitude and gyro bias estimation, b) time-delayed translational motion observer estimating position and linear velocity, c) input delays for inertial and magnetometer measurements, and d) a faster than real-time simulator. The delayed PVA and gyro bias estimates are computed using a semi-globally exponentially stable (SGES) nonlinear observer. The high-rate inertial measurements are delayed and synchronized with the GNSS measurements in the state observer. The fast simulator integrates the inertial measurements from the delayed state estimate to provide a state estimate at current time. The sensor measurements are carefully synchronized and the estimation procedure for the GNSS receiver delay is discussed. Experimental data from a small aircraft are used to validate the results.

Contributions of this Chapter: This chapter presents a method for handling time-delayed GNSS measurement in a loosely coupled strapdown GNSS/INS system. The observer structure is based on a SGES nonlinear PVA estimator, Grip et al. [72], where the high-rate inertial measurements are delayed to match the delayed GNSS measurements. A fast simulator uses inertial measurements to compensate for the delay in the state estimate. The main contribution is the modification and extension of the nonlinear observer to time-delayed position measurements. The observer makes a correction to the delayed state using the delayed GNSS measurement, which are integrated with delayed INS position estimates. The method can be generally applied to other GNSS/INS integration schemes that employ other state estimation algorithms. The presented approach is verified through simulations and in a

high-dynamic test environment using a small aircraft offering experimental validation.

Organization of this Chapter: The chapter is organized as follows: Section 4.2 gives an introduction to the experienced time delay in GNSS receivers and how it can be estimated. Section 4.3 states the delayed navigation problem formally. Section 4.4 introduces the solution involving the nonlinear attitude estimator, the translational motion observer and the fast simulator. Section 4.5 presents an alternative implementation of the observer structure, while Section 4.6 presents simulation results. Section 4.7 contains experimental results using an aircraft, while Section 4.8 gives the concluding remarks.

Publications: The material in this chapter is based on the conference paper Hansen et al. 2015 [83] and the journal Hansen et al. 2017 [86].

4.1 Introduction

Aiding an inertial navigation system (INS) with position and velocity updates from a Global Navigation Satellite System (GNSS) receiver is widely used for vehicle navigation. The inertial measurement unit (IMU) contributes with high sample rate linear acceleration and angular rate measurements, which are integrated to obtain position, velocity and attitude (PVA) estimates. However, the error builds up quickly resulting in poor accuracy for long-term predictions. The drift is compensated by using low sample rate GNSS measurements. The resulting system is a strapdown INS aided by GNSS measurements where the observer produces high sample rate state estimates.

The integration of inertial and GNSS measurements have traditionally been achieved using Kalman filters (KF) or extended Kalman filters (EKF) for nonlinear systems, see e.g. Grewal et al. [69]. Within the last decade another approach based on nonlinear observer design for estimating PVA has become increasingly popular. The design of nonlinear observers is grounded in systems theory where the stability properties are investigated. Thus the advantage of using nonlinear observers compared to EKFs is a significant reduction in computational load, guaranteed stability properties and reduced need for linearization of the system model. See e.g. Hua [94], Vik and Fossen [176], or Grip et al. [73] for recent attention of nonlinear observers with significantly stronger stability results than nonlinear KFs. The reduction in computational load when using nonlinear observers compared to nonlinear KFs were investigated in Grip et al. [72] and Mahony et al. [119], and especially in Johansen et al. [101], where a tightly coupled nonlinear observer was shown to comprise less than 25% of the computational load of a multiplicative EKF (MEKF). The smaller computational footprint allows for a reduction in hardware requirements or increased availability of processing power for other applications. Recent work by Mahony et al. [119], Roberts and Tayebi [149], Hua et al. [95], and Kingston and Beard [113] as well as Grip et al. [71, 72, 73] use nonlinear observers to estimate PVA, acceleration bias, and gyro bias.

GNSS receivers experience a time delay due to the computational time for position estimation and the data communication time from the receiver to the user. The time delay can be disregarded for low-dynamic applications (e.g. marine

vessels and pedestrian use), but it has great impact on high-dynamic systems such as high-precision automatic UAV and aircraft landing systems. For high-dynamic applications the sensor measurements should have high sample rate and accurate synchronization to minimize the estimation errors, Skog and Händel [158]. It is therefore important to identify and compensate for sensor time delays.

The work presented here aims to combine a nonlinear attitude observer with accurate position estimation taking the receiver time-delay into consideration. The paper is motivated by the increased interest in highly accurate GNSS applications. Due to the estimation inaccuracies introduced by time-delays in GNSS receivers it is believed time-delay compensation will be mandatory in future GNSS/INS applications with fast dynamics and high velocities.

Estimation in time-delayed systems have been subject to extensive research e.g. Jacovitti and Scarano [97] who investigated discrete-time systems. Latency determination and compensation are described by Solomon et al. [160] using an experimental setup. In Li and Mourikis [116] a navigation system based on inertial aided by delayed camera position measurements is investigated. The delay between inertial and camera measurements is included in the Kalman filter state vector, allowing for online estimation. The method proposed is verified through simulations and indoor as well as outdoor experiments. The approach of using Kalman filters for GNSS/INS systems with time delay have been investigated by Raff and Allgöwer [144] and Skog and Händel [159]. Time synchronization errors in GNSS/INS systems are discussed by Skog and Händel [158]. A Kalman filter handling delayed or asynchronous measurements is considered in Blanke [22, 23], where the focus is fault tolerant marine operations. Lyapunov functionals are used for stability analysis by Papachristodoulou et al. [137]. Stability of delayed systems is further investigated in Gu and Niculescu [78] and Albertos and Garcia [3]. Recently, a quadrotor helicopter application with time delays in the feedback loops was studied by Ailon and Arogeti [2]. In Battilotti [18] a class of nonlinear predictors for delayed measurements with a known and constant delay is proposed. The nonlinear observer consists of several couples of filters each estimating the state vector at some delayed time instant differing from the previous by a small fraction of the overall delay. By use of a small gain approach Ahmed-Ali et al. [1] presents a class of global exponentially stable nonlinear observers with sampled and delayed measurements, robust towards measurement errors and sampling schedule perturbations. Also, Briat [27] and Fridman [58] present extensive research on stability and control of time-delayed systems, and Khosravian et al. [108, 109, 110] propose an observer-predictor approach to delayed GNSS and magnetometer measurements where current position is determined from delayed position estimates. In Siccardi et al. [157] timing issues in the pulse-per-second signals from GNSS receivers are investigated.

4.2 Time Delay of GNSS Receivers

Using GNSS measurements as aid in inertial navigation systems is widely used. However the inertial sensors commonly have a much ($\sim$ 20–2.000 times) higher sample rate than the GNSS receiver. Accurate time stamping of the measurements

in relation to each other is therefore vital in the effort to minimize the error, as falsely time stamped data will introduced errors: if the time of use does not correspond to the time of validity the vehicle might have moved or rotated in the time in-between. If one of the sensors in the aided system experiences a delay the integration precision will suffer as the measurements will not correspond to the correct time-stamp.

It is widely known that the GNSS signal can experience delays when travelling from the satellites to the receiver (e.g. multipath, atmospheric delays, and timing errors between satellite and receiver clocks) but as the demand for increased accuracy of navigation solutions is growing, other delays will have to be taken into account as well. In the following the time delay arising between the time of validity of the satellite signals to the data is available to the user is considered. The time delay experienced in the GNSS receiver, stems from the computational time of the position estimation as well as the dissemination of the data from the receiver to the user. The total time delay is hence $\tau = \tau_{cal} + \tau_{dis}$, where the calculation time, τ_{cal}, depends on the number of satellites in the constellation, and the dissemination time, τ_{dis}, covers the time it takes the receiver to output the data to the user, which is directly dependent on the number of bytes to transmit and the communication protocol used. Ideally the position data should be available to the user exactly when the receiver obtains the satellite signals. However, even if the calculation of position could be done instantaneous the data would still be delayed with τ_{dis}. An illustration of the time delayed receiver system is shown in Fig. 4.1.

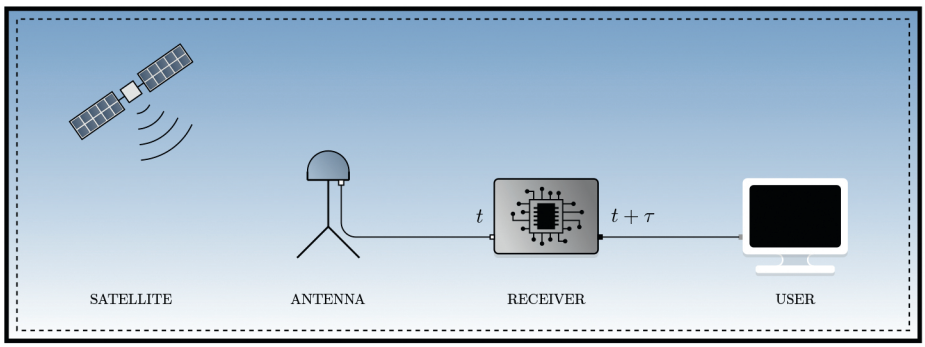

Figure 4.1: Structure and components of the GPS L1 and L2 signals.

To determine the delay, an accurate measure of the desired (without delay) time stamp is required: GNSS receivers often allow access to a pulse-per-second (PPS) signal, synchronized to satellite clock, indicating the arrival of new measurements. The PPS goes high when the GPS time is incremented with one second, leaving the PPS interval, as the time between two consecutive rising edges on the PPS signal, at one second. It is assumed that the PPS signal is not delayed in the receiver and can therefore be used as a reference for the ideal time-stamping of the GNSS measurements. The validity of the GNSS data can be related to such a pulse on the PPS signal, and it is therefore possible to directly measure the time delay by monitoring the edges on the PPS and data signals. Three edges are of interest: I)

the rising edge of the PPS signal denoted as the time of validity (TOV), II) the first rising edge of the data signal denoting time of transmit (TOT) from the receiver to the user, and III) the time of arrival (TOA) defined as the final falling edge of the data-package. Here data packages are defined as sets of binary values sent on the data signal. The total time delay can then be estimated as the time between the TOV and TOA edges. The situation is visualized in Fig. 4.2, with example times for clarification.

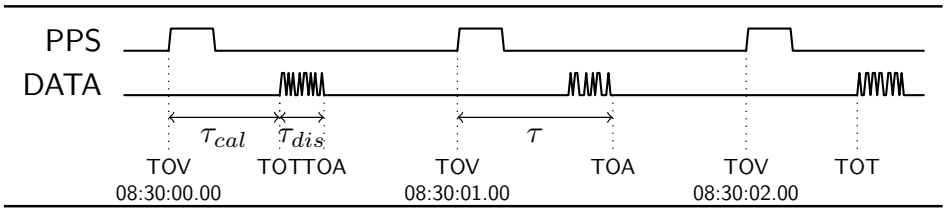

Figure 4.2: Visualization of PPS and data signal on a time-scale, depicting the time-delay estimation of a GNSS-receiver, see [173].

Fig. 4.2 shows the relation between when a GNSS measurement is valid, TOV, and when it is received, TOA, where data is sent from the receiver to the user between TOT and TOA. The data is shown for a receiver sample interval of $s_{\text{GNSS}} = 1\ s$. Example time stamps of the TOV values are introduced; the first TOV is registered at UTC 8:30:00, and the second TOV at UTC 8:30:01, with the intermediate TOT and TOA belonging to UTC 8:30:00 but arriving τ_{cal} and τ seconds later.

GNSS receivers usually offer position updates with a rate of 1–10 Hz, generating the need for determining the delay for multiple data packages within one PPS interval. This situation is shown in Fig. 4.3. When estimating the time delay for a data signal with higher frequency than the PPS signal, the first delay is determined as described in Fig. 4.2, and the consecutive delays are found as the time between a time shifted PPS signal and TOA times, i.e. the time between $PPS + ns_{\text{GNSS}}$ and the last falling edge of the data packages, where $n = [0, 1, 2, \ldots, s_{\text{GNSS}} - 1]$.

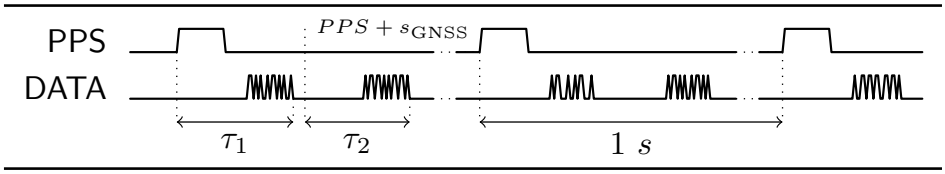

Figure 4.3: Visualization of time-delay for a GNSS receiver with data frequency higher than 1 Hz.

If the data rate is much higher than the PPS-signal it will become difficult to accurately determine the delays as the relation of a TOV and its corresponding TOA will be obscured: If the data has a much higher frequency than the PPS signal, it becomes uncertain which data package is the first of a PPS interval, as the delay might *displace* a package into the next PPS interval. Having prior

knowledge of the approximate delay is essential in determining the maximum data rate the system can support without timing ambiguities.

GNSS receivers can output a multitude of GNSS related data and the magnitude of the time delay will depend on which kind of output is desired. Different delays may be experienced with different data packages, e.g. the ephemeris package containing the satellite trajectories is often shorter than the package containing pseudoranges and carrier-phase measurements, leading to a shorter time delay. Furthermore, some GNSS packages might change size according to the number of satellites visible in the constellation, which will affect the dissemination delay. Some packages, such as the receiver position packages, have high sample rates ($1 - 10\ Hz$), whereas environmental packages (e.g. the ephemeris packages) are updated on a slower time scale (e.g. $\sim 30\ min$). The proposed method for determining the receiver delay does not depend on the sample rate, and can be used for all types of packages.

4.2.1 Case Study: Time-delay measurement using u-Blox LEA-6T

Let us consider the practical implications of measuring the receiver time delay. One way of visualizing the delay is to use an oscilloscope on the PPS and data signals, allowing for manual measurements of the delay, as shown in Fig. 4.2 and 4.3. Another approach is to use a timer to capture the rising edge of the PPS and the falling edge of the data signal, this can be achieved using a micro-controller.

A test setup including a u-Blox LEA-6T GNSS receiver and a micro-controller is utilized. The advantage of the LEA-6T receiver is that the PPS and data signals are readily available as a digital signal and over a RS-232 connection, respectively. The micro-controller is chosen such that the *input capture* method is available, which time-stamp measurements without interrupting the execution when an input is received. Additionally, large counters are available as well as a high-frequency clock to ensure accurate time stamping of TOV, TOT and TOA. Three triggers are used: one for PPS (determining TOV) and two for data signal (determining TOT and TOA), all time stamping in micro controller clock cycles, which can be converted to seconds with the known clock frequency.

GNSS measurements are collected using the test-setup with a sample frequency of 5Hz, yielding the results shown in Fig. 4.4 and Fig. 4.5. The test is carried out for the raw satellite data including the range and range-rate measurements. This is chosen as worst case as the raw data package is the longest one available on the u-Blox LEA-6T receiver.

The delays determined over time are shown in Fig. 4.4, where the time delay is seen to be slowly time-varying. It is clear that $\tau_{dis} \ll \tau_{cal}$ and that there is more variation on the calculation delay than on the dissemination delay. The calculation delay and especially the dissemination delay are seen to be dependent on the number of satellites in the constellation.

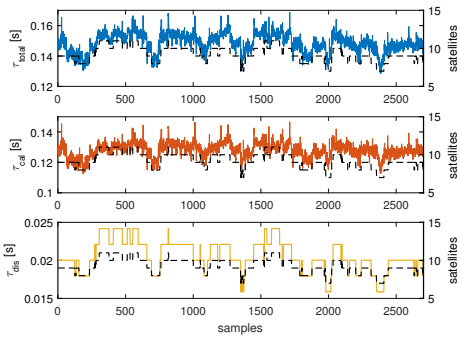

Figure 4.4: The dissemination (yellow), calculation (red) and total (blue) delay over time, shown with the number of satellites (dashed).

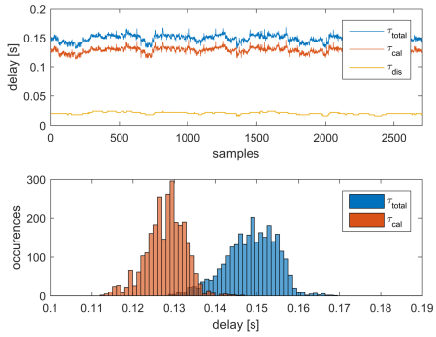

Figure 4.5: The delays over time and the histogram of calculation (red) and total (blue) delay for range and range-rate data.

The histogram of the observed time delays shown in Fig. 4.5 conveys that the calculation delay and thereby the total delay are not constant. The mean and standard deviation of the time delays are summarized in Table 4.1.

Table 4.1: Characteristics of delay distribution, (unit: seconds).

	τ_{dis}	τ_{cal}	τ_{total}
Mean:	0.0206	0.1281	0.1486
STD:	0.0020	0.0047	0.0062

A time delay of 150 ms will have small impact on e.g. pedestrian applications (position error of < 0.5 m), whereas for cars or UAVs the position error can be several meters (i.e. 5 m error at speeds of 120 km/h).

4.3 Problem Formulation

The objective is to estimate the current position of a vehicle based on strapdown inertial navigation aided by time-delayed GNSS measurements. The inertial measurements include accelerometer and gyroscope data, integrated with magnetometer and delayed GNSS data in a loosely coupled nonlinear observer.

Assumption 12. The GNSS data will be time delayed with τ_p or τ_v seconds, for position and velocity data respectively.

Remark 4.1. For some receivers these delays will be the same, however in the following the general delay will be represented as; $\tau = \max(\tau_p, \tau_v)$.

The position, linear velocity and attitude (PVA) of the vehicle are to be determined. The position, p^e, and linear velocity, v^e, are estimated in the ECEF-frame

while the attitude is represented as a unit quaternion, q_b^e, describing the rotation from ECEF- to Body-frame. Furthermore the gyro bias, b^b, is estimated.

The kinematic equations of the vehicle given in (2.7)–(2.9), see [71] and [72], will here be considered in a time-shifted version, where all measurements have been delayed to coincide with the GNSS measurements. The time shifted kinematic equations are:

$$\dot{p}^e(t-\tau) = v^e(t-\tau), \tag{4.1}$$

$$\begin{aligned}\dot{v}^e(t-\tau) = &-2S\left(\omega_{ie}^e(t-\tau)\right)v^e(t-\tau) + R(q_b^e(t-\tau))f^b(t-\tau) \\ &+ g^e(p^e(t-\tau)),\end{aligned} \tag{4.2}$$

$$\dot{q}_b^e(t-\tau) = \frac{1}{2}q_b^e(t-\tau)\otimes\bar{\omega}_{ib}^b(t-\tau) - \frac{1}{2}\bar{\omega}_{ie}^e\otimes q_b^e(t-\tau), \tag{4.3}$$

$$\dot{b}^b(t-\tau) = 0. \tag{4.4}$$

The specific force of the vehicle is denoted f^b, while the local gravitation vector, $g^e(p^e)$, is assumed known.

The goal of this chapter is the design of a loosely-coupled nonlinear observer integrating inertial measurements with time-delayed GNSS measurements, considering the delay as known such that the delay does not need estimating. Multiple tests in simulation and with experimental data will confirm the observer structure and investigate the impact of a time-varying or normally distributed delay.

4.3.1 Sensor configuration

The following measurements are assumed to be available:

Assumption 13. Global position estimate experiencing a time delay, $p_{\text{GNSS}}^e(t-\tau_p) = p^e(t-\tau_p)$, measured using a GNSS receiver.

Assumption 14. Global velocity estimates experiencing a time delay, $v_{\text{GNSS}}^e(t-\tau_v) = C_v v^e(t-\tau_v)$, measured by a GNSS receiver.

Remark 4.2. The velocity measurements can be a full or partial measurement $v_{\text{GNSS}}^e = C_v v^e$, where the selection matrix C_v may be zero.

Assumption 15. Specific force, $f^b(t)$, as measured by the IMU: $f_{\text{IMU}}^b(t) = f^b(t)$.

Assumption 16. Angular velocity, $\omega_{ib}^b(t)$, measured by the IMU, with a bias: $\omega_{ib,\text{IMU}}^b(t) = \omega_{ib}^b(t) + b^b(t)$.

Assumption 17. Magnetometer measurement of the Earth magnetic field measured using a magnetometer, $m^b(t)$.

Assumption 18. It is further assumed that the positioning data is available with a sample interval of s_{GNSS} while the inertial and magnetometer measurements are available with a higher frequency $s_{\text{IMU}} > s_{\text{GNSS}}$.

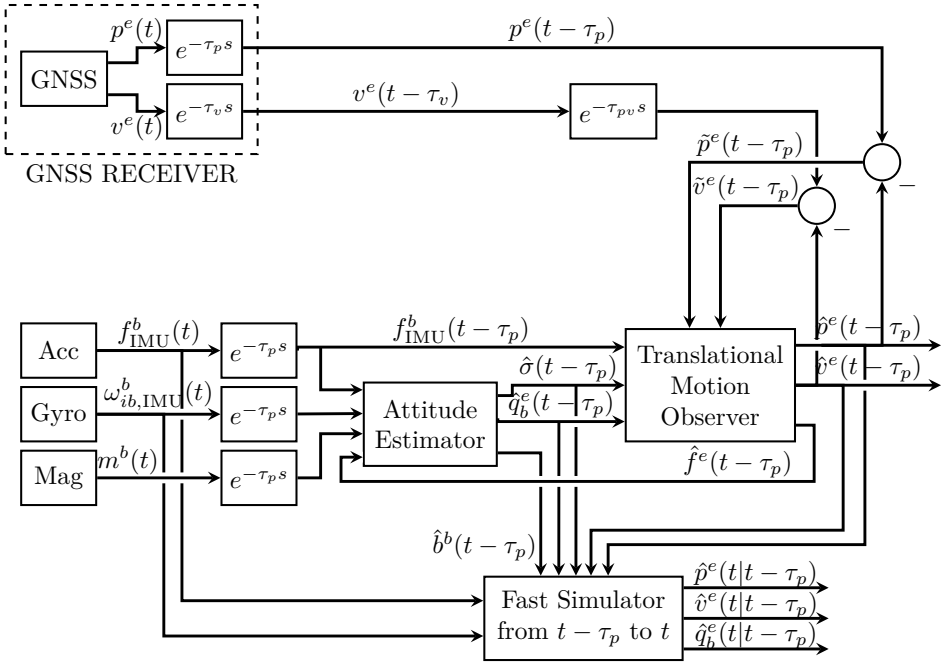

Figure 4.6: Block diagram structure of the proposed observer design, with; GNSS-receiver, IMU, magnetometer, attitude estimator, time-delayed state observer, and fast simulator.

4.4 Nonlinear Observer Design

The proposed observer structure consists of: an attitude estimator, delayed translational motion observer, delayed inertial measurements, and a fast simulator, see Fig. 4.6. The proposed approach can be generally applied to GNSS/INS integration schemes, and will here be demonstrated on a nonlinear observer. The fast (faster than real-time) simulator is used to estimate the current position and linear velocity from the time-delayed states and a window of IMU data. The attitude observer is developed by Grip et al. [72], and will here be time shifted from t to $t-\tau$ to accommodate for the delayed position measurements by delaying the inertial measurements at the input of the attitude observer. Since the signals are delayed at the input to the observer and therefore affects the entire observer the stability proof can be repeated by shifting the time argument. The origin of the error dynamics of the presented observer structure is therefore semi-global exponential stability. Consequently, the observer will be presented without proof. A similar observer could be used, but the attitude observer from [72] was chosen based on the global stability results. For the alternative implementation proposed in Section 4.5 it is important that the observer structure is modular.

Even though the GNSS receiver measures both position and velocity, some receivers will have different delays on the two outputs, as they are not subjected to the same computational process. In the following the delayed GNSS measurements

will have a distinction between the delay of the position measurement, τ_p, and the velocity measurement, τ_v. The presented approach offers a solution when $\tau_p \geq \tau_v$. In Fig. 4.6 the linear velocity estimate is delayed to coincide with the measurement, but since it is already delayed with τ_p the additional delay imposed is $\tau_{vp} = \tau_p - \tau_v$. If $\tau_v \geq \tau_p$ the position estimate should be delayed instead of the velocity estimate, and the observer should be delayed with τ_v rather than τ_p as shown here.

4.4.1 Attitude estimation

The INS attitude estimator is based on [71] and [72]. The main idea is to estimate the quaternion and gyro bias by using the rotation rate, $\omega^b_{ib,\text{IMU}}$, aided by two non-parallel Body-frame vector measurements with known ECEF reference vectors.

The attitude and gyroscope bias are estimated by:

$$\begin{aligned}\dot{\hat{q}}^e_b(t-\tau) = \frac{1}{2}\hat{q}^e_b(t-\tau) \otimes \left(\bar{\omega}^b_{ib,\text{IMU}}(t-\tau) - \bar{\hat{b}}^b(t-\tau) + \bar{\hat{\sigma}}(t-\tau)\right) \\ - \frac{1}{2}\bar{\omega}^e_{ie} \otimes \hat{q}^e_b(t-\tau),\end{aligned} \tag{4.5}$$

$$\dot{\hat{b}}^b(t-\tau) = \text{Proj}\left(\hat{b}^b(t-\tau), -k_I\hat{\sigma}(t-\tau)\right), \tag{4.6}$$

where $k_I > 0$ is a constant and $\text{Proj}(\cdot,\cdot)$ denotes the parameter projection where the bias estimate is restricted to a compact set given as a sphere with constant radius M_b, i.e. $\|\hat{b}^b\|_2 \leq M_b$. The injection term, $\hat{\sigma}$, used in (4.5) and (4.6) is given as:

$$\begin{aligned}\hat{\sigma}(t-\tau) := k_1 v^b_1(t-\tau) \times R(\hat{q}^e_b(t-\tau))^T v^e_1(t-\tau) \\ + k_2 v^b_2(t-\tau) \times R(\hat{q}^e_b(t-\tau))^T v^e_2(t-\tau),\end{aligned} \tag{4.7}$$

where the gains k_1 and k_2 satisfy $k_1 \geq k_p$ and $k_2 \geq k_p$ for some sufficiently large positive k_p. The vectors v^b_1 and v^b_2 are two vectors in the Body frame with their corresponding vectors v^e_1 and v^e_2 in the ECEF frame. The vectors can be chosen in various ways. Here they will be considered as:

$$v^b_1 = \frac{f^b_{\text{IMU}}}{\|f^b_{\text{IMU}}\|_2}, \quad v^b_2 = \frac{m^b}{\|m^b\|_2} \times v^b_1, \quad v^e_1 = \frac{\hat{f}^e}{\|\hat{f}^e\|_2}, \quad v^e_2 = \frac{m^e}{\|m^e\|_2} \times v^e_1, \tag{4.8}$$

where m^e is the local magnetic field of the Earth and $\hat{f}^e$ is an estimate of the specific force in the ECEF frame, which is provided as described by the translational motion observer.

4.4.2 Translational motion observer

The objective of the translational motion observer is to integrate IMU acceleration and GNSS position to produce estimates of position, linear velocity and specific force. Since the GNSS measurements are delayed it is proposed to delay the IMU measurements such that the measurements coincide in time, and estimate the delayed state. The delayed state observer becomes:

$$\begin{aligned}\dot{\hat{p}}^e(t-\tau_p) = \hat{v}^e(t-\tau_p) + \theta K_{pp}(p^e(t-\tau_p) - \hat{p}^e(t-\tau_p)) + K_{pv}\left(v^e(t-\tau_p)\right. \\ \left. -\hat{v}^e(t-\tau_p)\right),\end{aligned} \tag{4.9}$$

$$\begin{aligned}\dot{\hat{v}}^e(t-\tau_p) = &-2S(\omega_{ie}^e)\hat{v}^e(t-\tau_p) + \hat{f}^e(t-\tau_p) + g^e(\hat{p}^e(t-\tau_p)) \\ &+ \theta^2 K_{vp}(p^e(t-\tau_p) - \hat{p}^e(t-\tau_p)) \\ &+ \theta K_{vv}\left(v^e(t-\tau_p) - \hat{v}^e(t-\tau_p)\right),\end{aligned} \tag{4.10}$$

$$\begin{aligned}\dot{\xi}(t-\tau_p) = &-R(\hat{q}_b^e(t-\tau_p))S(\hat{\sigma}(t-\tau_p))f_{\text{IMU}}^b(t-\tau_p) + \theta^3 K_{\xi p}(p^e(t-\tau_p) \\ &- \hat{p}^e(t-\tau_p)) + \theta^2 K_{\xi v}\left(v^e(t-\tau_p) - \hat{v}^e(t-\tau_p)\right),\end{aligned} \tag{4.11}$$

$$\hat{f}^e(t-\tau_p) = R(\hat{q}_b^e(t-\tau_p))f_{\text{IMU}}^b(t-\tau_p) + \xi(t-\tau_p), \tag{4.12}$$

where ξ is an auxiliary state to help in estimating the specific force, $\hat{f}^e$. Here $\theta \geq 1$ is a tuning parameter, and K_{pp}, K_{vp}, $K_{\xi p}$, K_{pv}, K_{vv} and $K_{\xi v}$ are gain matrices chosen to ensure that the error dynamics defined by $\mathcal{A}-\mathcal{K}\mathcal{C}$ is Hurwitz. See Chapter 3.4.3 or [72] for details. The matrices are:

$$\mathcal{A} = \begin{bmatrix} 0 & I_3 & 0 \\ 0 & 0 & I_3 \\ 0 & 0 & 0 \end{bmatrix}, \quad \mathcal{K} = \begin{bmatrix} K_{pp} & K_{pv} \\ K_{vp} & K_{vv} \\ K_{\xi p} & K_{\xi p} \end{bmatrix}, \quad \mathcal{C} = \begin{bmatrix} I_3 & 0 & 0 \\ 0 & C_v & 0 \end{bmatrix}. \tag{4.13}$$

The gain matrix $\mathcal{K}$ can be determined in various ways. An advantage of this observer structure is that the gain $\mathcal{K}$ can be chosen constant, as shown in [72], leading to a small computational footprint. Another approach is to solve the discrete time-varying Riccatti equation, thereby computing the gain and covariance matrix similarly to the Kalman filter:

$$P_{k|k} = \Phi P_{k-1|k-1}\Phi^\intercal + Q, \tag{4.14}$$

$$\mathcal{K}_k = P_{k|k-1}\mathcal{C}^\intercal\left(\mathcal{C}P_{k|k-1}\mathcal{C}^\intercal + R\right)^{-1}, \tag{4.15}$$

$$P_{k|k} = \left(I - \mathcal{K}_k\mathcal{C}\right)P_{k|k-1}\left(I - \mathcal{K}_k\mathcal{C}\right)^\intercal + \mathcal{K}_k R\mathcal{K}_k^\intercal, \tag{4.16}$$

where P, R and Q are the covariance matrices of the estimate, measurements and process noises, respectively. The discretized system matrix, $\Phi = e^{\mathcal{A}T}$, where T is the IMU sample time and k is the time index signifying the discrete time update. More details about the discretization and implementation of the nonlinear observer can be found in Chapter 3.4 or [31].

4.4.3 Fast simulator

The outputs of the time-delayed translational motion observer are the delayed position and linear velocity estimates. In order to get the current position and linear velocity, $\hat{p}^e(t)$ and $\hat{v}^e(t)$, a fast simulator is implemented. The input to the fast simulator is the bias-compensated gyro measurements, as well as the acceleration measured by the IMU, without the gravitational component and rotated to the ECEF frame, $u(t) = a^e(t) = R(\hat{q}_b^e(t))f_{\text{IMU}}^b - g^e(\hat{p}^e(t))$. Moreover, the fast simulator is implemented as,

$$\hat{v}^e(t|t-\tau_p) = \hat{v}^e(t-\tau_p) + \int_{t-\tau_p}^{t} u(r)dr, \tag{4.17}$$

$$\hat{p}^e(t|t-\tau_p) = \hat{p}^e(t-\tau_p) + \tau_p\hat{v}^e(t-\tau_p) + \int_{t-\tau_p}^{t}\int_{t-\tau_p}^{s} u(r)drds, \tag{4.18}$$

$$\begin{aligned}\dot{\hat{q}}_b^e(t-\tau_p) = \frac{1}{2}\hat{q}_b^e(t-\tau_p) \otimes \left(\bar{\omega}_{ib}^b(t-\tau_p) - \bar{\hat{b}}^b(t-\tau_p) + \bar{\hat{\sigma}}(t-\tau_p)\right) \\ - \frac{1}{2}\bar{\omega}_{ie}^e \otimes \hat{q}_b^e(t-\tau_p),\end{aligned} \tag{4.19}$$

where $\hat{p}^e(t-\tau)$ and $\hat{v}^e(t-\tau)$ are estimated by the translational motion observer.

The fast simulator can be implemented offline where the attitude estimates of (4.5) can be saved in a buffer, avoiding the need for (4.19), or online where the attitude must be estimated in the fast simulator. Used online the fast simulator must have a data buffer for storing measurements for use in the integrations. The integral part of (4.17) can be implemented as a for-loop and can be used in the double integral of (4.18) to save computational effort. The frequency of the fast simulator is the runtime frequency of the implementation platform, with the minimal requirement of being faster than the IMU sample rate. To further save computations the latest value of $u(t)$ can be determined and appended to an array. The integrals can then be calculated by summing the elements in the array over the relevant time horizon. This solution uses a running horizon method and will limit the computational load as only one u is determined every iteration.

4.5 Alternative Implementation

An alternative implementation of the proposed observer can be designed by changing the placement of the delay that ensures the translational motion observer use coinciding data. In the proposed observer structure the delay was placed before the attitude estimator while in the alternative implementation, shown in Fig. 4.7, the delay is implemented after the attitude estimator. The attitude estimator thereby supply the present attitude estimate, negating the need for estimating the attitude in the fast simulator.

The fast simulator for determining the present position and velocity is identical to the fast simulator in the observer structure proposed in Section 4.4, and depends on; $\hat{v}^e(t-\tau_p)$, $\hat{p}^e(t-\tau_p)$, $f_{\text{IMU}}^b(t)$, and $\hat{q}_b^e(t-\tau_p)$. However, it is no longer necessary to estimate the present attitude.

The alternative implementation can be applied to any other modular GNSS/INS integration scheme where the attitude and translational motion observers are separated. The alternative implementation approach alters the observer structure and the stability proof is no longer valid. Here the alternative implementation is stated without stability proof. There might exist an observer where the stability is not violated by the structure of the alternative implementation. To the best of the authors knowledge there is no modular observer where the stability results account for a delay in the interconnection.

The delayed specific force estimate from the translational motion observer is used in the attitude observer. An additional fast simulator could be introduced to integrate the ξ state over the time delay horizon. However, to save computations an approximation is introduced such that ξ and $\hat{f}^e$ are estimated as:

$$\begin{aligned}\dot{\xi}(t) = -R(\hat{q}_b^e(t))S(\hat{\sigma}(t))f_{\text{IMU}}^b(t) + \theta^3 K_{\xi p}(p^e(t-\tau_p) - \hat{p}^e(t-\tau_p)) \\ + \theta^2 K_{\xi v}(v^e(t-\tau_p) - \hat{v}^e(t-\tau_p)),\end{aligned} \tag{4.20}$$

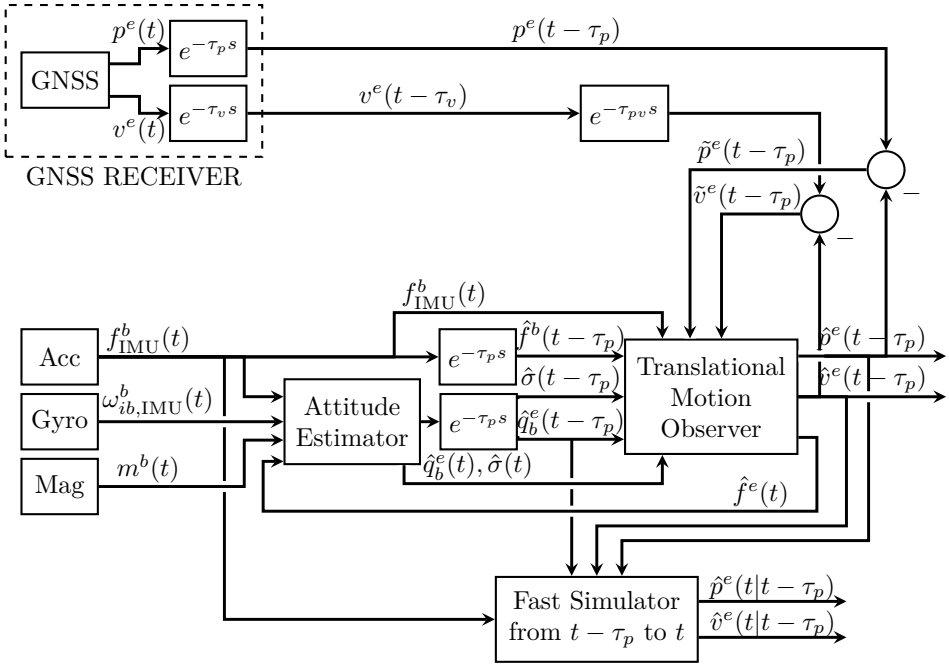

Figure 4.7: Block diagram structure of the alternative implementation, with; GNSS receiver, IMU, magnetometer, attitude estimator, time-delayed translational motion observer, and fast simulator.

$$\hat{f}^e(t) = R(\hat{q}_b^e(t))f_{\text{IMU}}^b(t) + \xi(t), \tag{4.21}$$

The approximation only lies in estimation of $\xi(t)$, whereas (4.21) is identical to (4.12) with the time shift from $t - \tau_p$ to t.

4.5.1 Computational load

The computational loads of the proposed observer and the alternative implementation are compared by counting the average number of multiplications and additions required. The comparison is shown in Table 4.2, where the attitude estimator operates at IMU frequency, 500 Hz, and the TMO gain computation runs at GNSS receiver frequency, 5 Hz. Furthermore, the time delay is considered constant with a ratio to the IMU frequency of 10, such that the integrals in the fast simulators are determined over 10 elements. The proposed observer is denoted NLO, while the alternative implementation is NLO-ALT. The observers are compared to a fixed TMO gain implementation of the proposed observer, here denoted NLO-FIX, and the uncompensated observer, denoted NLO-UNC, which does not take the time delay into account.

The computational load of the NLO-UNC observer is used as reference when determining the change in computational load of the proposed observers. The ratios between the computational load of the observers and the NLO-UNC are listed in

Table 4.2: Numerical comparison of computational load. The values are average number of arithmetic operations per second.

	NLO-UNC		**NLO**		**NLO-FIX**		**NLO-ALT**	
	Mult.	Add.	Mult.	Add.	Mult.	Add.	Mult.	Add.
Attitude estimation (500 Hz)	66500	58000	66500	58000	66500	58000	66500	58000
TMO prediction (500 Hz)	441500	399000	441500	399000	77000	70500	441500	399000
TMO correction (5 Hz)	24840	14745	24840	14745	9225	300	24840	14745
TMO gain computation (5 Hz)	8910	7740	8910	7740	–	–	8910	7740
Fast simulator (500 Hz)	–	–	44000	82000	44000	82000	24000	62000
Total	541750	479485	585750	561485	196725	210800	565750	541485
Ratio	1.00	1.00	1.08	1.17	0.36	0.44	1.04	1.13

the table. The fixed gain method offers a significant reduction in computational load despite inclusion of the fast simulator. The load of the proposed NLO is larger than the uncompensated observer due to the addition of the fast simulator, while the alternative implementation offers a reduction in load compared to the NLO, due to the removal of the attitude estimate in the fast simulator.

4.6 Simulation Study

The implementation and effect of the proposed observer structures are verified in simulation using the unmanned aerial vehicle (UAV) model of Beard and McLain [19], estimating UAV position in NED, linear velocity, attitude, acceleration, and angular velocity of the Aerosonde UAV.

The simulation setup will be the same for the three tests, with the reference position being a circular path with diameter of 1300 m. The simulated GNSS data is supplied with a frequency of 5 Hz with added Gaussian white noise. The standard deviation of the position measurements is 1 m, while the velocity measurements has a standard deviation of 0.01 m/s. These standard deviations are reasonably realistic with differential corrections chosen to better visualize the conceptual difference in performance between the observers. The inertial measurements will be supplied with a frequency of 500 Hz and Gaussian white noise comparable to the ADIS 16488 IMU (accelerometer: $1.5 \cdot 10^{-3}$ g, magnetometer: $0.45 \cdot 10^{-7}$ T, gyroscope: 0.0028 rad/s).

The observer parameters are chosen as; $M_b = 0.0087$ $[rad/s]$, $k_1 = 1.8$, $k_2 = 1.2$, $k_I = 0.004$, and $\theta = 1$. The parameters are tuned by the guidelines presented in the stability proof in Grip et al. [72] where $\theta \geq 1$, and $k_* \geq k_p > 0$ with M_b being sufficiently large. Futher suggestions for tuning can be found in Chapter 3.4 or in Bryne et al. [31]. The observer gain matrices are found by solving the discrete time-varying Riccati equation, where the covariance matrices are selected as: $R = \text{blockdiag}(I_3\ [m^2], 0.01 I_3\ [m^2/s^2])$, and $Q = \text{blockdiag}(0 I_3\ [m^2], 1 \cdot 10^{-3} I_3\ [m^2/s^2], 2.5 \cdot 10^{-4} I_3\ [m^2/s^4])$. The observers are implemented using a corrector-predictor representation of the discretized system [55] with two time scales: GNSS data and the time-delayed IMU data.

The observers robustness towards errors in the time-delay estimate is tested by distinguishing between the delay introduced by the GNSS receiver and the implemented delays, where the GNSS delay (τ_p and τ_v) is the actual time delay experienced in the GNSS receiver, whereas the implementation delay ($\tau_{p,imp}$ and $\tau_{v,imp}$) is the delay assumed in the observer. A perfect correspondence between the two delays gives the best result, however the GNSS delay might vary over time making a constant implementation delay inaccurate.

Several simulations are carried out comparing the proposed observer and the alternative implementation with the traditional observer structure without time delay compensation: I) the time delay is constant $\tau_p = \tau_v = \tau_{p,imp} = \tau_{v,imp} = 150$ ms, II) an inaccurate time-delay estimation is considered, where the observed time delay does not match the time delay used in the observer implementation, and III) a normal distributed observed delay while the implemented delay is fixed at the mean value.

4.6.1 Test I: Simulation with $\tau = 150\ ms$

The proposed observer and the alternative implementation are simulated with a time delay of $\tau = 150\ ms$, matching the delay found from experimental data in Section 4.2. The experienced and implemented delay coincide in this test; $\tau_* = \tau_{*,imp}$. The true position of the UAV is known, and the position estimation error is shown in Fig. 4.8. The position error of three observers are shown: a) the proposed observer, b) the alternative implementation, and c) an observer without delay compensation.

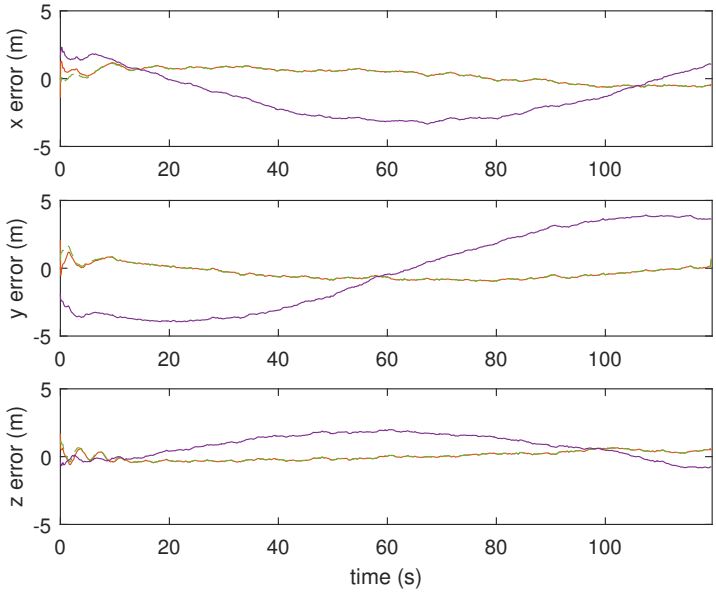

Figure 4.8: Position estimation error the proposed observer structure (red), the alternative implementation (green) and the observer without time-delay compensation (purple).

The observer without delay compensation is seen to introduce a sinusoid error characteristic, whereas the proposed observer and alternative implementation have estimation errors concentrated around zero. It is evident that taking the time delay of the GNSS receiver into account increases performance of the observer structure.

The root-mean-square (RMS) and standard deviation (STD) of the estimation error are summarized in Table 4.3. Since the GNSS receiver position measurements have a standard deviation of 1 m the delay compensated observer improves the accuracy compared to using only GNSS measurements, while the uncompensated observer leads to higher standard deviation.

4.6.2 Test II: Simulations with inaccurate time delay

In order to test the performance of the proposed observer structures when the magnitude of the time delay is not precisely known, a test is carried out where

the implemented delay is larger than the experienced delay, i.e $\tau_{*,imp} = 1.5\tau_* = 225\ ms$. The position estimation errors are shown in Fig. 4.9.

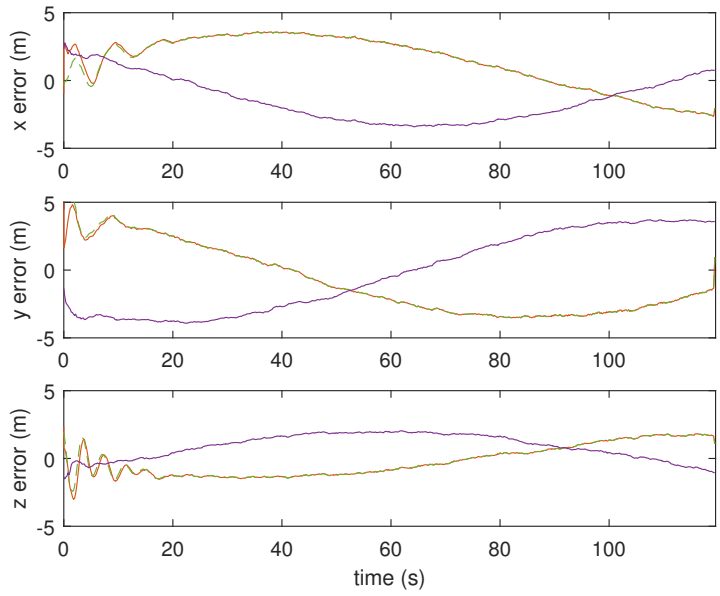

Figure 4.9: Position estimation error the proposed observer structure (red), the alternative implementation (green) and the observer without time-delay compensation (purple).

Comparing the position errors in Fig. 4.8 with Fig. 4.9 there is no difference in the error of the observer without time-delay compensation (as expected), however the error from the proposed observer and the alternative implementation have grown to a magnitude that is comparable to the error of the uncompensated observer. While a good estimate of the receiver delay is desired the simulation show that the estimate can be a factor of 1.5 larger than the true delay magnitude, without the uncompensated observer becoming a better candidate for position estimation. The results are summarised in Table 4.3.

4.6.3 Test III: simulations with normally distributed delay

To investigate the performance of the observer structures with respect to a non-constant time delay, the experienced delay is introduced as a time-varying delay with a mean of 0.150 s and normal distribution with a standard deviation of 0.0075 s, while the implemented delay, $\tau_{p,imp}$ is fixed at the mean value of the distribution. This case study will resemble the tendency of the experienced delay, while opting for the straightforward implementation of a constant delay in the observer structure.

The estimation errors can be seen in Fig. 4.10, closely resembling the performance shown in Fig. 4.8 for a constant and perfectly known delay.

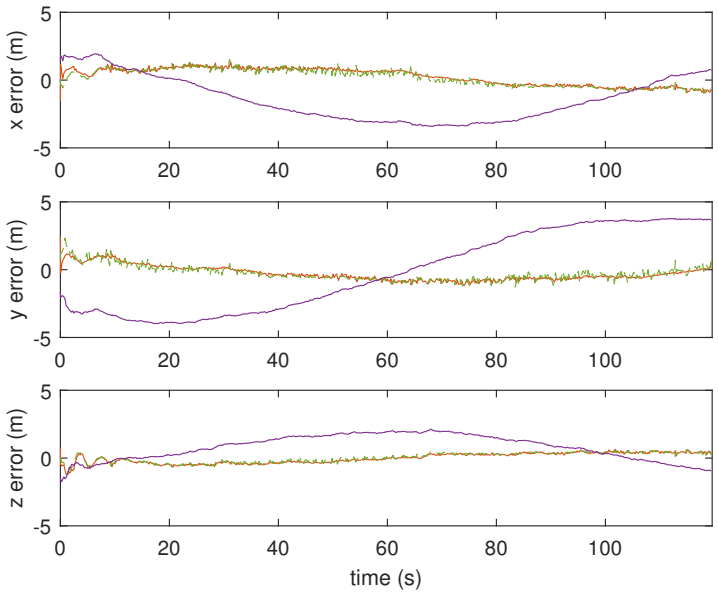

Figure 4.10: Position estimation error the proposed observer structure (red), the alternative implementation (green) and the observer without time-delay compensation (purple).

The estimation error of the proposed observer and the alternative implementation is concentrated around zero, with clear advantages compared to the observer without delay compensation. The results are summarized in Table 4.3.

Table 4.3: Simulation results, summarising the RMS and STD of position error signals of considered observer structures, unit: m. Note that the simulated GNSS position noise STD is 1 m.

		RMS			STD		
		x	y	z	x	y	z
Test I	Proposed Observer	0.688	0.568	0.323	0.617	0.481	0.311
	Alternative Implementation	0.663	0.584	0.317	0.601	0.508	0.302
	Uncompensated Observer	2.093	2.983	1.236	1.639	2.975	0.887
Test II	Proposed Observer	2.390	2.595	1.172	1.936	2.446	1.152
	Alternative Implementation	2.360	2.662	1.156	1.931	2.528	1.139
	Uncompensated Observer	2.130	2.888	1.262	1.646	2.878	0.913
Test III	Proposed Observer	0.685	0.607	0.378	0.631	0.538	0.378
	Alternative Implementation	0.659	0.620	0.366	0.629	0.560	0.365
	Uncompensated Observer	2.124	2.924	1.216	1.616	2.918	0.923

From Table 4.3 it is clear that the proposed observer and the alternative implementation have similar performance, throughout the test cases, while performing better than the observer without delay compensation. Furthermore, the performances in test I and test II are very similar, suggesting that when the receiver delay has a small standard deviation the implemented delay can be kept constant. The average delay of the receiver can be determined prior to implementation, and as test II showed, does not have to perfectly correspond to the experienced delays throughout the test. Moreover, the average delay of the receiver can be determined prior to use, possibly negating the need for online delay estimation for this specific receiver and thereby the use of the PPS signal in the on-board autopilot. In general it must be expected that other receivers and configurations might show larger variations in the time-delay estimation.

4.7 Experimental Results

This section describes the data acquisition and experimental results achieved with the introduced observers. A payload consisting of an ADIS 16488 IMU (1230 Hz), a u-Blox LEA-M8T GNSS receiver (5 Hz) and custom hardware for accurately time stamping the measurements with GPS clock was used for data acquisition. A description of the payload can be found in Appendix B. The proposed observers were implemented for post-processing of the acquired measurements. Both GNSS position and velocity measurements are used for estimation. The dataset were collected during flight with a GA Slingsby T67C, small manned aircraft, see Fig. 4.11, operated at an airfield in Prague.

Figure 4.11: Aircraft (GA Slingsby T67C)

The payload was mounted behind the passenger seat, powered by a car battery, with the GNSS antenna mounted on the inside of the transparent cover, directly above the payload to minimize the lever arm. The aircraft is highly manoeuvrable with maximum speed of approximately 280 km/h.

The trajectory reference was determined as a Real-Time-Kinematic (RTK) solution using dual frequency receiver onboard the aircraft with corrections from a local base station. The RTK solution, computed by the open source RTKLIB, exploiting carrier-phase measurements, provides more accurate data than the single-receiver code-based GPS solution, with three quality categories; single (the solution is comparable with the single receiver solution), float (relative positioning but unresolved ambiguities), and fixed (relative positioning with resolved ambiguities). The flight had predominant (over 90% of the time) "fixed" quality indicating a highly accurate reference. The remaining time the reference had "float" quality were the differential corrections are used, without the resolution of the integer ambiguity, resulting in approximately decimetre accuracy.

When comparing the observer position estimates with the RTK solution, the position estimates are down sampled to match the frequency of the RTK solution.

The receiver delay was measured in real time throughout the flight. The time delay was slowly time-varying over time, see Fig. 4.12, with distribution as shown in Fig. 4.13. The receiver used in the experimental verification is a newer version compared to the receiver presented in Section 4.2.1, which might account for the smaller magnitude in total delay. The mean of the distribution is 0.0505 s with standard deviation 0.0020 s. The error introduced at maximum speed of the aircraft will be approximately 4 m.

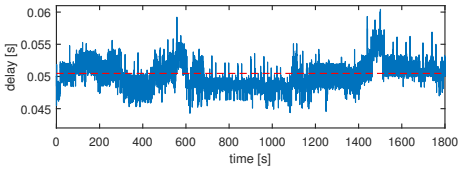

Figure 4.12: Total receiver delay (blue) with depicted average (red).

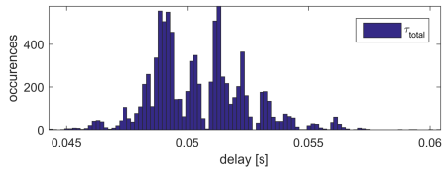

Figure 4.13: Histogram of total receiver delay.

When implementing the proposed observer structures the receiver delay is represented as an integer number of IMU samples. As the average receiver delay is equivalent to 62 IMU samples the delay is considered sufficiently well represented.

The observer parameters are chosen as; $M_b = 0.0087\ [rad/s]$, $k_1 = 0.8$, $k_2 = 0.2$, $k_I = 0.004$, and $\theta = 1$. The gain matrices of the TMO are determined by solving the discrete Ricatti equation with the noise covariance matrices; $R = \text{blockdiag}(14.4I_3\ [m^2], 1 \cdot 10^{-4} I_3\ [m^2/s^2])$, and $Q = \text{blockdiag}\left(0I_3\ [m^2], 0.096 I_3\ [m^2/s^2], 2.5 \cdot 10^{-2} I_3\ [m^2/s^4]\right)$. In the injection term for the attitude observer the magnetometer measurements are exchanged for velocity estimates making; $v_2^b = [1; 0; 0]$ and $v_2^e = \hat{v}^e / \|\hat{v}^e\|_2$.

In the following two tests are presented, both with the experienced delay as the actual distributed delay as shown in Fig. 4.12 and Fig. 4.13, while; I) the implemented delay is constant at the average value, and II) the implemented delay follows the actual delay. In both test scenarios the velocity delay will be considered the same as the position delay, $\tau_p = \tau_v$, since the information package used from the receiver included both position and velocity measurements. Three observers will be considered, as in the simulation study; a) the proposed observer, b) the

alternative implementation, and c) the uncompensated observer. The results of the observers will be summarised in Table 4.4, where they are compared using the RMS and STD values using the RTK solution as reference.

The flight trajectory is shown in Fig. 4.14 covering an area of over 120 km^2 with a flight duration of more than 25 min. Certain points of interest have been marked during the flight, where; ① denotes the take off, ② marks a sharp turn with small radius and high roll angle, ③ denotes a stall where the plane first climbed in altitude and then went into stall, and ④ denotes the second stall, where the plane experience accelerations from approximately 0.5 g to 2.1 g over a short time period, during the climb following the stall. These points of interest have been marked on the figures depicting the results for ease of comparison between the trajectory and the signals of interest.

4.7.1 Test 1: Average delay

The implemented delay is considered constant and fixed at the average of the actual experience delay, i.e. $\tau_p = \tau_v = \tau_{p,imp} = \tau_{v,imp} = 0.0505\ s$. The estimated position of the three observers are compared with the reference and the error in NED frame can be seen in Fig. 4.15 (a larger version can be found in Fig. D.1).

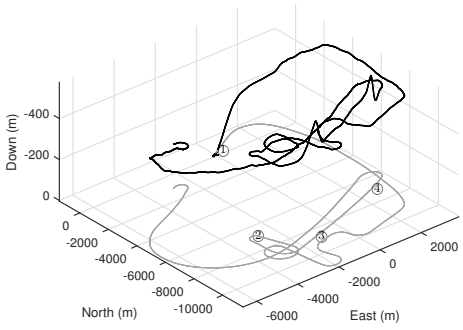

Figure 4.14: Measured (black) and ground track (gray) trajectory of the aircraft seen in NED frame.

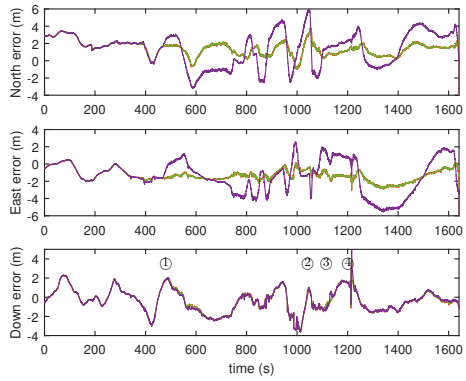

Figure 4.15: Position error the proposed observer structure (red), the alternative implementation (green) and the uncompensated observer (purple).

During taxiing on the runway, prior to take-off, the position errors of the three observers have comparable magnitude. However after take-off when the aircraft moves with higher speeds than during taxiing the difference between the uncompensated observer and the proposed observer is clear, with the proposed observer structure having smaller error magnitude. There is little difference in the vertical component (as the vertical velocity is small), whereas there is a significant improvement in the North and East components, compared to using the proposed observer instead of the uncompensated observer. The difference between the proposed observer and the alternative implementation is almost indistinguishable. During the sharp turn at ②, which is predominantly in the North direction, the error of the

proposed observer is seen to have a smaller magnitude than the uncompensated observer, as expected due to the high velocity. During the two stall manoeuvres the proposed observer also has better performance than the uncompensated observer.

4.7.2 Test 2: Actual delay

The actual time-varying receiver delay is considered for the implemented delay. The position error of the observers are very similar to the once presented in Test 1, as is the case for the attitude and gyro bias estimates shown in Fig. 4.16 (a larger version can be found in Fig. D.2) and Fig. 4.17.

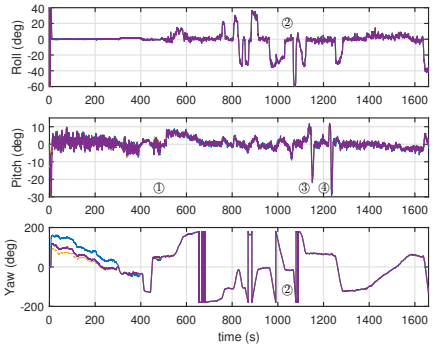

Figure 4.16: Attitude estimates of the proposed observer structure (red), the alternative implementation (green) and the observer without time-delay compensation (purple).

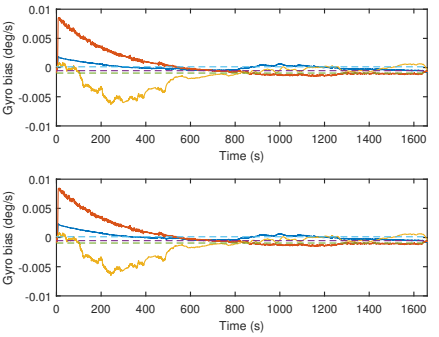

Figure 4.17: Gyro biases (solid) and biases determined at standstill (dashed) of the proposed observer (top) and alternative implementation (bottom).

The estimated attitude is seen to be very similar for the three observers, with only small differences during the flight. Similarly, the difference in determined gyro biases of the proposed observer and the alternative implementation very small, with convergence towards the biases determined at standstill. The roll angle is seen to be large during the sharp turn, while the pitch is small throughout the flight except for during take-off and the two stall manoeuvres.

From the summarised results in Table 4.4, it is clear that the proposed observer and the alternative implementation have similar performance, both being superior to the uncompensated observer. The RMS of the error signal is decreased with over 30% in the x and y direction by using the proposed observer structure (or the alternative implementation) compared to the traditional observer structure. The difference between considering the receiver delay constant (shown in Test 1) or time-varying (shown in Test 2) is small. It can be concluded that the proposed observer works well on highly accelerated vehicles experiencing fast dynamic manoeuvres.

4.7.3 Additional flights

To further verify the proposed observer additional flight data is tested. Here the actual delay is used and two observers are examined; a) the proposed observer,

Table 4.4: Summary on RMS and STD of error signals of the uncompensated and proposed, and alternative observers for the test scenarios. Units: m.

		RMS			STD		
		North	East	Down	North	East	Down
Test 1	Proposed Observer	1.678	1.459	1.237	0.838	0.699	1.189
	Alternative Implementation	1.679	1.460	1.237	0.839	0.700	1.189
	Uncompensated Observer	2.377	2.309	1.250	1.906	1.859	1.201
Test 2	Proposed Observer	1.671	1.436	1.237	0.832	0.673	1.189
	Alternative Implementation	1.674	1.439	1.237	0.836	0.678	1.189
	Uncompensated Observer	2.377	2.309	1.250	1.906	1.859	1.201

and b) the uncompensated observer. The alternative implementation will not be considered as it has been shown perform similar to the proposed observer.

The additional flights considered are all performed with the same aircraft at the same airfield on the same day. The difference between the flights are in manoeuvres and flight time. In the first flight the aircraft covers a wide area with some points of interest; ① shows take off, ② shows a sharp turn followed by ③ denoting a second sharp turn, ④ marks the time with highest altitude. The trajectory and estimation errors can be seen in Fig. 4.18 and Fig. 4.19 (a larger version can be found in Fig. D.3).

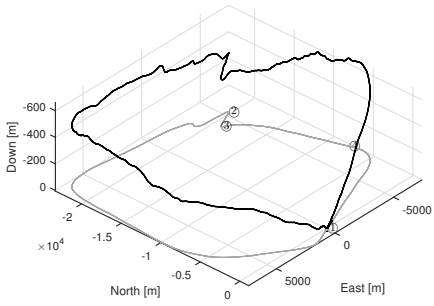

Figure 4.18: Trajectory of flight with ground track.

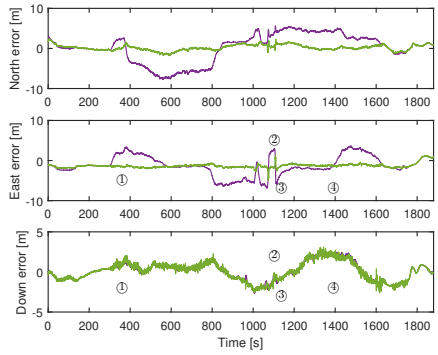

Figure 4.19: Estimation errors with proposed (green) and uncompensated (purple).

The second flight is longer, a total of approximately 44 minutes, and has the highest altitude of all the considered flights. Four points of interest are; ① denoting take off, ② shows a 360 degree turns with small radius, ③ marks the start of the final ascent which has some turns before reaching point ④ showing the time of maximum altitude. After ④ a sharp descent towards the landing area is performed.

The trajectory and estimation errors are shown in Fig. 4.20 and Fig. 4.21 (a larger version can be found in Fig. D.4).

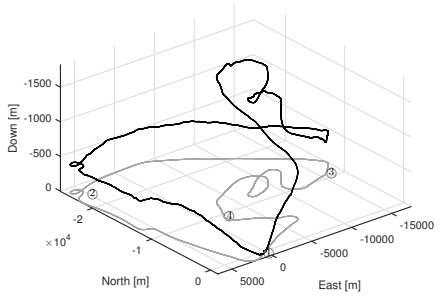

Figure 4.20: Trajectory of flight with ground track.

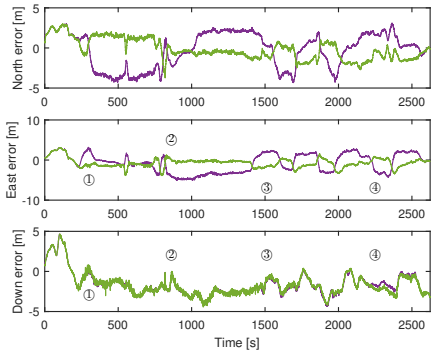

Figure 4.21: Estimation errors with proposed (green) and uncompensated (purple).

The performance of the proposed and the uncompensated observers are compared in Table 4.5 where the root-mean-square and standard deviation are listed. The first flight is given in the first two lines of the table, and the second flight is given by the two last lines of the table.

Table 4.5: Summary on RMS and STD of error signals during the additional flights. Units: m.

	RMS			STD		
	North	East	Down	North	East	Down
Proposed Observer	0.734	1.424	1.150	0.706	0.557	1.147
Uncompensated Observer	3.595	2.705	1.150	3.589	2.398	1.148
Proposed Observer	1.302	1.333	2.186	1.291	1.142	1.489
Uncompensated Observer	2.195	2.418	2.188	2.185	2.313	1.484

The proposed observer is seen to perform better than the uncompensated observer structure for both flights. Again it can be confirmed that for low velocities, such as taxiing on the runway, the difference between the observers is small. However, at higher velocities the proposed observer ensures high performance. The estimation of vertical position component is very similar between the two observers as the vertical velocity is small.

For the first flight in Fig. 4.18 and Fig. 4.19 the horizontal estimation is significantly better for the proposed observer, where even the sharp turns does not impact performance. During the second flight in Fig. 4.20 and Fig. 4.21 harder manoeuvres are performed and the errors of the proposed observer is larger than

for the first flight. However, the proposed observer still performs better than the uncompensated observer.

4.8 Chapter Summary

Nonlinear integration of INS and GNSS have been investigated where the GNSS measurements are delayed due to computational time in the receiver and data communication between receiver and the navigation computer. Initially the delay was investigated and a method for determining the magnitude of the delay was proposed.

An observer structure for compensating the time delay was introduced based on a uniformly semiglobally exponentially stable nonlinear observer. The proposed observer structure includes delaying the inertial and magnetometer measurements to coincide with the GNSS measurements, estimating position, linear velocity, attitude and IMU bias as delayed states, while a faster than real-time simulator supplies current estimates based on the delayed states and current inertial measurements.

Additionally, an alternative implementation was proposed where the current attitude is estimated with the delayed position and velocity. This approach offers a reduction in computational load as the fast simulator does not need to determine the attitude.

The two observer structures was compared to the uncompensated observer structure, where the time delay is not taken into account, through simulations and experimental data from a small manned aircraft. A significant improvement was evident using the proposed observer structures compared to the uncompensated observer.

Chapter 5

Tightly-Coupled GNSS/INS Integration

A modular nonlinear observer for inertial navigation aided by range and range-rate measurements is designed and analyzed. The observer includes an attitude estimator is based on a recent nonlinear complementary filter with magnetometer and accelerometer vector measurements for correction of the quaternion attitude estimate driven by gyro measurements. A tightly-coupled integrated translational motion observer (TMO) is driven by accelerometer measurements, employs the attitude estimates, and makes corrections using range and range-rate measurements from a GNSS receiver.

The TMO estimates position, range bias errors, velocity and specific force in an Earth-fixed Cartesian coordinate frame, where the specific force estimate is used as a reference vector for the accelerometer measurements in the attitude observer. The exponential stability of the feedback interconnection of the observer is analyzed and found to have a semi-global region of attraction with respect to attitude observer initialization, and local region of attraction with respect to translational motion observer initialization. The latter is due to linearization of the range and range-rate measurement equations utilized in the gain selection for the injection terms. In typical applications the pseudorange equations admit an explicit algebraic solution that can be easily computed and used to accurately initialize the position and velocity estimates. Hence, the limited region of attraction is not seen as a practical limitation of the approach for many applications. Advantages of the proposed nonlinear observer are low computational complexity and a solid theoretical foundation.

Contributions of this Chapter: The main contribution of this chapter is the proposal of a tightly-coupled nonlinear observer for inertial navigation aided by range measurements from a satellite constellation. The nonlinear observer structure consists of the nonlinear attitude estimator introduced and utilized in the previous chapters, as well as a translational motion observer utilizing the range measurements to correct the inertial navigation. Despite the nonlinearity of the range measurements the only linearization is in the output matrix when determining the observer gains. Furthermore, an initialization

method for the TMO is proposed. The computational complexity of the proposed observer is compared to a multiplicative extended Kalman filter. The observer is furthermore verified using experimental data from a UAV.

Organization of this Chapter: This chapter is organized as follows: Models and preliminaries are described in Section 5.2, where existence, uniqueness and computation of an algebraic solution to the pseudorange equations are presented. In Section 5.3 the observers for attitude and translational motion are presented, and the stability of their interconnections analyzed. Some possible extensions with dual frequency GNSS measurements are discussed in Section 5.4. The method is compared, in Section 5.5, to a multiplicative EKF using experimental pseudorange measurements before conclusions are made in Section 5.6.

Publications: The material in this chapter is based on the journals Johansen et al. 2017 [101] and Bryne et al. 2017 [31].

5.1 Introduction

Range measurement is the basis for global satellite navigation systems, hydroacoustic positioning systems, terrestrial radio navigation, and other positioning systems. Such systems commonly detect the time-of-arrival (TOA) of signals encoded in electromagnetic or acoustic waves to estimate the range, and are therefore prone to systematic errors such as clock synchronization errors or uncertain wave speed. Since the range measurements do not directly correspond to the true geometric range, they are often called pseudorange measurements.

Inertial sensors such as accelerometer and gyros can be used to estimate position and velocity by integrating the kinematic equation. Since biases and other errors are accumulated in this process, leading to unbounded errors on the estimates, inertial navigation systems are usually aided by range or position measurements that can be used to stabilize these errors using a state estimator. There are two main design philosophies for these such estimators: Loosely- and tightly-coupled integration, [52, 69, 76]. In a loosely-integrated scheme, a standalone estimator for position and velocity in an Earth-fixed Cartesian reference coordinate frame is first made using only the pseudorange measurements. These position and velocity estimates are in turn used as measurements in a state observer that integrates them with the inertial measurements. In a tightly-integrated scheme, the pseudorange measurements are used directly in the state observer together with the inertial measurements. While the advantage of loosely-coupled integration is a high degree of modularity, the advantage of tight integration is increased accuracy and fault tolerance, in particular in situations with highly accelerated vehicles and few range measurements, weak or noisy signals, unknown wave speed, poor transponder geometry, or other anomalies, e.g. [52, 69]. More accurate models of measurement errors can be used in the integration filter and a reduced number of pseudorange measurements can be used for aiding when a standalone position estimate cannot be determined, [52, 69, 76].

The state-of-the-art method for real-time fusion of the data from the individual sensors are nonlinear versions of the Kalman-filter (KF), [52, 69, 79], including the

extended KF, unscented KF, particle filter, and specially tailored variants such as the multiplicative KF for attitude estimation using quaternions, [39, 122]. While the KF is a general method that has found extremely wide applicability, it has some drawbacks. This includes the relatively high computational cost and a rather implicit and not so easily verifiable convergence properties that may require advanced supervisory functions and accurate initialization, [147]. Its major advantages are flexibility in tuning and application, as it is a widely known and used technology with intuitive and physically motivated tuning parameters interpreted as noise covariances, and providing certain optimality guarantees.

The objective of this chapter is to develop a low-complexity nonlinear observer for inertial navigation aided by magnetometer and pseudorange measurements, where the observer has properties founded on stability theory. The nonlinear observer structure is inspired by [72], where a loose integration between GNSS position and velocity measurements and inertial measurements was derived with semiglobal asymptotic stability conditions. Its extension to tightly integrated inertial navigation is non-trivial since the measurement equations are nonlinear when considering pseudorange and range-rate measurements for aiding, instead of being linear when position and velocity estimates in an Earth-fixed Cartesian coordinate frame are used for aiding.

A similar research objective is pursued in the series of articles represented by [9, 11, 15–17, 131]. Using a state transformation and a state augmentation they derive a linear time-varying (LTV) model which is closely related to the nonlinear model, and use this for the design of an estimator for attitude, position and velocity using hydro-acoustic range measurements. In slight contrast, the objective here is to avoid unnecessary computational complexity.

We base the design philosophy on the assumption that the line-of-sight (LOS) vectors between the vehicle and the used transponders are relatively slowly time-varying. This is a good assumption in many practical situations, such as terrestrial navigation using satellites, and surface ship positioning in deep waters using hydro-acoustic transponders at the seabed. In this case, time-varying observer gains multiplying pseudorange and range-rate errors in the injection terms can be designed to shape the dynamics of the observer using a time-varying linearized relationship between range and vehicle position. Note that the term transponder is used as a general concept that also includes navigation satellites in space, as well as hydro-acoustic navigation. Using the semiglobally exponentially stable nonlinear attitude observer of [119], see also [71, 72], a slowly time-varying Riccati equation for gain matrix updates to the translational motion observer is employed in contrast to using a KF. This allows the integration of the Riccati equation to be performed on a slower time-scale corresponding to the relative geometric configuration of the transponders and the receiver, or even solved periodically at low rate as an algebraic Riccati equation. This ensures low computational complexity, and a rigorous analysis of the observer error dynamics stability is made in the chapter.

A short and preliminary version of this paper is presented in [98], and some recent contributions by the authors are found in [31, 84].

5.2 Models and preliminaries

The kinematic vehicle model of (2.7)–(2.9) describing position, linear velocity and attitude is used in the following. The position and velocity are given in ECEF-frame, while the attitude is represented as a unit quaternion giving the rotation between Body- and ECEF-frame.

5.2.1 Measurement models

The inertial sensor model is based on the strapdown assumption, i.e. the IMU is fixed to the Body frame and supplies measurements of $f^b_{\text{IMU}} = f^b$ and $\omega^b_{ib,\text{IMU}} = \omega^b_{ib} + b^b$ where $b^b \in \mathbb{R}^3$ denotes the rate gyro bias that is assumed to satisfy $\|b^b\|_2 \leq M_b$ for some known bound M_b and is slowly time-varying:

$$\dot{b}^b = 0. \tag{5.1}$$

It is further assumed that any accelerometer bias and drift is compensated for. The magnetometer measures the direction of the 3-dimensional Earth magnetic vector field $m^b_{\text{MAG}} = m^b$.

Range measurements are typically generated by measuring the TOA of known signal waveforms (acoustic or electromagnetic). Due to errors in clock synchronization and wave propagation velocity, such measurements often contain systematic errors (biases) in addition to random errors, e.g. [40], and must therefore be treated as pseudorange measurements. The range measurement model is:

$$\rho_i = \psi_i + \zeta_i^\intercal \beta, \qquad \psi_i = \|p^e - p^e_i\|_2, \tag{5.2}$$

for $i = 1, 2, ..., m$ where ρ_i is a (pseudo-)range measurement, p^e_i is the known position of the ith transponder, m is the number of transponders, ψ_i is the geometric range, $\beta \in \mathbb{R}^n$ is a vector of range error model parameters (biases) to be estimated, and the coefficient vector ζ_i describes the influence of each element of β on pseudorange measurement ρ_i. This framework allows for both individual and common mode slowly time-varying errors such as receiver clock bias (i.e. $\zeta_i = 1$ and $\beta := c\Delta_c$ where Δ_c is the clock bias and c is the wave speed) or wave speed variations to be taken into account:

$$\dot{\beta} = 0. \tag{5.3}$$

Note that $\dot{\beta} = 0$ is the classical constant parameter assumption in adaptive estimation and does not prevent us from estimating a slowly time-varying β in practice. Also note that in [31] the model $\ddot{\beta} = 0$ is applied instead.

Range-rate measurements are usually found by considering Doppler-shift or tracking of features or codes in signals. Also here there may be systematic (bias) errors in some cases, depending on the sensor principle and technology. The range-rate (speed) measurement model is given by:

$$\nu_i = \frac{1}{\psi_i} (p^e - p^e_i)^\intercal (v^e - v^e_i) + \varrho_i^\intercal \beta, \tag{5.4}$$

where ν_i is the relative range-rate measurement, the coefficient vector ϱ_i describes the effect of each element of β on range speed measurement ν_i, and the following relation is defined $v_i^e := \dot{p}_i^e$. Equation (5.4) follows from time-differentiation of (5.2), assuming an independent error model. Hence, the term $\varrho_i^\intercal \beta$ will be used instead of $\zeta_i^\intercal \dot{\beta}$ in (5.4) since it provides additional flexibility in modeling.

5.2.2 Algebraic range and pseudorange solutions

Despite the nonlinear form of the pseudorange measurement equation (5.2),the quadratic structure is used to get a relatively simple algebraic solution, [7, 32, 40, 180]. Assume an arbitrary reference position $\hat{p}^e$ is given, and define LOS vectors $\breve{p}_i^e := \hat{p}^e - p_i^e$ for every i. The following explicit procedure can be used to determine a position estimate.

Lemma 5.1. *Assuming available pseudorange measurements ρ_1, ρ_2, ρ_3, and ρ_4 where the three first transponder line-of-sight vectors $\breve{p}_1^e, \breve{p}_2^e$, and $\breve{p}_3^e$ are linearly independent, and:*

$$\rho_4 \neq (\rho_1, \rho_2, \rho_3)\breve{A}^{-1}\breve{p}_4^e, \tag{5.5}$$

where $\breve{A} = \begin{pmatrix} \breve{p}_1^e & \breve{p}_2^e & \breve{p}_3^e \end{pmatrix}$. Assume $\zeta_i = 1$ for all $i = 1, 2, 3, 4$ (i.e. a single common mode error parameter $\beta \in \mathbb{R}$), then $p^e = \hat{p}^e + \tilde{p}^e$ is derived from $z = (\tilde{p}^e; \beta)$ where:

$$z = \frac{\check{r}\check{u} + \check{v}}{2}, \;\; \check{u} = \hat{A}^{-\intercal}\check{e}, \;\; \check{v} = \hat{A}^{-\intercal}\check{b} \tag{5.6}$$

$$\check{r} = \frac{-2 - \check{u}^\intercal M \check{v} \pm \sqrt{(2 + \check{u}^\intercal M \check{v})^2 - \check{u}^\intercal M \check{u} \cdot \check{v}^\intercal M \check{v}}}{\check{u}^\intercal M \check{u}}, \tag{5.7}$$

where $\check{e} = (1; 1; 1; 1)$, $\check{b} \in \mathbb{R}^4$ has components $\check{b}_i = \rho_i^2 - \|\breve{p}_i^e\|_2^2$, $M = diag(1, 1, 1, -1)$, and:

$$\hat{A} = \begin{pmatrix} \breve{p}_1^e & \breve{p}_2^e & \breve{p}_3^e & \breve{p}_4^e \\ y_1 & y_2 & y_3 & y_4 \end{pmatrix}. \tag{5.8}$$

Proof. The proof is similar to those found in [7, 32, 40, 180]. □

The computations are analytic and the most complex operations are the inversion of a 4×4-matrix as well as the square-root computation. Note that there are in general two solutions. This ambiguity can be solved in several ways. For example, by using five or more pseudorange measurements, the problem can be solved directly from a linear equation, cf. [7, 32, 40, 180]. The ambiguity may also be resolved using domain knowledge. One example is terrestrial navigation when there is a large distance to the navigation satellites such that non-terrestrial solutions for the vehicle position can be ruled out. Another example is underwater navigation where all transponders are located on the seabed and the vehicle is at the surface or at some distance from the seabed such that positions below the seabed can be ruled out. Additional sensors for e.g. depth or altitude can also be used directly to select the correct solution.

Remark 5.1. The velocity can be estimated by solving a linear problem by inserting the position and bias parameter estimates in the measurement equation (5.4).

Remark 5.2. If the condition (5.5) does not hold, the null-space of $\hat{A}$ is given by $\rho_4\beta + (\rho_1, \rho_2, \rho_3)\breve{p}_4^e = 0$. Solutions for p^e may be estimated by fixing β, or solved using another measurement if available.

Remark 5.3. With an error model that requires a vector $\beta \in \mathbb{R}^n$ rather than a scalar β, the solution may require more than 4 measurements and up to n coupled quadratic equations to be solved, possibly leading to additional ambiguity. A related example is carrier-phase measurements, where additional unknown integer variables are introduced, [84].

In typical range-measurements systems, the remaining measurement errors are typically so small that a good position and velocity initialization of an observer can be found using Lemma 5.1 such that a relatively small region of attraction with respect to position, velocity and bias parameter initialization error can be accepted.

Here it is chosen to only consider the effect of slowly time-varying systematic errors (parameterized by β), such as biases, in this presentation and analysis. Rapidly varying errors such as noise can possibly be handled by appropriate tuning of the gains and may not influence the structure of the observer. In some cases, better estimation accuracy can be achieved by further modeling of the errors using e.g. Markov-like models, which are straightforward to include in the proposed framework by augmenting the translational motion observer with the new states, see [31] for more details.

5.3 Nonlinear observer

The overall structure of the observer is given in Fig. 5.1. Sections 5.3.1 and 5.3.2 describes the two main modules, i.e. the attitude observer and the translational motion observer. In addition, the initialization based on the algebraic pseudorange solver was presented in Section 5.2.2, and the Riccati solution and gain computation in Section 5.3.3. An implementation overview of the nonlinear observer is included in Algorithm 1 and Algorithm 3 in Appendix C.

5.3.1 Attitude observer

We use the attitude observer from [71, 119]:

$$\dot{\hat{q}}_b^e = \frac{1}{2}\hat{q}_b^e\left(\overline{\omega}_{ib,\mathrm{IMU}}^b - \overline{\hat{b}}^b + \overline{\hat{\sigma}}\right) - \frac{1}{2}\overline{\omega}_{ie}^e\hat{q}_b^e, \tag{5.9}$$

$$\dot{\hat{b}}^b = \mathrm{Proj}\left(-k_I\hat{\sigma},\ \|\hat{b}^b\|_2 \leq M_{\hat{b}}\right), \tag{5.10}$$

$$\hat{\sigma} = k_1 m_{\mathrm{MAG}}^b \times R(\hat{q}_b^e)^\intercal m^e + k_2 f_{\mathrm{IMU}}^b \times R(\hat{q}_b^e)^\intercal \mathrm{sat}_{M_f}(\hat{f}^e), \tag{5.11}$$

where ω_{ie}^e and m^e have been assumed known. $\mathrm{Proj}(\cdot)$ is a projection operator that ensures $\|\hat{b}^b\|_2 \leq M_{\hat{b}}$ with $M_{\hat{b}} > M_b$, see [72]. Moreover, $\mathrm{sat}_{M_f}(\cdot)$ is a saturation

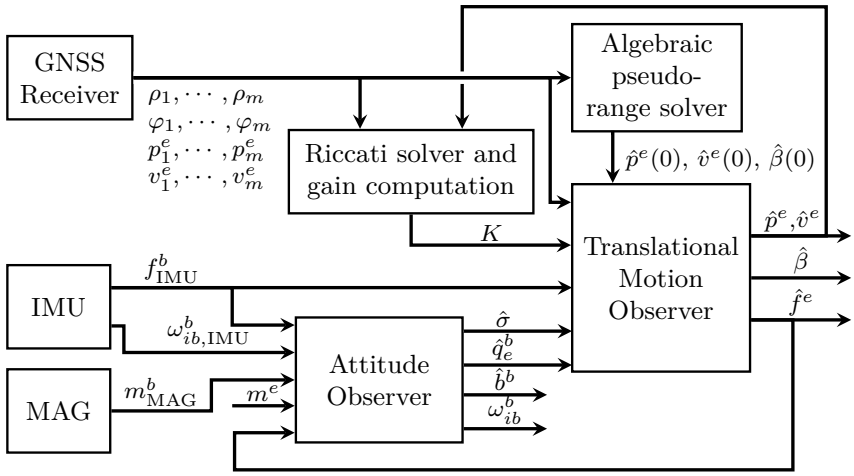

Figure 5.1: Block diagram of the tightly-coupled nonlinear observer.

operator, with M_f such that $\|f^e\|_2 \leq M_f$. The QUEST algorithm, [156], may be used for initialization of the attitude.

The estimation error is defined as $\tilde{q} = q_b^e \hat{q}_b^{e*}$ and $\tilde{b}^b = b^b - \hat{b}^b$, and it is defined that $\chi = (\tilde{s}; \tilde{b}^b)$ where $\tilde{s}$ denotes the scalar part of the quaternion $\tilde{q}$. Semiglobal stability of the origin $\chi = 0$ of the error dynamics of the attitude observer can be established under the following assumption:

Assumption 19. The acceleration f^b and its rate $\dot{f}^b$ are uniformly bounded, and there exist a constant $c_{obs} > 0$ such that $\|f^b \times m^b\|_2 \geq c_{obs}$ for all $t \geq 0$.

Initial conditions are restricted to the following sets:

Assumption 20. $\hat{q}_b^e(0) \in \mathcal{D}(\bar{\varepsilon})$, where $\mathcal{D}(\bar{\varepsilon}) = \{\tilde{q} \mid \tilde{s} > \bar{\varepsilon}\}$ represents a set of attitude errors bounded away from 180° by a margin determined by an arbitrary constant $\bar{\varepsilon} \in (0, \frac{1}{2})$. Moreover, $\hat{b}^b(0) \in \mathcal{B} = \{b \in \mathbb{R}^3 \mid \|b\|_2 \leq M_b\}$.

Lemma 5.2. *Assume $\hat{f}^e = f^e$. Then for each $\varepsilon \in (0, \frac{1}{2})$ there exists a $k_P^* > 0$ such that if $k_1, k_2 > k_P^*$ and $k_I > 0$ then:*

$$\|\chi(t)\|_2 \leq \kappa_a e^{-\lambda_a t} \|\chi(0)\|_2, \tag{5.12}$$

for some $\kappa_a, \lambda_a > 0$.

Proof. See [72]. □

5.3.2 Translational motion observer

The following observer for position, linear velocity, attitude and clock range bias is proposed:

$$\dot{\hat{p}}^e = \hat{v}^e + \sum_{i=1}^{m} \left(K_i^{p\rho} e_{\rho,i} + K_i^{p\nu} e_{\nu,i} \right), \tag{5.13}$$

$$\dot{\hat{v}}^e = -2S(\omega_{ie}^e)\hat{v}^e + \hat{f}^e + g^e(\hat{p}^e) + \sum_{i=1}^{m} \left(K_i^{v\rho} e_{\rho,i} + K_i^{v\nu} e_{\nu,i}\right), \tag{5.14}$$

$$\dot{\hat{\xi}} = -R(\hat{q}_b^e)S(\hat{\sigma})f_{\text{IMU}}^b + \sum_{i=1}^{m} \left(K_i^{\xi\rho} e_{\rho,i} + K_i^{\xi\nu} e_{\nu,i}\right), \tag{5.15}$$

$$\hat{f}^e = R(\hat{q}_b^e)f_{\text{IMU}}^b + \xi, \tag{5.16}$$

$$\dot{\hat{\beta}} = \sum_{i=1}^{m} \left(K_i^{\beta\rho} e_{\rho,i} + K_i^{\beta\nu} e_{\nu,i}\right), \tag{5.17}$$

where the gain matrices K_i^* are in general time-varying. While the structure is similar to [72], the injection terms are different, and [72] does not include estimation of parameters β. A common feature is that f^e is viewed as an unknown input, which is estimated using an auxiliary state in (5.15)–(5.16) to be used in (5.11). The injection errors from pseudorange and range-rate measurements are defined as $e_{\rho,i} := \rho_i - \hat{\rho}_i$ and $e_{\nu,i} := \nu_i - \hat{\nu}_i$, with estimated measurements:

$$\hat{\rho}_i = \hat{\psi}_i + \zeta_i^\intercal \hat{\beta}, \qquad \hat{\nu}_i = \left(\frac{\hat{p}^e - p_i^e}{\hat{\psi}_i}\right)^\intercal (\hat{v}^e - v_i^e) + \varrho_i^\intercal \hat{\beta}, \tag{5.18}$$

where $\hat{\psi}_i := \|\hat{p}^e - p_i^e\|_2$, and the estimation errors are $\tilde{p} := p^e - \hat{p}^e$, $\tilde{v} := v^e - \hat{v}^e$, and $\tilde{\beta} := \beta - \hat{\beta}$. Next, a linearization of the injection terms is considered.

Assumption 21. At all time, $\overline{\psi} \geq \psi_i \geq \underline{\psi} > 0$.

Assumption 22. At all time, $\|v^e - v_i^e\|_2 \leq \overline{\nu}$.

Assumption 23. The transponder positions p_i^e and their velocities v_i^e are known.

Remark 5.4. In hydro-acoustic applications the transponders are usually stationary with known positions. In GNSS applications the transponders are constantly moving where the position and velocity can be determined from the ephemeris navigation data, allowing for accurate transponder position and velocity determination.

Remark 5.5. The only linearization made is with respect to the pseudorange and range-rate measurement equations for the gain selection. This is similar to the operations of an EKF if the covariance estimates are propagated with the state estimates. However, for the nonlinear observer the covariance estimates are a design choice and are not required for gain calculation.

Lemma 5.3. *The injection errors satisfy:*

$$e_{\rho,i} = \left(\frac{\hat{p}^e - p_i^e}{\hat{\psi}_i}\right)^\intercal \tilde{p} + \zeta_i^\intercal \tilde{\beta} + \varepsilon_{\rho,i}, \tag{5.19}$$

$$e_{\nu,i} = \left(\frac{\hat{v}^e - v_i^e}{\hat{\psi}_i}\right)^\intercal \tilde{p} + \left(\frac{\hat{p}^e - p_i^e}{\hat{\psi}_i}\right)^\intercal \tilde{v} + \varrho_i^\intercal \tilde{\beta} + \varepsilon_{\nu,i}, \tag{5.20}$$

where:

$$\|\varepsilon_{\rho,i}\|_2 \leq \frac{1}{\underline{\psi}}\|\tilde{p}\|_2^2, \tag{5.21}$$

$$\|\varepsilon_{\nu,i}\|_2 \leq \frac{1}{\underline{\psi}}\|\tilde{p}\|_2 \cdot \|\tilde{v}\|_2 + \frac{3\overline{\nu}}{2\underline{\psi}^2}\|\tilde{p}\|_2^2. \tag{5.22}$$

Proof. It follows by Taylor's theorem that:

$$e_{\rho,i} = \left(\frac{\hat{p}^e - p_i^e}{\hat{\psi}_i}\right)^\intercal \tilde{p} + \zeta_i^\intercal \tilde{\beta} + \frac{1}{2}\tilde{p}^\intercal \breve{H}_i \tilde{p}, \tag{5.23}$$

where:

$$\breve{H}_i = \frac{1}{\breve{\psi}_i} I_3 - \frac{(\breve{p}^e - p_i^e)(\breve{p}^e - p_i^e)^\intercal}{\breve{\psi}_i^3}, \tag{5.24}$$

where $\breve{p}^e$ is on the line between $\hat{p}^e$ and p^e, $\breve{\psi}_i := \|\breve{p}^e - p_i^e\|_2$. The bound on $\varepsilon_{\rho,i}$ follows using the triangle and Cauchy-Schwarz inequalities.

Applying Taylor's theorem also gives:

$$e_{\nu,i} = \frac{(\hat{p}^e - p_i^e)^\intercal}{\hat{\psi}_i}\tilde{v} + \frac{(\hat{v}^e - v_i^e)^\intercal}{\hat{\psi}_i}\tilde{p} + \varphi_i^\intercal \tilde{\beta} + \frac{1}{2}(\tilde{p};\tilde{v})^\intercal \begin{bmatrix} \breve{J}_i & \breve{H}_i \\ \breve{H}_i & 0 \end{bmatrix} (\tilde{p};\tilde{v}), \tag{5.25}$$

where $\breve{H}_i$ is defined similar to (5.24), and it is straightforward to show that:

$$\begin{aligned}\breve{J}_i = &\frac{1}{\breve{\psi}_i^3}\left((\breve{p}^e - p_i^e)(\breve{v}^e - v_i^e)^\intercal + \breve{p}^e - p_i^e)^\intercal(\breve{v}^e - v_i^e)I_3\right) \\ &- \frac{3}{\breve{\psi}_i^5}(\breve{p}^e - p_i^e)(\breve{p}^e - p_i^e)^\intercal(\breve{p}^e - p_i^e)(\breve{v}^e - v_i^e)^\intercal,\end{aligned}$$

were $\breve{\psi}_i = \|\breve{p}^e - p_i^e\|_2$ for some $\breve{p}^e$ on the line between p^e and $\hat{p}^e$, and $\breve{v}^e$ is on the line between v^e and $\hat{v}^e$. The bound on $\varepsilon_{\nu,i}$ follows using the triangle and Cauchy-Schwarz inequalities. □

We define the state of the error dynamics as $x := (\tilde{p};\tilde{v};\tilde{f};\tilde{\beta})$, where $\tilde{f} := f^e - \hat{f}^e$ replaces ξ as a state by combining (5.15) and (5.16). Summarized, the equations for the predicted measurement error can now be written in the linearized time-varying form:

$$e_{\rho,i} = C_{\rho,i}x + \varepsilon_{\rho,i}, \tag{5.26}$$

$$e_{\nu,i} = C_{\nu,i}x + \varepsilon_{\nu,i}, \tag{5.27}$$

where the $2m$ rows $C_{\rho,i}$ and $C_{\nu,i}$ of the time-varying matrix $C := (C_{\rho,1};\ldots;C_{\rho,m};C_{\nu,1};\ldots;C_{\nu,m})$ are defined by $C_{\rho,i} := (\breve{d}_i^\intercal,\ 0,\ 0,\ \zeta_i^\intercal)$ and $C_{\nu,i} := (\breve{v}_i^\intercal,\ \breve{d}_i^\intercal,\ 0,\ \varrho_i^\intercal)$. The estimated line-of-sight vectors are $\breve{d}_i := (\hat{p}^e - p_i^e)/\hat{\psi}_i = \breve{p}_i^e/\hat{\psi}_i$ and the normalized estimated relative velocity vectors are $\breve{v}_i := (\hat{v}^e - v_i^e)/\hat{\psi}_i$, for $i = 1, 2, ..., m$. It is noted that:

$$C = \begin{bmatrix} G^\intercal & 0 & 0 & D_p^\intercal \\ B^\intercal & G^\intercal & 0 & D_v^\intercal \end{bmatrix}, \tag{5.28}$$

where $G = (\breve{p}_1^e, ..., \breve{p}_m^e) \in \mathbb{R}^{3\times m}$, $B = (\breve{v}_1^e, ..., \breve{v}_m^e) \in \mathbb{R}^{3\times m}$, and $D = (D_p, D_v)$ with $D_p = (\zeta_1, ..., \zeta_m)$ and $D_v = (\varrho_1, ..., \varrho_m)$.

It is noted that the time-varying matrix C is known at the current time and can be used for selection of gains. Furthermore it is observed that in typical applications with large distance between the vehicle and transponders, their relative positions and line-of-sight vectors will be slowly time-varying, and hence the measurement matrix C will be slowly time-varying, since due to Lemma 5.1 the transients resulting from initialization of position and velocity are not expected to be significant. Following similar steps as in [72] and Chapter 3.4.4, the error dynamics become:

$$\dot{x} = (A - KC)x + \theta_1(t, x) + \theta_2(t, \chi) + \theta_3(t, x), \tag{5.29}$$

where:

$$A := \begin{bmatrix} 0 & I_3 & 0 & 0 \\ 0 & 0 & I_3 & 0 \\ 0 & 0 & 0 & 0 \\ 0 & 0 & 0 & 0 \end{bmatrix}, \qquad K := \begin{bmatrix} K_1^{p\rho} & \dots & K_m^{p\rho} & K_1^{p\nu} & \dots & K_m^{p\nu} \\ K_1^{v\rho} & \dots & K_m^{v\rho} & K_1^{v\nu} & \dots & K_m^{v\nu} \\ K_1^{\xi\rho} & \dots & K_m^{\xi\rho} & K_1^{\xi\nu} & \dots & K_m^{\xi\nu} \\ K_1^{\beta\rho} & \dots & K_m^{\beta\rho} & K_1^{\beta\nu} & \dots & K_m^{\beta\nu} \end{bmatrix}.$$

The perturbation terms are defined as $\theta_1(t, x) := (0; \theta_{12}(t, x); 0; 0)$ with $\theta_{12}(t, x) = -2S(\omega_{ie}^e)x_2 + (g^e(p^e) - g^e(p^e - x_1))$ and $\theta_2(t, \chi) := (0; 0; \tilde{d}; 0)$ with:

$$\begin{aligned} \tilde{d} = {} & (I - R(\tilde{q})^\intercal)R(q_b^e)(S(\omega_{ib,\mathrm{IMU}}^b)f_{\mathrm{IMU}}^b + \dot{f}_{\mathrm{IMU}}^b) \\ & - S(\omega_{ie}^e)(I - R(\tilde{q})^\intercal)R(q_b^e)f_{\mathrm{IMU}}^b - R(\tilde{q})^\intercal R(q_b^e)S(\tilde{b})f_{\mathrm{IMU}}^b. \end{aligned} \tag{5.30}$$

In [72] it is shown that $\|\theta_2(t, \chi)\|_2 \leq \gamma_3\|\chi\|_2$ for some constant $\gamma_3 > 0$. A fundamental difference compared to [72] is that the matrix C is time-varying (rather than constant), and there is a third perturbation term $\theta_3(t, x) := K\varepsilon(t, x)$ that results from the linearization of the injection terms, where $\varepsilon := (\varepsilon_{\rho,1}; ...; \varepsilon_{\rho,m}; \varepsilon_{\nu,1}; ...; \varepsilon_{\nu,m})$. From Lemmas 5.1 and 5.3 it is known that ε is small when $\underline{\psi}$ is large compared to $\|\tilde{p}\|_2$, $\|\tilde{v}\|_2$ and $\overline{\nu}$. Compared to [72] this means that a different strategy for selection of gains is needed, and one can not hope for a global stability result. Nevertheless, as in [72], it is desired to employ a constant parameter $\theta \geq 1$ in order to assign a certain time-scale structure to the error dynamics (5.29). For this purpose, the non-singular state-transform matrix is introduced:

$$L_\theta := \mathrm{blockdiag}\left(I_3, \frac{1}{\theta}I_3, \frac{1}{\theta^2}I_3, \frac{1}{\theta^3}I_n\right), \tag{5.31}$$

and the state transform $\eta = L_\theta x$.

Lemma 5.4. *Let $K_0 \in \mathbb{R}^{(9+n)\times 2m}$ be an arbitrary time-varying gain matrix, and $\theta \geq 1$ be an arbitrary constant. Define:*

$$K := \theta L_\theta^{-1} K_0 E_\theta, \tag{5.32}$$

and assume the time-varying $E_\theta \in \mathbb{R}^{2m\times 2m}$ satisfies $E_\theta C = CL_\theta$. Then the error dynamics (5.29) is equivalent to:

$$\frac{1}{\theta}\dot{\eta} = (A - K_0C)\eta + \frac{1}{\theta}\theta_1(t, \eta) + \frac{1}{\theta^3}\theta_2(t, \chi) + K_0E_\theta\varepsilon(t, L_\theta^{-1}\eta). \tag{5.33}$$

Proof. The transformed dynamics are derived by substituting (5.29) in $\dot{\eta} = L_\theta \dot{x}$. It is straightforward to show that the structure of A leads to $L_\theta A x = \theta A \eta$. Moreover,

$$L_\theta K C x = \theta L_\theta L_\theta^{-1} K_0 E_\theta C x = \theta K_0 C L_\theta x = \theta K_0 C \eta. \tag{5.34}$$

The rest of the proof follows by change of variables according to $\eta = L_\theta x$. □

The existence of an E_θ satisfying $E_\theta C = C L_\theta$ depends on the null-space of C, as shown next.

Assumption 24. i) The number of transponders is $m \geq 3 + \lceil k/2 \rceil$, where $k = \text{rank}(D^\intercal)$. ii) 3 of the estimated line-of-sight vectors are linearly independent, i.e. $\text{rank}(G) = 3$. iii) 3 of the estimated normalized relative velocity vectors are linearly independent, i.e. $\text{rank}(B) = 3$.

Lemma 5.5. *$E_\theta = C L_\theta C^\dagger$ satisfies $E_\theta C = C L_\theta$, where $C^\dagger$ is the Moore-Penrose right pseudo-inverse of C.*

Proof. In order to characterize the null-space of C, let $Z \in \mathbb{R}^{n \times (n-k)}$ have $n - k$ columns that forms an orthonormal basis for the null-space of $D^\intercal$ and $Y \in \mathbb{R}^{n \times k}$ have $k = \text{rank}(D^\intercal)$ columns that forms an orthonormal basis for the range-space of $D^\intercal$. It follows that $D^\intercal Z = 0$ and $\text{rank}(D^\intercal Y) = k$. Consider a vector $x = (x_1; x_2; x_3; x_4)$, where $x_1, x_2, x_3 \in \mathbb{R}^3$ and $x_4 \in \mathbb{R}^n$. Let $x_4 = Z x_{4Z} + Y x_{4Y}$ where $x_{4Z} \in \mathbb{R}^{n-k}$ and $x_{4Y} \in \mathbb{R}^k$. The vector x belongs to the null-space of C if $Cx = 0$, which is equivalent to $M \cdot (x_1; x_2; x_{4Y}) = 0$ where:

$$M = \begin{bmatrix} G^\intercal & 0 & D_p^\intercal Y \\ B^\intercal & G^\intercal & D_v^\intercal Y \end{bmatrix}. \tag{5.35}$$

From Assumption 24 it follows immediately that $M \in \mathbb{R}^{2m \times (6+k)}$ has rank $6 + k$ and $2m \geq 6 + k$. From $M \cdot (x_1; x_2; x_{4Y}) = 0$ it follows that the null-space of C is characterized by $x_1 = 0, x_2 = 0, x_{4Y} = 0$ while x_3 and x_{4Z} can be arbitrary.

Now, consider a singular value decomposition $C = USV^\intercal$, where the Moore-Penrose pseudo-inverse is given by $C^\dagger = VS^\dagger U^\intercal$, cf. [93]. From the characterization of the null-space of C, thus:

$$C^\dagger C = VS^\dagger S V^\intercal = \text{blockdiag}(I_3, I_3, 0_3, J), \tag{5.36}$$

for some matrix $J \in \mathbb{R}^{n \times n}$, and $L_\theta C^\dagger C = C^\dagger C L_\theta$ due to both $C^\dagger C$ and L_θ sharing the same block diagonal structure. The result follows from $E_\theta C = C L_\theta C^\dagger C = C C^\dagger C L_\theta = C L_\theta$ since the Moore-Penrose pseudo-inverse satisfies $C C^\dagger C = C$, [93]. □

The assumption is reasonable and closely related to the assumptions underlying Lemma 5.1, as well as observability that will be considered shortly. If there are no range-rate measurements, it can be verified that condition i) can be replaced by $m \geq 3 + k$.

5.3.3 Stability analysis

As the first step towards the stability analysis, the LTV nominal error dynamics is considered:

$$\frac{1}{\theta}\dot{\eta} = (A - K_0 C)\eta, \tag{5.37}$$

and analyze its stability and robustness before the effect of the perturbations in (5.33) is considered.

Let $R > 0$ be a symmetric matrix that can be interpreted as the covariance of the pseudorange and range-rate measurement noises. The observability Gramian for the system $(A, R^{-1/2}C)$ is:

$$\mathcal{W}(t, t+\tau) = \int_t^{t+\tau} \Phi^\intercal(T) C^\intercal(T) R^{-1} C(T) \Phi(T) dT, \tag{5.38}$$

where the transition matrix is $\Phi(T) = e^{AT}$, and it should be recalled (from e.g. [4]) that the LTV system is said to be uniformly completely observable if there exist constants $\alpha_1, \alpha_2, \tau > 0$ such that for all $t \geq 0$ it is satisfied that $\alpha_1 I \leq \mathcal{W}(t, t+\tau) \leq \alpha_2 I$.

Assumption 25. The LTV system $(A, R^{-1/2}C)$ is uniformly completely observable.

Remark 5.6. Assumption 25 is related to Assumption 24, as well as the conditions of Lemma 5.1. This is further discussed in Section 5.3.4.

There may be many ways to choose a time-varying gain matrix K_0 such that (5.37) has desired performance and stability. A straightforward approach with considerable flexibility for tuning is to use a Riccati-equation similar to the gain of a Kalman-Bucy filter for the system (A, C) as described below. In this case, the close relationship between the complete uniform observability conditions and the boundedness of the covariance matrix estimate P is well known, e.g. [147], and can be monitored in real-time without much additional computations.

Assumption 26. C is uniformly bounded.

Remark 5.7. It can be observed that the only terms in C that may not be uniformly bounded are of the form $(\hat{v}^e - v_i^e)/\hat{\psi}_i$. Thus, unbounded C may only occur if $\tilde{v}$ goes unbounded. While this can be dealt with in many ways, a simple approach is resetting of $\hat{v}^e$ based on the velocity computed from range and range-rate measurements (cf. Lemma 5.1) if $\hat{v}^e$ grows out of bounds.

Lemma 5.6. *Let:*

$$K_0 := PC^\intercal R^{-1}, \tag{5.39}$$

where P satisfies the Riccati equation:

$$\frac{1}{\theta}\dot{P} = AP + PA^\intercal - PC^\intercal R^{-1} CP + Q, \tag{5.40}$$

for some positive definite symmetric matrices Q, R, and $P(0)$. Then P is uniformly bounded and the origin is a globally exponentially stable equilibrium point of the LTV nominal error dynamics (5.37) with any constant $\theta \geq 1$.

Proof. The proof follows from [4, 106], and the main ideas will be repeated since the Lyapunov function is needed later. Consider a Lyapunov function candidate $U(\eta, t) = \frac{1}{\theta}\eta^\intercal P^{-1}\eta$, which is positive definite and well-defined due to the time-varying matrix P satisfying (5.40) being symmetric, positive definite with some margin, and bounded. It follows by standard arguments that along the trajectories of (5.37) and (5.40) that $\dot{U} = -\eta^\intercal(P^{-1}QP^{-1} + C^\intercal R^{-1}C)\eta$ and the result follows by the positive definiteness of P^{-1} and Q. □

The structure of the observer is illustrated in the block diagram in Fig. 5.1. Two feedback loops are present where one is due to the use of $\hat{f}^e$ as a reference vector in the attitude observer and the other is caused by linearization of the pseudorange measurement equations to get the C-matrix in (5.39) and (5.40).

Initialization of position and velocity is based on the algebraic solution, cf. Lemma 5.1. If the vehicle is not strongly accelerated during initialization, then also the specific force initialization can be made accurately with $\xi(0) = 0$ that gives $\hat{f}^e(0) = R(\hat{q}_b^e(0))f_{\text{IMU}}^b(0)$. Below, the conditions for exponential stability of the origin of the estimation error dynamics is analyzed.

Assumption 27. Initial conditions are in the following sets:

1. $\mathcal{X} \subset \mathbb{R}^{9+n}$ is a ball containing the origin.
2. $\mathcal{P} \subset \mathbb{R}^{(9+n)\times(9+n)}$ is an arbitrary compact set of symmetric positive definite matrices.
3. $\mathcal{D}(\bar{\varepsilon}) = \{\tilde{q} \mid \tilde{s} > \bar{\varepsilon}\}$ represents a set of attitude errors bounded away from 180° by a (small) margin determined by an arbitrary constant $\bar{\varepsilon} \in (0, \frac{1}{2})$.
4. $\mathcal{B} = \{b \in \mathbb{R}^3 \mid \|b\|_2 \leq M_b\}$.

Assumption 28. Observer gains are chosen according to

1. $k_1, k_2 > 0$ are sufficiently large, cf. [72].
2. $k_I > 0$ is arbitrary.
3. K is chosen according to (5.32), (5.39) and (5.40) tuned by symmetric $P(0)$, Q, $R > 0$.

Proposition 1: There exists a $\theta^* \geq 1$ such that for all $\theta \geq \theta^*$, P is uniformly bounded and:

$$\sqrt{\|x(t)\|_2^2 + \|\chi(t)\|_2^2} \leq \kappa e^{-\lambda t}\sqrt{\|x(0)\|_2^2 + \|\chi(0)\|_2^2}, \tag{5.41}$$

for some $\kappa > 0$ and $\lambda > 0$.

Proof. Using $U(\eta, t) := \frac{1}{\theta}\eta^\intercal P^{-1}\eta$, it follows from the proof of Lemma 5.6 that:

$$\begin{aligned}\dot{U} = &-\eta^\intercal(P^{-1}QP^{-1} + C^\intercal R^{-1}C)\eta + \frac{2}{\theta}\eta^\intercal P^{-1}\theta_1(t,\eta) \\ &+ \frac{2}{\theta}\eta^\intercal P^{-1}PC^\intercal R^{-1}E_{\theta\varepsilon} + \frac{2}{\theta^3}\eta^\intercal P^{-1}\theta_2(t,\chi),\end{aligned}$$

$$\leq -\gamma_1\|\eta\|_2^2 + \frac{2}{\theta}\|\eta\|_2 \cdot \|C^\intercal R^{-1}\| \cdot \sum_{i=1}^{m} \|E_\theta\|(\varepsilon_{\rho,i}^2 + \varepsilon_{\nu,i}^2)$$
$$+ \frac{1}{\theta}\gamma_2\gamma_4\|\eta\|_2^2 + \frac{1}{\theta^3}\gamma_3\gamma_4\|\eta\|_2 \cdot \|\chi\|_2,$$

where $\gamma_1, \gamma_2, \gamma_3, \gamma_4 > 0$ are constants independent of θ. Note that a uniform bound on P^{-1} that does not depend on θ is established in Lemma 6 in [98]. Next, using Lemma 5.3, the derivative becomes:

$$\dot{U} \leq -\gamma_1\|\eta\|_2^2 + \frac{1}{\theta}\gamma_5(\underline{\psi}, \overline{\nu})\|\eta\|_2^3 + \frac{1}{\theta}\gamma_2\gamma_4\|\eta\|_2^2 + \frac{1}{\theta^3}\gamma_3\gamma_4\|\eta\|_2 \cdot \|\chi\|_2, \tag{5.42}$$

where $\gamma_5(\underline{\psi}, \overline{\nu})$ increases with $\overline{\nu}$ and decreases with $\underline{\psi}$, and is independent of θ.

Similar to [72], it can be shown that for any $\delta > 0$ and $T > 0$ there exists a $\theta_1^* \geq 1$ such that for $\theta \geq \theta_1^*$ there exists an invariant set $\mathcal{X}_1 \subset \mathbb{R}^{9+n}$ such that for $\|\eta(0)\|_2 \in \mathcal{X}_1$ for all $t \geq T$ it is satisfied that $\|\eta\|_2 \leq \delta$. As argued in [72] this implies $|\tilde{s}| \geq \bar{\varepsilon}$ such that $\tilde{q}$ never leaves $\mathcal{D}(\bar{\varepsilon})$. Inspired by [72], the function is defined as:

$$W(t, \tilde{r}, \tilde{s}, \tilde{b}) := \left(1 - \tilde{s}^2\right) + 2\ell\overline{sr}R(q_b^e)\tilde{b}^b + \frac{\ell}{k_I}(\tilde{b}^b)^\intercal\tilde{b}^b, \tag{5.43}$$

where $\ell > 0$ is a constant [71]. Under the condition $|\tilde{s}| \geq \bar{\varepsilon}$, W is shown in [72] to satisfy:

$$\dot{W} \leq -\gamma_7\|\chi\|_2^2 + \gamma_6\theta^2\|\chi\|_2 \cdot \|\eta\|_2, \tag{5.44}$$

for some constants $\gamma_6, \gamma_7 > 0$ that are independent of θ. Next the Lyapunov-function candidate is defined as $V(t, \eta, \chi) := U(t, \eta) + \frac{1}{\theta^5}W(t, \chi)$. Then:

$$\dot{V} \leq -z^\intercal S(\theta)z + \frac{\gamma_5(\underline{\psi}, \overline{\nu})}{\theta}\|\eta\|_2^3, \tag{5.45}$$

where $z := (\|\eta\|_2; \|\chi\|_2) \in \mathbb{R}^2$ is an auxiliary state, and the 2×2-matrix:

$$S(\theta) = \begin{bmatrix} \gamma_1 - \frac{\gamma_2\gamma_4}{\theta} & -\frac{\gamma_3\gamma_4 + \gamma_6}{2\theta^3} \\ -\frac{\gamma_3\gamma_4 + \gamma_6}{2\theta^3} & \frac{\gamma_7}{\theta^5} \end{bmatrix}, \tag{5.46}$$

Considering the first-order and second-order principal minors of S, $S(\theta) > 0$ is satisfied if:

$$\theta > \max\left(\frac{\gamma_2\gamma_4}{\gamma_1}, \frac{\gamma_2\gamma_4\gamma_7 + (\gamma_3\gamma_4 + \gamma_6)^2}{\gamma_1\gamma_7}\right). \tag{5.47}$$

Hence, a θ^* can be chosen satisfying (5.47) such that for all $\theta \geq \theta^*$ there exists an invariant set $\mathcal{X}_2$ and $\alpha_3, \alpha_4 > 0$, where for all $x \in \mathcal{X}_2$ it is satisfied that:

$$\dot{V} \leq -\alpha_3\|z\|_2^2 - \alpha_4\|\chi\|_2^2 \leq -2\lambda V, \tag{5.48}$$

for some $\lambda > 0$, and the result follows by choosing $\mathcal{X}$ as the largest invariant set such that $\mathcal{X} \subset \mathcal{X}_1 \cap \mathcal{X}_2$, and application of the comparison lemma, [107]. □

Remark 5.8. The translational motion observer is not a KF since the state estimate update equation contains certain nonlinear terms and the auxiliary state ξ. It has the attractive feature that its error dynamics are accurately represented by a nominal LTV system that is used as a basis for selection of the injection gain matrices using the formulas for the Riccati-equation and gain matrix of the Kalman-Bucy filter.

Remark 5.9. In some cases when the parameter vector β influences all measurements in the same way, the variable β (or at least some of its elements) can be eliminated from the estimation problem by forming new measurements that are differences between original measurements. This is known as Time-Difference-of-Arrival (TDOA) measurements, e.g. [40, 180], and can be employed in order to further reduce the computational complexity of the estimator since an estimate of β is not needed for most applications.

Since the LTV system (5.33) is slowly time-varying, it is possible to reap the benefits of solving the Riccati equation on a slower time-scale than the estimator updates, roughly speaking only when there is a significant change in the transponders' LOS vectors due to the relative motion of the vehicle and the transponders, or enabling or disabling some range measurements. In many practical applications this can be implemented by solving the algebraic Riccati-equation periodically at low rate. In the context of terrestrial GNSS this relates to the dynamics of the satellites relative to the Earth, and in the context of a surface ship on dynamic positioning using hydro-acoustic positioning this relates to the motion of the ship relative to the transponders at the seabed. Hence, the proposed solution will in many typical applications not incur much more computations than a fixed-gain strategy and typically less than both a direct and indirect extended KF approach that would require updating of the covariance matrix at a higher update frequency.

The rate of convergence of the estimation error depends on the tuning of the parameters, as well as the quality of the sensors. Bounds on the convergence rate and magnitude of the estimation error depends on the bounds stated in the assumptions above.

5.3.4 Observability analysis

Here the observability Gramian $\mathcal{W}(t, t+\tau)$ is studied, where it is assumed without loss of generality that $R = I$. The state transition matrix $\Phi(T) = e^{AT}$ is straightforward to compute:

$$\Phi(T) = \begin{bmatrix} I_3 & TI_3 & (T^2/2)I_3 & 0 \\ 0 & I_3 & TI_3 & 0 \\ 0 & 0 & I_3 & 0 \\ 0 & 0 & 0 & I_n \end{bmatrix}. \tag{5.49}$$

By multiplication with the C-matrix the expression becomes:

$$C(T)\Phi(T) = \begin{bmatrix} G^\intercal & TG^\intercal & \frac{T}{2}G^\intercal & D_p^\intercal \\ B^\intercal & TB^\intercal + G^\intercal & \frac{T^2}{2}B^\intercal + TG^\intercal & D_v^\intercal \end{bmatrix}. \tag{5.50}$$

Let $N(T) := \Phi(T)^\intercal C^\intercal(T) C(T) \Phi(T) \in \mathbb{R}^{(9+n)\times(9+n)}$ be the integrand of the observability Gramian.

It is instructive to consider some special cases.

Special case: Only range measurements, no pseudorange error parameters β.

Consider the case when $n = 0$ and there are only range measurements (i.e. no range-rate measurements). Then:

$$C(T)\Phi(T) = G^\intercal \begin{bmatrix} I_3 & TI_3 & \frac{T^2}{2} I_3 \end{bmatrix}. \tag{5.51}$$

With $N(T) = \Xi(T) \otimes GG^\intercal$, where:

$$\Xi(T) = \begin{bmatrix} 1 & T & \frac{T^2}{2} \\ T & T^2 & \frac{T^3}{2} \\ \frac{T^2}{2} & \frac{T^3}{2} & \frac{T^4}{4} \end{bmatrix}. \tag{5.52}$$

The integral is $\mathcal{W}(t+\tau, t) = \int_t^{t+\tau} \Xi(T) dT \otimes GG^\intercal$. It is observed that while $\Xi(T) \in \mathbb{R}^{3\times3}$ has rank one, it is straightforward to prove that rank $\left(\int_t^{t+\tau} \Xi(T) dT \right) = 3$ for all $\tau > 0$. Consequently, with three linearly independent transponder positions forming G, the rank$(GG^\intercal) = 3$ and rank$(\mathcal{W}(t+\tau, t)) = 9$ since rank$(A \otimes B) =$ rank$(A) \cdot$ rank(B).

Special case: Only range measurements, with receiver clock bias.

In this case $n = 1$, and $D_p = (1, 1, 1, 1)$ since the receiver clock bias is the same for all measurements made by the single receiver. In this case $\mathcal{W}(t+\tau, t) \in \mathbb{R}^{10\times10}$. Compared to the previous case, it is straightforward to see that a fourth transponder is needed such that $GG^\intercal \in \mathbb{R}^{4\times4}$ has full rank in this case.

5.3.5 Clock error model augmentation

The model of the clock bias range error can be extended from $\beta = c\Delta_c$ to consider the clock error as being dependent on the clock oscillator frequency error. Moreover, the clock bias range error can be determined from a state space model with clock oscillator frequency error, f_c, such that $\ddot{\beta} = 0$, [52, Section 8.4.3.2], [76, Section 9.4.2.3]:

$$\begin{bmatrix} \dot{\beta} \\ \dot{f}_c \end{bmatrix} = \begin{bmatrix} 0 & 1 \\ 0 & 0 \end{bmatrix} \begin{bmatrix} \beta \\ f_c \end{bmatrix} + \begin{bmatrix} n_\beta \\ n_f \end{bmatrix}, \tag{5.53}$$

the driving process noise, n_β and n_f, are assumed to be independent and white. The standard deviation of the noise distributions should be chosen small, e.g. less than 0.02 m/s according to [52, Section 8.4.3.2]. The clock frequency error is modelled as a slowly time-varying constant.

By introducing the additional clock error state, (5.17) in the TMO is replaced by:

$$\dot{\hat{\beta}} = \hat{f}_c + \sum_{i=1}^{m} \left(K_i^{\beta\rho} e_{\rho,i} + K_i^{\beta\upsilon} e_{\upsilon,i} \right), \tag{5.54}$$

$$\dot{\hat{f}}_c = \sum_{i=1}^{m} \left(K_i^{f\rho} e_{\rho,i} + K_i^{f\upsilon} e_{\upsilon,i} \right). \tag{5.55}$$

Furthermore, the state space vector and matrices are augmented accordingly, where the C-matrix is appended with $C_f = [0_{1\times m};\, 1_{1\times m}]$, such that the augmented C-matrix becomes; $C_a = [C, C_f]$.

The augmentation of the clock bias range error estimation have limited improvements over the common mode modelling proposed in [98]. Moreover, β can be considered a GNSS nuisance parameter in the TMO incorporating other common uncompensated residuals, e.g. higher order effects of atmospheric errors, multipath, etc. The modelling of (5.53) might simply move the residuals to f_c instead of β. Some improvements might be achieved when using receivers with resetting clock bias rather than the accumulated clock bias used by the receiver investigated in Section 5.5. However, the improvements are expected to be on sub-centimetre level.

5.4 Extension to Dual Frequency GNSS Measurements

A dual frequency GNSS receiver supplying measurements on the L_1 and L_2 band can be used to aid the inertial navigation instead of a single frequency receiver, by use of linear combinations of the pseudorange and carrier-phase measurements. An advantage to using dual frequency measurements is that the linear combination can be formed to enhance certain signal terms while suppressing others. Considering the general range measurement in meters, y, introduced as a common term for the code and phase range measurements, the linear combination of the L_1 and L_2 ranges can be stated as, see [140]:

$$y_{a,b} = a y_{L_1} + b y_{L_2}. \tag{5.56}$$

The general linear combinations of the pseudorange and carrier-phase measurements from the ith satellite are:

$$\begin{aligned}
\rho_{ab,i} &= (a+b)\left(\psi_i + \beta + T_i + E\right) + \alpha I_i + a\left(\epsilon_{L_1,i} + M_{L_1,\rho}\right) \\
&\quad + b\left(\epsilon_{L_2,i} + M_{L_2,\rho}\right), \\
\lambda_{L_{12}}\varphi_{ab,i} &= (a+b)\left(\psi_i + \beta + T_i + E\right) + \alpha I_i + a\left(N_{L_1,i}\lambda_{L_1} + e_{L_1,i} + M_{L_1,\rho}\right) \\
&\quad + b\left(N_{L_2,i}\lambda_{L_2} + e_{L_2,i} + M_{L_2,\rho}\right),
\end{aligned}$$

where the ionosphere constant is $\alpha = a f_{L_2}/f_{L_1} + b f_{L_1}/f_{L_2}$, and $\lambda_{L_{12}}$ is the wavelength of the combined carrier signal.

The linear combination is composed of common terms, such as geometric distance and atmospheric disturbances, which are enhanced by $(a+b)$, and frequency individual terms, such as multipath and carrier ambiguity. It can be advantageous

to assign the constants, a and b, based on the frequencies of the transmitted satellite signals. If the constants are chosen such that $a+b=1$ the range measurements can be utilized in the nonlinear observer structure proposed above without altering the stability results.

Apart from the single frequency case where $(a,b)=(1,0)$ or $(a,b)=(0,1)$ considered in the observer structure above there are several common combinations, which will be introduced in the following with their advantages and drawbacks. Some of the combinations can be used together to further strengthen some desired terms, e.g. such the integer ambiguities are determined using the geometry-free combination while the position is determined using the ionospheric-free combination.

5.4.1 Widelane combination

A signal with wide wavelength can be created by choosing the constants as; $a = f_{L_1}/(f_{L_1}-f_{L_2}) \approx 4.53$, and $b = -f_{L_2}/(f_{L_1}-f_{L_2}) \approx -3.53$. The longer wavelength is advantageous when detecting cycle-slips or fixing the phase ambiguities, which can be written as $N = N_{L_1,i} - N_{L_2,i}$ with wavelength; $\lambda = c/(f_{L_1}-f_{L_2}) \approx 0.86m$, [140]. A drawback of the widelane combination is the increase in noise due to the magnitude of a and b. In [140] it was shown that regardless of the constants chosen the stochastic errors will increase as the standard deviation of the combination is:

$$\sigma_{a,b} = \sqrt{a^2\sigma_{L_1}^2 + b^2\sigma_{L_2}^2}, \tag{5.57}$$

where σ_{L_1} and σ_{L_2} are the standard deviations for the L_1 and L_2 range measurements of interest. It should be noted that the effect of the noise terms can be averaged out over time.

5.4.2 Narrowlane combination

As opposed to the widelane combination the narrowlane constants are chosen to obtain a shorter wavelength. The constants are $a = f_{L_1}/(f_{L_1}+f_{L_2}) \approx 0.56$, and $b = f_{L_2}/(f_{L_1}+f_{L_2}) \approx 0.44$, resulting in a wavelength of $\lambda = c/(f_{L_2}+f_{L_1}) \approx 0.11m$ which also decreases the amplitude of the stochastic terms. The narrowlane combination has better stochastic error performance than the L_1 measurements, see [140], however resolving the phase ambiguities will be more difficult due to the shorter wavelength. This combination might therefore be preferred with code measurements.

5.4.3 Ionosphere-free combination

The ionospheric effect on the range measurements introduce the largest error source, as seen in Section 2.5.4, it is therefore desired to eliminate this disturbance. The first order ionospheric refraction bias of the range measurements can be cancelled by manipulating the range observable, [92], [52]. The constants are chosen as: $a = f_{L_1}^2/(f_{L_1}^2 - f_{L_2}^2) \approx 2.55$, $b = -f_{L_2}^2/(f_{L_1}^2 - f_{L_2}^2) \approx -1.55$, determining $\alpha = 0$.

The ambiguity difference is rewritten to; $N_{I,i} = (f_{L_1} N_{L_1,i} - f_{L_2} N_{L_2,i})$ which is no longer integer and therefore cannot be resolved as accurately as the previous combinations or the single-frequency measurement. The trade-off for cancelling the ionospheric effect is the non-integer ambiguity. With more detailed models of the atmosphere or satellite based augmentation systems such as WAAS and EGNOS are increasing in performance the need for this combination might be reduced, [139]. However, these models and augmentations are approximations and will not be able to eliminate the ionospheric effect perfectly due to low resolution and limited coverage.

5.4.4 Geometry-free combination

Common for the linear combinations above is that $a + b = 1$, ensuring that the common terms, e.g. the geometric distance, are sustained. The geometry-free combination assigns the constants to remove the geometric terms, thereby considering only the integer ambiguity and the stochastic and systematic error sources. With the constants chosen as; $a = 1$, and $b = -1$, the range measurements becomes:

$$\rho_{G,i} = f_G I_i + \epsilon_{L_1,i} - \epsilon_{L_2,i}, \tag{5.58}$$

$$\lambda_G \varphi_{G,i} = N_{L_1,i}\lambda_{L_1} - N_{L_2,i}\lambda_{L_2} - f_G I_i + e_{L_1,i} - e_{L_2,i}, \tag{5.59}$$

where the combined wavelength is λ_G and the combined frequency is $f_G = (f_{L_2}^2 - f_{L_1}^2)/(f_{L_1} f_{L_2}) \approx -0.504$. This linear combination cannot be used as aiding for inertial navigation as no range information is attained in the combined measurement. However, it might be advantageous to include the geometry-free measurements as additional aiding when estimating the integer ambiguities in a system with low measurement noise, or when analyzing the error sources.

5.4.5 Multipath combination

The multipath disturbance experienced by a standalone receiver can be analyzed with the multipath combination, created from dual-frequency phase measurements and a single-frequency code measurement, see [43]. The first order ionospheric effect and common geometric terms can be cancelled by the combination:

$$\begin{aligned} y_M &= \rho_{L_1} - \frac{f_{L_2} + f_{L_1}}{f_{L_2} - f_{L_1}} \varphi_{L_2} + \frac{2 f_{L_1}}{f_{L_2} - f_{L_1}} \varphi_{L_1} \\ &= M_{L_1,\rho} - \frac{f_{L_2} + f_{L_1}}{f_{L_2} - f_{L_1}} (M_{L_2,\varphi} + N_{L_2}\lambda_{L_2}) + \frac{2 f_{L_1}}{f_{L_2} - f_{L_1}} (M_{L_1,\varphi} + N_{L_1}\lambda_{L_1}), \end{aligned}$$

where the noise terms have been neglected and the frequencies used can be changed to accommodate other signal bands. In [43] the new GPS L5Q and Galileo E5aQ signals are considered, and several linear combinations are considered in the analysis of short and zero baselines. An assumption made in [43] is to neglect the phase multipath and thereby considering the multipath combination to consist of a varying term due to the code multipath and a constant term due to the ambiguities of the phase measurements, with some additional noise. By observing the linear combination over long time intervals and removing the mean value, to compensate for the phase ambiguities, the code multipath can be estimated.

5.5 Experimental Results

Experimental data is acquired using a Penguin B fixed-wing UAV equipped with a tactical grade IMU and GNSS receiver. The inertial and magnetometer measurement are available from an ADIS 16488 IMU at 410Hz, whereas pseudorange measurements are supplied by a u-Blox LEA-6T receiver at 5Hz. The measurements are collected by the payload shown in Appendix B. In the following the time-of-validity time stamps for the inertial and GNSS measurements will be used. The pseudorange measurements are corrected for time of transmission between satellite and receiver, as well as the tropospheric delay.

Additionally, a similar GNSS-receiver at a known and close location serves as a base station for a Real-Time-Kinematic (RTK) solution for the UAV position. The RTK position is determined using the open source program RTKLIB, and will be used as reference since the RTK position is known to have decimeter-level accuracy, [76], since a fix or float solution is achieved at every time during the experiments. The flight trajectory is illustrated in Fig. 5.2.

The nonlinear observer parameters are chosen as: $k_1 = 0.25$, $k_2 = 0.75$, $k_I = 0.004$, $R = 0.1^2 I_m \ [m^2]$, $Q = \text{blockdiag}\left(0I_3 \ [m^2], 10^{-10} I_3 \ [m^2/s^2], 2.5 \cdot 10^{-4} I_3 \ [m^2/s^4], 1 \ [m^2]\right)$.

A Multiplicative-Extended-Kalman-Filter (MEKF) is implemented for comparison. The MEKF integrates acceleration and angular velocity measured by the IMU with global ranges, see [39, 122]. The attitude is represented as a unit quaternion, see Chapter 3.3.1, where the attitude increment $\tilde{u}$ is included in the state vector resulting in 16 states, i.e. $x_{MEKF} = [\hat{p}^e; \hat{v}^e; \hat{f}^e; \tilde{u}; \hat{b}^b; \hat{\beta}]$. Note that the MEKF estimates $\hat{f}^e$ is to be used as an ECEF reference vector for the acceleration measurement in the attitude measurement model. The parameters for the MEKF are: $R_{MEKF} = \text{blockdiag}(0.1^2 I_m \ [m^2], 0.001 I_3 \ [T^2], 0.01 I_3 \ [m^2/s^4])$ where the six last elements correspond to the use of the magnetometer and accelerometer as aiding sensors for attitude, $Q_{MEKF} = \text{blockdiag}(0I_3 \ [m^2], 10^{-10} I_3 \ [m^2/s^2], 2.5 \cdot 10^{-4} I_3 \ [m^2/s^4], 10^{-5} I_3 \ [rad^2], 10^{-9} I_3 \ [rad^2/s^2], 1 \ [m^2])$.

It is interesting to note that the tuning of the TMO's of the nonlinear observers and the MEKF are compatible. The diagonal elements of the covariance matrices Q and R can be chosen based on the variances of the various measurements, and the same values can be used in the NLO and MEKF. This means that the nonlinear observer approach can take advantage of the extensive experiences with Kalman-filtering.

5.5.1 Estimation accuracy

Experimental results are depicted in Fig. 5.3, where the position estimation error is shown for the first 350 seconds of the flight. The position estimation performance of the proposed nonlinear observer is seen to be comparable to the MEKF, as shown in Table 5.1. Two versions of the nonlinear observer are compared, where the difference is related to the computation of the time-varying gain of the TMO: A discrete-time version where the TMO's Riccati-equation is updated at the 5 Hz GNSS frequency (denoted NLO) and a version where instead the algebraic Riccati-equation is solved periodically at 0.003 Hz (denoted NLO-ARE). It is easily seen

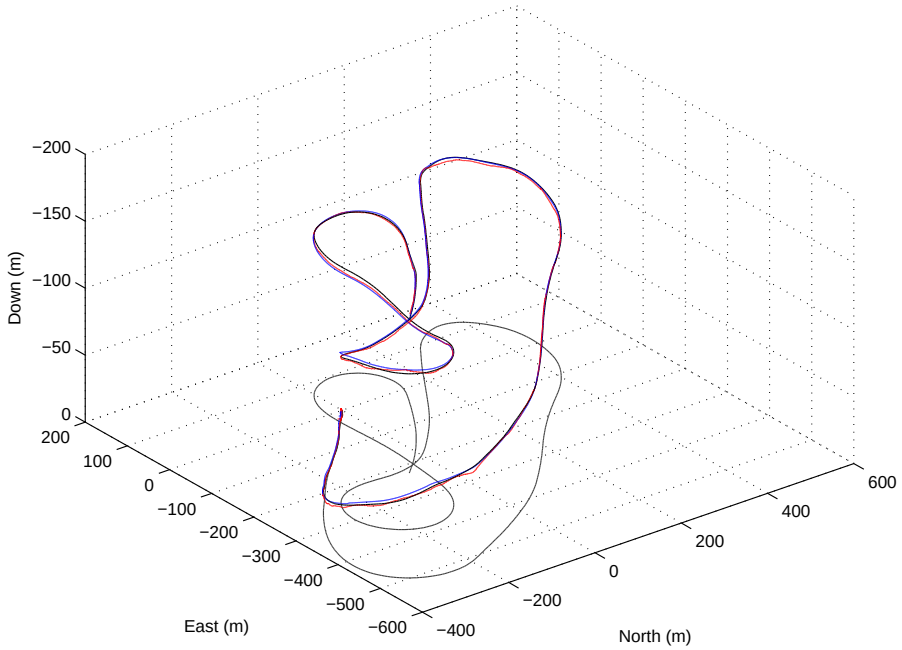

Figure 5.2: Trajectory of the UAV.

that their estimates are very similar since the red and black curves are almost indistinguishable in Fig. 5.3. Attitude estimates are shown in Fig. 5.5. Table 5.1 confirms that the performance of the two nonlinear observers is similar to the MEKF performance.

Improved estimates could possibly have been achieved by all methods with more realistic modeling of GNSS pseudorange measurement errors using Markov-models, see [31].

Table 5.1: Comparison of estimation accuracy, averaged over whole flight trajectory. Units: m.

	RMSE (N,E,D)			STD (N,E,D)		
NLO	2.316	3.867	2.074	0.753	0.462	1.951
NLO-ARE	2.196	3.849	1.553	0.683	0.385	1.529
MEKF	2.308	3.908	2.184	0.789	0.477	1.973

In Fig. 5.4 the position estimation error using the algebraic range and pseudorange solution proposed in Section 5.2.2 is shown. Comparing it to the estimation errors of the proposed nonlinear observer the algebraic solution is seen to have a larger spread. The position estimation is quite close to the nonlinear observer with a significantly computational lighter solution. However, it is important to note that the algebraic only have solutions at the GNSS receiver rate and not at the higher IMU rate, as the nonlinear observer. The algebraic solution cannot be used for

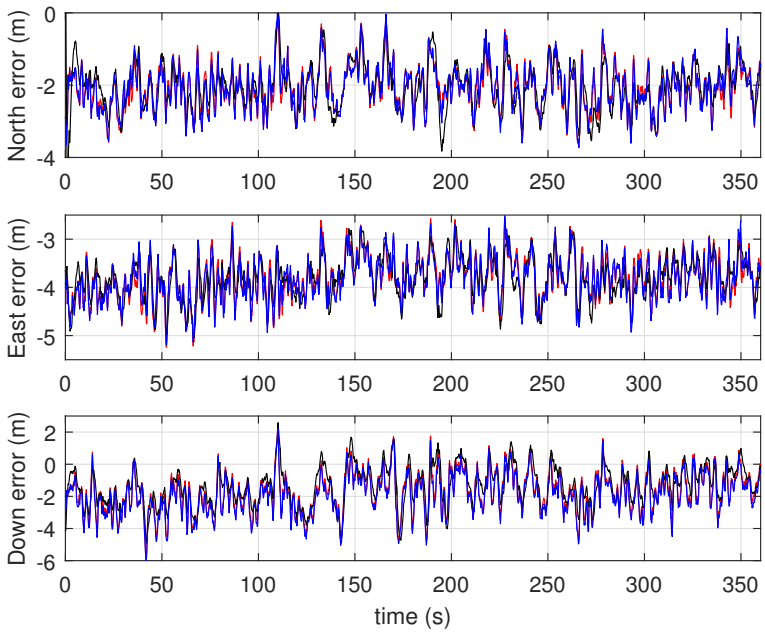

Figure 5.3: Position estimation errors of nonlinear observer (red), nonlinear observer with ARE (black) and MEKF (blue). The RTK solution is used as reference.

navigation on its own, but is confirmed to give a good initial position estimate within a couple of meters of the true position.

5.5.2 Computational load

The computational load of the proposed nonlinear observer is compared to the MEKF by counting the average number of arithmetic operations (additions and multiplications) per second. The number of operations are summarized in Table 5.2 for the three state estimators of interest, where implementation categories have been introduced based on implementation frequency. The computational load of the MEKF is in accordance with the results in [76, Table 3.1], where a KF is investigated, with some differences due to the change in structure. These results show that the NLO and NLO-ARE computational loads are in average 23.6% and 21.6% of the MEKF, respectively.

The reduction in computational complexity for attitude estimation is primarily related to the use of fixed gains and the exclusion of covariance estimation in the NLO and NLO-ARE. This can for some applications present a trade-off as the covariance estimates can be of importance.

For the TMO, the main difference in computational complexity is related to the use of slowly time-varying gains in the nonlinear attitude observer. In addition, the TMO's multi-rate implementation of the gain computations and Riccati-equation solutions allows some computations to be saved. The MEKF gain estimation runs at GNSS frequency, i.e. $5Hz$. On the other hand, the two versions of the nonlinear

Table 5.2: Numerical comparison of computational complexity. The values are average number of arithmetic operations per second.

	MEKF		**NLO**		**NLO-ARE**	
	Mult.	Add.	Mult.	Add.	Mult.	Add.
Attitude observer prediction (410 Hz)	82000	102500	8200	4920	8200	4920
Attitude observer correction (410 Hz)	81180	77080	54940	41000	54940	41000
Attitude observer gain computation (410 Hz)	147600	137760	–	–	–	–
TMO prediction (5 Hz)	10845	10280	10845	10280	10845	10280
TMO correction (5 Hz)	7750	7275	7750	7275	7750	7275
TMO gain computation (5 Hz)	4250	4875	4250	4875	–	–
TMO gain computation (0.003 Hz)	–	–	–	–	3	3
Total	333625	339770	85985	68350	81738	63478

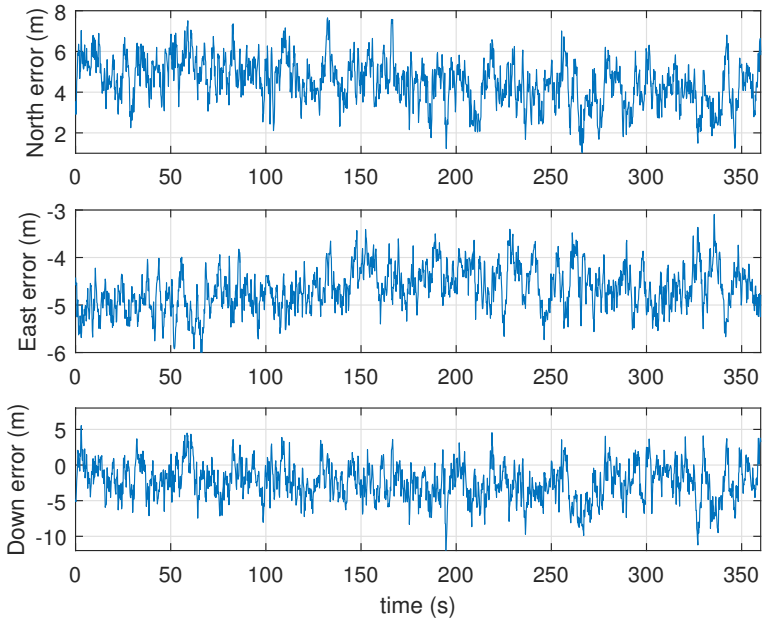

Figure 5.4: Position estimation errors of algebraic range and pseudorange solution. The RTK solution is used as reference.

observer updates the gains either by solving the Riccati equation at $5Hz$ (NLO) or an algebraic Riccati equation at $0.003Hz$ (NLO-ARE). The differences in estimation accuracy documented in Section 5.5.1 indicates that no significant loss of estimation accuracy results from updating the Riccati equation at $0.003Hz$ versus $5Hz$.

The TMO correction and TMO gain computation depend on the number of satellites in the constellation. In Table 5.2 a constellation consisting of five satellites is considered. The dependence on the number of satellites is shown in Fig. 5.6, where the computational load of the nonlinear observers compared to the MEKF are depicted as functions of the satellites in the constellation. The dashed vertical line indicates the situation depicted by Table 5.2.

The comparative computational load of the nonlinear observers in comparison to the MEKF is shown for 4 to 12 satellites. It is uncommon to have more than 12 satellites in the available constellation, due to signal path obstruction. The computational load of the nonlinear observer with TMO gains updated at GNSS receiver frequency is seen to approach the load of the MEKF with increasing numbers of satellites, whereas the NLO-ARE solution decreases slightly compared to the MEKF with more satellites. In the considered range of constellation size the nonlinear observers are always less than 32% of the computational load of the MEKF and is therefore considered significantly more efficient.

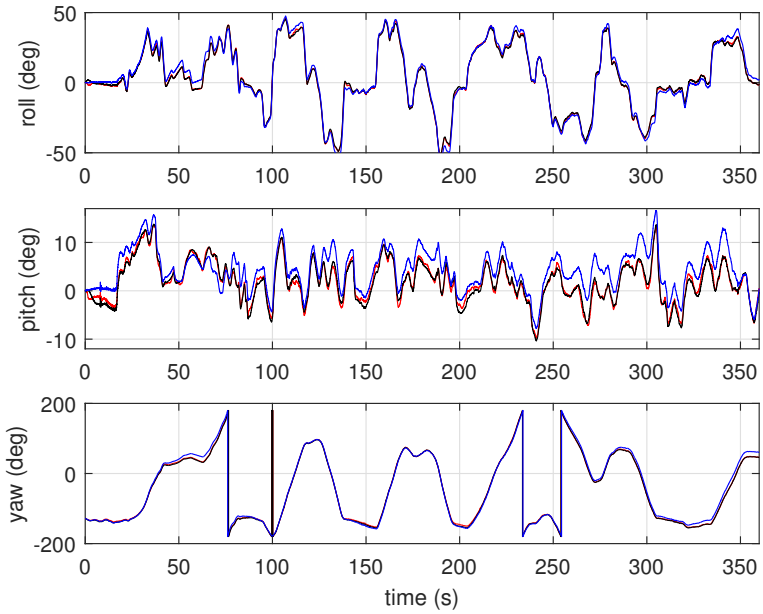

Figure 5.5: Estimated attitude of nonlinear observer (red), nonlinar observer with ARE (black) and MEKF (blue).

5.5.3 Performance of loosely- and tightly-coupled observers

The performance of the proposed tightly-coupled observer is compared to the loosely-coupled observer introduced in Section 3.4, using the experimental data described above. The RTK position is used as reference for comparison of the performance of the loosely- and tightly-coupled observer structures. To guarantee a fair comparison, the standalone GNSS position solution used in the loosely-coupled integration is based on the tightly-coupled observer using solely the pseudoranges as observables. Hence, no IMU is used to generate the aiding position solution for the loosely-coupled observer. The standalone solution will be denoted NLO-SA. The position estimate from the GNSS receiver is not used as unknown tuning or satellite prioritizing could take place.

The observers use the same constant attitude estimator gains: $k_I = 0.004$, $k_1 = 0.25$, and $k_2 = 0.75$. While the tuning parameters for the gain selection are gathered in the Q and R matrices. For the loosely-coupled observer the matrices are: $Q_l = \text{blockdiag}(0_3, 10^{-10} \cdot I_3, 2.5 \cdot 10^{-3} I_3)$, $R_l = 2.5 \cdot I_3$, while the tightly-coupled integration only utilizes the code measurements, leaving the tuning matrices: $Q_t = \text{blockdiag}(Q_l, 1)$ and $R_t = I_m$. For ease of notation the loosely-coupled observer will be denoted NLO-LO, while the tightly-coupled observer will be denoted NLO-TI.

The performance of the observers are compared in Fig. 5.7 and Fig. 5.8 showing the position error and estimated attitude, respectively. The NLO-LO estimates are shown in blue, while the NLO-TI estimates are shown in red with the standalone GNSS solution (used as input to the NLO-LO) is shown in yellow. A larger version

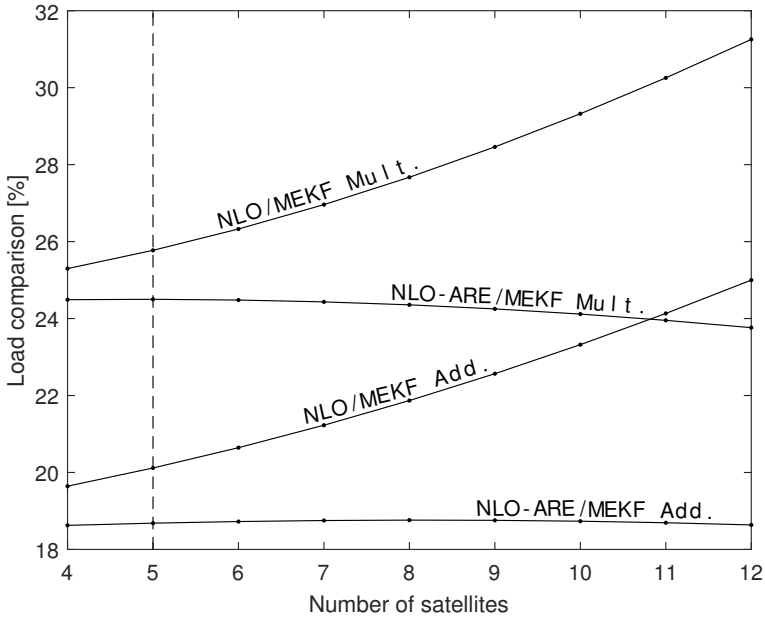

Figure 5.6: Computational load of the nonlinear observers compared to the MEKF.

of Fig. 5.7 is available in the Appendix as Fig. D.5. The position estimation is evaluated in Table 5.3 summarising the RMS and standard deviations of the position errors relative to the RTK solution. The results presented in Fig. 5.7 and Table 5.3 indicate that the tightly-coupled integration using inertial measurements yields more accurate position estimates compared to the loosely-coupled integration or standalone GNSS.

The difference between the standalone GNSS solution and loosely-coupled integration is less evident form Fig. 5.7 and Table 5.1. This is expected as the estimation error is only considered when the RTK solution is available, which is at lower rate than the inertial measurements. The benefit of loosely-coupled integration relative to a standalone solution is however evident from Fig. 5.10, where the relative position error for a small interval of the flight during a turn is shown. The position error shown here is relative to the RTK solution but at IMU rate, where it becomes evident that the loosely-coupled solution is more smooth estimate, as inertial data is available between GNSS samples, compared to the standalone solution. The loosely-couple solution is therefore better suited, than the standalone solution, to be used in an autopilot that operate at high sampling rate. Moreover, one large benefit of loosely-coupled GNSS/INS, relative to a standalone GNSS solution, is that the attitude estimates also are obtained with high accuracy.

The gyro bias estimation is shown in Fig. 5.9 with the NLO-LO estimates in dashed lines and the NLO-TI estimates in solid lines. The attitude and gyro bias estimation of the observers are seen to be mostly similar, which was expected as the attitude estimators used were identical and only the feedback of the specific force were observer specific.

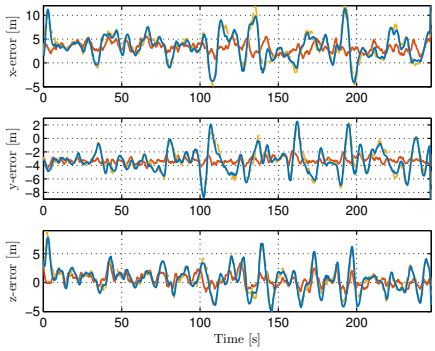

Figure 5.7: Position estimation error for NLO-LO (blue), NLO-TI (red), and NLO-SA (yellow).

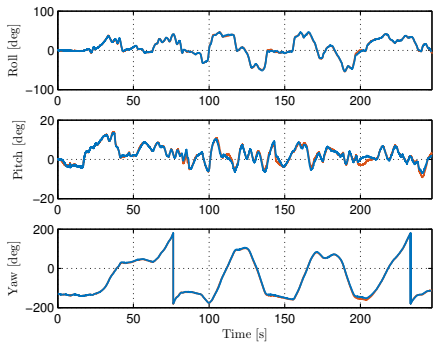

Figure 5.8: Attitude estimation for NLO-LO (blue) and NLO-TI (red). NLO-SA not available.

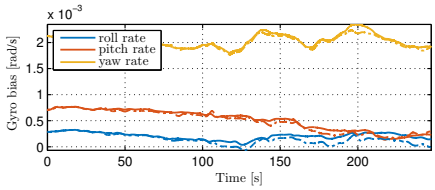

Figure 5.9: Gyro bias estimation for NLO-LO (dashed) and NLO-TI (solid).

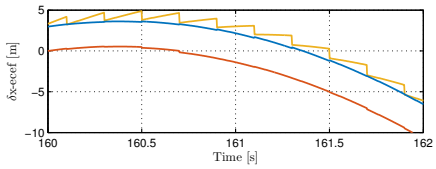

Figure 5.10: Relative x position error for NLO-LO (blue), NLO-TI (red), and NLO-SA (yellow).

Table 5.3: Navigation performance comparison, units: m.

	RMSE (x^n, y^n, z^n)			STD (x^n, y^n, z^n)		
NLO-TI	3.412	3.341	1.106	1.067	0.561	1.005
NLO-SA	4.541	3.732	2.184	2.951	1.756	2.065
NLO-LO	4.442	3.818	2.264	2.836	1.868	2.177

Since the pseudoranges are directly integrated with the inertial measurements in the NLO-TI, instead of calculating the GNSS position before using this as aid in loosely-coupled integration, more of the colored noise, embedded in the GNSS pseudoranges, is captured by the receiver's clock bias estimate. This is possible since the acceleration measurements are available between GNSS samples. Hence, every new position and clock error calculation, made by the observer, is based on the current predicted position between GNSS samples using inertial data rather than using a 0.2 to 1 second old estimate obtained at the previous GNSS update. If differential GNSS is utilized, more accurate position estimates can be obtained for tightly-coupled observers.

5.6 Chapter Summary

Position estimation based on pseudorange and range-rate measurements is an inherently nonlinear problem. In order to design an estimator for fusing the pseudorange and range-rate measurements with inertial and compass measurements, a nonlinear observer have been designed where the only linearization is made with respect to the pseudorange and range-rate measurement equations. The resulting observer is semiglobally exponentially stable with respect to attitude and gyro bias initialization errors, and locally exponentially stable with respect to position, velocity and acceleration initialization errors. The practical validity of the linearization is strongly motivated by the fact that a computationally simple analytic formula can be used to explicitly solve the pseudorange equations in order to accurately initialize (or reset, if necessary) the nonlinear observer position and velocity estimates. Experimental results show that the accuracy can be comparable to an MEKF.

A key feature of the method is a time-scale separation that allows different observer blocks to be updated at different rates:

1. Instantaneous resetting of position and velocity estimates using an algebraic solution to the pseudorange equations during initialization or change of transponder configuration. This approach justifies that only a local region of attraction may be required for the position and velocity estimates due to the good initialization accuracy.
2. Attitude estimation using a Riccati-free fixed-gain nonlinear observer, including gyro bias, on a fast time-scale driven by the sampling rate of the IMU and magnetometer.
3. Estimation of position, velocity, acceleration and error parameters for the pseudorange measurement system, using a nonlinear translational model observer with time-varying gains operating on a slower time-scale driven by the sampling rate of the range and range-rate sensors.
4. Computation of slowly time-varying gain matrices for the translational motion observer using a Riccati equation. These computations are made on the slowest time-scale driven by the change in relative position between the vehicle and the transponders, and for many applications it may be implemented by solving an algebraic Riccati equation periodically at low rate.

The time-scale separation can be directly exploited for computational efficiency in a multi-rate discrete-time implementation.

Chapter 6

INS/RTK-GNSS Integration

The atmospheric disturbances on the satellite pseudorange and carrier-phase measurements can have a large impact on the position accuracy. Utilizing a differential processing with two GNSS receiver these disturbances can largely be removed by differencing the measurements between a moving receiver and a base station. If the base station transmits the obtained satellite measurements to the rover for processing a real-time-kinematic (RTK) solution can be formed, where high accuracy can be achieved by resolving the phase ambiguities.

This chapter offers a modular observer structure for estimating the position, velocity and attitude of a moving vehicle, often called rover, while further estimating the position of a stationary base station. The observer structure is based on results by [119] and [94]. If the satellite measurements are double-differenced between the rover and base station the phase ambiguities can be resolved.

Contributions of this Chapter: This chapter presents a modular nonlinear observer for tight integration of inertial measurements aided by double-differenced satellite measurements. A real-time-kinematic approach is utilized where a rover and base station measures pseudo-ranges, carrier-phase, and Doppler, to be used in a dual receiver configuration. The modular observer design consists of a nonlinear attitude observer and a translational motion observer. The attitude observer represents the vehicle attitude as unit quaternions and estimates the gyro bias. A translational motion observer based on the double-differenced measurements between the rover and base station receiver is proposed. The ambiguities introduced by the carrier-phase measurements are included in the state vector and are initially considered real valued, to be later resolved to integer value. The proposed observer is verified using experimental data from flights with an unmanned aerial vehicle equipped with low-cost sensors, where the position estimates are shown to be within 2-4 centimetres of a GPS L_1 based real-time-kinematic reference solution.

Organization of this Chapter: This chapter is organized as follows. The problem is formally stated in Section 6.1 introducing the aiding measurements. In Section 6.2 the noise levels of the double-differenced satellite signals are investigated for use in later tuning. The observer structure is introduced in Section 6.3 with the translational motion observer presented in Section 6.4

which also presents gain selection and ambiguity resolution. An option for augmentation of the measurement suite is discussed in Section 6.5. Experimental results are presented in Section 6.6 using flight data with a fixed-wing UAV. The chapter is summarised in Section 6.7.

Publications: The material in this chapter is based on the conference papers Hansen et al. 2016 [84] and Gryte et al. 2017 [77], and the journal paper Hansen et al. 2017 [87].

6.1 Problem Formulation

A dual receiver configuration consisting of a moving rover and a stationary base station, each equipped with a GNSS receiver, is considered. The base station measures pseudorange, carrier phase and carrier phase derived Doppler and transmits these to the rover for processing, followed by position and velocity estimation. The rover will in addition be equipped with inertial sensors providing specific force and angular rate measurements.

The objective is to estimate position, linear velocity and attitude (PVA) of a moving vehicle by tightly-coupled integration of the mentioned measurements. Estimation of the rover PVA as well as the baseline, i.e. the vector (displacement) between rover and base station, are of interest.

The kinematic strapdown equations of the rover are given as (2.7)–(2.9) where the notation is altered to distinguish between rover and base station:

$$\dot{p}_r^e = v_r^e, \tag{6.1}$$

$$\dot{v}_r^e = -2S(\omega_{ie}^e)v_r^e + f^e + g^e(p_r^e), \tag{6.2}$$

$$\dot{q}_b^e = \frac{1}{2}q_b^e \otimes \bar{\omega}_{ib}^b - \frac{1}{2}\bar{\omega}_{ie}^e \otimes q_b^e, \tag{6.3}$$

where the position, linear velocity and attitude of the rover are described by p_r^e, v_r^e and q_b^e, respectively. The Earth rotation rate in ECEF with respect to ECI decomposed in the ECEF frame is denoted ω_{ie}^e, and is a known constant. The rotation rate ω_{ib}^b describes the Body rotation rate with respect to the ECI frame. The specific force is given by f^e while $g^e(p_r^e)$ specify the position dependent plumb-bob gravity vector.

Assumption 29. The base station is assumed to be stationary; $\dot{p}_s^e = 0$.

6.1.1 Measurement Assumptions

The following measurements are assumed available:

Assumption 30. Specific force measurements $f_{\text{IMU}}^b = f^b$ are available for the rover.

Assumption 31. Biased rotation rate from an IMU, $\omega_{ib,\text{IMU}}^b = \omega_{ib}^b + b^b$ is measured at the rover.

Assumption 32. The gyro bias, $b^b \in \mathbb{R}^3$ is assumed to be slowly time-varying, $\dot{b}^b = 0$, satisfying $\|b^b\|_2 \leq M_b$ for a known bound M_b.

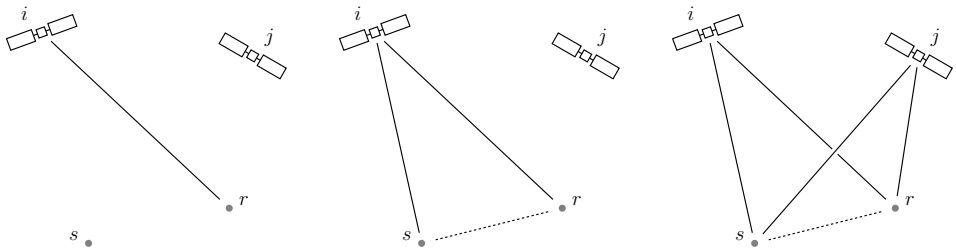

(a) Undifferenced (b) Single-differenced (c) Double-differenced

Figure 6.1: GNSS measurements for non-, single- and double-differenced configurations.

Assumption 33. A magnetometer measures the magnetic field vector at the rover, $m^b_{\text{MAG}} = m^b$, while the position dependent Earth magnetic field m^e in ECEF is assumed known.

Assumption 34. The rover and base station are assumed to be equipped with GNSS-receivers measuring; pseudo-range, carrier-phase and Doppler, from at least five common satellites, $m \geq 4$.

Assumption 35. The satellite positions and velocities are assumed known, which can be satisfied by determination using the broadcast ephemeris data.

The pseudorange and carrier phase measurements at a location p^e transmitted by the ith satellite, see Fig. 6.1a, can be generalized as:

$$\rho_i = \psi_i + \beta + \gamma_i + \varepsilon_\rho + n_{\rho,i}, \tag{6.4}$$

$$\lambda\varphi_i = \psi_i + \lambda N_i + \beta + \gamma_i + \varepsilon_\varphi + n_{\varphi,i}, \tag{6.5}$$

where the pseudo-range and carrier-phase measurements from the ith satellite are denoted ρ_i and φ_i, for $i = 1, 2, \ldots, m$. The geometric range between receiver and satellite is denoted $\psi_i := \|p^e - p^e_i\|_2$, where p^e_i is the satellite position. The carrier-phase integer ambiguity is denoted N_i with signal wavelength λ. The parameters ε_ρ and ε_φ denote the combined orbital, ionospheric and tropospheric delays of the satellite measurements. Furthermore, ε_φ includes antenna induced errors. The $n_\star$ parameters cover individual stochastic errors such as measurement noise and multipath effect. The noise terms have been explicitly included for the aiding measurements to ensure that the measurement noise is not considered cancelled in the differences introduced later. The measurement noise of the aiding measurement will change magnitude when differenced which should be taken into account in the tuning of the observer. The noise terms for the inertial measurements will not be explicitly included as they will not undergo operations that will change their characteristics. All noise sources will be systematically considered in the tuning of the observer. The satellite clock error γ_i can be corrected by applying the clock correction coefficients from the navigation data message. The receiver clock bias, describing the timing difference between receiver and system time, affects all coinciding range measurements similarly, [52, Section 8.4.3]. In the following the clock

range bias is treated as a common mode bias, $\beta \in \mathbb{R}$, and is assumed to be slowly time-varying.

The bias is expressed as $\beta = c\Delta_{r,i}$ with $\Delta_{r,i}$ being the receiver clock bias and c being the speed of light. Similarly, the satellite clock error can be expressed as $\gamma_i = c\Delta_{s,i}$ with $\Delta_{s,i}$ being the bias of the ith satellite clock.

Due to large measurement noise, the raw Doppler measurements are usually not included as aiding information. The measurements can either be filtered, which has the drawback of reducing the sample frequency, removing high frequency motion and introduce phase lag, or a substitute can be determined as the time derivative of the carrier-phase measurements. In [155] the carrier phase derived Doppler is obtained by use of a finite impulse response filter, resulting in accurate velocity measurements for a standalone GPS receiver. In the following the time derivative of the carrier-phase will be considered, [128]:

$$\lambda\dot{\varphi}_i = \dot{\psi}_i + \dot{\beta} + \dot{\gamma}_i + \dot{n}_{\varphi,i}, \tag{6.6}$$

where the ambiguity and multipath terms have been eliminated due to the short time horizon of the derivative. Furthermore, by assuming constant atmospheric delays over the time interval between consecutive phase measurements these can also be eliminated, where any residual delays will be absorbed by the noise term, [128].

A generalized model for the time derivative of the phase measurement can be expressed as:

$$\lambda\upsilon_i = h_i^{\intercal}\left(v^e - v_i^e\right) + \dot{\beta} + \dot{\gamma}_i + n_{\upsilon,i}, \tag{6.7}$$

where the satellite velocity is denoted v_i^e, and the line-of-sight vector is; $h_i = (p^e - p_i^e)/\psi_i$. The constructed carrier phase derived Doppler measurement is denoted υ_i, while $n_{\upsilon,i}$ describes the stochastic errors.

Remark 6.1. The carrier-phase measurements, φ, are given in units of cycles, and can be converted to meters by multiplication with the wavelength. The carrier-phase-derived Doppler measurements, υ, are given in Hertz and can be converted to a velocity described in meters per second by multiplication with the wavelength.

There will be distinguished between satellite measurements and their components at rover and base station by use of the superscripts r and s, respectively. These superscripts are not to be confused with the coordinate frame as the satellite measurements will always be given in the ECEF-frame.

Assumption 36. It is assumed that the rover is sufficiently close to the base station that the ionospheric and tropospheric delays are spatially correlated between the two receivers and will therefore cancel, i.e. $\varepsilon_\rho^r = \varepsilon_\rho^s$, $\varepsilon_\varphi^r = \varepsilon_\varphi^s$, $\varepsilon_\upsilon^r = \varepsilon_\upsilon^s$.

Remark 6.2. While it is possible to obtain centimetre accuracy of the position estimates with baseline of 20 km for resolved ambiguities, see [52, Section 10.2], maintaining high accuracy requires shorter baselines. Short baselines, less than 10 km, are preferred to reduce cycle-slips, while for longer baselines the accuracy degrades due to decorrelation of the atmospheric propagation errors. This can be mitigated by use of dual-frequency GNSS measurements and modelling of the troposphere.

The atmospheric disturbances can therefore be corrected for by differencing measurements at rover position with measurements at the base station. The GNSS measurement configuration is depicted in Fig. 6.1b showing two satellites, i and j, and two receivers, r and b, where the baseline is shown as a dashed line. It is vital when differencing measurements that the they are acquired at the same time epoch.

The single-differenced (SD) measurements between rover and base station are given as:

$$\Delta\rho_i = \Delta\psi_i + \Delta\beta + n_{\Delta\rho,i}, \tag{6.8}$$

$$\lambda\Delta\varphi_i = \Delta\psi_i + \Delta N_i\lambda + \Delta\beta + n_{\Delta\varphi,i}, \tag{6.9}$$

$$\lambda\Delta\upsilon_i = h_i^{r\intercal}\left(v_r^e - v_i^e\right) + h_i^{s\intercal} v_i^e + n_{\Delta\upsilon,i}, \tag{6.10}$$

where $\Delta\rho_i := \rho_i^r - \rho_i^s$, $\Delta\varphi_i := \varphi_i^r - \varphi_i^s$, $\Delta\upsilon_i := \upsilon_i^r - \upsilon_i^s$, $\Delta N_i := N_i^r - N_i^s$, $\Delta\beta := \beta^r - \beta^s$, and $\Delta\psi_i := \psi_i^r - \psi_i^s$ is the geometric baseline between rover and base station. The differenced noise terms are given as; $n_{\Delta\rho,i} := n_{\rho,i}^r - n_{\rho,i}^s$, $n_{\Delta\varphi,i} := n_{\varphi,i}^r - n_{\varphi,i}^s$, and $n_{\Delta\upsilon,i} := n_{\upsilon,i}^r - n_{\upsilon,i}^s$. The normalised line-of-sight vectors h_i^r and h_i^s, between the ith satellite and rover and base station are given as:

$$h_i^r = \frac{p_r^e - p_i^e}{\|p_r^e - p_i^e\|_2}, \qquad h_i^s = \frac{p_s^e - p_i^e}{\|p_s^e - p_i^e\|_2}. \tag{6.11}$$

From (6.8) and (6.9) it is evident that $\Delta\beta$ is the same for all satellites so it can be cancelled by further differencing the measurements this time between satellites. This is typically achieved by selecting the satellite with highest elevation as reference. The double-differenced (DD) measurement principle is depicted in Fig. 6.1c while the measurement model is given as:

$$\nabla\Delta\rho_{ij} = \nabla\Delta\psi_{ij} + n_{\nabla\Delta\rho,ij}, \tag{6.12}$$

$$\lambda\nabla\Delta\varphi_{ij} = \nabla\Delta\psi_{ij} + \nabla\Delta N_{ij}\lambda + n_{\nabla\Delta\varphi,ij}, \tag{6.13}$$

$$\lambda\nabla\Delta\upsilon_{ij} = h_j^{r\intercal}\left(v_r^e - v_j^e\right) - h_i^{r\intercal}\left(v_r^e - v_i^e\right) + h_j^{s\intercal} v_j^e - h_i^{s\intercal} v_i^e + n_{\nabla\Delta\upsilon,ij} \tag{6.14}$$

where $\nabla\Delta\rho_{ij} := \Delta\rho_j - \Delta\rho_i$, $\nabla\Delta\varphi_{ij} := \Delta\varphi_j - \Delta\varphi_i$, $\nabla\Delta\upsilon_{ij} := \Delta\upsilon_j - \Delta\upsilon_i$, $\nabla\Delta\psi_{ij} := \Delta\psi_j - \Delta\psi_i$, and $\nabla\Delta N_{ij} := \Delta N_j - \Delta N_i$ with the jth satellite representing the reference satellite. The measurement noise is; $n_{\nabla\Delta\rho,ij} := n_{\Delta\rho,j} - n_{\Delta\rho,i}$, $n_{\nabla\Delta\varphi,ij} := n_{\Delta\varphi,j} - n_{\Delta\varphi,i}$ and $n_{\nabla\Delta\upsilon,ij} := n_{\Delta\upsilon,j} - n_{\Delta\upsilon,i}$.

Due to measurement differencing between satellites, the number of available observations will be $m-1$, with m is the number of tracked satellites. The double-differenced measurements will be used in injection terms of the proposed observer structure. The single-differenced measurements are not utilized in the observer structure due to the presence of the receiver clock bias.

When differencing GNSS measurements a rule of thumb is that the stochastic error will increase in standard deviation by $\sqrt{2}$, while the systematic errors will decrease, see [138].

6.2 Noise Analysis

A common assumption of the Extended Kalman filter is that the measurement and process noise are Gaussian. The nonlinear observer structure proposed here

does not make any specific assumptions on the distribution of GNSS measurement noise in; (6.4)–(6.7), (6.8)–(6.10) and (6.12)–(6.14), or the inertial measurement noise introduced with the specific force, angular rate and magnetometer measurements. However, when tuning the observer gains it is advantageous to have the knowledge of the noise levels and types. It is therefore desired to investigate the noise distribution and determine the standard deviation of the undifferenced (UD) and double-differenced GNSS measurement noise. The noise type is the same for all types and brands of receivers, whereas the standard deviations are receiver and antenna specific. For the inertial measurement noise industrial data sheets offer accurate noise characteristics and the state space can be augmented to include non-Gaussian inertial measurement noise. The following section will therefore only consider the GNSS measurement noise.

Experimental data was collected at 1 Hz, by two identical u-Blox LEA-6T receivers with a baseline of 1 m. The experiment was carried out at latitude 63.4° and longitude 10.5°, Norway, on a rooftop. Some multipath effect is experienced which affect the undifferenced measurements, while it can be mostly mitigated for the double-differenced measurements due to the short baseline. The positions of the receivers were determined by averaging over an 24 hour long data set. Some satellites were occasionally obstructed and the noise levels of the GNSS measurements are therefore found during a time interval with multiple common satellites visible by both receivers. The satellites are commonly visible for $3-6$ hours during good open sky conditions.

In the case of the undifferenced measurements the raw pseudorange, carrier-phase and carrier phase derived Doppler measurements are corrected for: time of transmission (the satellite moves during the signal transmission time), atmospheric disturbances, and receiver clock bias (estimated using a Kalman filter). Furthermore, the geometric range from satellite to receiver ψ_i^r and ψ_i^s are computed. The tropospheric delay can be modelled using e.g. [64], whereas the ionospheric delay might be modelled using the Klobuchar model. For the UD noise terms some residual errors will be present due to the imperfection of the applied models. Furthermore, uncertainty of the estimated receiver clock and multipath effects remain.

For the double-differenced measurements the noise terms are found by isolation of $n_\star$ in (6.12)–(6.14). Given the short baseline (1 meter), the ionospheric and tropospheric delays are considered to be completely removed, whereas the residual atmospheric effects are negligible such that the noise term only consists of receiver noise and multipath.

The noise estimates of the DD measurements are shown in Fig. 6.2a–6.2c, with 6 available satellites; resulting in 5 DD measurements. The noise estimates have been de-trended to remove first order dependencies and initial offset, which is common practice e.g. when determining scintillation effects, see [134] or [133]. The colors indicate measurements from different satellites. The average standard deviations of the estimated measurement noise are presented in Table 6.1, with the noise of the UD measurements for comparison. The standard deviations corresponds well with the results found in [76, Section 9.4.2.4] for an update rate of 1 Hz. Moreover, according to [76, Section 9.4.2.4] the standard deviations might be increased with higher receiver sampling rates.

To obtain a large time window for noise analysis some of the satellites have low

elevation at the edges of the time window, this results in an increase in standard deviation, as seen in e.g. the yellow and red graphs in Fig 6.2c around $9000-10000$ seconds. Nevertheless these satellites have been included, to estimate an average standard deviation of the noise terms under various conditions. Similar effects can be seen in [20] where a filter for separation of the multipath components is proposed, while also locating reflecting objects. Short and long baselines are considered in [42] and [43], where undifferenced, single- and double-differenced GNSS signals from several constellations are analysed.

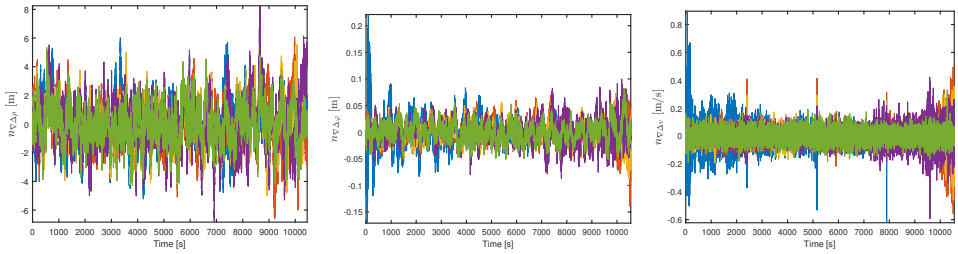

(a) Double-differenced pseudo-ranges (b) Double-differenced Carrier-phase (c) Double-differenced derived Doppler

Figure 6.2: Noise analysis of double-differenced GNSS measurements, over a 3 hours period, with a baseline of 1 m.

Table 6.1: Standard deviations of GNSS measurements.

	UD	DD
Pseudorange, ρ, $[m]$	1.560	1.597
Carrier-phase, φ, $[m]$	0.207	0.020
Derived Doppler, υ, $[m/s]$	0.682	0.055

The double-differenced pseudorange and carrier phase derived Doppler measurements appear almost white, whereas the carrier phase measurements include non-white behaviour. There are two common practices for handling this in observer structures: a) augment the observer to model states for the non-white noise processes, or b) assume a white distribution with larger standard deviation than the actual distribution to over-bound the measurement noise. The over-bounding method was proposed in [46], and used e.g. in [41] where multipath, receiver noise and atmospheric delays were investigated for pseudoranges in a single-differenced configuration. In general the code and phase noise can be represented by over-bounding white noise, even though a Gauss Markov process is a more suitable model it too should use slightly inflated noise characteristics. Additionally, the distributions cannot be expected to be stationary as several factors can cause changes on the fly such as: multipath (especially at the rover), elevation angle, rover dynamics and C/N_0 levels. In conclusion; it might be advantageous to use higher values for the standard deviations when used for observer tuning to accommodate for imperfect Gaussian white noise behaviour.

6.3 Observer Structure

In the following sections a nonlinear observer is proposed based on double-differenced GPS L_1 measurements. A modular observer structure consisting of a nonlinear attitude estimator and a translational motion observer (TMO) is considered. The framework is the same as presented in [101] and [84] although a different TMO is used: here the dual receiver configuration is used leading to differenced measurements, whereas in [101] a single receiver was used to obtain a tightly-coupled navigation solution.

The observer structure can be seen in Fig. 6.3 consisting of; two GNSS receivers, IMU, magnetometer (MAG), nonlinear attitude observer, a TMO, and a Riccati solver with a gain estimator. Two feedback loops are present in the structure; the feedback of $\hat{f}^e$ from the TMO to the attitude observer, and a feedback of the estimated rover position and velocity to the computation of gain matrices.

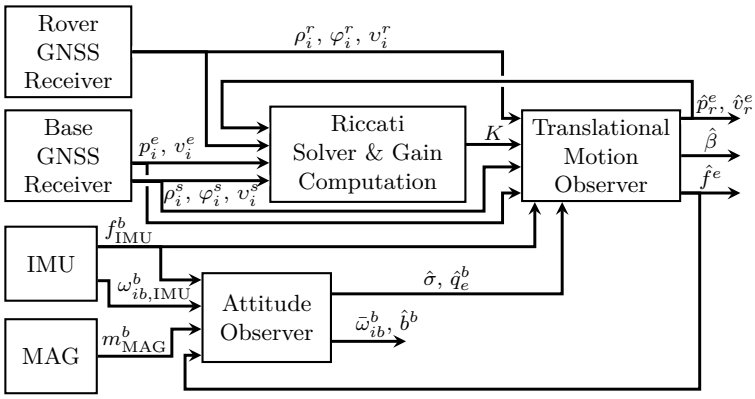

Figure 6.3: Block diagram of observer structure.

The GNSS measurements (ρ_i^r, φ_i^r, v_i^r, ρ_i^s, φ_i^s, and v_i^s) are measured by the receivers in the ECEF frame, while the satellite positions and velocities (p_i^e and v_i^e) are computed from the ephemeris data, see Appendix A. These computations are included in the "Base GNSS Receiver" block for convenience.

Remark 6.3. The carrier phase derived Doppler measurement is based on the carrier-phase change, and expresses the change in geometric distance and clock drift over a time interval, see [52, Section C.4.2]. The carrier phase derived Doppler measurement therefore needs to be compensated for satellite motions during the time interval when compared to v_i^e. Several options are available for estimating the average satellite velocity of the interval. Here v_i^e will express the satellite velocity averaged over the beginning and end of the relevant GNSS receiver sample interval.

The "Riccati Solver & Gain Estimator" block considers the choice of gain matrix K for the TMO. In order to compute the injection terms the estimated position and velocity of the rover and base station is fed back from the TMO.

When considering the stability of the observer structure it is advantageous to examine the individual parts of the modular structure. The nonlinear attitude observer

was proven to be semi-globally exponentially stable (SGES) with respect to attitude initialization in [72]. Following the results of [101], the equilibrium point of the double-differenced observer proposed in Section 6.4, is exponentially stable. The complete observer structure will be exponentially stable with a semi-global region of attraction with respect to attitude initialization due to the feedback interconnection and the SGES properties of the attitude estimator. The observer position and velocity estimates can be accurately initialized with the procedure proposed in [101].

The nonlinear attitude observer is identical to the one introduced in Section 5.3.1, while the TMO will be introduced utilizing the double-differenced receiver configuration in Section 6.4.

6.4 Double-Differenced Nonlinear Observer

Denoting the ith satellite as the reference satellite, the double-differenced measurement errors can be used as injection terms in the proposed translational motion observer:

$$\dot{\hat{p}}_r^e = \hat{v}_r^e + \sum_{j=1}^{m-1} \left(K_j^{p\rho} e_{\rho,ij} + K_j^{p\varphi} e_{\varphi,ij} + K_j^{pv} e_{v,ij} \right), \tag{6.15}$$

$$\begin{aligned} \dot{\hat{v}}_r^e = &-2S(\omega_{ie}^e)\hat{v}_r^e + \hat{f}^e + g^e(\hat{p}_r^e) \\ &+ \sum_{j=1}^{m-1} \left(K_j^{v\rho} e_{\rho,ij} + K_j^{v\varphi} e_{\varphi,ij} + K_j^{vv} e_{v,ij} \right), \end{aligned} \tag{6.16}$$

$$\dot{\xi} = -R(\hat{q}_b^e)S(\hat{\sigma})f_{\text{IMU}}^b + \sum_{j=1}^{m-1} \left(K_j^{\xi\rho} e_{\rho,ij} + K_j^{\xi\varphi} e_{\varphi,ij} + K_j^{\xi v} e_{v,ij} \right), \tag{6.17}$$

$$\hat{f}^e = R(\hat{q}_b^e)f_{\text{IMU}}^b + \xi, \tag{6.18}$$

$$\dot{\hat{p}}_s^e = \sum_{j=1}^{m-1} \left(K_j^{s\rho} e_{\rho,ij} + K_j^{s\varphi} e_{\varphi,ij} + K_j^{sv} e_{v,ij} \right), \tag{6.19}$$

$$\nabla\Delta\dot{\hat{N}} = \sum_{j=1}^{m-1} \left(K_j^{Np} e_{\rho,ij} + K_j^{N\varphi} e_{\phi,ij} + K_j^{Nv} e_{v,ij} \right). \tag{6.20}$$

The gains to be determined, $K_i^{\star\star}$, are considered slowly time-varying. The advantage of using double-differenced measurements is that the receiver clock bias is cancelled and can therefore be excluded from estimation, while in single receiver configurations it is included in the state vector, see e.g. [98]. The double-differenced phase ambiguities, $\nabla\Delta\hat{N}$, are represented as a vector with $m-1$ elements described as the difference between the single-differenced ambiguities of the ith and jth satellite, i.e. $\nabla\Delta\hat{N} = \left[\Delta\hat{N}_1 - \Delta\hat{N}_i; \Delta\hat{N}_2 - \Delta\hat{N}_i; \ldots; \Delta\hat{N}_j - \Delta\hat{N}_i\right]$. The ambiguity estimates are propagated by the translational motion observer as real valued estimates and can after some convergence be fixed to integer value, which will be discussed in detail in Section 6.4.2.

It is desired to include the base station position in the observer estimation, such that the observer does not rely on access to a pre-surveyed position, but can be initialized with a more inaccurate estimate of the base station position.

The structure of the TMO is similar to [84] with additional injection terms based on the carrier phase derived Doppler measurements. The injection terms are the difference between measured and estimated double-differenced satellite signals: $e_{\rho,ij} := \nabla\Delta\rho_{ij} - \nabla\Delta\hat{\rho}_{ij}$, $e_{\varphi,ij} := \lambda(\nabla\Delta\varphi_{ij} - \nabla\Delta\hat{\varphi}_{ij})$ and $e_{\upsilon,ij} := \lambda(\nabla\Delta\upsilon_{ij} - \nabla\Delta\hat{\upsilon}_{ij})$, where the estimated terms are:

$$\nabla\Delta\hat{\rho}_{ij} = \nabla\Delta\hat{\psi}_{ij}, \tag{6.21}$$

$$\lambda\nabla\Delta\hat{\varphi}_{ij} = \nabla\Delta\hat{\psi}_{ij} - \nabla\Delta\hat{N}_{ij}\lambda, \tag{6.22}$$

$$\lambda\nabla\Delta\hat{\upsilon}_{ij} = \hat{h}_j^{r\intercal}\left(\hat{v}_r^e - v_j^e\right) - \hat{h}_i^{r\intercal}\left(\hat{v}_r^e - v_i^e\right) + \hat{h}_j^{s\intercal} v_j^e - \hat{h}_i^{s\intercal} v_i^e, \tag{6.23}$$

and the estimated double-differenced geometric baseline is:

$$\nabla\Delta\hat{\psi}_{ij} = \|\hat{p}_r^e - p_j^e\|_2 - \|\hat{p}_r^e - p_i^e\|_2 - \|\hat{p}_s^e - p_j^e\|_2 + \|\hat{p}_s^e - p_i^e\|_2, \tag{6.24}$$

and the estimated line-of-sight vectors are:

$$\hat{h}_i^r = \frac{\hat{p}_r^e - p_i^e}{\|\hat{p}_r^e - p_i^e\|_2}, \qquad \hat{h}_i^s = \frac{\hat{p}_s^e - p_i^e}{\|\hat{p}_s^e - p_i^e\|_2}. \tag{6.25}$$

Investigating the observer stability, the error states are introduced as $\tilde{p}_r := p_r^e - \hat{p}_r^e$, $\tilde{v}_r := v_r^e - \hat{v}_r^e$, $\tilde{f} := f^e - \hat{f}^e$, $\tilde{p}_s := p_s^e - \hat{p}_s^e$, and $\nabla\Delta\tilde{N} := \nabla\Delta N - \nabla\Delta\hat{N}$, and the state vector of the error dynamics is defined as; $x = [\tilde{p}_r; \tilde{v}_r; \tilde{f}; \tilde{p}_s; \nabla\Delta\tilde{N}]$. Here a combination of (6.17) and (6.18) is used to substitute the state ξ with $\hat{f}^e$, as done in [98].

In order to determine the gains, $K_i^{\star\star}$, the injection terms are linearised with respect to the observer states, see Section 6.7:

$$e_{\rho,ij} = C_{\rho,ij}\tilde{x} + \eta_{\rho,ij}, \tag{6.26}$$

$$e_{\varphi,ij} = C_{\varphi,ij}\tilde{x} + \eta_{\varphi,ij}, \tag{6.27}$$

$$e_{\upsilon,ij} = C_{\upsilon,ij}\tilde{x} + \eta_{\upsilon,ij}, \tag{6.28}$$

where $\eta_{\star,ij}$ consists of measurement noise and higher order nonlinear terms, which can be disregarded in the gain selection under the assumption that the TMO is accurately initialized. The row vectors consists of elements according to: $C_{\rho,ij} = [\hat{h}_{ij}^{r\intercal}, 0, 0, -\hat{h}_{ij}^{s\intercal}, 0]$, $C_{\varphi,ij} = [\hat{h}_{ij}^{r\intercal}, 0, 0, -\hat{h}_{ij}^{s\intercal}, \lambda 1_{i,m-1}]$ and $C_{\upsilon,ij} = [\hat{h}_{v,ij}^{r\intercal}, \hat{h}_{ij}^{r\intercal}, 0, \hat{h}_{ij}^{s\intercal}, 0]$, where $1_{i,m-1}$ is a row of $m-1$ zeros with a 1 as the ith element. The differenced line-of-sight vectors are described by:

$$\hat{h}_{ij}^r = \frac{\hat{p}_r^e - p_j^e}{\|\hat{p}_r^e - p_j^e\|_2} - \frac{\hat{p}_r^e - p_i^e}{\|\hat{p}_r^e - p_i^e\|_2}, \tag{6.29}$$

$$\hat{h}_{ij}^s = \frac{\hat{p}_s^e - p_j^e}{\|\hat{p}_s^e - p_j^e\|_2} - \frac{\hat{p}_s^e - p_i^e}{\|\hat{p}_s^e - p_i^e\|_2}, \tag{6.30}$$

$$\hat{h}_{v,ij}^r = \frac{\hat{v}_r^e - v_j^e}{\|\hat{p}_r^e - p_j^e\|_2} - \frac{\hat{v}_r^e - v_i^e}{\|\hat{p}_r^e - p_i^e\|_2}. \tag{6.31}$$

A time-varying measurement matrix consisting of $3(m-1)$ rows can be defined as; $C := \left[C_{\rho,i1}; \ldots; C_{\rho,i(m-1)}; C_{\varphi,i1}; \ldots; C_{\varphi,i(m-1)}; C_{v,i1}; \ldots; C_{v,i(m-1)}\right]$. The C matrix is slowly time-varying as the relative motion of the satellites with respect to the receivers is small due to the large separation.

The error dynamics can be determined as:

$$\dot{\tilde{x}} = (A - KC)\,\tilde{x} + \theta_1(t, \tilde{x}) + \theta_2(t, \chi) + \theta_3(t, \tilde{x}), \tag{6.32}$$

Here $\tilde{\chi}$ is the combined error variable $\tilde{\chi} := [\tilde{r}; \tilde{b}]$ consisting of the vector part of the quaternion, $\tilde{r} = r - \hat{r}$, and the gyro bias error. The perturbation terms are described as, [72]: $\theta_1(t,x) := [0; -2S(\omega_{ie}^e)x_2 + (g^e(p_r^e) - g^e(p_r^e - x_1)); 0; 0; 0; 0]$, $\theta_2(t, \tilde{\chi}) := [0; 0; \tilde{d}; 0; 0; 0]$, where:

$$\begin{aligned}\tilde{d} = {} & (I - R(\tilde{q})^\intercal) R(q_b^e)(S(\omega_{ib,\mathrm{IMU}}^b) f_{\mathrm{IMU}}^b + \dot{f}^b) \\ & - S(\omega_{ie}^e)(I - R(\tilde{q})^\intercal) R(q_b^e) f_{\mathrm{IMU}}^b - R(\tilde{q})^\intercal R(q_b^e) S(\tilde{b}) f_{\mathrm{IMU}}^b.\end{aligned} \tag{6.33}$$

In [72] it is shown that $\|\theta_2(t, \tilde{\chi})\|_2 \leq \gamma_3 \|\tilde{\chi}\|_2$, for some positive γ_3. As in [84] the last perturbation term is a result of the injection term linearisation; $\theta_3(t,x) := K\eta(t,x)$, where $\eta(t,x) := [\eta_{\rho,1}; \ldots; \eta_{\rho,m}; \eta_{\varphi,1}; \ldots; \eta_{\varphi,m}; \eta_{v,1}; \ldots; \eta_{v,m}]$.

The gain matrices should be chosen such that the nominal linear time-varying closed loop dynamics $(A - KC)$ is stable, see Section 6.4.1, where:

$$A = \begin{bmatrix} 0 & I_3 & 0 & 0 & 0 \\ 0 & 0 & I_3 & 0 & 0 \\ 0 & 0 & 0 & 0 & 0 \\ 0 & 0 & 0 & 0 & 0 \\ 0 & 0 & 0 & 0 & 0 \end{bmatrix}, \tag{6.34}$$

$$K = \begin{bmatrix} K_1^{p\rho} & \ldots & K_{m-1}^{p\rho} & K_1^{p\varphi} & \ldots & K_{m-1}^{p\varphi} & K_1^{pv} & \ldots & K_{m-1}^{pv} \\ K_1^{v\rho} & \ldots & K_{m-1}^{v\rho} & K_1^{v\varphi} & \ldots & K_{m-1}^{v\varphi} & K_1^{vv} & \ldots & K_{m-1}^{vv} \\ K_1^{\xi\rho} & \ldots & K_{m-1}^{\xi\rho} & K_1^{\xi\varphi} & \ldots & K_{m-1}^{\xi\varphi} & K_1^{\xi v} & \ldots & K_{m-1}^{\xi v} \\ K_1^{s\rho} & \ldots & K_{m-1}^{s\rho} & K_1^{s\varphi} & \ldots & K_{m-1}^{s\varphi} & K_1^{sv} & \ldots & K_{m-1}^{sv} \\ K_1^{N\rho} & \ldots & K_{m-1}^{N\rho} & K_1^{N\varphi} & \ldots & K_{m-1}^{N\varphi} & K_1^{Nv} & \ldots & K_{m-1}^{Nv} \end{bmatrix}. \tag{6.35}$$

The observer system (6.15)–(6.20) has a semi-globally exponentially stable region of attraction with respect to attitude initialization errors and local exponential stablility with respect to TMO initialization errors, following the results of [98].

Selection of the reference satellite has great impact on the performance of the observer, as errors in the measurements from the reference satellite are propagated to all double-differenced measurements. The reference satellite is therefore often chosen as the satellite with the highest elevation since propagation and multipath errors will generally be the smallest, [126, Section 7.3.4]. Another advantage of choosing the satellite with the highest elevation is that this satellite is less likely to be obstructed, thereby keeping phase-lock with the receiver. If the chosen reference satellite is obstructed, a new reference has to be selected in order to construct the double-differenced measurements.

6.4.1 Gain Selection

The TMO gains can, like in [72], be chosen to be constant, thereby reducing the computational load of the observer. However, better performance can be achieved by considering the gains as time-varying, see e.g. [31]. Several options for gain selection are available where in the following the Riccati equation will be considered. In general, the method for determining the gain matrices will not affect the observer stability as long as K satisfies the conditions imposed by the TMO stability requirements. The method described here is similar to a Kalman filter where the gain is chosen based on the solution of the discrete time-varying Riccati equation:

$$P_{k|k-1} = \Phi P_{k-1|k-1}\Phi^\intercal + Q, \tag{6.36}$$

$$K_k = P_{k|k-1}C^\intercal \left(CP_{k|k-1}C^\intercal + R\right)^{-1}, \tag{6.37}$$

$$P_{k|k} = \left(I - K_k C\right) P_{k|k-1} \left(I - K_k C\right)^\intercal + K_k R K_k{}^\intercal, \tag{6.38}$$

where k is the discrete incrementing index and $\Phi = e^{AT}$ is the discrete transition matrix, with the sample rate and system order denoted as T and n, respectively. The dynamics of the TMO is the same as for Kalman filters, and the P, R, and Q matrices can therefore be interpreted as covariance matrices. The error covariance matrix, P, has elements corresponding to the state vector, and will therefore vary in size when the number of available satellites changes due to the inclusion of the carrier phase ambiguities. The covariance of the ambiguities, P_N, is found as the lower right $m-1 \times m-1$ sub-matrix of P. The gain selection can be tuned by choosing the measurement, R, and state, Q, covariance matrices, where it is common to consider them as consisting of the elements pertaining to the covariance of the states or measurements, $\sigma^2_\star$, [76, Section 14.4.2]:

$$Q = \text{diag}\left(\sigma^2_{p_r}, \sigma^2_{v_r}, \sigma^2_f, \sigma^2_{p_s}, Q_{\nabla\Delta N}\right), \tag{6.39}$$

$$R = \text{blockdiag}\left(R_{\nabla\Delta\rho}, R_{\nabla\Delta\varphi}, R_{\nabla\Delta v}\right). \tag{6.40}$$

The diagonal elements of the Q matrix correspond to the state vector elements describing the expected level of noise in the state. Similarly for the R matrix, the diagonal elements correspond to variances of the aiding double-differenced satellite measurements. In [76, Section 9.4.2.4] a time-varying R-matrix is proposed where the coefficients are determined based on the satellite elevation and range acceleration. Here the matrices (6.39)–(6.40) are kept constant. Due to the differencing with a reference satellite, $R_{\nabla\Delta\star}$ has correlation elements such that the covariance matrix is not diagonal. The sub-matrices of R are in general given as:

$$R_{\nabla\Delta\star} = \begin{bmatrix} \sigma^2_{\nabla\Delta\star} & \frac{1}{2}\sigma^2_{\nabla\Delta\star} & \cdots & \frac{1}{2}\sigma^2_{\nabla\Delta\star} \\ \frac{1}{2}\sigma^2_{\nabla\Delta\star} & \sigma^2_{\nabla\Delta\star} & \cdots & \frac{1}{2}\sigma^2_{\nabla\Delta\star} \\ \vdots & \vdots & \ddots & \vdots \\ \frac{1}{2}\sigma^2_{\nabla\Delta\star} & \frac{1}{2}\sigma^2_{\nabla\Delta\star} & \cdots & \sigma^2_{\nabla\Delta\star} \end{bmatrix}, \tag{6.41}$$

where $\star$ is a placeholder for pseudorange, carrier-phase or carrier phase derived Doppler measurements. The $Q_{\nabla\Delta N}$ is constructed in a similar way where the diagonal is $\sigma^2_{\nabla\Delta N}$ with the remaining elements being $1/2\sigma^2_{\nabla\Delta N}$.

It is possible to reduce the computational load without jeopardizing the performance significantly by determining the TMO gains on a slower time-scale, as shown in [101]. The observer can be implemented using the corrector-predictor architecture of [55, Section 11.3.4], where the observer estimates are propagated at IMU frequency and corrected at the lower GNSS receiver frequency whenever satellite measurements are available. The gain selection can then be implemented on a third and slower time scale where the gains are updated for every 100-2.000 GNSS correction. This slower time-scale can be chosen since the C matrix is slowly time-varying.

6.4.2 Integer Ambiguities

The ambiguities in the double-differenced observer are initially considered real valued, however, the precision can be further improved by if they are correctly resolved to integers. Several methods for fixing the carrier-phase ambiguity have been proposed. Here the "fix and hold" method from [76] will be used to fix the combined variable $\nabla\Delta\hat{N} := \left[\nabla\Delta\hat{N}_1; \nabla\Delta\hat{N}_2; \ldots; \nabla\Delta\hat{N}_{m-1}\right]$ to integer values.

The initial estimate of the ambiguity vector can be determined as the difference between carrier-phase and pseudo-range measurements, i.e. subtraction of (6.12) from (6.13):

$$\nabla\Delta\hat{N} = \frac{1}{\lambda}\left(\nabla\Delta\varphi - \nabla\Delta\rho\right), \tag{6.42}$$

where the combined variables for pseudorange and carrier-phase measurements are given by $\nabla\Delta\varphi := [\nabla\Delta\varphi_1; \nabla\Delta\varphi_2; \ldots; \nabla\Delta\varphi_{m-1}]$ and $\nabla\Delta\rho := [\nabla\Delta\rho_1; \nabla\Delta\rho_2; \ldots; \nabla\Delta\rho_{m-1}]$. The initialization offered by (6.42) can be used when new satellites are introduced to the constellation. Initialization should also be carried out if a satellite is re-introduced after a period of obstruction or loss-of-lock, as the ambiguity will have changed.

The initial ambiguity estimates depend strongly on a good initial position of the rover and base station. As these might be difficult to obtain prior to flight the ambiguities should be iterated by the TMO before trying to fix to integer value, to decrease the risk of fixing to the wrong integers. After initialization the ambiguities will therefore be propagated by the TMO as real-valued estimates. The estimate can be tested for convergence to integer values by minimizing, [76]:

$$\Omega = \min_{\nabla\Delta\check{N}\in\mathbb{Z}^{m-1}} \left(\nabla\Delta\check{N} - \nabla\Delta\hat{N}\right)^{\mathsf{T}} P_N^{-1} \left(\nabla\Delta\check{N} - \nabla\Delta\hat{N}\right), \tag{6.43}$$

where $P_N \in \mathbb{R}^{m-1\times m-1}$ is the covariance matrix of the ambiguities, and $\nabla\Delta\check{N}$ is an integer candidate vector. The candidate vector belongs to the search space of:

$$S := \{\nabla\Delta\check{N} \in \mathbb{Z}^{m-1} | \nabla\Delta\hat{N} - c_r\sigma_N \leq \nabla\Delta\check{N} \leq \nabla\Delta\hat{N} + c_r\sigma_N\}, \tag{6.44}$$

where σ_N is the variance of the ambiguity estimates determined by the diagonal elements of P_N; $\sigma_N = \sqrt{\text{diag}(P_N)}$. The constant c_r denotes the confidence interval, which in the following will be considered as; $c_r = 3.29$ for 99.9% confidence interval, assuming normal distribution.

All possible candidate vectors in the search space is tested to see which minimizes (6.43). The relation between the smallest and second smallest value of (6.43), respectively called Ω_1 and Ω_2, is used to determined whether significant convergence to a candidate vector is achieved. Here significant is used in a covariance sense, as the search space depends on the covariance matrix of the ambiguities. The convergence test consists of verifying that the best solution, Ω_1, is sufficiently far from the next best solution:

$$\Omega_2 \Omega_1^{-1} \geq t_N, \tag{6.45}$$

where t_N is a threshold value. If the ratio is larger than the threshold the test is accepted and the ambiguities are fixed to the candidate set corresponding to Ω_1. This test can be carried out at every observer iteration until the ambiguities are fixed. However, the search space, S, will initially be too large to computationally feasibly search through all candidate sets, which encourages the use of methods such as the LAMBDA method to decrease the search space. The Least-squares AMbiguity Decorrelation Adjustment (LAMBDA) method was proposed by [169], [170], [171] and uses a change in variables to transform the confidence interval of the ambiguities to cover a smaller area, see Section 2.5.6.

There are two alternatives for handling the fixed ambiguities: a) Once the ambiguities are fixed to integer values they are removed from the state vector, decreasing the A, C, K, Q and P matrices in size, or b) The fixed ambiguities are introduced as an additional measurement augmenting the R matrix and the injection terms. The result will be very similar for the two methods. Method a) might be preferred to b) for the decrease in computational power.

According to [143] the residual measurement error should be less than 25% of a wavelength for the integer ambiguity resolution to have high probability of resolving to the correct integer. This implies that with high noise levels on the phase measurements, or uncertainty in the estimated geometric distance the resolution of the ambiguities might lead to the wrong integers resulting in a position error. In the event of loss-of-lock of satellite signals the code measurements can be smoothed by use of the raw Doppler measurements to reduce the convergence time.

6.5 Additional Aiding

A drawback of the RTK positioning is the sensitivity to agile manoeuvres and obstructed GNSS signal path, which can lead to loss-of-lock of the satellite signals. If the RTK positioning looses sight of a satellite in the constellation, the integer ambiguity have to be determined again when the satellite is reintroduced. In order to improve the resistance to precision deterioration when satellites are obstructed the sensor configuration can be augmented with use of further aiding sensors, e.g. cameras, air speed sensors, or ultra wideband transceivers. Ultra wideband (UWB) technology has typically been used for indoor navigation due to its short range. A setup consisting of a UWB receiver measuring the distance to one (or several) UWB nodes acting as pseudo-satellites. The UWB cannot, in practice, substitute the GNSS measurements in outdoor environment due to the short range, however it can aid the inertial navigation in GNSS denied or challenged areas, e.g. the UWB

nodes can be placed strategically around the landing area to aid during the final part of a UAV flight. A conceptual setup is shown in Fig. 6.4, where the rover and base station are denoted r and s, while satellites are marked $S_\star$ and UWB nodes are denoted $\mathcal{N}_\star$. The UWB range measurements are given by μ, where the horizontal coverage of the UWB notes are shown as gray circles.

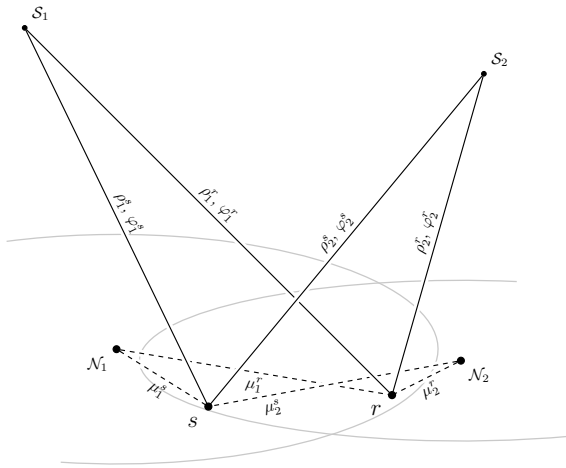

Figure 6.4: Conceptual setup of rover, base station, GNSS-satellites and UWB nodes

UWB technology have been used in other outdoor applications such as in [142] where inter-vehicle positioning was achieved using DGPS in combination with UWB, or in [136] where position and heading of smoke divers equipped with IMU and UWB was estimated. Other previous work include [75] where double-differenced GPS measurements are coupled with a single UWB range measurement in a tight manner, using an unscented Kalman filter and a two-frequency GPS receiver. Their goal is to accurately determine the relative position between two UAVs in formation flight, with increased robustness to GPS loss-of-fix.

The nonlinear observer structure presented in the sections above can be augmented to include UWB aiding measurements, as shown in [77]. The main alterations include additional injection terms and expansion of the TMO state vector by inclusion of timing parameters for the UWB propagation. In [77] the UWB augmentation was shown through simulations to enhance performance during GNSS denied periods of flight. The UWB aiding will not be considered further in this chapter.

6.6 Experimental Results

Experimental data from a flight with a fixed-wing Penguin B UAV, see Fig. 6.5, is used to verify the proposed double-differenced observer structure. The flight was carried out at Eggemoen airport in Norway (60°12′52″N, 10°19′07″E). The UAV was equipped with an ADIS 16488 IMU (with internal magnetometer) collecting

acceleration, rotation rate and magnetic field data at 410 Hz, while a u-Blox LEA-6T receiver gathered navigation satellite measurements at 5 Hz coinciding with measurements obtained at a stationary base station at the airport. The base station receiver is of the same brand and type as the rover receiver. The base station additionally logged the ephemeris data required for satellite position and velocity computation. Throughout the flight the baseline is kept under 1 km, such that the assumption of the atmospheric delays experienced by the two receivers are spatially correlated holds.

Figure 6.5: Penguin B used for experimental verification.

The sensors (IMU, GNSS receiver and antenna) used are considered low-cost and while even cheaper models are available these are thought to represent the general level of sensors used for UAV flights. The resolution of the sensors and the stability characteristics of the inertial sensors are seen as a limitation on the performance. Better performance can be expected by including better inertial sensors, especially increasing the performance of the navigation solution when GNSS signals are obstructed. Higher grade GNSS receivers might decrease the experienced measurement noise, supply higher C/N_0 ratios and offer higher sample rates. If the measurements are not accurately synchronized errors in the GNSS/INS integration will arise, as investigated in [86] and Chapter 4. Here synchronization is achieved with custom printed circuit boards and a PIC32 micro-controller, see Appendix B.

In the following two versions of the presented observer structure will be investigated where the difference is in the included aiding measurements; Case A uses pseudorange and carrier-phase measurements, while Case B additionally uses the carrier phase derived Doppler measurements. For both cases the inertial measurements are utilized. The structure of Case A was introduced and simulated by the authors in [84].

To ascertain the performance of the proposed observer structure an RTK ref-

erence solution is computed using the open source RTKLIB. No cycle slips were present allowing the reference to maintain resolved ambiguities throughout the flight thereby ensuring centimetre level accuracy. The initial 2.3% of the flight has unresolved ambiguities resulting in a reference with decimetre level accuracy, while the remainder of the flight has centimetre level accuracy. The RTK solution is determined from the same GNSS data as is available to the observer implementations. However, the sampling rate of the reference solution will be at GNSS receiver sampling rate while the observer estimates will be at IMU sampling rate. The observer solution will therefore be down-sampled when compared.

The tuning parameters for the Q matrix are chosen as: $Q = \text{blockdiag}\left(0_3\ [m^2], I_3\ [m^2/s^2], 0.00025 I_3\ [m^2/s^4], 0_3\ [m^2], Q_{\nabla\Delta N}\right)$, where $\sigma_{\nabla\Delta N} = 0.01\ [\lambda^2]$, while the parameters for R are chosen based on the standard deviations of Table 6.1; $\sigma_{\nabla\Delta\rho} = 1.1\ [m^2]$, $\sigma_{\nabla\Delta\varphi} = 0.03\ [m^2]$, and $\sigma_{\nabla\Delta v} = 0.06\ [m^2/s^2]$ increased to accommodate for bounding Gaussian white noise and higher sample rate as discussed in [76, Section 9.4.2.4]. The pseudorange standard deviation has been decreased compared to Table 6.1 to ensure faster convergence. Units have been given in square parenthesis such as not to confuse with variables or constants. The remaining parameters are: $M_b = 0.0087\ [rad^2/s^2]$, $k_1 = 0.8$, $k_2 = 0.2$, $k_I = 0.004$ and $\lambda = 0.1903\ m$ corresponding to the GPS L_1 wavelength. The ambiguity threshold is chosen as $t_N = 3$, as suggested by RTKLIB.

The position of the base station is initialized as an average of the receiver position measurements determined over 25 minutes of logged data. This is considered to be sufficiently accurate for this application. However, more accurate initial position estimates will increase the transient performance, encouraging to average over longer periods when possible. Precise Point Positioning (PPP) can ensure a decimetre accurate estimate of the base station, however the drawbacks are long initialization time and access to preceise ephemeris and atmospheric data. The initialization process presented in [98] can be used to initialize the position of the rover and base station, to ensure that the initial positions are close to the true position.

In Fig. 6.6 the sky plot of the constellation throughout the experiment is shown. The satellite trajectories are marked with individual colors and the last position has been marked with the satellite ID indicating the direction. The reference satellite is chosen as SV1 (shown in red) due to the high initial elevation to minimize atmospheric delays. A minimum elevation requirement of 15° is enforced for dismissal of satellites with high propagation errors.

The rover GNSS receiver antenna is placed on top of the UAV between the wings. Due to the high dynamics of the flight, with sharp turns the rover looses track of satellites with low elevation. Only five satellites are considered in the following test to ensure that the integer ambiguities do not require frequent resetting. The satellites to be included are chosen as SV1, SV4, SV11, SV17, SV20, and SV32, which all have high elevation angles. The dilution of precision (DOP) will be large due to the clustering of the used satellites, and higher performance might be expected when using a broader satellite constellation, especially in the vertical component. Here the constellation can be considered akin to a worst-case scenario with regards to the dilution of precision.

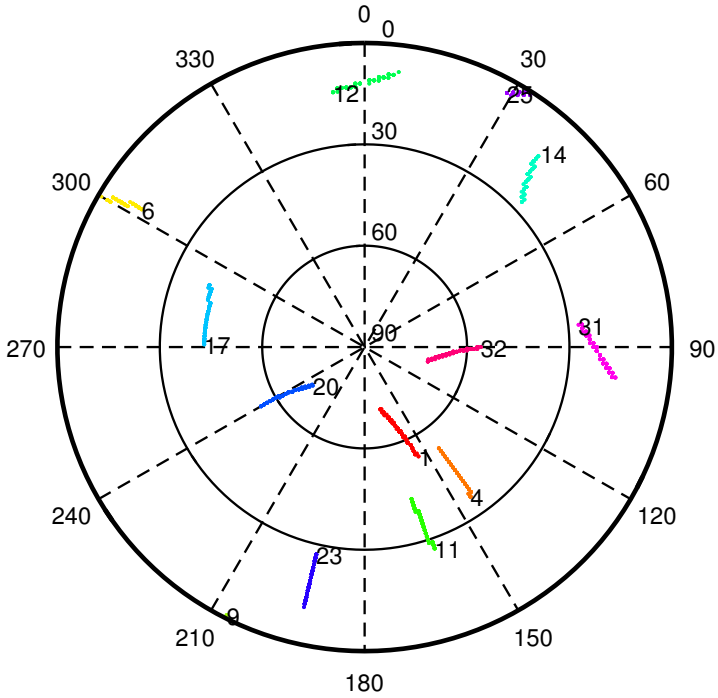

Figure 6.6: Sky plot showing elevation and azimuth of satellites. The satellite IDs are included for ease of reference.

The trajectory of the UAV includes several fast dynamic manoeuvres such as figures-of-eights and circles with radius of approximately 210 m. Some points of interest have been marked during the flight; ① denotes take-off, ② notes when the UAV has reached the desired altitude beginning a figure-of-eight flight sequence, at ③ the flight pattern is changed to circles, followed by ④ marking the descent with the reference reverting to lower accuracy making it unfit for further comparison shortly prior to landing. These points of interest will be marked in the following figures for ease of performance comparison throughout the flight. The take-off, initial trajectory and landing was performed with manual control, whereas the figures-of-eight and circles were operated by the autopilot.

The initial part of the trajectory can be seen in Fig. 6.7, while the attitude estimation is shown in Fig. 6.8 with the points of interest marked. The attitude is converted to Euler angles describing the rotation from Body to NED-frame for more intuitive understanding. The attitude estimation is similar for both cases considered, which is attributed to the modular observer structure where only the specific force estimate changes with the case. The point of Fig. 6.8 is not to be able to compare the attitude estimation between the two cases but rather to visualize that there is little difference between the cases. It should be noted that the oscillatory behaviour of the pitch estimate between ③ and ④ corresponds to the observed behaviour during flight resulting in a slightly sinusoidal vertical trajectory

during the circular flight pattern. This was due to an uncompensated issue in the autopilot.

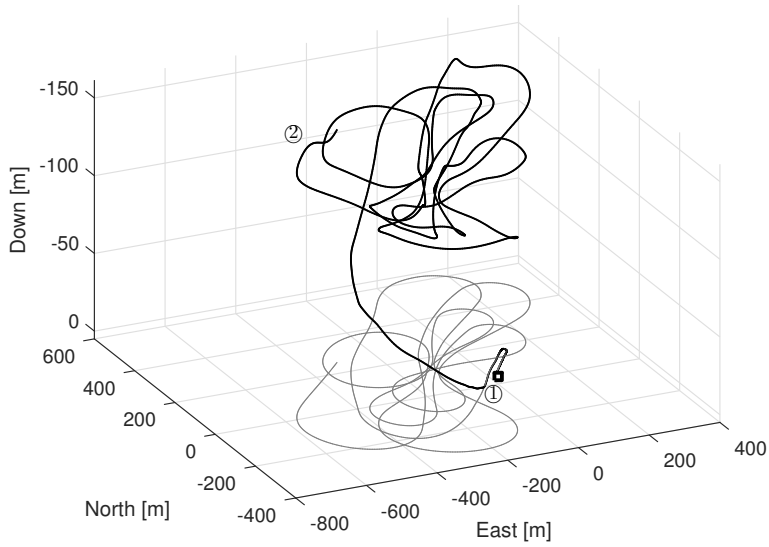

Figure 6.7: Trajectory of rover (lines), projected ground (grey), and base station (square) during first 400 sec.

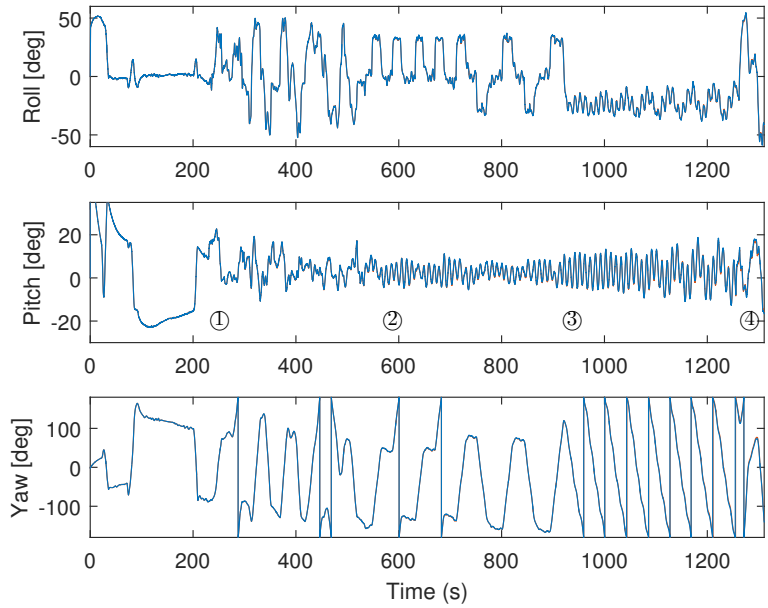

Figure 6.8: Rover attitude estimation; Case A (red) and Case B (blue).

The relative position between rover and base station is determined and com-

pared to the relative position offered by the reference. The relative position estimation errors for the proposed observer can be seen in Fig. 6.9. It is clear that the integer ambiguities are resolved well in advance of take-off. The transient period of 35 s is not visible in the figure, due to the initial offset. However, the transient behaviour can be seen in Fig. 6.10. The performance of the position estimates are compared in Table 6.2, where root-mean-square errors (RMSE) and standard deviations (STD) are summarised. The values are determined after the initial transient period of 35 s. An additional test case is included in Table 6.2 where the base station position has been excluded from the state vector and is considered constant at the initial position. This test will be denoted Case C and will utilize pseudorange and carrier-phase aiding. The accuracy obtained by Case C is greatly dependent on the quality of the base station position estimate, while Case A and B estimate the base station position as part of the state vector.

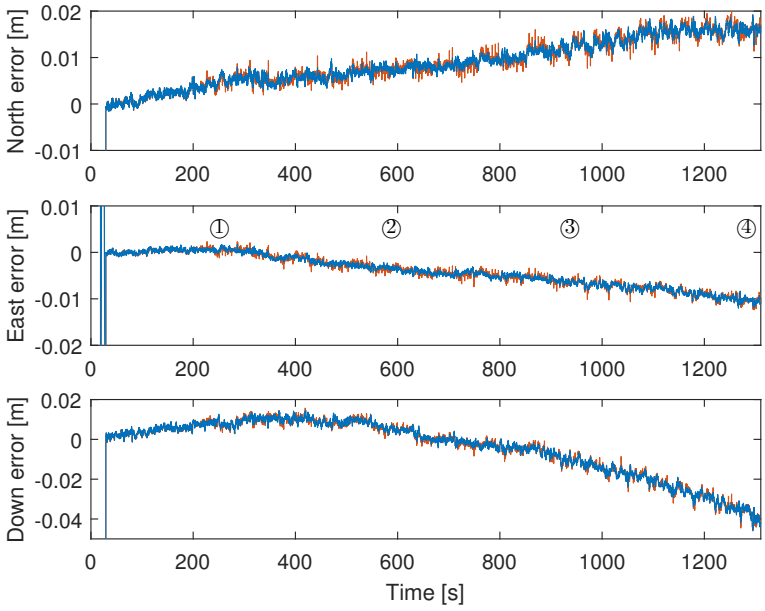

Figure 6.9: NED relative position estimation error for Case A (blue) and Case B (red).

The performance of Case A and Case B are very similar and are not influenced by the dynamics of the flight. Case B might have advantages in velocity estimation, however, as no reliable velocity reference is available this cannot be confirmed. Small drifts are present in the position estimation, e.g. of approximately $1.7 \cdot 10^{-5} m/s$ in North direction.

The fast convergence and high accuracy shown in Fig. 6.9 are attributed to the ambiguity resolution. In Fig. 6.11 the ambiguities for Case A are shown for the first 35 s, with similar results obtained for Case B. The real-valued estimate is shown in blue, with the RTKLIB reference integers in black. The rounded estimates are shown in red and only serve as a visual comparison to the reference integers, as

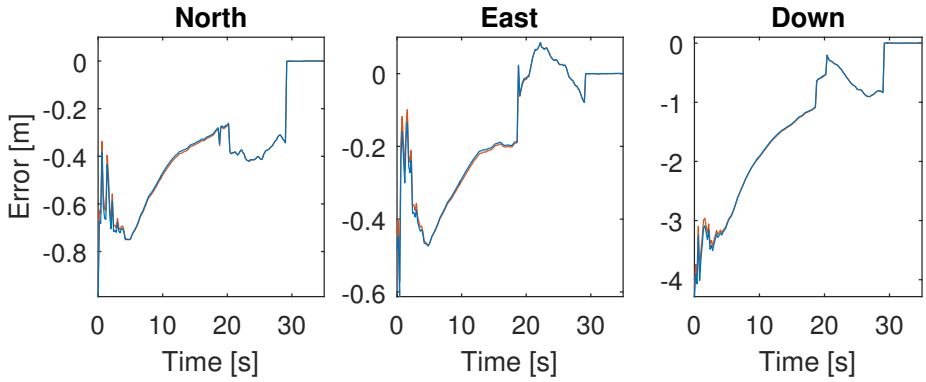

Figure 6.10: Transient behaviour of NED relative position estimation error for Case A (blue) and Case B (red).

the resolved integers are not guaranteed to be the same as the rounded real-valued estimates. The estimated ambiguities are seen to quickly converge to the reference value, with one exception for SV17, where the stationary value is one wavelength off. This is considered acceptable and will ensure high precision as seen in Fig. 6.9 and Table 6.2.

Table 6.2: Performance comparison of relative NED position estimation error (unit: **centimetre**).

	AIDING			RMSE			STD		
	ρ	φ	υ	N	E	D	N	E	D
Case A:	X	X		1.005	0.534	1.482	0.481	0.343	1.421
Case B:	X	X	X	1.008	0.534	1.485	0.487	0.344	1.423
Case C:	X	X		1.005	0.533	1.482	0.481	0.343	1.421

Looking at Table 6.2 the RMSE and standard deviations are seen to be on centimetre-level for all three cases, with sub-centimetre level STD for the horizontal components. The vertical components are seen to have less performance than the horizontal components for all three cases. This can be attributed in part to the clustered satellite constellation, and the general result of less accurate vertical channel offered by GNSS measurements. Case C has slightly better performance than Case A. However, as the difference is on sub-millimetre level Case A and Case C practically offers the same solution. It is therefore concluded that the inclusion of the base station position in the state vector does not lead to poorer state estimates and will be encouraged, especially in case of a slightly moving base station such as a base station on a ship during station keeping. These performance results are considered good in view of the low-cost sensors used and the clustered satellite constellation.

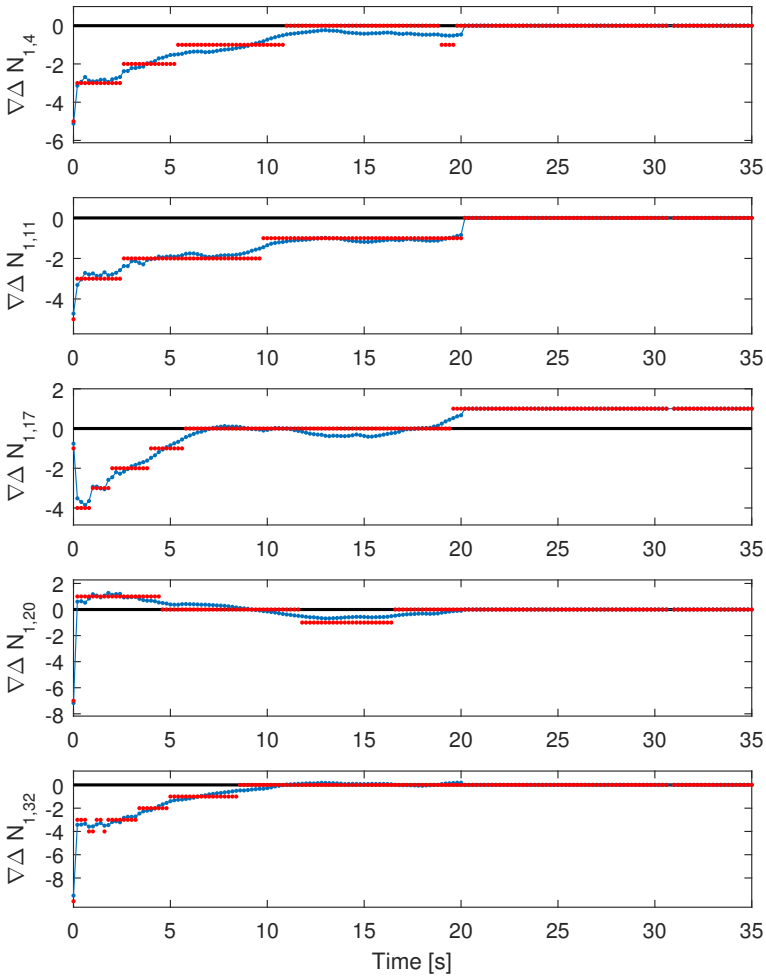

Figure 6.11: Example of real-valued ambiguity error for Case A (blue), rounded ambiguities (red), with reference integer (black).

6.6.1 Float vs. Fixed Ambiguities

In order to ascertain the influence of the ambiguities a test with only real-valued ambiguities is compared to Case A. This test will be denoted Case D, and will not differ in any way from Case A, apart from the carrier-phase ambiguities being unresolved. In Fig. 6.12 Case D and Case A are compared.

For Case D the RMSE value is $[1.277; 0.942; 4.399]$ m with standard deviations of $[1.212; 0.865; 1.711]$ m, which is approximately two orders of magnitude larger than with resolved ambiguities. It is clear that for applications with demands of high accuracy the ambiguities need to be resolved, which is expected.

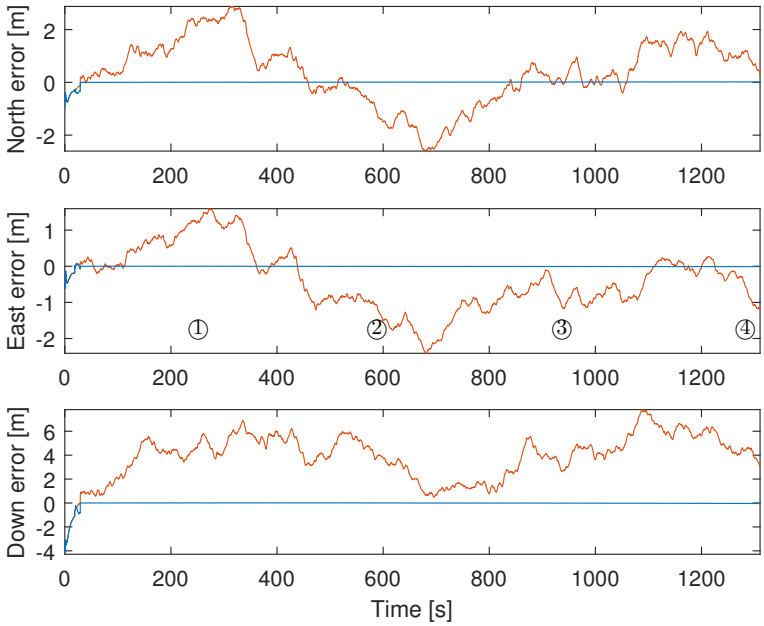

Figure 6.12: NED relative position estimation for Case A (blue) and Case D (red).

6.6.2 Low Elevation Constellation

A low elevation test is carried out to evaluate the performance when using satellites with low elevation angles. This can simulate a high latitude flight close to the poles where the GPS constellation coverage is poor granting only access to satellites at low elevation. The same data as used in the test above is utilized, here with an elevation mask of 5°. The atmospheric disturbances experienced will differ compared to a high latitude flight, however, this test can give an impression on the possible performance achievable.

In a high latitude, e.g. Arctic, setting the environment would be different from the one considered here where major differences include: a) the terrain will in the Arctic be completely open sky, whereas here some obstruction is offered by trees and mountains, b) the ionospheric and tropospheric conditions, c) different number of satellites, and d) choice of satellites, the best set of satellites based on e.g. DOP and C/N will be selected, whereas here a poor subset of the satellites is chosen.

Satellites with high elevation are masked out. The satellites; SV4, SV6, SV11, SV14, SV23 and SV31 are used, where SV11 has been included to satisfy the $m \geq 4$ assumption, as the low elevation satellites often are obstructed jeopardizing the constellation size assumption. The satellite SV12 is excluded as several cycle slips were detected. The ambiguities estimates are re-initialized if a satellite is re-introduced in the constellation.

The proposed observer without carrier phase derived Doppler aiding (as in Case A above) is tested with the low elevation constellation, where the performance is shown in Fig. 6.13. Instances when $m < 5$ are marked with vertical grey lines,

e.g. at time 1085 seconds. The test is shortened by a approximately 45 seconds, compared to the previous tests, due to extensive loss of low elevation satellites towards the end of the flight.

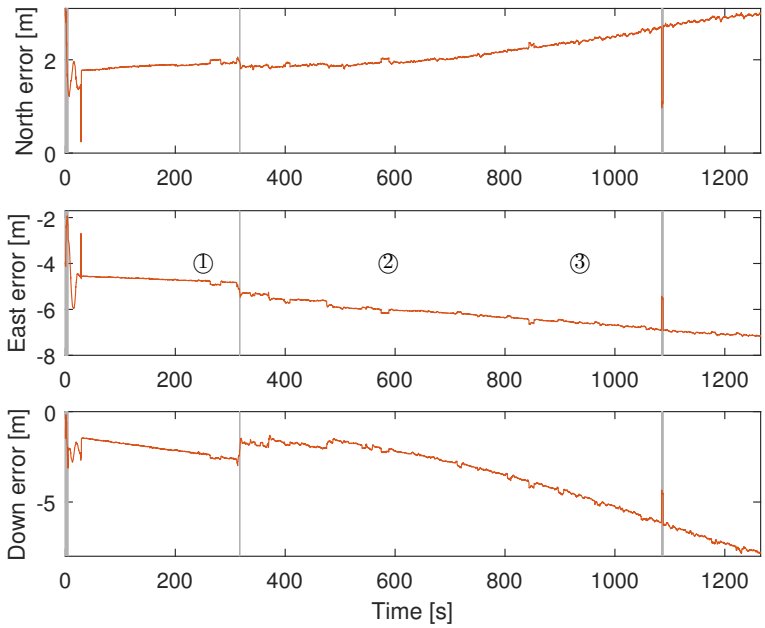

Figure 6.13: NED relative position estimation error for Case A using low elevation satellites.

It is not possible to resolve the ambiguities reliantly due to frequent loss of satellite lock and re-introduction of the satellites. This has a clear impact on the performance of the position estimation. The RMSE values are $[2.200; 6.001; 3.961]$ m with standard deviations $[0.367; 0.821; 1.909]$ m which is significantly larger than the values listed in Table 6.2 and for the real-valued test in Section 6.6.1. However, the horizontal accuracy for the rover is seen to be on meter level. This is an improvement over standalone solutions where larger deviations would be expected for a low elevation constellation.

6.7 Chapter Summary

A tightly-coupled GNSS/INS integration scheme using a dual GNSS-receiver configuration between a stationary base station and a moving rover was proposed where the position and linear velocity of a rover were estimated by a proposed translational motion observer while attitude was determined with a nonlinear attitude observer. The proposed translational motion observer utilizes the error of the double-differenced pseudorange, carrier-phase and carrier phase derived Doppler satellite measurements between the receivers as injection terms.

The observer was verified using flight data from an UAV equipped with low-cost sensors, where position estimates were shown to be within 2-4 centimetres of the RTK reference solution throughout a 20 minutes long flight. Convergence of the ambiguities introduced by the carrier-phase measurements was achieved by inclusion in the state vector where they were initially considered real valued later to be resolved to integer values.

Proof: TMO Injection Terms

The double-differenced injection terms are expressed as:

$$
\begin{aligned}
e_{\rho,ij} &= \|p_r^e - p_j^e\|_2 - \|p_r^e - p_i^e\|_2 - \|p_s^e - p_j^e\|_2 + \|p_s^e - p_i^e\|_2 \\
&\quad - \|\hat{p}_r^e - p_j^e\|_2 + \|\hat{p}_r^e - p_i^e\|_2 + \|\hat{p}_s^e - p_j^e\|_2 - \|\hat{p}_s^e - p_i^e\|_2, \\
e_{\varphi,ij} &= e_{\rho,ij} + \nabla\Delta\tilde{N}_{ij}\lambda, \\
e_{\upsilon,ij} &= \left(h_j^r - h_i^r\right)^\intercal v_r^e - \left(\hat{h}_j^r - \hat{h}_i^r\right)^\intercal \hat{v}_r^e + \left(h_j^s - \hat{h}_j^s\right)^\intercal v_j^e - \left(h_i^s - \hat{h}_i^s\right)^\intercal v_i^e,
\end{aligned}
$$

Linearisation the injection terms as the first-order Taylor approximation yields:

$$
\begin{aligned}
e_{\rho,ij} &= \left(\frac{\hat{p}_r^e - p_j^e}{\|\hat{p}_r^e - p_j^e\|_2} - \frac{\hat{p}_r^e - p_i^e}{\|\hat{p}_r^e - p_i^e\|_2}\right)^\intercal \tilde{p}_r \\
&\quad - \left(\frac{\hat{p}_s^e - p_j^e}{\|\hat{p}_s^e - p_j^e\|_2} - \frac{\hat{p}_s^e - p_i^e}{\|\hat{p}_s^e - p_i^e\|_2}\right)^\intercal \tilde{p}_s + \eta_{\rho,ij}, \\
e_{\varphi,ij} &= \left(\frac{\hat{p}_r^e - p_j^e}{\|\hat{p}_r^e - p_j^e\|_2} - \frac{\hat{p}_r^e - p_i^e}{\|\hat{p}_r^e - p_i^e\|_2}\right)^\intercal \tilde{p}_r + \lambda\nabla\Delta\tilde{N}_{ij} \\
&\quad - \left(\frac{\hat{p}_s^e - p_j^e}{\|\hat{p}_s^e - p_j^e\|_2} - \frac{\hat{p}_s^e - p_i^e}{\|\hat{p}_s^e - p_i^e\|_2}\right)^\intercal \tilde{p}_s + \eta_{\varphi,ij}, \\
e_{\upsilon,ij} &= \left(\frac{\hat{v}_r^e - v_j^e}{\|\hat{p}_r^e - p_j^e\|_2} - \frac{\hat{v}_r^e - v_i^e}{\|\hat{p}_r^e - p_i^e\|_2}\right)^\intercal \tilde{p}_r + \left(\frac{\hat{p}_r^e - p_j^e}{\|\hat{p}_r^e - p_j^e\|_2} - \frac{\hat{p}_r^e - p_i^e}{\|\hat{p}_r^e - p_i^e\|_2}\right)^\intercal \tilde{v}_r \\
&\quad + \left(\frac{\hat{p}_s^e - p_j^e}{\|\hat{p}_s^e - p_j^e\|_2} - \frac{\hat{p}_s^e - p_i^e}{\|\hat{p}_s^e - p_i^e\|_2}\right)^\intercal \tilde{p}_s + \eta_{\upsilon,ij},
\end{aligned}
$$

where the higher order terms are limited to:

$$
\begin{aligned}
\eta_{\rho,ij} &= \frac{1}{2}\tilde{p}_r^\intercal \left(\check{H}_j^r - \check{H}_i^r\right)\tilde{p}_r - \frac{1}{2}\tilde{p}_s^\intercal \left(\check{H}_j^s - \check{H}_i^s\right)\tilde{p}_s, \\
\eta_{\varphi,ij} &= \frac{1}{2}\tilde{p}_r^\intercal \left(\check{H}_j^r - \check{H}_i^r\right)\tilde{p}_r - \frac{1}{2}\tilde{p}_s^\intercal \left(\check{H}_j^s - \check{H}_i^s\right)\tilde{p}_s, \\
\eta_{\upsilon,ij} &= \frac{1}{2}[\tilde{p}_r\ \tilde{v}_r]\begin{bmatrix} \check{J}_j - \check{J}_i & \check{H}_j^r - \check{H}_i^r \\ \check{H}_j^r - \check{H}_i^r & 0 \end{bmatrix}\begin{bmatrix} \tilde{p}_r \\ \tilde{v}_r \end{bmatrix} + \frac{1}{2}\tilde{p}_s^\intercal \left(\check{H}_j^s - \check{H}_i^s\right)\tilde{p}_s,
\end{aligned}
$$

for some point $\check{p}_r^e$ between p_r^e and $\hat{p}_r^e$ and:

$$
\check{H}_\star^r = \frac{1}{\check{\psi}_{r,\star}} I_3 - \frac{(\check{p}_r^e - p_\star^e)(\check{p}_r^e - p_\star^e)^\intercal}{\check{\psi}_{r,\star}^3},
$$

$$\check{J}_\star = \frac{1}{\check{\psi}^3_{r,\star}}\left((\check{p}^e_r - p^e_\star)(\check{v}^e_r - v^e_\star)^\intercal + (\check{p}^e_r - p^e_\star)^\intercal(\check{v}^e_r - v^e_\star)I_3\right) - \frac{3}{\check{\psi}^5_{r,\star}}(\check{p}^e_r - p^e_\star)(\check{p}^e_r - p^e_\star)^\intercal(\check{p}^e_r - p^e_\star)(\check{v}^e_r - v^e_\star),$$

with $\check{\psi}_{r,\star} := \|\check{p}^e_r - p^e_\star\|_2$, where $\star$ is a placeholder for i or j. Similar expressions can be found for $\check{H}^s_\star$ and $\check{\psi}_{s,\star}$ by substitution of r with s. The higher order terms can be bounded, as shown in [98]:

$$\begin{aligned}
\|\eta_{\rho,ij}\|_2 &\leq \check{\psi}_r\|\tilde{p}_r\|_2^2 - \check{\psi}_s\|\tilde{p}_s\|_2^2,\\
\|\eta_{\varphi,ij}\|_2 &\leq \check{\psi}_r\|\tilde{p}_r\|_2^2 - \check{\psi}_s\|\tilde{p}_s\|_2^2,\\
\|\eta_{\upsilon,ij}\|_2 &\leq \check{\psi}_r\|\tilde{p}_r\|_2 \cdot \|\tilde{v}_r\|_2 + \frac{3}{2}\check{\psi}_{r^2}\underline{\upsilon}\|\tilde{p}_r\|_2^2 + \check{\psi}_s\|\tilde{p}_s\|_2^2,
\end{aligned}$$

where:

$$\check{\psi}_r = \frac{\underline{\psi}_{r,j} - \underline{\psi}_{r,i}}{\underline{\psi}_{r,i}\underline{\psi}_{r,j}}, \quad \check{\psi}_{r^2} = \frac{\underline{\psi}^2_{r,j} - \underline{\psi}^2_{r,i}}{\underline{\psi}^2_{r,i}\underline{\psi}^2_{r,j}}, \quad \check{\psi}_s = \frac{\underline{\psi}_{s,j} - \underline{\psi}_{s,i}}{\underline{\psi}_{s,i}\underline{\psi}_{s,j}}.$$

with $\underline{\psi}_{r,i}$ and $\underline{\psi}_{s,i}$ being the lower bounds on the geometric distance between receiver and ith satellite, and $\|v^e_r - v^e_i\|_2 \leq \underline{\upsilon}$.

Chapter 7

Conclusive Remarks and Future Challenges

7.1 Conclusions

The contributions are listed here in order of appearance.

Conclusions of Chapter 3 - Loosely-Coupled GNSS/INS Integration
A modular nonlinear observer was adapted for navigation using inertial and GNSS measurements. The observer consists of an attitude estimator and a translational motion observer. The attitude was represented as a unit quaternion allowing for semi-global exponential stability results to be achieved for the observer. Gyro bias estimation is included in the observer to increase performance. Furthermore, accelerometer bias estimation can be included to increase robustness when facing GNSS outage.

Implementation and discretization considerations have been presented, as well as multiple attitude reference vectors for use in the attitude estimator. Reference vectors were introduced for measurements of; magnetic field, specific force, optical flow, velocity, and compass.

The nonlinear observer was compared to an Extended Kalman Filter using experimental data from a UAV, and was concluded to have similar performance for attitude as well as position and velocity estimation. The nonlinear observer have the advantage of fixed gains for the attitude observer and the option for fixed or slowly time-varying gains in the TMO. The effect of fixed gains compared to time-varying gains were investigated where the fixed gain solution did not reduce the performance significantly. The gains of the TMO can furthermore, be tuned similarly as for an EKF allowing for flexible tuning based on expected noise distributions in the system.

Conclusions of Chapter 4 - Time-Delayed GNSS Measurements
GNSS measurements suffer from a time delay introduced by the computational and dissemination time of the GNSS receiver. A nonlinear observer consisting of a nonlinear attitude estimator and a translational motion observer was developed to

take the time-delay into account. The proposed observer was proven to be semi-global exponential stability with respect to initialization. Initially a method for determining the time delay was proposed, followed by an analysis of the delay and its distribution.

The nonlinear observer delays the inertial measurements such that they correspond in time to the GNSS measurements, thereby ensuring the stability results established for the nominal observer. A fast simulator was introduced to propagate the delayed state estimates to current time by use of dead reckoning over the time-delay horizon. As the time-delay is small and the propagation is reset for each time-step the fast simulator does not diverge. An alternative implementation was proposed without stability proof, where the delay was shifted from inertial measurements to the attitude estimates. The alternative implementation thereby allows for accurate attitude estimation and can limit the fast simulator propagation to only include position and velocity. The computational load of the proposed and alternative implementation was compared to the nominal nonlinear observer, where both had larger computational load due to the inclusion of the fast simulator. However, if a fixed gain version of the proposed observer was used the load was smaller than the nominal observer even with inclusion of the fast simulator.

The framework presented was general and can be used for other nonlinear observers. For the alternative implementation a requirement was a modular structure allowing for insertion of delays between the attitude and translational motion observers.

The presented observers were studied using a UAV simulator where the effect of accurate, inaccurate and distributed delays were investigated. Even with an implemented delay a factor of 1.5 larger than the true delay the proposed method was preferable to the uncompensated observer. The observers were furthermore tested on experimental data from a small aircraft during high velocity manoeuvres. The proposed and alternative observers were seen to outperform the uncompensated observer during flight.

Conclusions of Chapter 5 - Tightly-Coupled GNSS/INS Integration

A tightly-coupled nonlinear observer was proposed. The modular structure of the loosely-coupled observer was used with the same attitude estimator. The translational motion observer was altered to use range and range-rate GNSS measurements rather than position and velocity measurements. The stability results of the observer were presented as well as an algebraic initialization method ensuring reasonable initial position estimates.

Observability requirement, and expansions to dual-frequency GNSS measurements without altering the stability results were introduced. The computational load of the tightly-coupled observer was compared to a MEKF, where the attitude is represented as a unit quaternion. The nonlinear observer was, for this comparison, considered in two variants where the TMO gains are updated either; on the implemented time-scale (here the IMU time-scale), or on a lower time-scale (at a fraction of the IMU frequency). Updating the TMO gains on a lower time-scale is seen to decrease the computational load significantly, thereby allowing for implementation on smaller and cheaper platforms.

The proposed methods were verified on experimental data from a UAV flight, where the performance of the nonlinear observer was compared to the MEKF performance, and was concluded to have similar estimation accuracy. Furthermore, the tightly-coupled observer was compared to the loosely-coupled observer presented in Chapter 3, using experimental data, and was seen to offer a significant improvement in position accuracy.

Conclusions of Chapter 6 - INS/RTK-GNSS Integration
The tightly-coupled nonlinear observer presented in Chapter 5 was here expanded to consider the differential receiver configuration, where a stationary receiver was introduced to serve as a reference for the GNSS measurements received at the moving rover. GNSS measurements are transmitted from the base station to the rover allowing for creation of single- and double-differenced measurements. If the rover is sufficiently close ($< 10 - 20\ km$) to the base station the atmospheric disturbances on the GNSS measurements can be cancelled.

An approach was proposed where double-differenced measurements were utilized in the translational motion observer, where a reference satellite was introduced resulting in smaller noise terms on the measurements. The integer ambiguities introduced by the carrier-phase measurements were included in the state vector and initially considered real-valued, later to be fixed to integer values. The performance of two versions of the proposed observer structure (with and without carrier phase derived Doppler measurements) were investigated and experimentally verified using flight data from a fixed-wing UAV, where the estimated positions were shown to be within $2 - 4$ centimetres of the GPS L_1 RTK reference.

7.2 Future Work

The results presented in this thesis is focused on loosely- and tightly-coupled GNSS/INS integration systems for navigation. The presented research can be extended to obtain even better results. This section offers some possible extensions:

- **Multi-constellation:** By allowing multiple GNSS constellations to be used in the GNSS/INS integration better coverage can be achieved, especially in high latitude regions by inclusion of GLONASS signals. Furthermore, the geometry of the constellation available for each epoch could improve since more satellites are available, which could improve the navigation solution in areas with severe signal obstruction, such as urban canyons.
- **Multi-frequency:** If a multi-frequency GNSS receiver is used the ionospheric disturbance could be cancelled thereby removing a severe disturbance on the GNSS range measurements. The proposed tightly-coupled observers in Chapter 5 and Chapter 6 directly allow for use of dual-frequency range and range-rate signals. Experimental verification could be of interest.
- **Combination:** It could be of interest to investigate the performance increase by implementing the differential GNSS receiver integration proposed in Chapter 6 where the time delay on the GNSS measurements is taken into account, as in Chapter 4.

- **Rotation matrix:** The attitude can be represented as a 3×3 rotation matrix instead of a unit quaternion. This can give global stability results, in contrast to the semi-global results achieved here.
- **XKF;** The results can be adapted to the eXogenous Kalman filter structure thereby providing covariance estimates. It would be of interest to compare this with an extended Kalman filter.

Appendices

Appendix A

Ephemeris - Satellite Position

When using GNSS systems it is vital to know the position of the satellites in view of the receiver. In loosely coupled GNSS/INS integration, the satellite position determination is carried out by the receiver. However, for tightly coupled systems the computation must be carried out in the observer implementation. The position of the satellites are determined from ephemeris data, either broadcasted or obtained from reference stations. The sample rate of the broadcasted ephemeris data is receiver specific, where it in some cases can be sampled up to every 30 seconds, however the most common sample rate is approximately 30 *min*. The validity of the ephemeris data is typically two to four hours, depending on the desired accuracy, in which time interval the satellite orbit can be determined with high accuracy. The only input to the algorithms, apart from the ephemeris parameters, is the time, at which the satellite position is desired, which allows for determination of the position at any time and sample rate.

The ephemeris algorithms consists of three parts; a) clock corrections to the satellite clock, b) position determination of the satellite vehicle, and c) velocity determination of the satellites. The term *determination* is used instead of *estimation* to signify that the satellite position and velocity are found with high accuracy and not subject to high levels of uncertainty. Each satellite broadcasts a set of parameters for the algorithms, and position and velocity has to be determined for each satellite individually.

The algorithms for determining the satellite positions and velocities can be found in several sources with slight changes in notation, e.g. [154], [175], and [126]. This appendix is written based on the equations found in [52], and has been included for completeness.

This chapter will first introduce the ephemeris parameters and then state the equations necessary for each of the three parts of the ephemeris algorithms.

A.1 Ephemeris Parameters

Each satellite broadcasts a set of ephemeris parameters, which includes the six Keplerian elements; Inclination, eccentricity, semi-major axis, mean anomaly, rate of right ascension, and longitude of the ascending node, in addition to correction

terms for the pertubation model. The ephemeris parameters are listed in Table A.1, see [52] for a more thorough description of the variables. Here *sc* denotes the unit semi-circle.

Table A.1: Contents of the ephemeris packages

Name	Unit	Description
t_{oc}	s	Clock data reference time
a_{f0}	s	Constant correction to satellite clock
a_{f1}	s/s	First order correction to satellite clock
a_{f2}	s/s^2	Second order correction to satellite clock
t_{oe}	s	Ephemeris reference time
C_{rs}	m	Amplitude of sine harmonic correction to the orbit radius
C_{rc}	m	Amplitude of cosine harmonic correction to the orbit radius
C_{uc}	rad	Amplitude of cosine harmonic correction, latitude
C_{ic}	rad	Amplitude of cosine harmonic correction, inclination
C_{us}	rad	Amplitude of sine harmonic correction, latitude
C_{is}	rad	Amplitude of sine harmonic correction, inclination
i_0	sc	Inclination angle at reference time
e	[ ]	Eccentricity
ω	sc	The perigee argument
$\sqrt{A}$	$\sqrt{m}$	Semi-major axis square root
Ω_0	sc	Longitude of ascension node
M_0	sc	Mean anomaly
$\dot{\Omega}$	sc/s	Rate of right ascension
Δn	sc/m	Mean motion difference
$\dot{i}$	sc/s	Rate of inclination angle

A.2 Satellite Clock Corrections

The time update corrects the satellite clock and determines the Keplerian eccentricity anomaly, E_k, by use of the following equations:

$$\Delta t_r = Fe\sqrt{A}\sin(E_k) \tag{A.1}$$

$$\Delta t_{sv} = a_{f0} + a_{f1}(t_{sv} - t_{oc}) + a_{f2}(t_{sv} - t_{oc})^2 + \Delta t_r \tag{A.2}$$

$$t = t_{sv} + \Delta t_{sv} \tag{A.3}$$

$$A = \sqrt{A}^2 \tag{A.4}$$

$$n_0 = \sqrt{\frac{\mu}{A^3}} \tag{A.5}$$

$$t_k = t - t_{oe} \tag{A.6}$$

$$n = n_0 + \Delta n \tag{A.7}$$
$$M_k = M_0 + t_k n \tag{A.8}$$
$$E_k = M_k + e\sin(E_k), \tag{A.9}$$

where $F = -4.442807633 \cdot 10^{-10} \frac{s}{\sqrt{m}}$ is constant. The mean anomaly, M_k, is the mean motion correction of the satellite. Notice that (A.1) depends on E_k, which is first determined in (A.9), hence the equations (A.1)–(A.9) are iterated until E_k saturates. According to [76] 22 iterations are sufficient for centimetre accuracy. The input to the clock correction equations is the requested time, $t_s v$, indicating the time at which the corrections should be applied.

A.3 Satellite Position Algorithm

The position of the satellites in ECEF-frame given by; $p_k^e = [x_k^e; y_k^e; z_k^e]$ for the kth satellite, can be calculated individually by use of the equations:

$$v_k = \arctan\left(\frac{\sqrt{1-e^2}\sin(E_k)}{1-e\cos(E_k)}, \frac{\cos(E_k)-e}{1-e\cos(E_k)}\right) \tag{A.10}$$
$$\delta u_k = C_{us}\sin(2v_k + 2\omega) + C_{uc}\cos(2v_k + 2\omega) \tag{A.11}$$
$$\delta r_k = C_{rs}\sin(2v_k + 2\omega) + C_{rc}\cos(2v_k + 2\omega) \tag{A.12}$$
$$\delta i_k = C_{is}\sin(2v_k + 2\omega) + C_{ic}\cos(2v_k + 2\omega) \tag{A.13}$$
$$r_k = A(1 - e\cos(E_k)) + \delta r_k \tag{A.14}$$
$$X_k = r_k\cos(v_k + \omega + \delta u_k) \tag{A.15}$$
$$Y_k = r_k\sin(v_k + \omega + \delta u_k) \tag{A.16}$$
$$\Omega_k = \Omega_0 + \left(\dot{\Omega} - \dot{\Omega}_e\right)t_k - \dot{\Omega}_e t_{oe} \tag{A.17}$$
$$x_k = X_k\cos(\Omega_k) - Y_k\cos(i_0 + \delta i_k + \dot{i}t_k)\sin(\Omega_k) \tag{A.18}$$
$$y_k = X_k\sin(\Omega_k) + Y_k\cos(i_0 + \delta i_k + \dot{i}t_k)\cos(\Omega_k) \tag{A.19}$$
$$z_k = Y_k\sin(i_0 + \delta i_k + \dot{i}t_k) \tag{A.20}$$

The equations, (A.10)–(A.16), constitutes the ground station modelled corrections an the Earth oblateness effects, where (A.11)–(A.13) are second order harmonic perturbations to correct the radius, inclination and argument of latitude. The satellite position is described in the orbital plane by X_k and Y_k, where the satellite position is converted to the ECEF frame by use of (A.18)–(A.20).

The only input, apart from the ephemeris parameters, required for the position determination is the iterated eccentricity anomaly from the clock correction. It is therefore possible to determine the satellite position at any time within the valid time period of the ephemeris.

A.4 Satellite Velocity Algorithm

By implementing the following equations the satellite velocity in ECEF-frame, given as $v_k^e = [\dot{x}_k^e; \dot{y}_k^e; \dot{z}_k^e]$, can be estimated:

$$\dot{E}_k = \frac{n_0 + \Delta n}{1 - e\cos(E_k)} \tag{A.21}$$

$$\dot{\phi}_k = \frac{\sqrt{1-e^2}}{1 - e\cos(E_k)}\dot{E}_k \tag{A.22}$$

$$\dot{u}_k = (1 + 2C_{us}\cos(2\phi_k) - 2C_{uc}\sin(2\phi_k))\,\dot{\phi}_k \tag{A.23}$$

$$\dot{r}_k = 2\,(C_{rs}\cos(2\phi_k) - C_{rc}\sin(2\phi_k))\,\dot{\phi}_k + Ae\sin(E_k)\dot{E}_k \tag{A.24}$$

$$\dot{X}_k = \dot{r}_k\cos(u_k) - r_k\sin(u_k)\dot{u}_k \tag{A.25}$$

$$\dot{Y}_k = \dot{r}_k\sin(u_k) + r_k\cos(u_k)\dot{u}_k \tag{A.26}$$

$$\dot{i}_k = 2\,(C_{is}\cos(2\phi_k) - C_{ic}\sin(2\phi_k))\,\dot{\phi}_k + \dot{i} \tag{A.27}$$

$$\dot{\Omega}_k = \dot{\Omega} - \dot{\Omega}_e \tag{A.28}$$

$$\dot{x}_k = \dot{X}_k\cos(\Omega_k) - \dot{Y}_k\cos(i_k)\sin(\Omega_k) + Y_k\sin(i_k)\sin(\Omega_k)\dot{i}_k - y_k\dot{\Omega}_k \tag{A.29}$$

$$\dot{y}_k = \dot{X}_k\sin(\Omega_k) + \dot{Y}_k\cos(i_k)\cos(\Omega_k) - Y_k\sin(i_k)\cos(\Omega_k)\dot{i}_k + x_k\dot{\Omega}_k \tag{A.30}$$

$$\dot{z}_k = \dot{Y}_k\sin(i_k) + Y_k\cos(i_k)\dot{i}_k \tag{A.31}$$

The ephemeris data logged by the receiver can be verified or replaced by data logged at fixed GNSS receiver stations. Some of these offer free access, e.g.; at the web page for the National Geospatial-Intelligence Agency: http://earth-info.nga.mil/GandG/sathtml/PEexe.html precise ephemeris data can be downloaded for each GPS satellite around the Earth. GLONASS ephemeris data can be downloaded at https://www.glonass-iac.ru/en/archive/index.php. It can be beneficial to compare the implementation with copde provided by others when determining the satellite position. An implementation in *C* can be found at the web page of National Geodetic Survey: http://www.ngs.noaa.gov/gps-toolbox/bc_velo/bc_velo.c, which is part of the National Oceanic and Atmospheric Administration, American government.

Appendix B

Navigation Payload

This appendix outlines the navigation payload used for the experimental verification of the observers proposed throughout this thesis. The payload have undergone numerous iterations, with several improvements. However, the general outline of the payload has stayed the same for all the presented experiments. The payload have been designed by Sigurd Mørkved Albrektsen, NTNU. The description of the payload is included for better understanding of the high quality of the measurements obtained, especially regarding the time stamping of the measurements.

B.1 Component Overview

The objective of the navigation payload is to obtain measurements from inertial sensors and a GNSS receiver, while accurately time stamping the measurements for precise relation of the sensor measurements despite different sample rates. The payload includes the following components:

- **STIM 300:** tactical grade IMU measuring specific force and angular rate at sample rates of 125, 250, 500, 1000, or 2000 Hz.
- **ADIS 16488:** tactical grade IMU measuring specific force, angular rate and magnetic field, using a SPI interface.
- **u-Blox LEA-M8T:** GNSS receiver allowing logging of navigation data (global position and velocity), range data (pseudo-range and carrier-phase), and environmental data (ephemeris, satellite health, ionospheric parameters). In early versions of the payload the LEA-6T was used. The GNSS receiver additionally has a pulse-per-second (PPS) signal synchronized with satellite time, which is utilized for time stamping.
- **Synchronization Board:** A custom printed circuit board for accurately time stamping the measurements of the inertial and GNSS sensors. The PCB has undergone several iterations for inclusion of additional sensors, and consists of a micro controller with the input capture method accurately time stamping arriving measurements without affecting the runtime. The synchronization board is the main component of the payload.

- **Data storage:** Either SD card or SSD Harddrive depending on the amount of data. It is vital that the storage unit is resistant to vibrations. All data is stored in binary format and parsed offline.
- **ODROID-XU4:** Computer for handling, parsing and storing of data.

Compared to the ADIS IMU the STIM IMU has better performance, but is also more expensive. It has been desired to compare the performance of the low-cost ADIS sensor with the STIM sensor, in an attempt to design low-cost navigation systems. This is the reason for including two IMUs in the payload.

Additional sensors can be included in the payload, e.g.; camera, altimeter, autopilot logging, wind speed sensor, etc.

B.2 Hardware Design

The framework of the payload is shown in Fig. B.1, where the interface between the sensors, the synchBoard and the computer is shown.

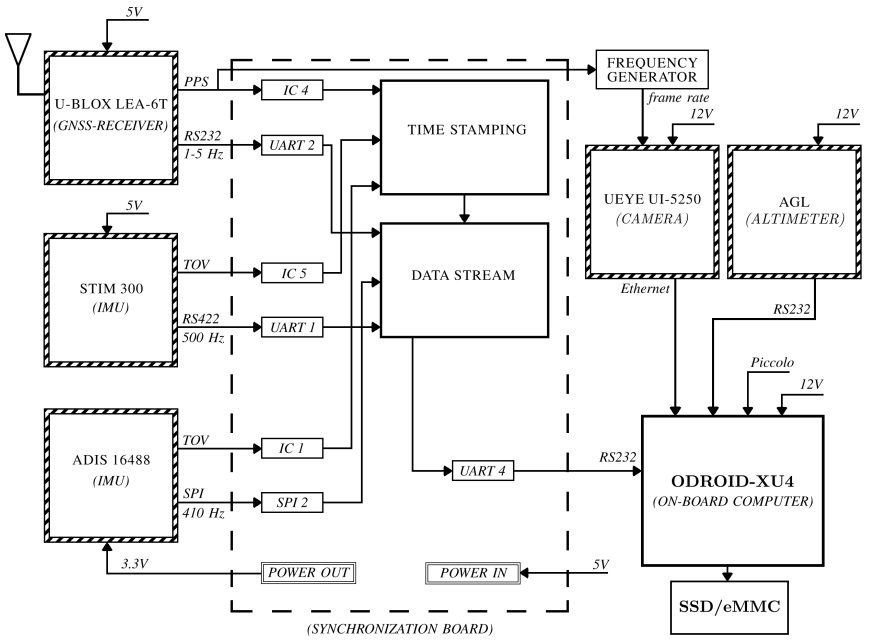

Figure B.1: Payload framework and components; the synchronization board (framed with a dashed line), and the sensors (striped edges).

The inertial and GNSS sensors are interfaced to the synchronization board, which time stamps them compresses all the measurements into one data stream, which is then parsed to the computer for handling and storing. The synchronization board also handles the various interfaces to the sensors; SPI for the ADIS sensor, RS-422 for the STIM sensor, and RS-232 for the u-Blox receiver. Furthermore, a

trigger signal based on the PPS signal of the GNSS receiver, is created by the synchronization board if a camera is included in the payload.

The synchronization board is powered externally with 5V, and also powers the ADIS IMU with 3.3V. The STIM sensor and GNSS receiver are powered externally.

B.3 Time Stamping

The main feature of the synchronization board is the handling and time stamping of the measurements from the inertial sensors and the GNSS receiver. Multiple time stamps are considered; time-of-validity (TOV), time-of-transmit (TOT), and time-of-arrival (TOA). A measurement from a general sensor is first valid at TOV, then it is send from the sensor at TOT, and finally arrives at the synchronization board at TOV, introducing a delay between when the measurement was valid and when it was received for processing. For the inertial sensors the delay is insignificant, and only the TOA measurements are considered. However, for the GNSS receiver a delay is present, as discussed in Chapter 4, which require consideration when handling the data. For the GNSS receiver the TOV time is indicated by the PPS signal, the TOT signals as the arrival of the first bit in a data package, and TOA as the arrival of the final bit in the data package.

The time stamps of TOV, TOT, and TOA are indicated by an integer number of clock cycles of the micro controller, and can be related to seconds by division with the clock rate of the micro controller. With the clock rate chosen high it is possible to get sub-millisecond resolution of the time stamps.

Since the GNSS receiver data packages contains time stamps of Coordinated Universal Time (UTC) and integer Time Of Week (iTOW) the time stamps of the synchronization board can be related to more intuitive time scales. Moreover, since all GNSS receivers are synchronized to UTC or iTOW time, it is possible to accurately relate GNSS measurements from another receiver not in the payload to the payload data. It is not possible to measure the time delay introduced by the receiver if not included in the payload, however the TOV time stamps are direct transferable. This feature allows e.g. ground station data to be accurately related to the payload data, for use in a dual receiver configuration, which was utilized in Chapter 6.

B.4 Pictures

The payload can be mounted in various ways depending on the vehicle limitations such as connectivity (e.g. to an autopilot), power consumption (possible to exclude some sensors), size, weight, etc. For some vehicles the required power for the payload is readily available, whereas for others a power converter has to be included.

In Fig. B.2 and Fig. B.3 the payload is shown mounted in a peli case 1400 (dimensions: $339 \times 295 \times 152$ mm), to be water and shock resistant. This mounting was used for experiments on boat (Maritime Robotics Telematron: 845 Polarcirkel) and a small aircraft (GA Slingsby T67C). A mounting plate is placed inside the box for ease of mounting the equipment while retaining the water resistant properties

of the box. The two IMUs are placed on opposite sides of the plate at the center in order to experience the same acceleration and rotation. A rotation of the sensor measurements for one of the sensors is required to obtain corresponding measurements. The ADIS 16488 with the magnetometer is placed as far from the power converter as possible.

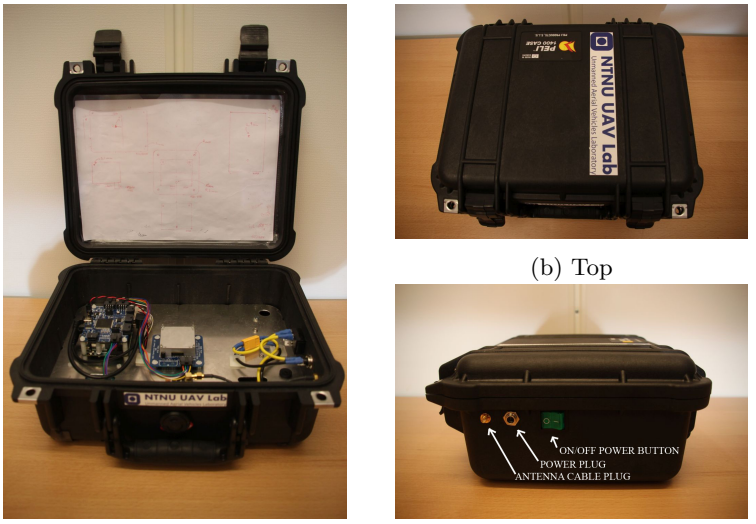

(a) Open (b) Top (c) Side

Figure B.2: The peli case 1400 payload.

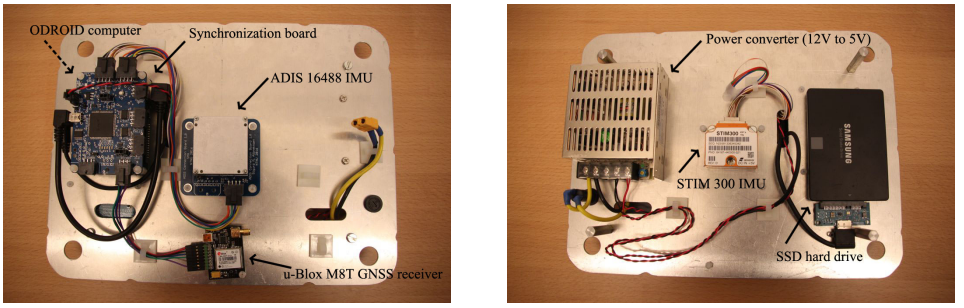

(a) Top view of the mounting plate. (b) Bottom view of the mounting plate.

Figure B.3: The mounting plate with components.

For mounting on unmanned aircraft size and weight are strict limitations, enforcing a more compact solution, which often excludes the ADIS 16488 sensor as the magnetometer readings might get affected by the proximity to power cables and other hardware.

Appendix C

Implementation

This appendix includes the implementation examples for the nonlinear observers introduced in the thesis.

C.1 Attitude Estimator

The implementation for the nonlinear attitude estimator is included in Algorithm 1, where the magnetometer measurements are used in the attitude injection term. Other vectors for the second pair of attitude injection vectors can be used, as discussed in Section 3.4.1.

The global magnetic field can be determined from lookup tables, e.g. in MATLAB by the function igrfmagm$(\cdot)$.

C.2 Loosely Coupled

The implementation of the loosely coupled translational motion observer is shown Algorithm 2, where a time-varying gain selection is employed. If a fixed gain observer is implemented the steps (C.17), (C.19), (C.21), and (C.26) can be ignored.

C.3 Tightly Coupled

The implementation of the tightly coupled translational motion observer is shown in Algorithm 3. There are many similarities to the loosely coupled implementation with the differences being the C matrix, the content of the measurement vector and satellite selection. The implementation is shown for the use of pseudo-range measurements. If additional measurements are included the y vector, and C and R matrices should be expanded accordingly.

Algorithm 1 Discrete-Time Attitude Observer in Indirect Form

Require: Initializing the observer,

1: $\hat{q}_b^e[0] = q_0(\phi[0], \theta[0], \psi[0])$, $\hat{b}_g^b = 0_{3\times 1}$, where q_0 is the quaternion mapping from the initial Euler angles $\phi[0]$, $\theta[0]$, $\psi[0]$.

2: Enforcing $\|\hat{q}_b^e[0]\| = 1$, using $\hat{q}_b^e[0] = \hat{q}_b^e[0]/\|\hat{q}_b^e[0]\|$.

3: Extracting $s_q[0]$ and $r_q[0]$ from $\hat{q}_b^e[0]$ and calculating the initial rotation matrix

$$R(\hat{q}_b^e[0]) = I_3 + 2s_q[0]S(r_q[0]) + 2S(r_q[0])^2 \tag{C.1}$$

Ensure: k

4: Get $\hat{f}^e[k]$ from the TMO,

5: Get $f_{\text{IMU}}^b[k]$, $\omega_{ib,\text{IMU}}^b[k]$, and $m_{\text{MAG}}^b[k]$ from the IMU and calculated the attitude injection vectors,

$$\underline{v}_1^b[k] = f_{\text{IMU}}^b[k]/\|f_{\text{IMU}}^b[k]\|_2, \tag{C.2}$$

$$\underline{v}_1^e[k] = \text{sat}_{M_f}(\hat{f}^e[k])/\|\text{sat}_{M_f}(\hat{f}^e[k])\|_2, \tag{C.3}$$

$$\underline{v}_2^b[k] = m_{\text{mag}}^b[k]/\|m_{\text{mag}}^b[k]\|_2, \tag{C.4}$$

$$\underline{v}_2^e[k] = m^e/\|m^e\|_2, \tag{C.5}$$

6: Calculate the attitude injection term:

$$\hat{\sigma}[k] = k_1[k]\underline{v}_1^b[k] \times R(\hat{q}_b^e[k-1])^\intercal \underline{v}_1^e[k] + k_2[k]\underline{v}_2^b[k] \times R(\hat{q}_b^e[k-1])^\intercal \underline{v}_2^e[k] \tag{C.6}$$

7: Calculating the attitude estimation update

$$\delta\hat{q}_b^e[k] = \frac{1}{2}\hat{q}_b^e[k-1] \otimes \begin{bmatrix} 0 \\ \omega_{ib,\text{IMU}}^b[k] - \hat{b}^b[k-1] + \hat{\sigma}[k] \end{bmatrix} - \frac{1}{2}\begin{bmatrix} 0 \\ \omega_{ie}^e \end{bmatrix} \otimes \hat{q}_b^e[k-1], \tag{C.7}$$

8: Calculate the gyro bias estimate update

$$\delta\hat{b}^b[k] = -k_I\hat{\sigma}[k]; \tag{C.8}$$

9: Project the gyro bias estimate update.

10: Calculate the accelerometer bias estimate update

$$y_f[k] = \max(f^{e\intercal} f^e, M_f^2) - f_{\text{IMU}}^{b\intercal} f_{\text{IMU}}^b, \tag{C.9}$$

$$\vartheta[k] = \begin{bmatrix} 1 \\ -2f_{\text{IMU}}^b \end{bmatrix}, \tag{C.10}$$

$$\delta\hat{\Xi}[k] = \Gamma\vartheta[k]\left(y_f[k] - \vartheta[k]^\intercal\hat{\Xi}[k-1]\right), \tag{C.11}$$

11: Project the accelerometer bias estimate vector update.

12: Updating estimates,

$$\hat{q}_b^e[k] = \hat{q}_b^e[k-1] + T_{\text{IMU}}\delta\hat{q}_b^e[k], \tag{C.12}$$

$$\hat{b}^b[k] = \hat{b}^b[k-1] + T_{\text{IMU}}\delta\hat{b}^b[k], \tag{C.13}$$

$$\hat{\Xi}[k] = \hat{\Xi}[k-1] + T_{\text{IMU}}\delta\hat{\Xi}[k], \tag{C.14}$$

13: Accessing the accelerometer bias, $\hat{b}_f^b[k]$, as the lower three elements of $\hat{\Xi}[k]$.

14: Enforcing unit quaternion constraint, $\hat{q}_b^e[k] = \hat{q}_b^e[k]/\|\hat{q}_b^e[k]\|$,

15: Extracting $s_q[k]$ and $r_q[k]$ from $\hat{q}_b^e[k]$ and calculating the rotation matrix

$$R(\hat{q}_b^e[k]) = I_3 + 2s_q[k]S(r_q[k]) + 2S^2(r_q[k]) \tag{C.15}$$

16: Provide $R(\hat{q}_b^e[k])$, $\hat{b}^b[k]$, $\hat{b}_f^b[k]$, and $\hat{\sigma}[k]$ to the TMO.

17: $k \leftarrow k + 1$.

Algorithm 2 Discrete-Time Loosely Coupled TMO in Indirect Form

Require: Initializing the observer.

1: $\hat{p}^e[0] = p_0^e \in \mathbb{R}^3$, $\hat{v}^e[0] = v_0^e \in \mathbb{R}^3$, $\xi[k] = 0_{3\times 1}$, where p_0 is the initial position and v_0 is the initial velocity.

2: $\hat{x}^-[0] \leftarrow [\hat{p}^e[0]; \hat{v}^e[0]; \xi[0]]$.

3: Assign

$$F = \begin{bmatrix} I_3 & T_{\text{IMU}} I_3 & \frac{T_{\text{IMU}}^2}{2} I_3 \\ 0 & I_3 & T_{\text{IMU}} I_3 \\ 0 & 0 & I_3 \end{bmatrix}, \quad C = \begin{bmatrix} I_3 & 0 & 0 \\ 0 & C_v & 0 \end{bmatrix} \tag{C.16}$$

4: Get R and Q matrices.

Ensure: k,

5: **if** new GNSS measurement is available **then**

6: Get $y[k]$ from GNSS receiver.

7: Correction is applied,

$$K_d[k] = P^-[k]C[k]^\intercal (C[k]P^-[k]C^\intercal[k] + R[k])^{-1}, \tag{C.17}$$

$$\hat{x}^+[k] = \hat{x}^-[k] + K_d[k]\left(y[k] - C[k]\hat{x}^-[k]\right), \tag{C.18}$$

$$P^+[k] = (I_9 - K_d[k]C[k])P^-[k]. \tag{C.19}$$

8: **else**

$$\hat{x}^+[k] = \hat{x}^-[k] \tag{C.20}$$

$$P^+[k] = P^-[k] \tag{C.21}$$

9: **end if**

10: Store the state vector in available estimates

$$\hat{p}^e[k] = \hat{x}^+(1:3)[k], \tag{C.22}$$

$$\hat{v}^e[k] = \hat{x}^+(4:6)[k], \tag{C.23}$$

$$\xi[k] = \hat{x}^+(7:9)[k], \tag{C.24}$$

11: Get $f_{\text{IMU}}^b[k]$ from the IMU,

12: Get $\hat{b}_f^b[k-1]$ from the attitude observer.

13: Provide $\hat{f}^e[k] = R(\hat{q}_b^e[k-1])(f_{\text{IMU}}^b[k] - \hat{b}_f^b[k-1]) + \xi[k]$ to the attitude observer.

14: Get $R(\hat{q}_b^e[k])$, $\hat{\sigma}[k]$ from the attitude observer,

15: Update $B_{d,1}[k]$, $B_d[k]$, $D_d[k]$, $u[k]$.

16: Propagation in time,

$$\hat{x}^-[k+1] = A_d[k]\hat{x}^+[k] + B_{d,1}[k]u[k] + D_d[k], \tag{C.25}$$

$$P^-[k+1] = A_d[k]P^+[k]A_d^\intercal[k] + B_d[k]Q_d[k]B_d^\intercal[k]. \tag{C.26}$$

17: Enforcing symmetry of $P^-[k+1] = 1/2(P^-[k+1] + P^-[k+1]^\intercal)$.

18: $k \leftarrow k+1$.

Algorithm 3 Discrete-Time Tightly Coupled TMO in Indirect Form

Require: Initializing the observer.
1: $\hat{p}^e[0] = p_0^e \in \mathbb{R}^3$, $\hat{v}^e[0] = v_0^e \in \mathbb{R}^3$, $\xi[k] = 0_{3\times 1}$, where p_0 is the initial position and v_0 is the initial velocity.
2: Get $\hat{\beta}[0] = \beta_0$, where β_0 is the initial clock range bias.
3: $\hat{x}^-[0] \leftarrow [\hat{p}^e[0]; \hat{v}^e[0]; \xi[0]]$.
4: Discretize system matrix to $F \in \mathbb{R}^n$.
5: Get R and Q matrices.
Ensure: k,
6: **if** new GNSS measurement is available **then**
7: Get $y[k] = \rho[k]$ (code measurements) from GNSS receiver.
8: Select $m \geq 4$ satellites based on signal strength and geometry.
9: Correct range measurements according to tropospheric disturbance etc.
10: Determine satellite positions, $p_i^e,\ i = 1..m$.
11: Determine geometric range estimate, $\psi_i = \|\hat{p}^e - p_i^e\|_2,\ i = 1..m$.
12: Determine $C[k] \in \mathbb{R}^{4\times m}$ matrix,

$$C[k] = \begin{bmatrix} (\hat{p}^e - p_1^e)/\psi_1 & 1 \\ \vdots & \vdots \\ (\hat{p}^e - p_m^e)/\psi_m & 1 \end{bmatrix} \tag{C.27}$$

13: Correction is applied,

$$K_d[k] = P^-[k]C[k]^\intercal (C[k]P^-[k]C^\intercal[k] + R[k])^{-1}, \tag{C.28}$$

$$\hat{x}^+[k] = \hat{x}^-[k] + K_d[k]\left(y[k] - C[k]\hat{x}^-[k]\right), \tag{C.29}$$

$$P^+[k] = (I_n - K_d[k]C[k])P^-[k]. \tag{C.30}$$

14: **else**

$$\hat{x}^+[k] = \hat{x}^-[k] \tag{C.31}$$

$$P^+[k] = P^-[k] \tag{C.32}$$

15: **end if**
16: Store the state vector in available estimates

$$\hat{p}^e[k] = \hat{x}^+(1:3)[k], \tag{C.33}$$

$$\hat{v}^e[k] = \hat{x}^+(4:6)[k], \tag{C.34}$$

$$\xi[k] = \hat{x}^+(7:9)[k], \tag{C.35}$$

$$\hat{\beta}[k] = \hat{x}^+(10)[k], \tag{C.36}$$

17: Get $f_{\text{IMU}}^b[k]$ from the IMU,
18: Get $\hat{b}_f^b[k-1]$ from the attitude observer.
19: Provide $\hat{f}^e[k] = R(\hat{q}_b^e[k-1])(f_{\text{IMU}}^b[k] - \hat{b}_f^b[k-1]) + \xi[k]$ to the attitude observer.
20: Get $R(\hat{q}_b^e[k])$, $\hat{\sigma}[k]$ from the attitude observer,
21: Update $B_{d,1}[k]$, $B_d[k]$, $D_d[k]$, $u[k]$.
22: Propagation in time,

$$\hat{x}^-[k+1] = A_d[k]\hat{x}^+[k] + B_{d,1}[k]u[k] + D_d[k], \tag{C.37}$$

$$P^-[k+1] = A_d[k]P^+[k]A_d^\intercal[k] + B_d[k]Q_d[k]B_d^\intercal[k]. \tag{C.38}$$

23: Enforcing symmetry of $P^-[k+1] = 1/2(P^-[k+1] + P^-[k+1]^\intercal)$.
24: $k \leftarrow k+1$.

Appendix D

Figures

This appendix includes larger versions of figures included in the previous chapters, to allow for ease of reading.

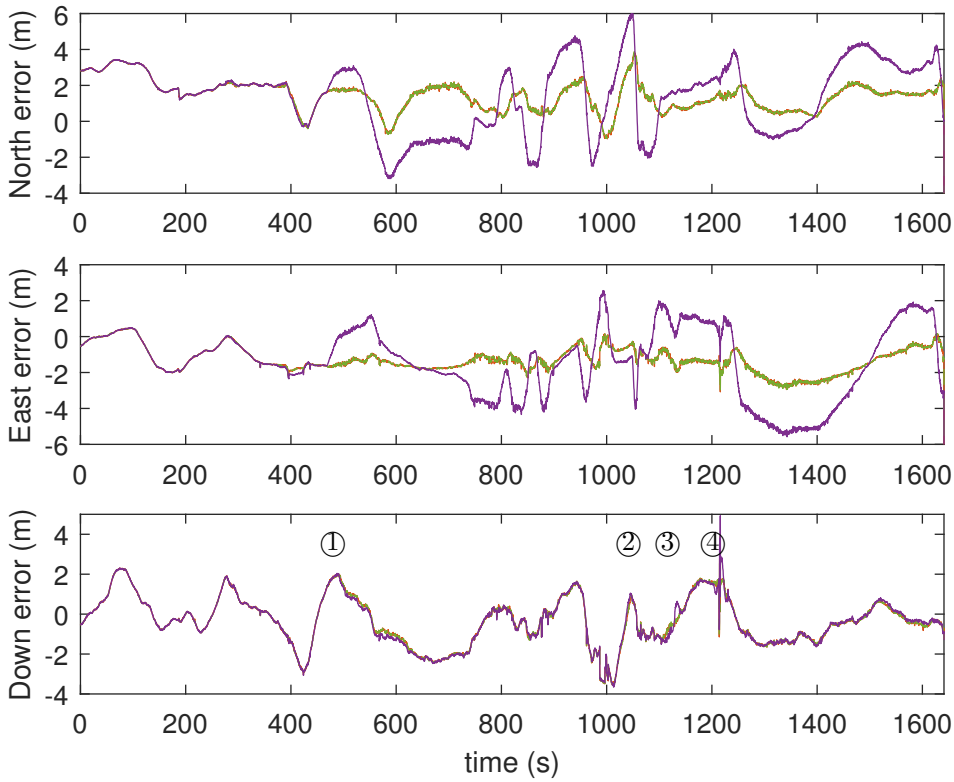

Figure D.1: Position error the proposed observer structure (red), the alternative implementation (green) and the observer without time-delay compensation (purple). See page 89.

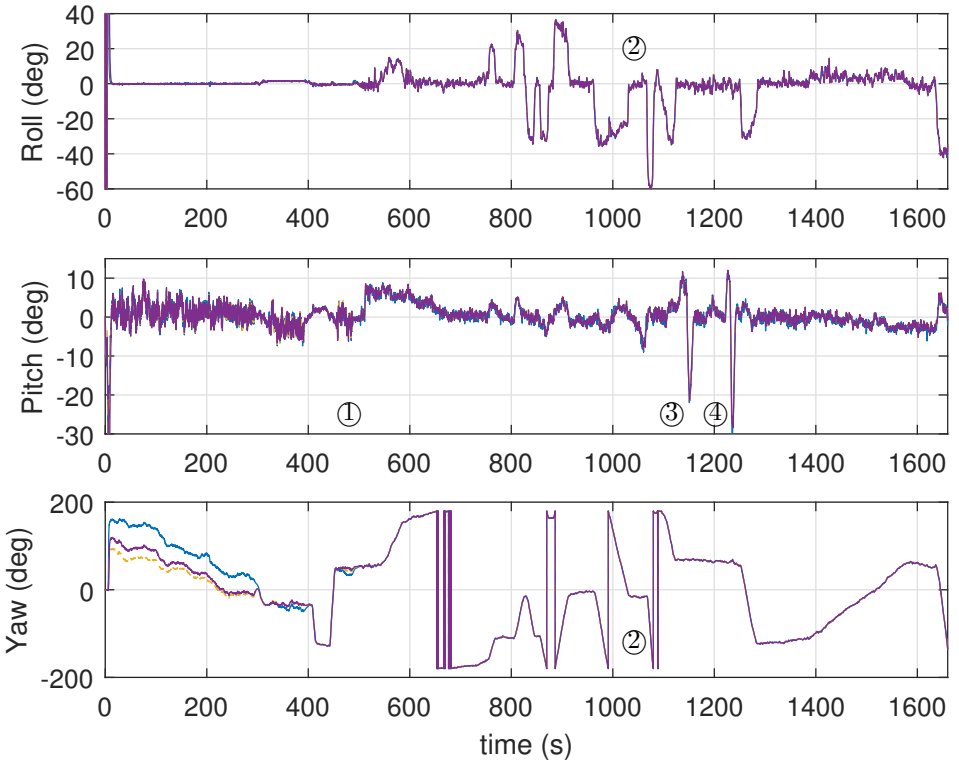

Figure D.2: Attitude estimates of the proposed observer structure (red), the alternative implementation (green) and the observer without time-delay compensation (purple). See page 90.

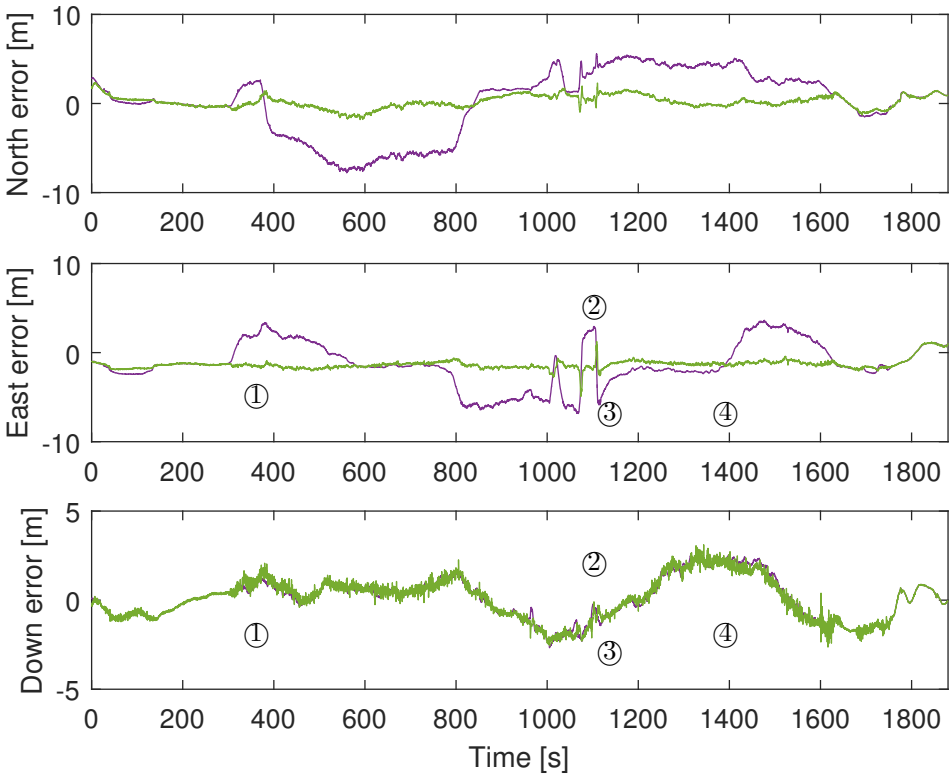

Figure D.3: Estimation errors with proposed (green) and uncompensated (purple). See page 91.

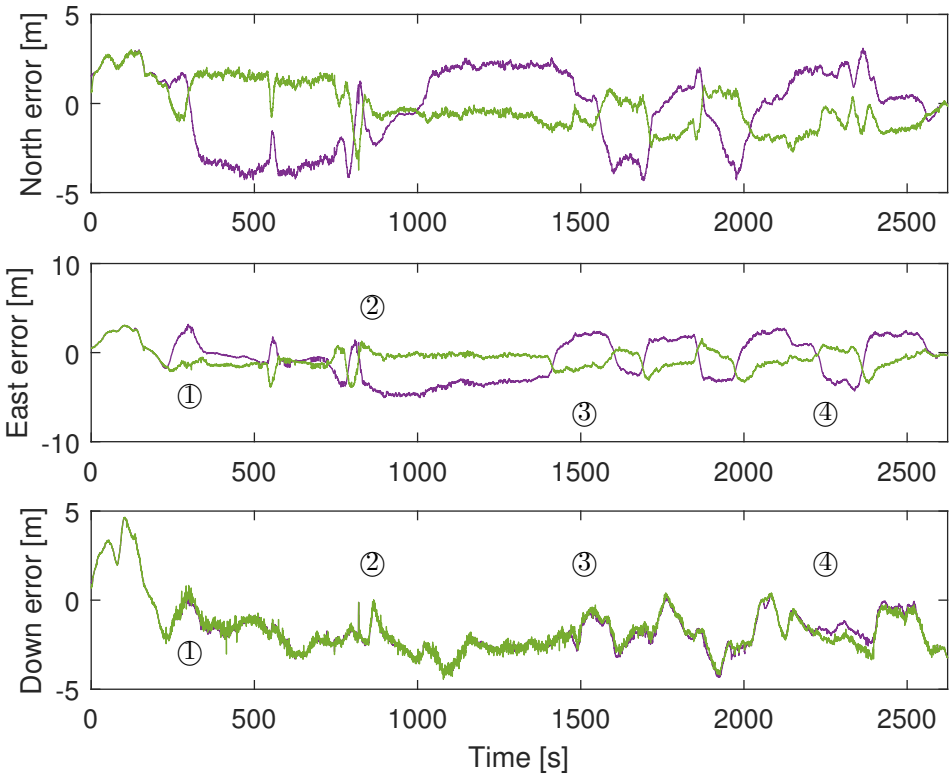

Figure D.4: Estimation errors with proposed (green) and uncompensated (purple). See page 92.

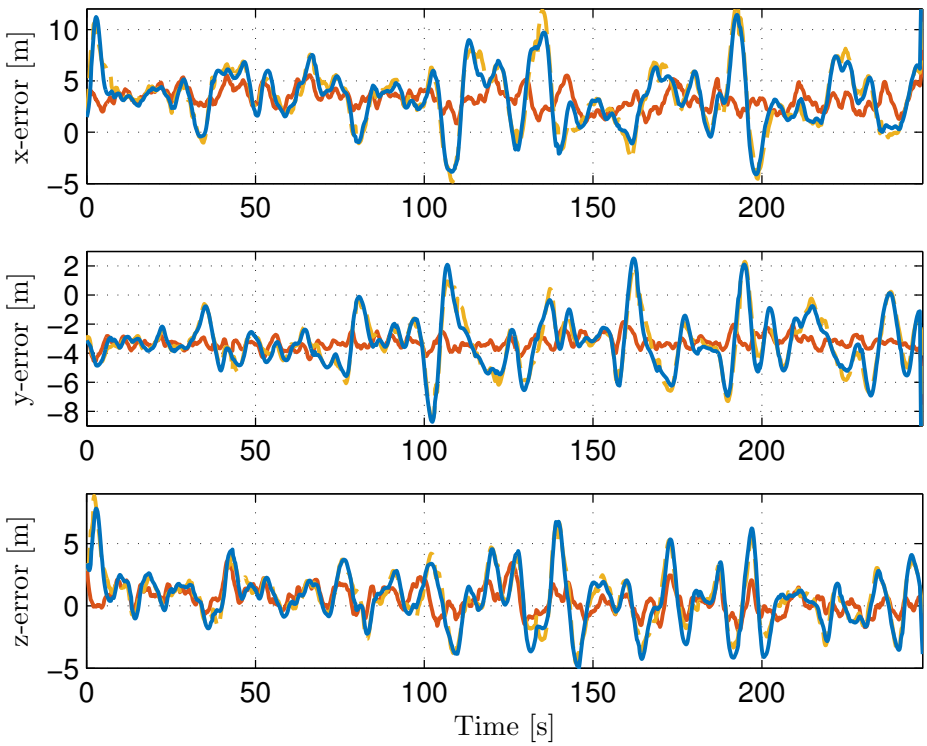

Figure D.5: Position estimation error for NLO-LO (blue), NLO-TI (red), and standalone (yellow). See page 121.

References

[1] T. Ahmed-Ali, I. Karafyllis, and F. Lamnabhi-Lagarrigue. Global Exponential Sampled-Data Observers for Nonlinear Systems with Delay Measurements. *Systems and Control Letters*, Vol. 62:539–549, 2013.

[2] A. Ailon and S. Arogeti. Study on the effects of time-delay on quadrotor-type helicopter dynamics. *Mediterranean Conference on Control and Automation (MED)*, -:305–310, 2014.

[3] P. Albertos and P. Garcia. Predictor-observer-based control of systems with multiple input/output delays. *Journal of Process Control*, 22:1350–1357, 2012.

[4] B. D. O. Anderson. Stability Properties of Kalman-Bucy Filters. *J. Franklin Institute*, 291:137–144, 1971.

[5] A. Bachrach, S. Prentice, R. He, and N. Roy. RANGE - Robust Autonomous Navigation in GPS-denied Environments. *Journal of Field Robotics*, vol. 28, no. 5:pp. 644–666, 2011.

[6] M. Bahrami and M. Zeibart. Doppler-Aided Positioning - Improving Single-Frequency RTK in the Urban Environment. *GPS World - Innovation, Algorithms and Methods*, May:47–56, 2011.

[7] S. Bancroft. An Algebraic Solution to the GPS Equations. *IEEE Trans. Aerospace Electronic Systems*, 21:56–59, 1985.

[8] B. C. Barker, J. W. Betz, J. E. Clark, J. T. Correia, J. T. Gillis, S. Lazar, K. A. Rehborn, and J. R. Straton III. Overview of the GPS M Code Signal. *Proc. ION NTM*, pages pp. 542–549, 2000.

[9] P. Batista. GES Long Baseline Navigation with Clock Offset Estimation. In *Proc. European Control Conference, Strasbourg, France*, pages 3011–3016, 2014.

[10] P. Batista. Long Baseline Navigation With Clock Offset Estimation and Discrete-Time Measurements. *Control Engineering Practice*, 35:43–53, 2015.

[11] P. Batista. GES Long Baseline Navigation With Unkown Sound Velocity and Discrete-Time Range Measurements. *IEEE Transactions on Control Systems Technology*, 23:219–230, 2015.

[12] P. Batista, C. Silvestre, and P. Oliveira. GES Attitude Observers - Part I: Multiple General Vector Observations. *IFAC World Congress*, pages 2985–2990, 2011.

[13] P. Batista, C. Silvestre, and P. Oliveira. GES Attitude Observers - Part II: Single Vector Observations. *IFAC World Congress*, pages 2991–2996, 2011.

[14] P. Batista, C. Silvestre, and P. Oliveira. Single Range Aided Navigation and Source LocalizLocal: Observability and Filter Design. *Systems and Control Letters*, 60:665–673, 2011.

[15] P. Batista, C. Silvestre, and P. Oliveira. GAS Tightly Coupled LBL/USBL Position and Velocity Filter for Underwater Vehicles. In *Proc. European Control Conference, Zurich, Switzerland*, pages 2982–2987, 2013.

[16] P. Batista, C. Silvestre, and P. Oliveira. Sensor-based long baseline navigation: observability analysis and filter design. *Asian J. Control*, 16:974–994, 2014.

[17] P. Batista, C. Silvestre, and P. Oliveira. Tightly Coupled Long Baseline/Ultra-Short Baseline Integrated Navigation System. *International Journal of Systems Science*, pages 1–19, 2014.

[18] S. Battilotti. Nonlinear Predictors for Systems with Bounded Trajectories and Delayed Measurements. *Automatica*, 59:127–138, 2015.

[19] R. W. Beard and T. W. McLain. *Small Unmanned Aircraft - Theory and Practice*. Princeton University Press, 2012.

[20] C. J. Benton and C. N. Mitchell. Isolating the Multipath Component in GNSS Signal-to-Noise Data and Locating Reflecting Objects. *Radio Science*, Vol. 46:1–11, 2011.

[21] S. P. Bhat and D. S. Bernstein. A Topological Obstruction to Continuous Global Stabilization of Rotational Motion and the Unwinding Phenomenon. *Systems and Control Letters*, 39:63–70, 2000.

[22] M. Blanke. Fault-tolerant and Diagnostic Methods for Navigation. *International Conference on Marine Engineering Systems (ICMES)*, pages 1–6, 2003.

[23] M. Blanke. Fault-tolerant Sensor Fusion for Mairne Navigation. *IFAC Conference on Maneuvering and Control of Marine Craft*, pages 1–6, 2006.

[24] K. T. Borup, T. I. Fossen, and T. A. Johansen. A Nonlinear Model-Based Wind Velocity Observer for Unmanned Aerial Vehicles. *10th IFAC Symposium on Nonlinear Control Systems*, 2016.

[25] A. Brack. On Reliable Data-Driven Partial GNSS Ambiguity Resolution. *GPS Solution*, 19:411–422, 2015.

[26] A. Brack. Partial Ambiguity Resolution for Reliable GNSS Positioning - a Useful Tool? *IEEE Aerospace Conference*, 2016.

[27] C. Briat. *Linear Parameter-Varying and Time-Delay Systems - Analysis, Observation, Filtering and Control*. Springer, 2014.

[28] R. G. Brown and Y. C. Hwang. *Introduction to Random Signals and Applied Kalman Filtering*. John Wiley & Sons, Inc. New York, 1998.

[29] A. Bry, A. Bachrach, and N. Roy. State Estimation for Aggressive Flight in GPS-denied Environments using Onboard Sensing. *Proc. IEEE Int. Conf. Robotics Automation*, 2012.

[30] T. H. Bryne, T. I. Fossen, and T. A. Johansen. Nonlinear Observer with Time-Varying Gains for Inertial Navigation Aided by Satellite Reference Systems in Dynamic Positioning. *Mediterranean Conference on Control and Automation (MED)*, 1:1353–1360, 2014.

[31] T. H. Bryne, J. M. Hansen, R. H. Rogne, N. Sokolova, T. I. Fossen, and T. A. Johansen. Nonlinear Observers for Integrated INS/GNSS Navigation - Implementation Aspects. *IEEE Control Systems Magazine*, (to appear), 2017.

[32] J. Chaffee and J. Abel. On the Exact Solutions of Pseudorange Equations. *IEEE Trans. Aerospace and Electronic Systems*, 30:1021–1030, 1994.

[33] A. Chen, D. Zheng, A. Ramanandan, and J. A. Farrell. INS Aided GPS Integer Ambiguity Resolution. *IEEE International Conference on Control Applications (CCA), Part of 2011 IEEE Multi-Conference on Systems and Control.*, -:567–572, 2011.

[34] A. Chen, D. Zheng, A. Ramanandan, and J. A. Farrell. Near-real-time GPS Integer Ambiguity Resolution. *IEEE Conference on Decision and Control and European Control Conference*, pages 7281–7286, 2011.

[35] D. Chen and G. Lachapelle. A Comparison of the FASF and Least-Squares Search Algorithms for on-the-fly Ambiguity Resolution. *Navigation: Journal of The Institute of Navigation*, Vol. 42, No. 2:pp. 371–390, 1995.

[36] Y. Chen, S. Zhao, and J. A. Farrell. Computationally Efficient Carrier Integer Ambiguity Resolution in Multiepoch GPS/INS: A Common-Position-Shift Approach. *IEEE Transactions on Control Systems Technology*, pages 1–16, 2015.

[37] Z. Chen. Bayesian filtering: From kalman filters to particle filters, and beyond. *Statistics*, 182(1):1–69, 2003.

[38] C. C. Counselman and S. A. Gourevitch. Miniature Interferometer Terminals for Earth Surveying: Ambiguity and Multipath with Global Positioning System. *IEEE Transactions on Geoscience and Remote Sensing*, Vol. GE-19, No. 4:244–252, 1981.

[39] J. L. Crassidis, F. L. Markley, and Y. Cheng. Survey of nonlinear attitude estimation methods. *Journal of Guidance, Control, and Dynamics*, 30(1): 12–28, 2007.

[40] D. Dardari, E. Falletti, and M. Luise. *Satellite and Terrestrial Radio Positioning Techniques*. Academic Press, 2012.

[41] T. Dautermann, C. Mayer, F. Antreich, A. Konovaltsev, B. Belabbas, and U. Kälberer. Non-Gaussian Error Modeling for GBAS Integrity Assessment. *IEEE Transactions on Aerospace and Electronic Systems*, Vol. 48:693–706, 2012.

[42] P. F. de Bakker, H. van der Marel, and C. C. J. M. Tiberius. Geometry-Free Undifferenced, Single and Double Differenced Analysis of Single Frequency GPS, EGNOS and GIOVE-A/B Measurements. *GPS Solution*, 13:305–314, 2009.

[43] P. F. de Bakker, C. C. J. M. Tiberius, H. van der Marel, and R. J. P. van Bree. Short and Zero Baseline Analysis of GPS L1 C/A, L5Q, GIOVE E1B, and E5aQ Signals. *GPS Solution*, 16:53–64, 2012.

[44] P. de Jonge and C. Tiberius. The LAMBDA Method for Integer Ambiguity Estimation: Implementation Aspects. *Publications of the Delft Geodetic Computing Centre, LGR-Series*, -:–, 1996.

[45] H. G. de Marina, F. J. Pereda, J. M. Giron-Sierre, and F. Espinosa. UAV Attitude Estimation using Unscented Kalman Filter and TRIAD. *IEEE Trans. on Industrial Electronics*, vol. 59, no. 11:pp. 4465–4474, 2012.

[46] B. DeCleene. Defining Pseudorange Integrity-Overbounding. *Proc. 13th International Technical Meeting of the Satellite Division of the Institute of Navigation*, 2000.

[47] G. Dissanayake, S. Sukkarieh, E. Nebot, and H. Durrant-Whyte. The aiding of a lowcost strapdown inertial measurement unit using vehicle model constraints for land vehicle applications. *IEEE Transactions on Robotics and Automation*, 17(5):731–747, 2001.

[48] A. Doucet and A. M. Johansen. A Tutorial on Particle Filtering and Smoothing: Fifteen years later. *in Oxford Handbook of Nonlinear Filtering (C. Crisan and B. Rozovsky, Oxford)*, pages 656–704, 2011.

[49] A. Doucet, N. de Freitas, and N. Gordon. *Sequential Monte Carlo Methods in Practice*. New York: Springer, 2001.

[50] A. Draganov, L. Haas, and M. Harlacher. The IMRE Kalman Filter - A New Kalman Filter Extension for Nonlinear Applications. *Proc. IEEE/ION PLANS*, pages 428–440, 2012.

[51] M. Euston, P. Coote, R. Mahony, J. Kim, and T. Hamel. A Complementary Filter for Attitude Estimation of a Fixed-wing UAV. *IEEE International Conference on Intelligent Robots and Systems*, 2008.

[52] J. A. Farrell. *Aided Navigation: GPS with High Rate Sensors*. McGraw Hill, 2008.

[53] J. A. Farrell, T. D. Givargis, and M. J. Barth. Real-Time Differential Carrier Phase GPS-Aided INS. *IEEE Transactions on Control Systems Technology*, 8, 4:709–720, 2000.

[54] Y. Feng. GNSS Three Carrier Ambiguity Resolution using Ionosphere-Reduced Virtual Signals. *Journal of Geodesy*, 82(12):847–862, 2008.

[55] T. I. Fossen. *Handbook of Marine Craft Hydrodynamics and Motion Control*. John Wiley & Sons, Ltd, 2011.

[56] D. C. Fraser and J. E. Potter. The Optimum Linear Smoother as a Combination of Two Optimum Linear Filters. *IEEE Trans. on Automatic Control*, Vol. 7:387–390, 1969.

[57] E. Frei and G. Beutler. Rapid Static Positioning Based on the Fast Ambiguity Resolution Approach "FARA": Theory and First Results. *Manustripta Geodaetica*, Vol. 15, No. 4:pp. 325–356, 1990.

[58] E. Fridman. *Introduction to Time-Delay Systems - Analysis and Control*. Springer, 2014.

[59] L. Fusini, T. I. Fossen, and T. A. Johansen. A Uniformly Semiglobally Exponentially Stable Nonlinear Observer for GNSS- and Camera-Aided Inertial Navigation. *Proc. 22nd IEEE Mediterranean Conference on Control and Automation, Italy*, pages 1031–1036, 2014.

[60] L. Fusini, J. Hosen, H. H. Helgesen, T. A. Johansen, and T. I. Fossen. Experimental Validation of a UnUniform Semi-globally Exponentially Stable Non-linear Observer for GNSS- and Camera-aided Inertial Navigation for Fixed-wing UAVs. *International Conference on Unmanned Aircraft Systems, Denver*, 2015.

[61] J. D. Gautier and B. W. Parkinson. Using the GPS/INS Generalized Evaluation Tool (GIGET) for the Comparison of Loosely Coupled, Tightly Coupled and Ultra-Tightly Coupled Integrated Navigation Systems. *Proc. ION CIGTF*, pages 65–76, 2003.

[62] A. Gelb, J. F. K. Jr., R. A. N. Jr., C. F. Price, and A. A. S. Jr. *Applied Optimal Estimation*. MIT Press. Boston, MA, 1988.

[63] M. George and S. Sukkarieh. Tightly Coupled INS/GPS With Bias Estimation for UAV Application. *Proceedings of Australiasian Conference on Robotics and Automation (ACRA)*, -:–, 2005.

[64] C. Goad and L. Goodman. Modified Hopfield Tropospheric Refraction Correction Model. *Transations - American Geophysical Union*, Vol. 55, 1974.

[65] N. J. Gordon, D. J. Salmond, and A. F. M. Smith. A Novel Approach to Nonlinear/Non-Gaussian Bayesian State Estimation. *Proc. IEE Radar Signal Process*, Vol. 140:170–113, 1993.

[66] D. Grejner-Brzezinska and C. K. Toth. Performance Study of High-End Dual Frequency GPS Receivers Tightly Integrated with a Strapdown INS. *Proc. 3rd International Symposium on Mobile Mappig*, 2001.

[67] D. A. Grejner-Brzezinska, R. Da, and C. Toth. GPS Error Modeling and OTF Ambiguity Resolution for High-Accuracy GPS/INS Integrated System. *Journal of Geodesy*, Vol. 72:626–638, 1998.

[68] M. S. Grewal and A. P. Andrews. Kalman Filtering: Theory and Practice using MATLAB. *John Wiley & Sons*, 2011.

[69] M. S. Grewal, L. R. Weill, and A. P. Andrews. *Global Positioning Systems, Inertial navigation, and Integration*. John Wiley & Sons, Ltd, 2007.

[70] H. F. Grip, T. I. Fossen, T. A. Johansen, and A. Saberi. A Nonlinear Observer for Integration of GNSS and IMU Measurements with Gyro Bias Estimation. *Proceedings of the American Control Conference*, 2012.

[71] H. F. Grip, T. I. Fossen, T. A. Johansen, and A. Saberi. Attitude Estimation Using Biased Gyro and Vector Measurements With Time-Varying Reference Vectors. *IEEE Transactions on Automatic Control*, 57:1332–1338, 2012.

[72] H. F. Grip, T. I. Fossen, T. A. Johansen, and A. Saberi. Nonlinear Observer for GNSS-Aided Inertial Navigation with Quaternion-Based Attitude Estimation. *American Control Conference*, -:272–279, 2013.

[73] H. F. Grip, T. I. Fossen, T. A. Johansen, and A. Saberi. Globally Exponentially Stable Attitude and Gyro Bias Estimation with Application to GNSS/INS Integration. *Automatica*, 51:158–166, 2015.

[74] H. F. Grip, T. I. Fossen, T. A. Johansen, and A. Saberi. Nonlinear Observer for Attitude, Position and Velocity: Theory and Experiments. *Chapter 17 in "Multisensor Attitude Estimation" (H. Fourati and D. C. Belkhia, Eds.), CRC Press (Taylor & Francis Group)*, pages 291–314, 2016.

[75] J. N. Gross, Y. Gu, and B. Dewberry. Tightly-Coupled GPS/UWB-Ranging for Relative Navigation During Format Flight. *ION GNSS*, 2014.

[76] P. D. Groves. *Principles of GNSS, Inertial, and Multisensor Integrated Navigation Systems*. Artech House, 2013.

[77] K. Gryte, J. M. Hansen, T. A. Johansen, and T. I. Fossen. Robust Navigation of UAV using Inertial Sensors Aided by UWB and RTK GPS. *AIAA Guidance, Navigation, and Control Conference*, (to appear), 2017.

[78] K. Gu and S.-I. Niculescu. Advanced Topics in Control Systems Theory. *Chapter 4 in Lecture Notes in Control and Information Science (A. Loria, F. Lamnabhi-Lagarrigue, E. Panteley)*, 328:139–170, 2006.

[79] F. Gustafsson. *Statistical Sensor Fusion*. Studentliteratur, 2012.

[80] F. Gustafsson, F. Gunnarsson, N. Bergman, U. Forssell, J. Jansson, R. Karlsson, and P. J. Nordlund. Particle Filters for Positioning, Navigation and Tracking. *IEEE Trans. on Signal Processing*, Vol. 50:425–437, 2002.

[81] T. Hamel. and R. Mahony. Attitude Estimation on SO(3) Based on Direct Inertial Measurements. *Proc. IEEE Int. Conf. Robotics Automation*, pages 2170–2175, 2006.

[82] S. Han and C. Rizos. Improving the Computational Efficiency of the Ambiguity Function Algorithm. *Journal of Geodesy*, Vol. 70, Issue 6:pp. 330–341, 1996.

[83] J. M. Hansen, T. I. Fossen, and T. A. Johansen. Nonlinear Observer for INS Aided by Time-Delayed GNSS Measurements - Implementation and UAV Experiments. *Proc. of International Conference on Unmanned Aircraft Systems, Denver*, pages pp. 157–166, 2015.

[84] J. M. Hansen, T. A. Johansen, and T. I. Fossen. Tightly Coupled Integrated Inertial and Real-Time-Kinematic Poisitioning Approach Using Nonlinear Observer. *American Control Conference, Boston*, pages pp. 5511–5518, 2016.

[85] J. M. Hansen, J. Roháč, M. Šipoš, T. A. Johansen, and T. I. Fossen. Validation and Experimental Testing of Observers for Robust GNSS-Aided Inertial Navigation. *Chapter 6 in the book "Recent Advances in Robotics Systems", Intech, Editor: Guanghui Wang, ISBN 978-953-51-2571-6, Print ISBN 978-953-51-2570-9*, 2016.

[86] J. M. Hansen, T. I. Fossen, and T. A. Johansen. Nonlinear Observer Design for GNSS-Aided Inertial Navigation Systems with TIme-Delayed GNSS Measurements. *Control Engineering Practice*, (to appear), 2017.

[87] J. M. Hansen, T. A. Johansen, N. Sokolova, and T. I. Fossen. Nonlinear Observer for Tightly-Coupled Integrated Inertial Navigation Aided by RTK-GNSS Measurements. *IEEE Transactions on Control Systems Technology*, (submitted), 2017.

[88] R. Hatch. Instantaneous Ambiguity Resolution. *Proc. of KIS'90*, pages pp. 299–308, 1990.

[89] P. E. Henderson, J. F. Raquet, and P. S. Maybeck. A Multiple Filter Approach for Precise Kinematic DGPS Positioning and Carrier-Phase Ambiguity Resolution. *Navigation*, 49:149–160, 2002.

[90] E. Hendricks, O. Jannerup, and P. H. Sørensen. *Linear Systems Control - Deterministic and Stochastic Methods*. Springer, 2008.

[91] R. Hirokawa and T. Ebinuma. A Low-Cost Tightly Coupled GPS/INS for Small UAVs Augmented with Multiple GPS Antennas. *Navigation: JION*, Vol. 56, No. 1:35–44, 2009.

[92] M. M. Hoque and N. Jakowski. Higher Order Ionospheric Effects in Precise GNSS Positioning. *Journal of Geodesy*, 81:259–268, 2007.

[93] R. A. Horn and C. R. Johnson. *Matrix Analysis*. Cambridge, 2 edition, 2013.

[94] M.-D. Hua. Attitude Estimation for Accelerated Vehicles using GPS/INS Measurements. *Control Engineering Practice*, 18:723–732, 2010.

[95] M.-D. Hua, G. Ducard, T. Hamel, R. Mahony, and K. Rudin. Implementation of a Nonlinear Attitude Estimator for Aerial Robotic Vehicles. *IEEE Transactions on Control Systems Technology*, 22, No 1.:201–213, 2014.

[96] M. D. Hua, G. D. D. Hamel, and R. Mahony. Introduction to Nonlinear Attitude Estimation for Aerial Robotic Systems. *Aerospace Lab*, Issue 8: AL08–04, 2014.

[97] G. Jacovitti and G. Scarano. Discrete Time Techniques for Time Delay Estimation. *IEEE Transactions on Signal Processing*, 41:525–533, 1993.

[98] T. A. Johansen and T. I. Fossen. Nonlinear Observer for Inertial Navigation Aided by Pseudo-Range and Range-Rate Measurements. *European Control Conference*, 2015.

[99] T. A. Johansen and T. I. Fossen. The eXogenous Kalman Filter (XKF). *International Journal of Control*, 2017.

[100] T. A. Johansen, A. Cristofaro, K. L. Sørensen, J. M. Hansen, and T. I. Fossen. On Estimation of Wind Velocity, Angle-of-Attack and Sideslip Angle of Small UAVs using Standard Sensors. *Proc of International Conference on Unmanned Aircraft Systems, Denver*, pages pp. 510–519, 2015.

[101] T. A. Johansen, J. M. Hansen, and T. I. Fossen. Nonlinear Observer for Tightly Integrated Inertial Navigation Aided by Pseudo-Range Measurements. *ASME J. Dynamic Systems, Measurement and Control*, Vol. 139, Paper DS-15-1088, 2017; DOI 10.1115/1.4034496, 2017.

[102] P. Joosten and C. Tiberius. LAMBDA: FAQs. *GPS Solutions*, 6:109–114, 2002.

[103] J. M. Juan, J. Sanz, M. Hermandez-Pajares, J. Samson, M. Tossaint, A. Aragon-Angel, and D. Salazar. Wide Area RTK: A Satellite Navigation System Based on Precise Real-Time Ionospheric Modelling. *Radio Science*, Vol. 47, 2016.

[104] S. J. Julier and J. K. Uhlmann. A New Extension of the Kalman Filter to Nonlinear Systems. *Proc. SPIE Signal Processing, Sensor Fusion, and Target Recognition VI*, 3068:182–193, 1997.

[105] R. E. Kalman. A New Approach to Linear Filtering and Prediction Theory. *Trans. Amer. Soc. of Mech. Eng., Series D, Journal of Basic Eng.*, Vol 82: 35–45, 1960.

[106] R. E. Kalman and R. S. Bucy. New Results in Linear and Prediction Theory. *Trans. Amer. Soc. of Mech. Eng., Series D, Journal of Basic Eng.*, Vol. 83: 95–108, 1961.

[107] H. K. Khalil. *Nonlinear Systems (Third Edition)*. Prentice Hall, 2002.

[108] A. Khosravian, J. Trumpf, R. Mahony, and T. Hamel. Velocity Aided Attitude Estimation on SO(3) with Sensor Delay. *IEEE Conference on Decision and Control*, 14:114–120, 2014.

[109] A. Khosravian, J. Trumpf, R. Mahony, and T. Hamel. Recursive Attitude Estimation in the Presence of Multi-rate and Multi-delay Vector Measurements. *American Control Conference*, -:–, 2015.

[110] A. Khosravian, J. Trumpf, R. Mahony, and C. Lageman. Observers for Invariant Systems on Lie Groups with Biased Input Measurements and Homogeneous Outputs. *Automatica*, -:–, 2015.

[111] D. Kim and R. B. Langley. An Optimized Least-Squares Technique for Improving Ambiguity Resolution Performance and Computational Efficiency. *Proc. of ION GPS'99*, pages pp. 1579–1588, 1999.

[112] D. Kim and R. B. Langley. GPS Ambiguity Resolution and Validation: MethodoMethod, Trends and Issues. *Proc. 7th GNSS Workshop - International Symposium on GPS/GNSS*, 2000.

[113] D. B. Kingston and R. W. Beard. Real-Time Attitude and Position Estimation for Small UAVs Using Low-Cost Sensors. *American Institute of Aeronautics and Astronautics, "Unmanned Unlimited"*, -:1–9, 2004.

[114] KVH Industries Inc. Guide to Comparing Gyro and IMU Technologies - Micro-Electro-Mechanical Systems and Fiber Optic Gyros. Technical report, KVH Industries, Inc, 2014.

[115] S. Leutenegger and R. Siegwart. A Low-Cost and Fail-Safe Inertial Navigation System for Airplanes. *IEEE Conference on Robotics and Automation*, 2012.

[116] M. Li and A. I. Mourikis. Online Temporal Calibration for Camera-IMU Systems: Theory and Algorithms. *The International Journal of Robotics Research*, Vol. 33 (7):pp. 947–964, 2014.

[117] Y. Li, J. Wang, C. Rizos, P. Mumford, and W. Ding. Low-Cost Tightly Coupled GPS/INS Integration Based on a Nonlinear Kalman Filtering Design. *ION*, 2006.

[118] D. T. Magill. Optimal Adaptive Estimation of Sampled Stochastic Processes. *IEEE Trans. on Automatic Control*, Vol. AC-10:434–439, 1965.

[119] R. Mahony, T. Hamel, and J.-M. Pflimlin. Nonlinear Complementary Filters on the Special Orthogonal Group. *IEEE Transactions on Automatic Control*, 53, No 5:1203–1218, 2008.

[120] R. Mahony, T. Hamel, J. Trumpf, and C. Lageman. Nonlinear Attitude Observer on SO(3) for Complementary and Compatible Measurements: A Theoretical Study. *IEEE Conference on Decision and Control*, pages 6407–6412, 2009.

[121] R. Mahony, M. Euston, J. Kim, P. Coote, and T. Hamel. A Non-linear Observer for Attitude Estimation of a Fixed-Wing Unmanned Aerial Vehicle without GPS Measurements. *Transations of the Institute of Measurement and Control*, 33, 6.:pp. 699–717, 2011.

[122] F. L. Markley. Attitude error representations for Kalman filtering. *Journal of guidance, control, and dynamics*, 26(2):311–317, 2003.

[123] MathWorks®. gravityzonal: Implement zonal harmonic representation of planetary gravity. Technical report, MathWorks®, Matlab®: https://se.mathworks.com/help/aerotbx/ug/gravityzonal.html, Introduced in R2009b.

[124] MathWorks®. igrfmagm: International Geomagnetic Reference Field. Technical report, MathWorks®, Matlab®: https://se.mathworks.com/help/aerotbx/ug/igrfmagm.html, Introduced in R2015b.

[125] R. K. Mehra. Approaches to Adaptive Filtering. *IEEE Symposium on Adaptive Processess, Decision and Control*, 1970.

[126] P. Misra and P. Enge. *Global Positioning System - Signals, Measurements, and Performance*. Ganga-Jamuna Press, 2006.

[127] S. Miura, L.-T. Hsu, F. Chen, and S. Kamijo. GPS Error Correction With Pseudorange Evaluation Using Three-Dimensional Map. *IEEE Trans. on Intelligent Transportation Systems*, Vol. 16, No. 6:3104–3115, 2015.

[128] S. Moafipoor, D. A. Grejner-Brzezinska, and C. K. Toth. Tightly Coupled GPS/INS Integration Based on GPS Carrier Phase Velocity Update. *ION NTM*, -:–, 2004.

[129] A. H. Mohammed and K. P. Schwarz. Adaptive Kalman Filtering for INS/GPS. *Journal of Geodesy*, Vol. 73:193–203, 1999.

[130] S. C. Mohleji and G. Wang. Modeling ADS-B position and velocity errors for airborne merging and spacing in interval management application. Available online at http://www.mitre.org/publications/technical-papers/, The MITRE Corporation, 7515 Colshire Drive, McLean VA 22102, September 2010 (last accessed Des, 2015).

[131] M. Morgado, P. Batista, P. Oliveira, and C. Silvestre. Position and Velocity USBL/IMU Sensor-based Navigation Filter. In *Proc. IFAC World Congress, Milano*, pages 13642–13647, 2011.

[132] R. Munguia and A. Grau. A Practical Method for Implementing an Attitude and Heading Reference System. *International Journal of Advanced Robotic Systems*, 11(62), 2014.

[133] S. C. Mushini, P. T. Jayachandran, R. B. Langley, J. W. MacDougall, and D. Pokhotelov. Improved Amplitude- and Phase-scintillation indices derived from Wave Detrended High-latitude GPS Data. *GPS Solution*, Vol. 16:p. 363–373, 2012.

[134] F. Niu, Y. Morton, J. Wang, and W. Pelgrum. GPS Carrier Phase Detrending Methods and Performances for Ionosphere Scintillation Studies. *International Technical Meeting of The Insitute of Navigation*, 2012.

[135] Official U. S. Government Information About the Global Positioning System (GPS) and Related Topics. Webpage, http://www.gps.gov/systems/gps/modernization/civilsignals/. Technical report, GPS.gov is maintained by the National Coordination Office for Space-Based Positioning, Navigation, and Timing., Visited 12 Nov. 2016.

[136] F. Olsson, J. Rantakokko, and J. N. rds. Cooperative Localization Using a Foot-mounted Inertial Navigation System and Ultrawideband Ranging. *International Conference on Indoor Positioning and Indoor Navigation*, pages 122–131, 2014.

[137] A. Papachristodoulou, M. Peet, and S. Lall. Constructing Lyapunov-Krasovskii Functionals For Linear Time Delay Systems. *American Control Conference*, 4:2845–2850, 2005.

[138] M. Petovello. The Differences in Differencing. *Inside GNSS - GNSS Solutions*, September/October:28–32, 2011.

[139] M. G. Petovello and P. G. Mattos. Markets and Multi-Frequency GNSS. *Inside GNSS - GNSS Solutions*, January/February, 2013.

[140] M. G. Petovello, A. Grant, and P. Williams. GPS Jamming and Linear Carrier Phase Combinations. *Inside GNSS - GNSS Solutions*, January/February, 2009.

[141] M. G. Petovello, K.O'Keefe, G. Lachapelle., and M. E. Cannon. Consideration of Time-Correlated Errors in a Kalman Filter Application to GNSS. *Journal of Geodesy*, Vol. 83, No. 1:51–56, 2009.

[142] M. G. Petovello, K. O'Keefe, B. Chan, S. Spiller, C. Pedrosa, P. Xie, and C. Basnayake. Demonstration of Inter-Vehicle UWB Ranging to Augment DGPS for Improved Relative Positioning. *Journal of Global Positioning Systems*, Vol. 11, No. 1:11–21, 2012.

[143] M. G. Petovello, S. Feng, and W. Ochieng. How do you Trust Centimeter Level Accuracy Positioning? *Inside GNSS - GNSS Solutions*, September/October, 2014.

[144] T. Raff and F. Allgöwer. An EKF-Based Observer For Nonlinear Time-Delay Systems. *American Control Conference*, -:4, 2006.

[145] J. Rankin. GPS and Differential GPS: An Error Model for Sensor Simulation. In *IEEE Position Location and Navigation Symposium*, pages 260–266, Las Vegas, NV, 11–15. Apr 1994.

[146] H. E. Rauch, F. Tung, and C. T. Striebel. Maximum Likelihood Estimates of Linear Dynamic Systems. *AIAA Journal*, Vol. 3:1445–1450, 1965.

[147] K. Reif, F. Sonnemann, and R. Unbehauen. An EKF-based Nonlinear Observer with a Prescribed Degree of Stability. *Automatica*, 34:1119–1123, 1998.

[148] B. Ristic, S. Arulampalam, and N. J. Gordon. *Beyond the Kalman Filter: Particle Filters for Tracking Applications*. Artech house, 2004.

[149] A. Roberts and A. Tayebi. On the Attitude Estimation of Accelerating Rigid-Bodies Using GPS and IMU Measurements. *50th IEEE Conference on Decision and Control, European Control Conference (CDC-ECC)*, -:8088–8093, 2011.

[150] S. Salcudean. A Globally Convergent Angular Velocity Observer for Rigid Body Motion. *IEEE Trans. on Automatic Control*, Vol. 36:1493–1497, 1991.

[151] B. F. L. Scala, R. R. Bitmead, and M. R. James. Conditions for Stability of the Extended Kalman Filter and Their Application to the Frequency Tracking Problem. *Mathematics of Control, Signals, and Systems*, 8:1–26, 1995.

[152] G. T. Schmidt. INS/GPS Technology Trends. *NATO. USA: Charles Stark Draper Laboratory, Cambridge, RTO-EN-SET-116*, 2010.

[153] S. F. Schmidt. Application of State-Space Methods to Navigation Problems. *in Advances in Control Systems: Theory and Applications*, Vol. 3, New York: Academic Press:293–340, 1966.

[154] M. Seppänen, J. Ala-Luhtala, R. Piché, S. Martikainen, and S. Ali-Löytty. Autonomous prediction of GPS and GLONASS satellite orbits. *Navigation*, 59, no 2:119–134, 2012.

[155] L. Serrano, D. Kim, and R. B. Langley. A Single GPS Receiver as a Real-Time, Accurate Velocity and Acceleration Sensor. *Proceedings of the the 17th International Technical Meeting of the Satellite Division of The Institute of Navigation (ION GNSS 2004), Long Beach, CA, USA*, 2124, 2004.

[156] M. Shuster and S. Oh. Three-Axis Attitude Determination for Vector Observations. *J. Guidance, Control and Dynamics*, 4:70–77, 1981.

[157] M. Siccardi, D. Rovera, and S. Romisch. Delay Measurements of PPS Signals in Timing Systems. *Frequency Control Symposium*, 2016.

[158] I. Skog and P. Händel. Effects of time synchronization errors in GNSS-aided INS. In *Position, Location and Navigation Symposium, 2008 IEEE/ION*, pages 82–88, May 2008.

[159] I. Skog and P. Händel. Time Synchronization Errors in Loosely Coupled GPS-Aided Inertial Navigation Systems. *IEEE Transactions on Intelligent Transportation Systems*, 12:1014–1023, 2011.

[160] P. D. Solomon, J. Wang, and C. Rizos. Latency Determination and Compensation in Real-Time GNSS/INS Integrated Navigation Systems. *International Archives of the Photogrammetry, Remote Sensing and Spatial Information Sciences*, XXXVIII-1/C22:–, 2011.

[161] M. Sotak, M. Sopata, and F. Kmec. Navigation Systems using Monte Carlo Method. *Guidance, Navigation and Control Systems*, 2006.

[162] L. Stimac and T. A. Kennedy. Sensor Alignment Kalman Filters for Inertial Stabilization Systems. *Proc. IEEE PLANS*, pages 321–334, 1992.

[163] P. Swerling. First Order Error Propagation in a State-Wise Smooting Procedure for Satellite Observations. *Journal of Astro. Sciences*, Vol 6:1–31, 1959.

[164] T. Takasu and A. Yasuda. Evaluation of RTK-GPS Performance with Low-cost Single-frequency GPS Receivers. *Proceedings of international symposium on GPS/GNSS*, 2008.

[165] T. Takasu and A. Yasuda. Development of the Low-cost RTK-GPS Receiver with an Open Source Program Package RTKLIB. *International Symposium on GPS/GNSS*, 2009.

[166] M. Tarhan and E. Altug. EKF based Attitude Estimation and Stabilization of a Quadrotor UAV using Vanishing Point in Catadioptric Images. *Journal of Intelligent & Robotic Systems*, Vol. 62, no. 3-4:pp. 587–607, 2011.

[167] P. J. G. Teunissen. Least-Squares Estimation of the Integer GPS Ambiguities. *Invited lecture, Section IV: Theory and Methodology, IAG General Meeting*, 1993.

[168] P. J. G. Teunissen. A New Method for Fast Carrier Phase Ambiguity Estimation. *Proc. IEEE PLANS'94*, pages pp. 562–573, 1994.

[169] P. J. G. Teunissen. The Least-Squares Ambiguity Decorrelation Adjustment: A Method for Fast GPS Integer Ambiguity Estimation. *Journal of Geodesy*, 70:65–82, 1995.

[170] P. J. G. Teunissen., P. J. de Jonge, and C. C. J. M. Tiberius. The LAMBDA-Method for Fast GPS Surveying. *GPS Technology Applications, international sympositum*, -:1–8, 1995.

[171] P. J. G. Teunissen, P. J. de Jonge, and C. C. J. M. Tiberius. The Volume of the GPS Ambiguity Search Space and its Relevance for Integer Ambiguity Resolution. *ION GPS 1996*, -:889 – 898, 1996.

[172] J. Thienel and R. M. Sanner. A Coupled Nonlinear Space Attitude Controller and Observer with an Unkown Constant Gyro Bias and Gyro Noise. *IEEE Trans. on Automatic Control*, Vol. 48:2011–2015, 2003.

[173] u Blox. Data sheet - LEA-6 Receiver Description - Including Protocol Specification, https://www.u-blox.com/images/downloads/Product_Docs/u-blox6_ReceiverDescriptionProtocolSpec_%28GPS.G6-SW-10018%29.pdf. Technical report, u-Blox, 2011.

[174] S. Verhagen and P. J. G. Teunissen. The Ratio Test for Future GNSS Ambiguity Resolution. *GPS Solutions*, 17:535–548, 2013.

[175] B. Vik. *Integrated Satellite and Inertial Navigation Systems (Lecture Notes)*. Department of Engineering Cybernetics, NTNU, 2012.

[176] B. Vik and T. I. Fossen. A Nonlinear Observer for GPS and INS Integration. *Proc. Conference on Decision and Control*, Vol. 3:2956–2961, 2001.

[177] R. M. Watson, V. Sivaneri, and J. N. Gross. Performance Characterization of Tightly-Coupled GNSS Precise Point Positioning Inertial Navigation wi-with a Simulation Environment. *AIAA Guidance, Navigation, and Control Conference*, pages 1–18, 2016.

[178] S. Weiss, M. Achtelik, M. Chli, and R. Siegwart. Versatile Distributed Pose Estimation and Sensor Self-calibration for an Autonomous MAV. *International Conference on Robotics and Automation (ICRA)*, 2012.

[179] J. Wendel, O. Meister, R. Mönikes, and G. F. Trommer. Time-Difference Carrier Phase Measurements for Tightly Coupled GPS/INS Integration. *IEEE/ION Position, Location, and Navigation Symposium*, 2016.

[180] J. Yan, C. C. J. M. Tiberus, G. J. M. Janssen, P. J. G. Teunissen, and G. Bellusci. Review of Range-Based Positioning Algorithms. *IEEE Aerospace and Electronic Systems Magazine*, pages 2–27, August, Part II 2013.

[181] D. Zachariah and M. Jansson. Self-motion and Wind Velocity Estimation for Small-scale UAVs. *International Conference on Robotics and Automation*, 2011.